Author:
Castillo Hernandez, Tania F

Title:
Study of polymeric micelles as a drug delivery system for carrier internalisation and cargo release in epithelial cell barriers

Study of polymeric micelles as a drug delivery system for carrier internalisation and cargo release in epithelial cell barriers

Tania Fernanda Castillo Hernandez

A dissertation submitted to the University of Bristol in accordance with the requirements for award of the degree of Doctor of Philosophy in the Faculty of Life Sciences

School of Biochemistry

May 2019

Word Count 35,675

Abstract

Many drugs have complex chemical properties which limit solubility in common solvents like water. Alternative formulations such as polymeric micelles formed by self-assembly of amphiphilic macromolecules may alleviate problems associated with bioavailability of poorly water-soluble drugs. The mechanisms underlying uptake and trafficking of polymeric micelles and the extent to which they are transported across epithelia remain largely unknown. This thesis provides insight into the nature of micellar drug delivery by focussing on the interactions of poloxamer P407 micelles and a model cargo with kidney and placental epithelia.

Fluorescent (RITC) poloxamer P407 micelles encapsulating DiO as a model fluorescent cargo were synthesised and characterised. The resultant micelles had a hydrodynamic diameter of 12nm and a critical micelle temperature of 25°C that was influenced by the presence of DiO. Fluorimetric analysis confirmed FRET between DiO and RITC that could be used to monitor cargo loading and release.

The kinetics of uptake and subcellular distribution of fluorescent micelles in epithelial cell lines (dog kidney MDCK and human placental BeWo b30 cells) was examined by confocal microscopy. Immunofluorescence identified punctate structures accumulating fluorescent micelles as late endosomes/lysosomes. Inhibition of receptor-mediated endocytosis partially blocked micelle uptake supporting the role of endocytosis in the process but suggesting the possible operation of alternative uptake pathways.

MDCK and BeWo b30 cells were grown on permeable Transwell supports and their development into polarised epithelia with significant barrier function confirmed by microscopy and electrical resistance measurements. Fluorescent micelles were taken up by both polarised cell barrier models but in MDCKs the extent of endocytosis appeared reduced compared to non-polarised cells. A minor proportion of apically applied DiO-loaded micelles was transported across both cell barriers. BeWo cells were also cultured under flow to mimic physiological conditions. Preliminary data indicated flow affected morphological and functional differentiation and accelerated micelle uptake.

Acknowledgements

I am extremely grateful to my supervisory team, Dr Mark Jepson, Dr Margaret Saunders, and Dr Sean Davis for their invaluable guidance, insights and support during my PhD. Thank you for sharing your thoughts and experience during those long meetings and making sure I stayed motivated, particularly when science was not being cooperative.

I would like to thank the Bristol Centre for Functional Nanomaterials and CONACyT in Mexico for the opportunity to enrich my scientific career with this priceless international opportunity. Particularly to Dr Annela Seddon for her support and guidance during all my time at the BCFN.

I would also like to thank the personnel of the Wolfson bioimaging facility whose help, and support helped me acquire all the skills I needed for my research. Thank you to Dr Katy Jepson for her support in the tissue culture lab and imaging. Thank you to Dr Dominic Alibhai and Dr Stephen Cross, the image analysis 'gurus' for always helping me figuring out how to make the most out of my data. Thank you to Dr Chris Neal, Mr Tom Stewart, and Mrs Judith Mantell for their support with my EM experiments.

Thank you to my BCFN 2014 cohort for sharing this PhD experience together. Especially to Dr Samuel Pearce, Dr Rosalia Cuahtecontzi, and Dr Omar Gomez for making my adaptation process so enjoyable.

I also wish to thank everyone in the C13 office for all the moral support and friendship during all these years. Thank you to Dr Lorna Hodgson for sharing her ideas, expertise and positivity in the lab, especially when science was not easy. Thank you to Miss Jen Coombs for all the chats about life, crochet afternoons, and for bringing Reuben to cheer us up. Thank you to Mr Hugh Tanner for always reminding me there is an easier way of thinking.

Thank you to my flatmates Sam Brooks, Andy James, and Rosy Cuahtecontzi for their friendship, for always cheering me up and making me feel at home.

A special thank you to my boyfriend Eduardo for his unconditional support and for being 'my rock' when things got complicated. Thank you for all the positiveness and for helping me becoming a better version of myself.

Finally, I would like to thank my parents and my sister for always being there to listen to my stories even on the other side of the screen. Their ambition, determination, love, and strength have always inspired me to become the scientist I am now.

Author’s declaration

I declare that the work in this dissertation was carried out in accordance with the requirements of the University's Regulations and Code of Practice for Research Degree Programmes and that it has not been submitted for any other academic award. Except where indicated by specific reference in the text, the work is the candidate's own work. Work done in collaboration with, or with the assistance of, others, is indicated as such. Any views expressed in the dissertation are those of the author.

SIGNED: ..... DATE:.....

Table of Contents

List of Figures

List of Tables

List of Equations

Abbreviations

Amp B	Amphotericin B
BCPs	Block copolymers
BSA	Bovine serum albuminum
BeWo b30	Human placenta choriocarcinoma cells (subclone b30)
CDI	N,N0-carbonyldiimidazol
CLSM	Confocal laser scanning microscopy
CMC	Critical micellar concentration
CMT	Critical micellar temperature
CNTs	Carbon nanotubes
DiO	3,3'-dioctadecyloxacarbocyanine perchlorate
DLS	Dynamic light scattering
DMEM	Dulbecco's modified Eagle's medium
EDTA	Ethylendiaminetetraacetic acid
EMEM	Eagle's minimal essential medium
EPR	Enhanced permeability and retention
FBS	Fetal bovine serum
FRET	Fluorescence resonance energy transfer
FSS	Fluid shear stress
HD	Hydrodynamic diameter
HDMS	Hexamethyldisilazane
IJ	Intercellular junctions
LD	Lipid-droplets

LUT	Look-up table
MDCK	Madin-Darby canine kidney
MiTMAB	Myristyl trimethyl ammonium bromide
MV	Microvilli
NA	Numerical aperture
NCs	Nanocarriers
NEAA	Nonessential amino acids
NPs	Nanoparticles
PA	Peri-juntional actin
PBS	Phosphate-buffered saline
PDI	Polydispersity index
PE	Polyester
Pe	Permeability coefficient
PFA	Paraformaldehyde
PSLG	Penicillin streptomycin L-glutamine
RITC	Rhodamine B isothiocyanate
RME	Receptor-mediated endocytosis
ROI	Region of interest
SEM	Scanning electron microscopy
TBCPs	Triblock copolymers
TEER	Trans epithelial electrical resistance
TEM	Transmission electron microscopy
TJ	Tight junctions
WD	Working distance

Chapter 1. Introduction

This chapter will introduce the concepts that outline the foundations and motivations of this work as well as the structure of this thesis. First, an overview of the drug-encapsulation formulations most commonly used in nanomedicine will be presented. Then, the drug delivery properties of polymeric micelles will be explained as well as the relevance of using triblock copolymers as drug delivery models. The cellular uptake mechanisms, found so far, of such drug delivery models will be then discussed to explain the importance and key requirements for developing *in vitro* models to test carrier internalisation and drug release in epithelial cell barriers.

1.1 Nanoencapsulation for drug delivery

Over the past decades, the use of nanoparticles has become an important option for drug delivery systems. Many drugs of potential interest for treatment of several diseases such as cancer, schizophrenia or epilepsy[1] have a complex chemical formulation which may compromise their solubility in common solvents like water. This insolubility compromises drug bioavailability in the organism and thus their therapeutic value. Nanoencapsulation using nanocarriers (NCs) has proved to be a viable method for delivering drugs in the body by increasing their solubility, efficacy, specificity, and targeting capacity[1,2]. Furthermore, such drug delivery systems, have been shown to increase the therapeutic effect of the drugs by specifically delivering them to targets, thus minimising toxic side effects[2–4]. The principal factors dictating NC uptake by cells and penetration into biological barriers are their size distribution, their surface chemistry and charge as well as their drug release mechanisms[5–8].

The most commonly used NCs are carbon nanotubes (CNTs), dendrimers, liposomes, and micelles (Figure 1.1). Carbon nanotubes consist of cylinders formed from graphene sheets. Because of their hollow structure, CNTs have been successfully used to encapsulate a wide range of water insoluble anticancer drugs such as doxorubicin, paclitaxel, and carboplatin[9–11]. Dendrimers are monodispersed, branched and multivalent molecules. These molecules have been used as NCs since drug molecules can be covalently or ionically attached to their surface or encapsulated in their hydrophobic cores[1,12]. Dendrimers have been shown to effectively

encapsulate anticancer drugs (paclitaxel and doxorubicin) and anti-inflammatory drugs such as flurbiprofen[13–15]. Liposomes are spherical particles made of phospholipid bilayer which have been used as drug delivery systems in order to avoid any drug toxicity by protecting drugs from degradation[16]. Examples of encapsulated drugs in liposomes are ciprofloxacin and doxorubicin[17,18]. Polymeric micelles are being studied as NCs because of their small size and high stability[19]. These micelles have successfully encapsulated many drugs such as cyclosporine, paclitaxel and other anticancer dugs[20–22].

This thesis focuses on the study of polymeric micelles as drug delivery systems.

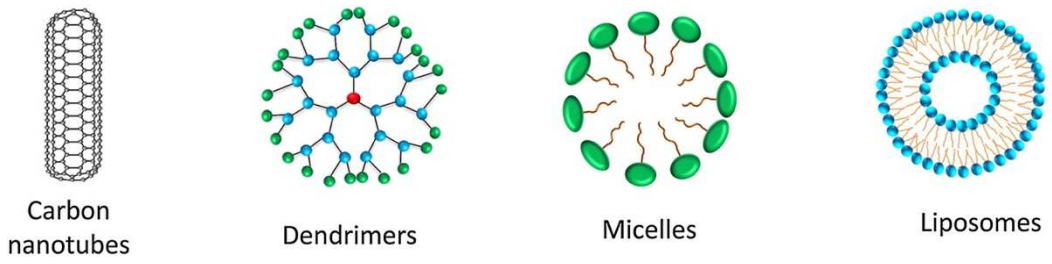

Figure 1.1 *Commonly used nanocarriers for drug delivery. Figure adapted from Hossen et al.[23] under CC license.*

1.2 Polymeric micelles

Micelles are self-assembled colloids of amphiphilic molecules usually between 5 and 100 nm diameter[24] which form spontaneously at specific temperatures (critical micellar temperature, CMT) and concentrations of solute (critical micellar concentration, CMC). Since amphiphilic molecules contain both hydrophobic and hydrophilic properties simultaneously, the driving force responsible for such self-assembly relies on the difference in affinity of the polar and non-polar groups with the solvent[25]. When the solvent consists of an aqueous solution, the amphiphilic molecules orientate so their hydrophobic parts are sheltered in the core of a micelle leaving the hydrophilic groups exposed and thus reaching a state of minimum free energy (Figure 1.2). Micelle formation is thermodynamically favoured relative to its disassembly when the amphiphile is found in solution above a particular concentration, CMC, and temperature, CMT. At lower concentration and temperature values than the CMC and CMT respectively, the micelles disassemble at a specific rate depending on the nature of the amphiphilic molecule[24,26,27]. Polymeric micelles are a type of micelles made from amphiphilic block copolymers and characterised by their low CMC[25,28]. In aqueous environments, the hydrophobic blocks of the copolymer assemble forming the hydrophobic core of the micelle and the hydrophilic blocks of the polymer assemble to form the corona. The core of the micelles represents a highly hydrophobic microenvironment commonly used for incorporation of hydrophobic solutes. In these cases, the micelle corona

acts as an interface for stabilisation of the hydrophobic core and the solvent[26].

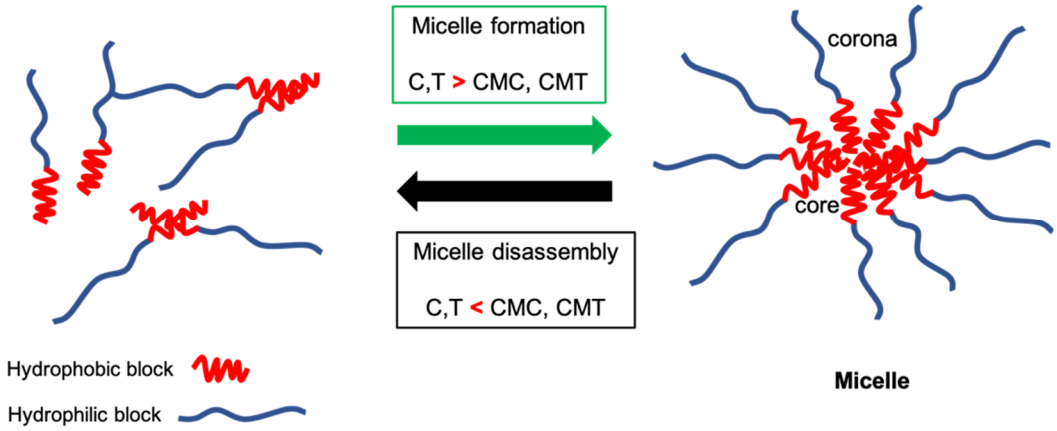

Figure 1.2 *Diagram of micelle formation and disassembly in an aqueous solvent*

1.2.1 Drug delivery function of polymeric micelles

Historically, the number of formulation approaches has been limited for drugs that are poorly soluble in water and are non-ionisable, as ionisable drugs can be formulated as salts[29]. The next alternative for produce formulations with water-insoluble drugs is the use of cosolvents (e.g. ethanol, propylene glycol, polyethylene glycol) but there is a solvent toxicity limit in those cases. The more recent approach to address the delivery of water-insoluble drugs is the use of encapsulating agents. There are examples of formulations where the surfactant used resulted to be biologically active and led to market retrievals[30,31]. These issues have driven the research efforts towards developing drug delivery systems using polymeric micelles. The most common administration of polymeric micelles is by injection into the blood stream for tumour targeting therapies. Once injected, the corona of the micelles protects the interactions of the encapsulated drug with the blood components[32]. Furthermore, the polymer used for encapsulation reduces the recognition by the reticuloendothelial system prolonging circulation of the micelles in the blood system[32,33]

1.2.1.1 Drug targeting mechanisms in polymeric micelles

After blood administration, polymeric micelles extravasate and deliver their cargo selectively by accumulating into the tissue of interest by enhanced permeability and retention (EPR) effect[34,35]. This last delivery process is known as passive targeting[32,34,36] (Figure 1.3 a). Passive

targeting has proven to happen in tissues with pathological conditions such as tumours or infarcts where the tissue presents inflammation or hypoxia[37]. These unhealthy tissues present characteristics such as leaky vessels with larger intercellular gaps (Figure 1.3 a) as well as reduced lymphatic drainage facilitating the retention of polymeric micelles[38,39].

Alternatively, specific targeting can be achieved by active targeting. This consists on functionalising the hydrophilic block of the polymer with specific ligands or antibodies interacting with the receptors of the target tissue [40–43] (Figure 1.3b). These interactions ensure selective accumulation of the micelles in target tissues decreasing potential side effects in other tissues[34,44].

Another alternative for targeting is the incorporation of specific fragments sensitive to temperature, pH or to specific chemical reactions such as redox or enzymatic reactions[45–48]. In this case, polymeric micelles become stimuli-responsive and may interact chemically to specific conditions found in the cells or external stimuli such as heat, light, magnetic field or ultrasound[37]. This has important implications for controlling the drug release from the micelles.

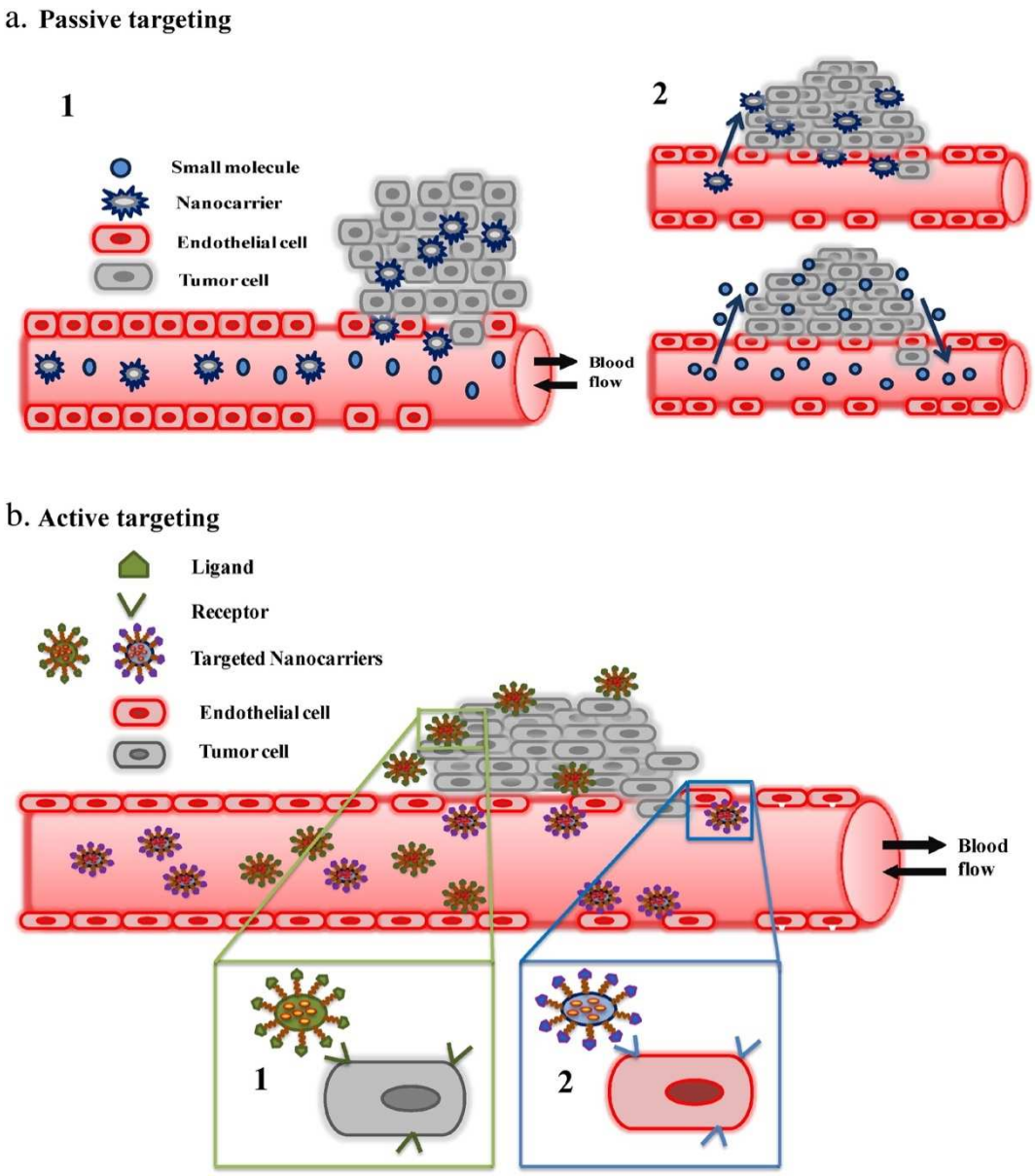

Figure 1.3 *Schematic representation of targeting mechanisms of polymeric micelles when administrated into the blood stream. Polymeric micelles can reach the targeted tissue via passive targeting* ***(a)****. Particles can enter cancerous tissue via leaky vessels surrounding the tumour* ***(a1)****. In this case, the size of the particle administrated determines the retention in the targeted tissue* ***(a2)****. Low molecular weighted particles can diffuse in and out of the blood vessels causing their effective concentration in the tissue to decrease fastly. Contrarily, high molecular weight particles, such as polymeric micelles, cannot permeate back easily to the blood stream leading to progressive accumulation (EPR effect). Alternatively, polymeric micelles can reach the targeted tissue by active targeting* ***(b)*** *where a ligand attached to the surface of the carrier binds to cell membrane receptors overexpressed by cancer cells* ***(b1)*** *or angiogenic endothelial cells* ***(b2)****. Image reprinted with permission from Biswas et al.*[32]

1.2.1.2 Drug release mechanism of polymeric micelles

Drug encapsulation into micelles happens by chemical conjugation or by physical entrapment of the hydrophobic drug into the hydrophobic core of the micelle[49]. When the drug is physically entrapped into the micelles, release happens via diffusion. Thus, the release depends on the partition coefficient between the core of the micelle and the aqueous solvent[1]. Some stimuli responsive micelles have been engineered to release the drug into cells after being internalised by applying external stimuli. Other polymeric micelles rely on the intercellular stimuli, such as pH changes to release their cargo[50].

1.2.2 Block copolymers

Block copolymers (BCPs) are amphiphilic molecules able to self-assemble in solution into different structures, most notably micelles. BCPs are formed of at least two monomers with different chemical structures conferring them different affinities to the solvent. These monomers can group into blocks which can be combined in different ways to form various types of BCPs. The type of combination of these blocks allows the classification of BCPs into diblock, triblock or multiblock copolymers[51] (Figure 1.4). Diblock copolymers are the simplest type of BCP. They are formed of two different blocks linearly arranged (AB configuration) (Figure 1.4 A). Triblock copolymers (TBCPs) are also linear structures formed of two or three different blocks arranged as ABC or ABA configurations (Figure

1.4 B). Multiblock copolymers are BCPs with more than three consecutive blocks aligned to form either a linear or branched structure[52] (Figure 1.4C).

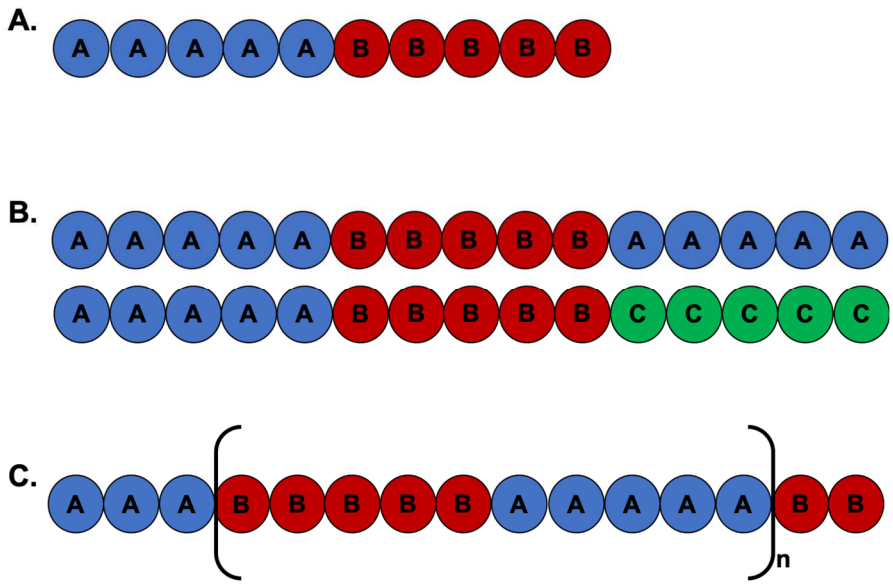

Figure 1.4 *Classification of block copolymers.* ***(A)*** *AB type diblock copolymer* ***(B)*** *ABA and ABC types of triblock copolymers* ***(C)*** *$(AB)_n$ type multiblock copolymers.*

1.2.2.1 Poloxamer block copolymer

Poloxamers are a class of non-ionic TBCPs also known as Pluronics®. Poloxamers are made of poly(ethylene-oxide) (PEO) and poly(propylene-oxide) (PPO) blocks arranged into an ABA type configuration[53–55] (Figure 1.5 A). This structure is arranged in a way that the hydrophilic groups are terminal groups (PEO) of the chain with the hydrophobic group in between (PPO). The general formula of these polymers can be expressed as $PEO_{m/2}$ -PPO_n -$PEO_{m/2}$ where m and n are the average of PEO and PPO monomers respectively[34]. The properties of the specific poloxamer depends on the total molecular weight and the relative ratio of the PEO and PPO monomers. For

the purpose of drug delivery and solubilisation in general, the number of PEO and PPO blocks in the polymer are key parameters to consider when selecting a poloxamer as carrier system. Table 1.1 presents the number of PEO and PPO blocks sound in various commercially available Pluronics®. The self-assembly of poloxamer units into micelles in aqueous solution has been thoroughly studied[56]. Self-assembly of the polymer into micelles is promoted by increasing the temperature, at a given concentration. This thermo-responsive property has had an important impact on the design of drug delivery systems[53,57]. Additionally, the PEO terminal chain has shown to facilitate the functionalisation of the micelles for active targeting[53]. Furthermore, the degradation of these polymers in biological systems results in non-toxic monomers making these TBCPs good candidates for drug encapsulation[58,59] (Figure 1.5 B).

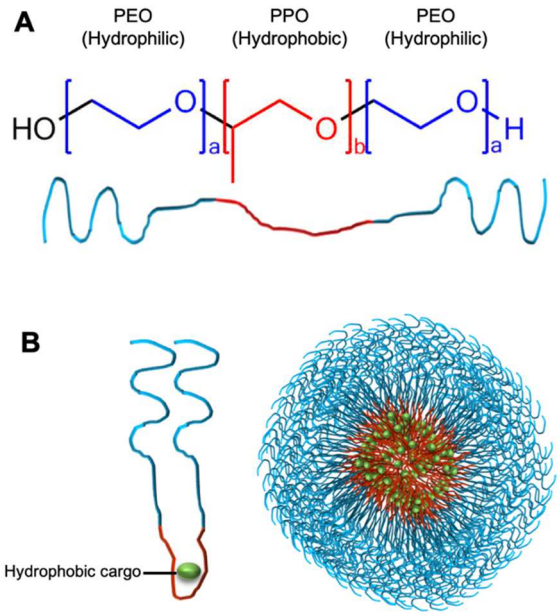

Figure 1.5 *Diagram of poloxamer P407 micelles.* ***(A)*** *P407 triblock copolymer A-B-A structure with two PEO hydrophilic end blocks (blue) and one hydrophobic middle PEO block (red)* ***(B)*** *Micelle encapsulating a hydrophobic cargo (green).*

Table 1.1 *List of commercially available Pluronics® TBCPs used for drug formulations. Data obtained from Alexandridis et al.*[56]

Pluronic®	MW (g/mol)	PPO monomers (m)	PEO monomers (n)
L64	2900	30	26
P65	3400	17	36
P84	4200	43	38
P85	4600	40	52
F88	11400	39	206
P103	4950	60	34
P104	5900	61	54
P105	6500	56	74
F108	14600	50	264
P123	5750	69	38
F127	12600	65	200

1.2.2.2 Poloxamer P407 micelles a model to study carrier internalisation and drug release

This research has focussed specifically on Poloxamer 407 (P407) also known as Pluronic® F127. The structure of this polymer consists of two large external chains of approximatively 100 PEO monomers with a shorter chain of approximatively 65 PPO monomers in the middle. The triblock arrangement favours the polymer to fold itself forming a “U-shaped” configuration with the hydrophilic side tails aligned together and the hydrophobic middle chain in the middle of the U (Figure 1.5 B). In aqueous

solution, the hydrophobic middle chains, made of PPO, self-assemble with other hydrophobic chains from other polymer strands. This leaves the hydrophilic PEO side tails exposed to the aqueous solution. The PEO long side tails act as a protection shield for the PPO middle chains. When this polymer reaches its CMC and CMT in solution, a micellar structure is formed by self-assembly. (Figure 1.5 B). This way, the polymer allows to trap water insoluble particles in the core of the self-assembled micelles. As part of the poloxamer classification, P407 micelles have shown thermo-responsive micellisation at physiological temperatures (Table 1.2). Furthermore, this polymer has been approved for use by the U.S Food and Drugs Administration (FDA)[57,60].

An extensive number of works using Poloxamers to facilitate drug transport in epithelial cells are reported in literature. Relevant examples are presented here. One of the most pioneering findings on epithelial cells was made by Batrakova *et al*[61,62] where *in vitro* studies examined the effects of Pluronics® block copolymers on drug absorption and permeability in Caco-2 monolayers. This study was then performed *in vivo* by Banerjee *et al.*[63]. In both cases, evidence showed that Pluronic block copolymers increased oral absorption of selected drugs by inhibiting drug efflux systems in intestinal epithelial cells[54]. Nidhi *et al.*[64] tested the effects of F127/chitosan mixed micelles on the delivery of dexamethasone trough the corneal epithelial membrane. This study resulted on the improvement of the intraocular absorption of dexamethasone due to the enhancement of the permeability of the corneal membrane facilitated by encapsulation with F127 and chitosan[64]. More recently, the focus of encapsulating drugs into

Poloxamer micelles has been to overcome the epithelial mucus barrier. This barrier can be found in various parts of the body critical for drug delivery such as the respiratory, gastro-intestinal, and female genital tracts as well as in nasal passages and eyes[65]. Notably, P 407 has been used successfully to coat acyclovir monophosphate nanoparticles which resulted in enhanced penetration into mucus[66]. All these successful findings on Poloxamer micelles and especially P407 illustrate the importance and potential of understanding the properties behind their internalisation mechanisms in epithelial cell barriers.

Table 1.2 *Variations of CMT for P407 at different concentrations. Data obtained from Alexandridis et al.* [56]

Concentration (% w/v)	**CMT (ºC)**
0.025	35.5
0.05	33
0.1	31
0.25	28
0.5	26.5
1.0	24
2.5	21.5
5.0	19.5

1.2.2.3 Lipophilic fluorescent dye for micelle loading

In this work, P407 micelles were loaded with a lipophilic fluorescent dye, 3,3'-dioctadecyloxacarbocyanine perchlorate (DiO) (excitation:484, emission 501). This dye belongs to the family of cyanine dyes commonly used to fluorescently label lipid bilayers[67]. The positively charged rings of DiO confers it the fluorescence properties while the long carbon chains are responsible of its hydrophobic properties[68](Figure 1.6). DiO dissolves in cell membranes by inserting its hydrophobic tail into the phospholipid membrane. This dye labels entirely the cell membrane and resides stably for long periods of time (up to 24 hours)[69]. Together with its analogue dye 1,1'-dioctadecyl-3,3,3',3'-tertamethylindocarbocyanine perchlorate (DiI), DiO is one of the most commonly used dyes for fluorescence resonant energy transfer studies[70,71].

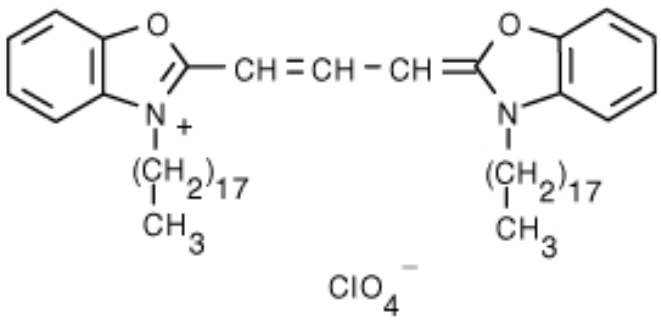

Figure 1.6 *Chemical structure of DiO.*

1.3 Cellular uptake mechanisms of polymeric micelles

1.3.1 Overview of cell uptake mechanisms

Cellular uptake is the process by which particles or nutrients, from the external milieu, are internalised by cells via passive or active transport mechanisms. Active transport is achieved when the cellular membrane compartmentalises to form vesicles encapsulating particles or nutrients before being transported to different cell organelles. This internalisation process is also called endocytosis and it can be subdivided into two categories, depending on the size of the particles, phagocytosis 'cell eating' and pinocytosis 'cell drinking'. Whilst phagocytosis occurs only in specialised cells, as part of the immune system, pinocytosis occurs in most eukaryotic cells[72]. Pinocytosis can occur through distinct mechanisms differentiated by the proteins involved in the entry processes, the primary classification being into clathrin-dependent or -independent mechanisms.

Clathrin-dependent uptake, also referred to as clathrin-mediated endocytosis, is one of the most studied endocytic mechanisms. This mechanism is one of the most important for nutrient internalisation in cells[73]. In clathrin-mediated endocytosis, membrane pits are coated with clathrin-cages. These cages represent recognition sites for different cargoes and add structural properties for internalisation veiscles[74]. The particles internalised via this method have diameters < 300 nm[72]. Clathrin independent processes do not involve clathrin cages. However, a similar type of endocytosis is caveolin-mediated endocytosis. This process

involves pits coated with caveolin proteins (caveolin-1 and 2) and, along with clathrin-mediated endocytosis, is part of receptor mediated endocytosis mechanisms. Particles with diameters < 80 nm have shown to undertake this mechanism of entry in cells[72,75]. Another clathrin-independent internalisation pathway of nutrients and particles is by macropinocytosis. This mechanism involves plasma membrane deformations engulfing external fluid to form macropinosomes. This process is actin-regulated and independent from the interaction of membrane receptors and cargoes[76]. All the processes mentioned so far, transport the internalised particles to early endosomes. After entering early endosomes, the cargo is transported into late endosomes to be finally transported into lysosomes for degradation. However, some particles in the clathrin and caveolae coated pits can be transcytosed without reaching the endosomes[77,78] (Figure 1.7). Other clathrin-independent internalisation mechanisms such as Arf6, Flotillin, Cdc42, and RhoA-dependent endocytosis (Figure 1.7 and Figure 1.8) have little relevance for the purpose of this work but can be found in other reviews[72,79].

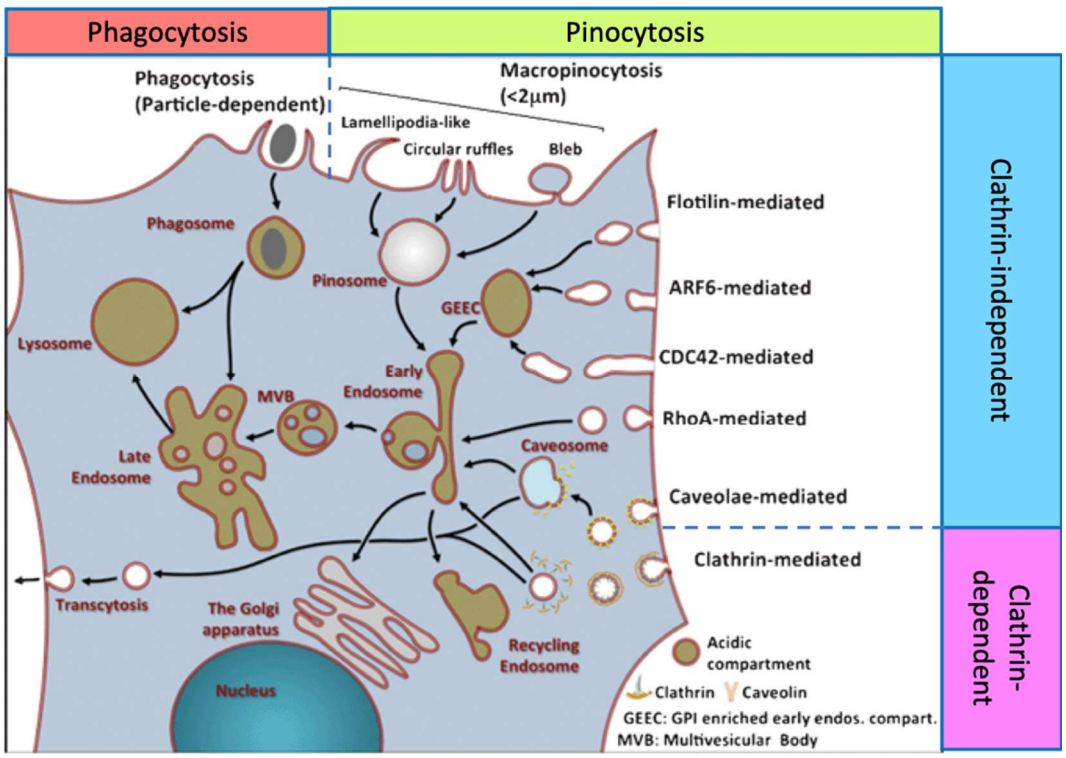

Figure 1.7 *Mechanisms of different endocytosis uptake mechanisms in typical eukaryotic cells. Image adapted with permission from Canton et al.*[72]

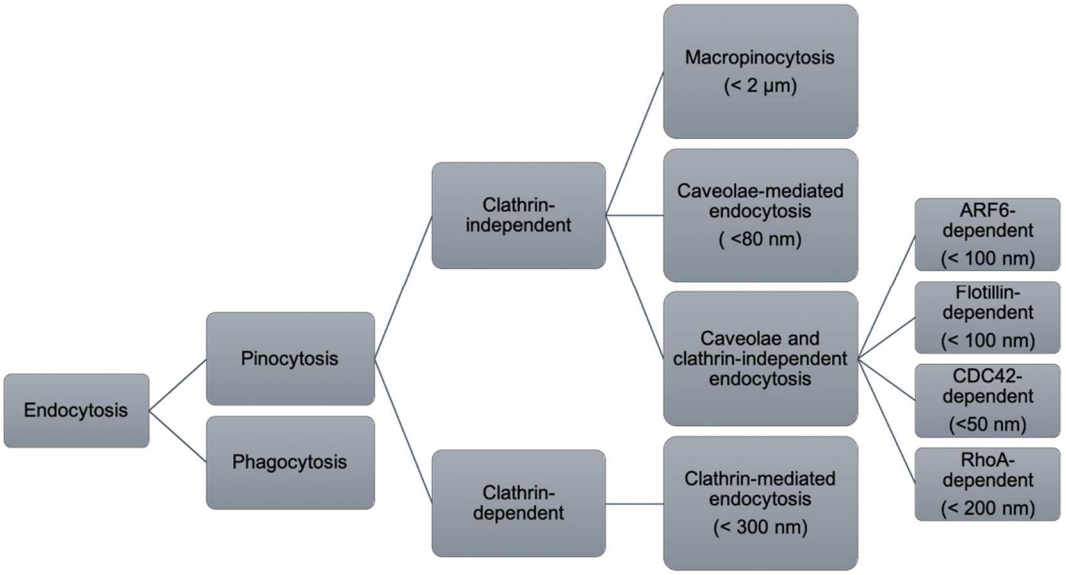

Figure 1.8 *Classification of different endocytic mechanisms.*

1.3.2 Cellular uptake mechanism of polymeric micelles

TBCPs have previously been shown to enter mammalian cells through different mechanisms depending on the micellisation of the polymer. Below the CMC, when the polymer has not self-assembled into micelles, unimers can enter cells through caveolae mediated endocytosis. In cells lacking caveolae such as polarised MDCK cells[80,81], unimers are internalised via caveolae independent pathways[79]. When micelles are present, above the CMC, the internalisation happens via clathrin-mediated endocytosis. Under these conditions, caveolae mechanism are disrupted by the high number of TBCPs interacting with the membrane while this does not affect the clathrin-mediated pathway[79,82] (Figure 1.9).

Additionally, TBCPs have shown sealant and permeabilising effects on the cellular membrane (Figure 1.10). This two-state mechanism acts on the basis that initially unimers adsorb on the membrane conferring a sealing effect. Successively, unimers are inserted into the lipid-bilayer opening up pores causing membrane permeabilisation. These two effects are seen with all Pluronics® polymers. However, the transition between adsorption and insertion depends on the hydrophilic-hydrophobic balance of the specific polymer[83–85].

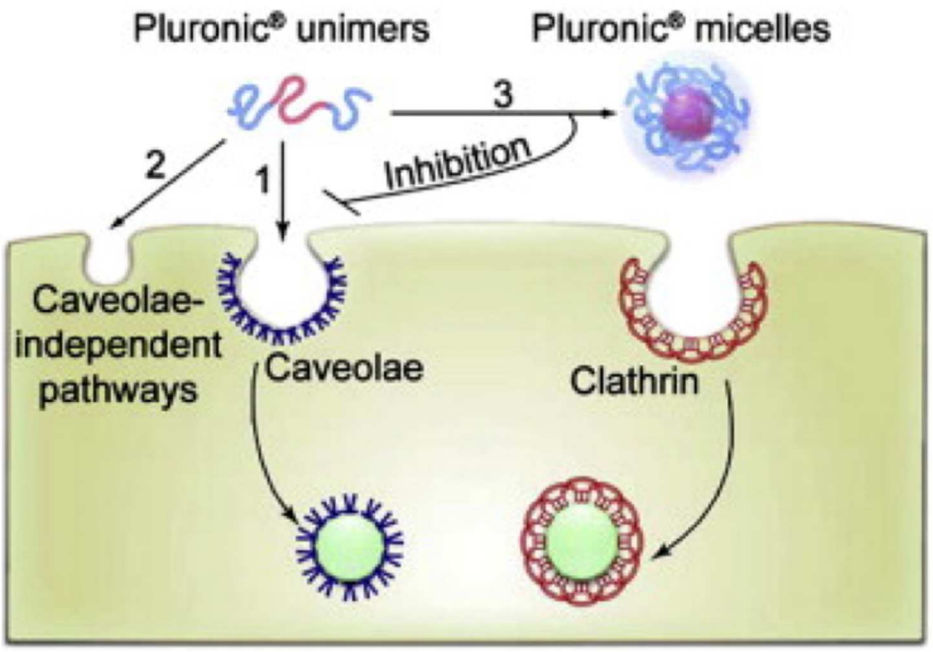

Figure 1.9 *Mechanism of uptake of Pluronic ® unimers and micelles* ***(1)*** *in epithelial cells.* ***(2)*** *In cells lacking caveolae, such as confluent MDCK cells unimers can be internalised through caveolae-independent pathways.* ***(3)*** *Above the CMC, the high concentration of polymer inhibits caveolae mediated endocytosis and micelles enter through clathrin-mediated endocytosis. Image adapted with permission from Sahay et al.*[79]

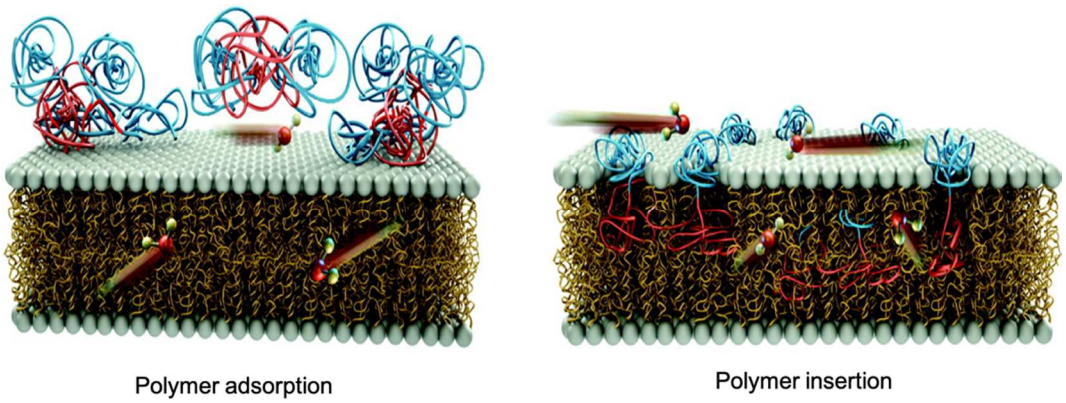

Figure 1.10 *Adsorption and insertion of Pluronic® polymers into lipid bilayers. Figure adapted from Cheng et al.*[83]

1.4 Cell barrier models

1.4.1 Biological barriers

Biological barriers are responsible for separating two compartments in different organs of the body. These barriers can be formed by epithelial or endothelial cells. Epithelial cells are present in external and internal organs of the body while endothelial cells are only found in the interior of lymphatic and blood vessels and are considered to be specialised epithelial cells[86]. One of the main challenges in drug delivery is to overcome these biological barriers to effectively transport therapeutics into specific organs or tissues[87,88]. These barriers are made of confluent cells expressing intercellular tight junctions separating apical and basolateral membrane compartments[89]. Endocytic pathways can differ substantially between apical and basolateral membranes[90–93]. In order to cross biological barriers, drug delivery particles need to enter the cells using via endocytic pathways on the apical side followed by transcytosis to the basal side[94–96]. Having raised these challenges for particles crossing biological barriers, it is important to develop *in vitro* models expressing tight junctions and polarised cells to study their interactions with drug delivery systems. This work focuses on biological barriers made of epithelial cells (placenta and kidney). Examples of previous studies using epithelial cell models to study drug delivery can be found in literature[97–101].

1.4.2 Cell polarity and barrier development

Cell polarity refers to the morphological and functional differences seen between distinct regions of a cell. This is characterised in epithelial cells by the asymmetry between two opposite sides of the cell membrane (apical and basolateral sides)[102]. The presence of these two membrane domains in cells are responsible of the polarisation of organelles seen in developed epithelial barriers and are regulated by the formation of a junctional complex at the apical-lateral border of cells[103]. The intercellular junctional complex is specific to polarised epithelial cells and is essential to the establishment of the epithelium and its function as a paracellular barrier[102]. The intercellular junctional complex consists of tight junctions, adherens junctions, and desmosomes, described in more detail in chapter 5.

Cell polarisation can be obtained by applying an external gradient such as nutrient gradient or a mechanical force (blood flow). When external cues are applied to cells, actin concentrates in one side of the cell creating membrane protrusions (microvilli) affecting the membrane tension and causing the inhibition of the microvilli formation in the opposite side of the cell. This triggers actin rearrangements within the cells resulting in the morphological differences seen in polarised cells[104–106]. Following the idea of using a nutrient gradient as an effector for cell polarisation, it is possible to obtain polarised cell models by growing them on permeable membrane filters [101,107–110] (chapter 5).

1.4.3 Fluid shear stress (FSS) and barrier development

As mentioned in section 1.4.2, external mechanical stimuli can induce structural reorganisation of cells having important implications for development of cell barrier models. Fluid shear stress (FSS) has been used in *in vitro* models to reproduce the vascular blood flow in tissues. This mechanical stress is a tangential force exerted on cells by applying a laminar flow onto the apical surface of cells[111]. FSS has been shown to trigger the formation of microvilli on the apical surface of the cells [112]. This has implications on the barrier differentiation since these membrane protrusions are present on differentiated epithelial cells *in vivo*. Additionally, in human placenta cells, FSS has been shown to affect expression and localisation of membrane transport proteins such as glucose transporters which are essential for placental barrier function and development[113]. FSS has also been shown to affect regulation of permeability in endothelial barriers [114]. Furthermore, FSS plays a key role in cell differentiation of cells into cells found in *in vivo* barriers alongside promoting formation of tight junctions, cell division and expression of multidrug resistance transporters[111]. All these features developed by applying a FSS on cells suggest the potential importance of incorporating such stimulus into *in vitro* models in order to obtain models reproducing *in vivo* conditions specially for drug transport experiments. This can be achieved by using microfluidics devices[112,115–118].

1.4.4 Kidney barrier model

The kidney barrier is the interface regulating the transport between urine and blood in the kidney. This model is based on the reproduction of a renal proximal tubule using MDCK cells[119]. MDCK cells were first isolated by S. H. Madin and N. B Darby in 1958 from the kidney tubule of a normal adult Cocker Spaniel[120]. MDCK cells grown on permeable supports develop tight junctions making them a good model to study transepithelial transport[107,121] and clearly differentiated apical and basolateral membranes allowing their use to study the differences between apical and basal endocytosis in epithelial cells[93,99,122]. MDCK cells represent one of the most characterised cell lines and are commonly used to model the renal epithelial barrier and as a more general model of epithelial transport in other locations including gastrointestinal and nasal tissues[120].

1.4.5 Human placental cell barrier model

The placental barrier acts as an interface between the mother and the foetus. During pregnancy, the main role of the placenta is to allow the transfer of nutrients and oxygen, from the maternal blood to the foetus, as well as the waste from the foetus to the mother for excretion. The placenta allows particles under 300 nm to cross and enter foetal circulation[123]. This highlights the importance of studying particle transport across this biological barrier to human health. The placental model used in this thesis is based on the immortalised BeWo b30 cell line. This cell line was first isolated in 1968 from a human choriocarcinoma (a trophoblastic cancer) by Pattillo and Gey[124]. This cell line expresses transferrin receptors, tight junctions, and chemokines receptors which makes it a suitable model for the study of nanoparticle transport across the placenta[100,125,126]. Furthermore, upon differentiation, trophoblastic cells have shown syncytiotrophoblast cells properties. These cells can be found in the intervillous space of the maternal blood[115] (Figure 1.11) acting an interface between maternal blood and foetal extracellular fluid facilitating material exchange.

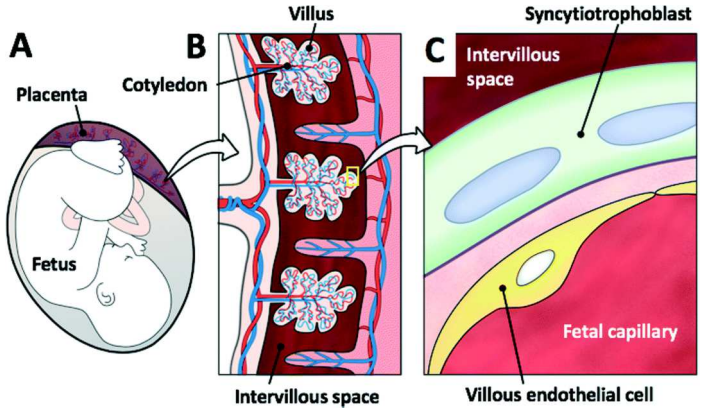

Figure 1.11 (A) *Schematic of a human foetus and placenta.* ***(B)*** *Cross-sectional view of the placenta showing the placental villus in contact with the maternal blood.* ***(C)*** *Surface of a placental villus containing differentiated trophoblasts into syncytiotrophoblasts. Image adapted with permission from Blundell et al.*[115]

1.5 Aims and objectives

Polymeric micelles represent a promising vector for delivering hydrophobic drugs into the body. In order to design new micellar drug delivery systems and assess their efficacy it is essential to first understand their interactions with cells and tissues in the human body. Previous work has provided evidence that triblock copolymers can effectively incorporate hydrophobic drugs and carry these into cells but relatively little is known about the mechanisms underlying their uptake and trafficking or the extent to which they are transported across epithelia.

This thesis provides insight into the nature of micellar drug delivery by focussing on the interactions of poloxamer P407 micelles and a model cargo with kidney and placental epithelia. This was accomplished by undertaking a series of experiments with the following objectives:

1. To develop and characterise a micellar drug delivery model based on poloxamer P407, its fluorescent derivative (RITC-P407) and the hydrophobic fluorophore DiO as model cargo.
2. To investigate the uptake mechanisms of P407-DiO micelles into non-polarised epithelial cells (BeWo b30 and MDCK) using advanced microscopy and biochemistry techniques.
3. To explore more complex tissue culture techniques for developing *in vitro* models capable of mimicking features found in fully developed placental and kidney barriers and use these to assess particle transport and test the hypothesis that P407-DiO uptake is affected by the differentiation state of epithelial cells.

1.6 References

1. Kumari, A., Singla, R., Guliani, A. & Yadav, S. K. Nanoencapsulation for drug delivery. *EXCLI J.* **13**, 265–286 (2014).

2. Soppimath, K. S., Aminabhavi, T. M., Kulkarni, A. R. & Rudzinski, W. E. Biodegradable polymeric nanoparticles as drug delivery devices. *J. Control. Release* **70**, 1–20 (2001).

3. Pereverzeva, E. *et al.* Toxicological study of doxorubicin-loaded PLGA nanoparticles for the treatment of glioblastoma. *Int. J. Pharm.* **554**, 161–178 (2019).

4. Malam, Y., Loizidou, M. & Seifalian, A. M. Liposomes and nanoparticles: nanosized vehicles for drug delivery in cancer. *Trends Pharmacol. Sci.* **30**, 592–599 (2009).

5. Kumari, A., Yadav, S. K. & Yadav, S. C. Biodegradable polymeric nanoparticles based drug delivery systems. *Colloids Surf. B. Biointerfaces* **75**, 1–18 (2010).

6. Yoo, H. S., Oh, J. E., Lee, K. H. & Park, T. G. Biodegradable nanoparticles containing doxorubicin-PLGA conjugate for sustained release. *Pharm. Res.* **16**, 1114–1118 (1999).

7. Singh Suri, S., Fenniri, H. & Singh, B. Nanotechnology-based drug delivery systems. *J. Occup. Med. Toxicol. 2007* **2**, 1–6 (2007).

8. Verma, A. & Stellacci, F. Effect of surface properties on nanoparticle-cell interactions. *Small* **6**, 12–21 (2010).

9. Niu, L., Meng, L. & Lu, Q. Folate-conjugated PEG on single walled carbon nanotubes for targeting delivery of doxorubicin to cancer cells. *Macromol. Biosci.* **13**, 735–744 (2013).

10. Liu, Z. *et al.* Drug delivery with carbon nanotubes for in vivo cancer treatment. *Cancer Res.* **68**, 6652–6660 (2008).

11. Hampel, S. *et al.* Carbon nanotubes filled with a chemotherapeutic agent: A nanocarrier mediates inhibition of tumor cell growth. *Nanomedicine* **3**, 175–182 (2008).

12. Crampton, H. L. & Simanek, E. E. Dendrimers as drug delivery vehicles: non-covalent interactions of bioactive compounds with dendrimers. *Polym. Int.* **56**, 489–496 (2007).

13. Li, X., Takashima, M., Yuba, E., Harada, A. & Kono, K. PEGylated PAMAM dendrimer-doxorubicin conjugate-hybridized gold nanorod for combined photothermal-chemotherapy. *Biomaterials* **35**, 6576–6584 (2014).

14. Asthana, A., Chauhan, A. S., Diwan, P. V. & Jain, N. K. Poly(amidoamine) (PAMAM) dendritic nanostructures for controlled sitespecific delivery of acidic anti-inflammatory active ingredient. *AAPS PharmSciTech* **6**, E536–E542 (2006).

15. Ooya, T., Lee, J. & Park, K. Effects of ethylene glycol-based graft, star-shaped, and dendritic polymers on solubilization and controlled release of paclitaxel. in *Journal of Controlled Release* **93**, 121–127 (2003).

16. Vemuri, S. & Rhodes, C. T. Preparation and characterization of liposomes as therapeutic systems : a review delivery N ,/? **70**, 95–111 (1995).

17. Luo, D. *et al.* Doxorubicin encapsulated in stealth liposomes conferred with light-triggered drug release. *Biomaterials* **75**, 193–202 (2016).

18. Karathanasis, E., Ayyagari, A. L., Bhavane, R., Bellamkonda, R. V & Annapragada, A. V. Preparation of in vivo cleavable agglomerated liposomes suitable for modulated pulmonary drug delivery. *J. Control. Release* **103**, 159–175 (2005).

19. Yamamoto, T. *et al.* What are determining factors for stable drug incorporation into polymeric micelle carriers? Consideration on physical and chemical characters of the micelle inner core. *J. Control. Release* **123**, 11–18 (2007).

20. Grimaudo, M. A. *et al.* Poloxamer 407/TPGS Mixed Micelles as Promising Carriers for Cyclosporine Ocular Delivery. *Mol. Pharm.* **15**, 571–584 (2018).

21. Singleton, W. G. *et al.* Convection enhanced delivery of panobinostat (LBH589)-loaded pluronic nano-micelles prolongs survival in the F98 rat glioma model. *Int. J. Nanomedicine* **12**, 1385–1399 (2017).

22. Gothwal, A., Khan, I. & Gupta, U. Polymeric Micelles: Recent Advancements in the Delivery of Anticancer Drugs. *Pharmaceutical Research* **33**, 18–39 (2016).

23. Hossen, S. *et al.* Smart nanocarrier-based drug delivery systems for cancer therapy and toxicity studies: A review. *Journal of Advanced Research* **15**, 1–18 (2019).

24. Letchford, K. & Burt, H. A review of the formation and classification of amphiphilic block copolymer nanoparticulate structures: micelles, nanospheres, nanocapsules and polymersomes. *Eur. J. Pharm. Biopharm.* **65**, 259–269 (2007).

25. Rana, S. *et al.* Interfacial engineering of nanoparticles for cancer therapeutics. in *Nanostructures for Cancer Therapy* 177–209 (Elsevier, 2017). doi:10.1016/B978-0-323-46144-3.00007-6

26. Allen, C., Maysinger, D. & Eisenberg, A. Nano-engineering block copolymer aggregates for drug delivery. *Colloids Surfaces B Biointerfaces* **16**, 3–27 (1999).

27. Bang, J., Viswanathan, K., Lodge, T. P., Park, M. J. & Char, K. Temperature-dependent micellar structures in poly(styrene-b-isoprene) diblock copolymer solutions near the critical micelle temperature. *J. Chem. Phys.* **121**, 11489–11500 (2004).

28. Ahmad, Z., Shah, A., Siddiq, M. & Kraatz, H. B. Polymeric micelles as drug delivery vehicles. *RSC Advances* **4**, 17028–17038 (2014).

29. Croy, S. & Kwon, G. Polymeric Micelles for Drug Delivery. *Curr. Pharm. Des.* **12**, 4669–4684 (2006).

30. Alade, S. L., Brown, R. E. & Paquet, A. Polysorbate 80 and E-Ferol toxicity. *Pediatrics* **77**, 593–597 (1986).

31. Varma, R. K. *et al.* Polysorbate 80: A pharmacological study. *Arzneimittel-Forschung/Drug Res.* **35**, 804–808 (1985).

32. Biswas, S., Kumari, P., Lakhani, P. M. & Ghosh, B. Recent advances in polymeric micelles for anti-cancer drug delivery. *Eur. J. Pharm. Sci.* **83**, 184–202 (2016).

33. Lu, J., Owen, S. C. & Shoichet, M. S. Stability of self-assembled polymeric micelles in serum. *Macromolecules* **44**, 6002–6008 (2011).

34. Kedar, U., Phutane, P., Shidhaye, S. & Kadam, V. Advances in polymeric micelles for drug delivery and tumor targeting. *Nanomedicine Nanotechnology, Biol. Med.* **6**, 714–729 (2010).

35. Maeda, H. & Matsumura, Y. A new concept for macromolecular therapeutics in cancer chemotherapy: mechanism of tumoritropic accumulation of proteins and the antitumor agent smancs. *Cancer Res.* **46**, 6387–6392 (1986).

36. Gaiser, B. K. *et al.* Interspecies comparisons on the uptake and toxicity of silver and cerium dioxide nanoparticles. *Environ. Toxicol. Chem.* **31**, 144–54 (2012).

37. Movassaghian, S., Merkel, O. M. & Torchilin, V. P. Applications of polymer micelles for imaging and drug delivery. *Wiley Interdiscip. Rev. Nanomedicine Nanobiotechnology* **7**, 691–707 (2015).

38. Berk, D. A. *et al.* Vascular permeability in a human tumor xenograft: molecular size dependence and cutoff size. *Cancer Res.* **55**, 3752–3756 (1995).

39. Fang, J., Nakamura, H. & Maeda, H. The EPR effect: Unique features of tumor blood vessels for drug delivery, factors involved, and limitations and augmentation of the effect. *Adv. Drug Deliv. Rev.* **63**, 136–151 (2011).

40. Jhaveri, A. M. & Torchilin, V. P. Multifunctional polymeric micelles for delivery of drugs and siRNA. *Front. Pharmacol.* **5**, 1–26 (2014).

41. Sawant, R. R. *et al.* Targeted transferrin-modified polymeric micelles: Enhanced efficacy in vitro and in vivo in ovarian carcinoma. *Mol. Pharm.* **11**, 375–381 (2014).

42. Liao, C., Sun, Q., Liang, B., Shen, J. & Shuai, X. Targeting EGFR-overexpressing tumor cells using Cetuximab-immunomicelles loaded with doxorubicin and superparamagnetic iron oxide. *Eur. J. Radiol.* **80**, 699–705 (2011).

43. Chung, E. J. *et al.* Fibrin-binding, peptide amphiphile micelles for targeting glioblastoma. *Biomaterials* **35**, 1249–1256 (2014).

44. Bae, Y., Jang, W. D., Nishiyama, N., Fukushima, S. & Kataoka, K. Multifunctional polymeric micelles with folate-mediated cancer cell targeting and pH-triggered drug releasing properties for active intracellular drug delivery. *Mol. Biosyst.* **1**, 242–250 (2005).

45. Cheng, R., Meng, F., Deng, C., Klok, H. A. & Zhong, Z. Dual and multi-stimuli responsive polymeric nanoparticles for programmed site-specific drug delivery. *Biomaterials* **34**, 3647–3657 (2013).

46. Guan, J. *et al.* Folate-conjugated and pH-responsive polymeric micelles for target-cell-specific anticancer drug delivery. *Acta Biomater.* **60**, 244–255 (2017).

47. Shi, Y., Van Nostrum, C. F. & Hennink, W. E. Interfacially Hydrazone Cross-linked Thermosensitive Polymeric Micelles for Acid-Triggered Release of Paclitaxel. *ACS Biomater. Sci. Eng.* **1**, 393–404 (2015).

48. Deng, B., Ma, P. & Xie, Y. Reduction-sensitive polymeric nanocarriers in cancer therapy: a comprehensive review. *Nanoscale* **7**, 12773–12795 (2015).

49. Gaucher, G. *et al.* Block copolymer micelles: preparation, characterization and application in drug delivery. *J. Control. Release* **109**, 169–88 (2005).

50. Xu, W., Ling, P. & Zhang, T. Polymeric Micelles, a Promising Drug Delivery System to Enhance Bioavailability of Poorly Water-Soluble Drugs. *J. Drug Deliv.* **2013**, 1–15 (2013).

51. Samaddar, P., Deep, A. & Kim, K. H. An engineering insight into block copolymer self-assembly: Contemporary application from biomedical research to nanotechnology. *Chem. Eng. J.* **342**, 71–89 (2018).

52. Kumar, N., Ravikumar, M. N. V. & Domb, A. J. Biodegradable block copolymers. *Advanced Drug Delivery Reviews* **53**, 23–44 (2001).

53. Bodratti, A. M. & Alexandridis, P. Formulation of poloxamers for drug delivery. *Journal of Functional Biomaterials* **9**, 11 (2018).

54. Kabanov, A. V, Batrakova, E. V & Yu, V. Pluronic® block copolymers as novel polymer therapeutics for drug and gene delivery. *J. Control. Release* **82**, 189–212 (2002).

55. Batrakova, E. V. & Kabanov, A. V. Pluronic block copolymers: Evolution of drug delivery concept from inert nanocarriers to biological response modifiers. *Journal of Controlled Release* **130**, 98–106 (2008).

56. Alexandridis, P., Holzwarthf, J. F. & J, T. A. H. Micellization of Poly(ethylene oxide)-Poly(propylene oxide)-Poly(ethylene oxide) Triblock Copolymers in Aqueous Solutions Thermodynamics. *Macromolecules* **27**, 2414–2425 (1994).

57. Linse, P. & Malmsten, M. Temperature-Dependent Micellization in Aqueous Block Copolymer Solutions. *Macromolecules* **25**, 5434–5439 (1992).

58. Wu, X. S. & Wang, N. Synthesis, characterization, biodegradation, and drug delivery application of biodegradable lactic/glycolic acid polymers. Part II: Biodegradation. *J. Biomater. Sci. Polym. Ed.* **12**, 21–34 (2001).

59. Anseth, K. S. *et al.* In situ forming degradable networks and their application in tissue engineering and drug delivery. *J. Control. Release* **78**, 199–209 (2002).

60. Khattak, S. F., Bhatia, S. R. & Roberts, S. C. Pluronic F127 as a Cell Encapsulation Material: Utilization of Membrane-Stabilizing Agents. *Tissue Eng.* **11**, 974–983 (2005).

61. Batrakova, E. V., Han, H. Y., Miller, D. W. & Kabanov, A. V. Effects of pluronic P85 unimers and micelles on drug permeability in polarized BBMEC and Caco-2 cells. *Pharm. Res.* **15**, 1525–1532 (1998).

62. Batrakova, E. V., Han, H. Y., Alakhov, V. Y., Miller, D. W. & Kabanov, A. V. Effects of pluronic block copolymers on drug absorption in Caco-2 cell monolayers. *Pharm. Res.* **15**, 850–855 (1998).

63. Banerjee, S. K., Jagannath, C., Hunter, R. L. & Dasgupta, A. Bioavailability of tobramycin after oral delivery in FVB mice using CRL-1605 copolymer, an inhibitor of P-glycoprotein. *Life Sci.* **67**, 2011–2016 (2000).

64. Nidhi, K., Indrajeet, S., Khushboo, M., Gauri, K. & Sen, D. J. Microstructural Imaging of Early Gel Layer Formation in HPMC Matrices. *J. Pharm. Sci.* **95**, 2145–2157 (2006).

65. Yang, R. *et al.* Getting Drugs Across Biological Barriers. *Advanced Materials* **29**, 1606596 (2017).

66. Ensign, L. M., Cone, R. & Hanes, J. Oral drug delivery with polymeric nanoparticles: The gastrointestinal mucus barriers. *Advanced Drug Delivery Reviews* **64**, 557–570 (2012).

67. Hume, R. I. & Honig, M. G. Fluorescent Carbocyanine Dyes Allow Living Neurons of Identified Origin to Be Studied in Long-Term Cultures. *J. Cell Biol.* **103**, 171–187 (1986).

68. Ragnarson, B., Bengtsson, L. & Hægerstrand, A. Labeling with fluorescent carbocyanine dyes of cultured endothelial and smooth muscle cells by growth in dye-containing medium. *Histochemistry* **97**, 329–333 (1992).

69. Höppner, M., Luhm, J., Schlenke, P., Koritke, P. & Frohn, C. A flow-cytometry based cytotoxicity assay using stained effector cells in combination with native target cells. *J. Immunol. Methods* **267**, 157–163 (2002).

70. Chen, H. *et al. Release of hydrophobic molecules from polymer micelles into cell membranes revealed by Fö rster resonance energy transfer imaging*. *PNAS May* **6**, (2008).

71. Zou, P., Chen, H., Paholak, H. J. & Sun, D. Noninvasive fluorescence resonance energy transfer imaging of in vivo premature drug release from polymeric nanoparticles. *Mol. Pharm.* **10**, 4185–4194 (2013).

72. Canton, I. & Battaglia, G. Endocytosis at the nanoscale. *Chemical Society Reviews* **41**, 2718–2739 (2012).

73. Chaudhuri, A., Battaglia, G. & Golestanian, R. The effect of interactions on the cellular uptake of nanoparticles. *Phys. Biol.* **8**, 1–9 (2011).

74. Traub, L. M. Tickets to ride: Selecting cargo for clathrin-regulated internalization. *Nature Reviews Molecular Cell Biology* **10**, 583–596 (2009).

75. Plapied, L., Duhem, N., des Rieux, A. & Préat, V. Fate of polymeric nanocarriers for oral drug delivery. *Current Opinion in Colloid and Interface Science* **16**, 228–237 (2011).

76. McNeil, P. L. Mechanisms of nutritive endocytosis. III. A freeze-fracture study of phagocytosis by digestive cells of Chlorohydra. *Tissue Cell* **16**, 519–533 (1984).

77. Tuma, P. L. & Hubbard, A. L. Transcytosis: Crossing Cellular Barriers. *Physiol. Rev.* **83**, 871–932 (2003).

78. Frank, P. G., Pavlides, S. & Lisanti, M. P. Caveolae and transcytosis in endothelial cells: Role in atherosclerosis. *Cell Tissue Res.* **335**, 41–47 (2009).

79. Sahay, G., Alakhova, D. Y. & Kabanov, A. V. Endocytosis of nanomedicines. *Journal of Controlled Release* **145**, 182–195 (2010).

80. Vogel, U., Sandvig, K. & van Deurs, B. Expression of caveolin-1 and polarized formation of invaginated caveolae in Caco-2 and MDCK II cells. *J. Cell Sci.* **111 (Pt 6**, 825–32 (1998).

81. Verkade, P., Harder, T., Lafont, F. & Simons, K. Induction of caveolae in the apical plasma membrane of Madin-Darby canine kidney cells. *J. Cell Biol.* **148**, 727–739 (2000).

82. Sahay, G., Batrakova, E. V & Kabanov, A. V. Different internalization pathways of polymeric micelles and unimers and their effects on vesicular transport. *Bioconjug. Chem.* **19**, 2023–2029 (2008).

83. Cheng, C. Y. hydration dynamics reveale, Wang, J. Y., Kausik, R., Lee, K. Y. C. & Han, S. Nature of interactions between PEO-PPO-PEO triblock copolymers and lipid membranes: (II) Role ofd by dynamic nuclear polarization. *Biomacromolecules* **13**, 2624–2633 (2012).

84. Wang, J. Y., Marks, J. & Lee, K. Y. C. Nature of interactions between PEO-PPO-PEO triblock copolymers and lipid membranes: (I) Effect of polymer hydrophobicity on its ability to protect liposomes from peroxidation. *Biomacromolecules* **13**, 2616–2623 (2012).

85. Wang, J. Y., Chin, J., Marks, J. D. & Lee, K. Y. C. Effects of PEO-PPO-PEO triblock copolymers on phospholipid membrane integrity under osmotic stress. *Langmuir* **26**, 12953–12961 (2010).

86. Kovacic, J. C., Mercader, N., Torres, M., Boehm, M. & Fuster, V. Epithelial-to-mesenchymal and endothelial-to-mesenchymal transition from cardiovascular development to disease. *Circulation* **125**, 1795–1808 (2012).

87. Blanco, E., Shen, H. & Ferrari, M. Principles of nanoparticle design for overcoming biological barriers to drug delivery. *Nat. Biotechnol.* **33**, 941–51 (2015).

88. Muro, S. Challenges in design and characterization of ligand-targeted drug delivery systems. *J. Control. Release* **164**, 125–137 (2012).

89. Dejana, E. Endothelial cell-cell junctions: Happy together. *Nature Reviews Molecular Cell Biology* **5**, 261–270 (2004).

90. Sandvig, K. & van Deurs, B. Delivery into cells: Lessons learned from plant and bacterial toxins. *Gene Therapy* **12**, 865–872 (2005).

91. Shin, K., Fogg, V. C. & Margolis, B. Tight Junctions and Cell Polarity. *Annu. Rev. Cell Dev. Biol* **22**, 207–235 (2006).

92. Fölsch, H. Regulation of membrane trafficking in polarized epithelial cells. *Current Opinion in Cell Biology* **20**, 208–213 (2008).

93. Naim, H. Y., Dodds, D. T., Brewer, C. B. & Roth, M. G. Apical and basolateral coated pits of MDCK cells differ in their rates of maturation into coated vesicles, but not in the ability to distinguish between mutant hemagglutinin proteins with different internalization signals. *J. Cell Biol.* **129**, 1241–1250 (1995).

94. Francia, V., Aliyandi, A. & Salvati, A. Effect of the development of a cell barrier on nanoparticle uptake in endothelial cells. *Nanoscale* **10**, 16645–16656 (2018).

95. Ulbrich, K., Knobloch, T. & Kreuter, J. Targeting the insulin receptor: Nanoparticles for drug delivery across the blood-brain barrier (BBB). *J. Drug Target.* **19**, 125–132 (2011).

96. Ghaffarian, R., Bhowmick, T. & Muro, S. Transport of nanocarriers across gastrointestinal epithelial cells by a new transcellular route induced by targeting ICAM-1. in *Journal of Controlled Release* **163**, 25–33 (Elsevier, 2012).

97. Harush-Frenkel, O., Rozentur, E., Benita, S. & Altschuler, Y. Surface Charge of Nanoparticles Determines Their Endocytic and Transcytotic Pathway in Polarized MDCK Cells. doi:10.1021/bm700535p

98. Ye, D. *et al.* Low uptake of silica nanoparticles in Caco-2 intestinal epithelial barriers. *Beilstein J. Nanotechnol.* **8**, 1396–1406 (2017).

99. Wang, C., De Jong, E., Sjollema, K. A. & Zuhorn, I. S. Entry of PIP3-containing polyplexes into MDCK epithelial cells by local apical-basal polarity reversal. *Sci. Rep.* **6**, 1–13 (2016).

100. Correia Carreira, S., Walker, L., Paul, K. & Saunders, M. The toxicity, transport and uptake of nanoparticles in the in vitro BeWo b30 placental cell barrier model used within NanoTEST. *Nanotoxicology* **9**, 66–78 (2015).

101. Cartwright, L. *et al.* In vitro placental model optimization for nanoparticle transport studies. *Int. J. Nanomedicine* **7**, 497–510 (2012).

102. St Johnston, D. & Ahringer, J. Cell polarity in eggs and epithelia: Parallels and diversity. *Cell* **141**, 757–774 (2010).

103. Rodriguez-Boulan, E., Kreitzer, G. & Müsch, A. Organization of vesicular trafficking in epithelia. *Nature Reviews Molecular Cell Biology* **6**, 233–247 (2005).

104. Kozlov, M. M. & Mogilner, A. Model of Polarization and Bistability of Cell Fragments. *Biophys. J.* **93**, 3811–3819

105. Roth, S. Mathematics and biology: A Kantian view on the history of pattern formation theory. *Development Genes and Evolution* **221**, 255–279 (2011).

106. Turing, A. M. The chemical basis of morphogenesis. *Bull. Math. Biol.* **52**, 153–197 (1990).

107. Irvine, J. D. *et al.* MDCK (Madin-Darby canine kidney) cells: A tool for membrane permeability screening. *J. Pharm. Sci.* **88**, 28–33 (1999).

108. Ye, D., Dawson, K. A. & Lynch, I. A TEM protocol for quality assurance of in vitro cellular barrier models and its application to the assessment of nanoparticle transport mechanisms across barriers. *Analyst* **140**, 83–97 (2015).

109. Cereijido, M., Robbins, E. S., Dolan, W. J., Rotunno, C. A. & Sabatini, D. D. Polarized monolayers formed by epithelial cells on a permeable and translucent support. *J. Cell Biol.* **77**, 853–880 (1978).

110. Misfeldt, D. S., Hamamoto, S. T. & Pitelka, D. R. Transepithelial transport in cell culture. *Proc. Natl. Acad. Sci. U. S. A.* **73**, 1212–6 (1976).

111. Cucullo, L., Hossain, M., Puvenna, V., Marchi, N. & Janigro, D. The role of shear stress in Blood-Brain Barrier endothelial physiology. *BMC Neurosci.* **12**, 1–15 (2011).

112. Miura, S., Sato, K., Kato-Negishi, M., Teshima, T. & Takeuchi, S. Fluid shear triggers microvilli formation via mechanosensitive activation of TRPV6. *Nat. Commun.* **6**, 1–11 (2015).

113. Blundell, C. *et al.* A microphysiological model of the human placental barrier. *Lab Chip* **16**, 3065–3073 (2016).

114. Seebach, J. *et al.* Endothelial barrier function under laminar fluid shear stress. *Lab. Investig.* **80**, 1819–1831 (2000).

115. Blundell, C. *et al.* From chip-in-a-lab to lab-on-a-chip: towards a single handheld electronic system for multiple application-specific lab-on-a-chip (ASLOC). **16**, (2016).

116. Blundell, C. *et al.* Placental Drug Transport-on-a-Chip: A Microengineered In Vitro Model of Transporter-Mediated Drug Efflux in the Human Placental Barrier. *Adv. Healthc. Mater.* **7**, 1700786 (2018).

117. Fede, C. *et al.* Evaluation of gold nanoparticles toxicity towards human endothelial cells under static and flow conditions. *Microvasc. Res.* **97**, 147–55 (2015).

118. van der Helm, M. W., van der Meer, A. D., Eijkel, J. C. T., van den Berg, A. & Segerink, L. I. Microfluidic organ-on-chip technology for blood-brain barrier research. *Tissue Barriers* **4**, e1142493-1–13 (2016).

119. Lavelle, J. P. *et al. Low permeabilities of MDCK cell monolayers: a model barrier epithelium*.

120. Cho, M. J., Thompson, D. P., Cramer, C. T., Vidmar, T. J. & Scieszka, J. F. The Madin Darby Canine Kidney (MDCK) Epithelial Cell Monolayer as a Model Cellular Transport Barrier. *Pharm. Res. An Off. J. Am. Assoc. Pharm. Sci.* **6**, 71–77 (1989).

121. Cho, M. J., Thompson, D. P., Cramer, C. T., Vidmar, T. J. & Scieszka, J. F. The Madin Darby Canine Kidney (MDCK) Epithelial Cell Monolayer as a Model Cellular Transport Barrier. *Pharmaceutical Research: An Official Journal of the American Association of Pharmaceutical Scientists* **6**, 71–77 (1989).

122. von Bonsdorff, C. H., Fuller, S. D. & Simons, K. Apical and basolateral endocytosis in Madin-Darby canine kidney (MDCK) cells grown on nitrocellulose filters. *EMBO J.* **4**, 2781–92 (1985).

123. Wick, P. *et al.* Barrier capacity of human placenta for nanosized materials. *Environ. Health Perspect.* **118**, 432–436 (2010).

124. Pattillo, R. A. & Gey, G. O. The Establishment Trophoblastic of a Cell Line of Human Cells in Vitro. *Cancer Res.* **28**, 1231–1236 (1968).

125. Cohran, V., Fang, J., Milio, L., Smith, C. H. & Fant, M. Type I insulin-like growth factor receptors in the BeWo choriocarcinoma cell (b30 clone) during cell differentiation. *Placenta* **17**, 313–320 (1996).

126. Heaton, S. J. *et al.* The use of BeWo cells as an in vitro model for placental iron transport. *Am. J. Physiol. Physiol.* **295**, C1445–C1453 (2008).

Chapter 2. Materials and methods

2.1 Synthesis of micelles

Different combinations of micelles were synthesised to find a suitable system to help understand their uptake and cargo release in cells. To follow the cargo release mechanism, two hydrophobic fluorescent dyes were used; 1,6-diphenyl-1, 3, 5-hexatriene (DPH) and 3,3'-dioctadecyloxacarbocyanine perchlorate (DiOC18(3) or DiO). The cargoes were encapsulated into a micelle made of the triblock copolymer Poloxamer 407 (P407). To follow the uptake of the polymer, P407 was tagged with a red fluorescent dye, Rhodamine B isothiocyanate (RITC).

2.1.1 P407-DiO micelles

The preparation of P407-DiO micelles was done using the solvent evaporation method (Figure 2.1 A). 1 mL of a 0.4 mM solution of the fluorescent fluorophore DiO (Merck, 34215-57-1) ($\lambda_{excitation}$= 484; $\lambda_{emission}$=501) in chloroform was added to 10 mL of a 5% (w/v) solution of P407 (Merck, 9003-11-6) in water giving a final concentration of DiO of 40 μM. The mixture was then vortexed for 2-5 minutes until a white emulsion was obtained (Figure 2.1 B). Following this, the solution was placed into a rotary evaporator (Buchi Rotavapor R-200) for 20 minutes at 37 ºC (Buchi heating bath B-409) to remove the chloroform from the solution. A visual indicator of chloroform removal is that the solution becomes clear again (Figure 2.1 C & D).

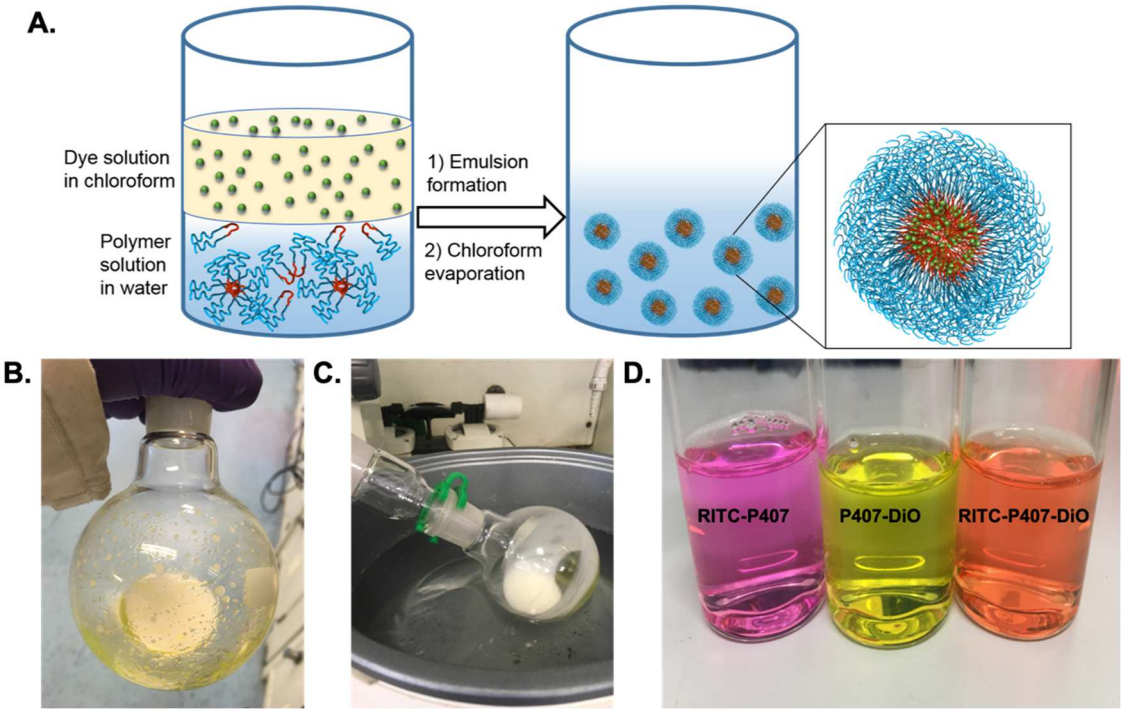

Figure 2.1 *Preparation of micelles by solvent evaporation method.* ***(A)*** *Diagram of steps required to obtain polymeric micelles by solvent evaporation method.* ***(B)*** *Emulsion formation.* ***(C)*** *Solvent evaporation.* ***(D)*** *Obtention of polymeric micelles in suspension.*

2.1.2 RITC-P407-DiO micelles

2.1.2.1 Functionalisation of P407 with RITC

2.1.2.1.1 Synthesis of amino-terminated P407

The synthesis of the amino-terminated P407 (P407-NH_2) was achieved by a modified procedure of Lu *et al. and* Zhang *et al.* [1–3]. P407 was purified by dissolving in acetone and precipitating into an excess amount of cooled hexane followed by drying the precipitate under vacuum. 5.75g, 1mmol of purified P407 was dissolved into 15 mL of dry acetonitrile and added dropwise to an excess amount of N,N_0-carbonyldiimidazol (CDI, Merck, 530-62-1) (1.62 g, 10 mmol) in 15 ml of dry acetonitrile at room temperature during a 2h period under nitrogen atmosphere. The mixture was then stirred for an additional 2 h period. After this step, 0.2 mL of water

was added to the mixture for 20 mins to neutralize the nonreacted CDI. The solution was then added dropwise to 10 mL of 1,2-ethylenediamine at room temperature over a 2h period. The mixture was then allowed to react overnight and any unreacted 1,2-ethylenediamine was removed by evaporation. The resulting oily mixture was dialyzed against water for 5 days then freeze-dried to obtain P407- NH_2.

2.1.2.1.2 Crosslinking of RITC to P 407-NH_2

0.25g of P407-NH_2, obtained as described in the previous section, was added to 67.5 mg of RITC (Merck, 36877-69-7) (in 10 mL DMF and stirred in a nitrogen atmosphere at room temperature in a dark environment overnight. The mixture was subsequently dialysed (MWCO 3500) against a weakly alkaline aqueous solution of NaOH (pH 8.0). RITC-labelled P407 was then obtained by freeze-drying the solution. A summary of the full functionalisation process can be found in Figure 2.2.

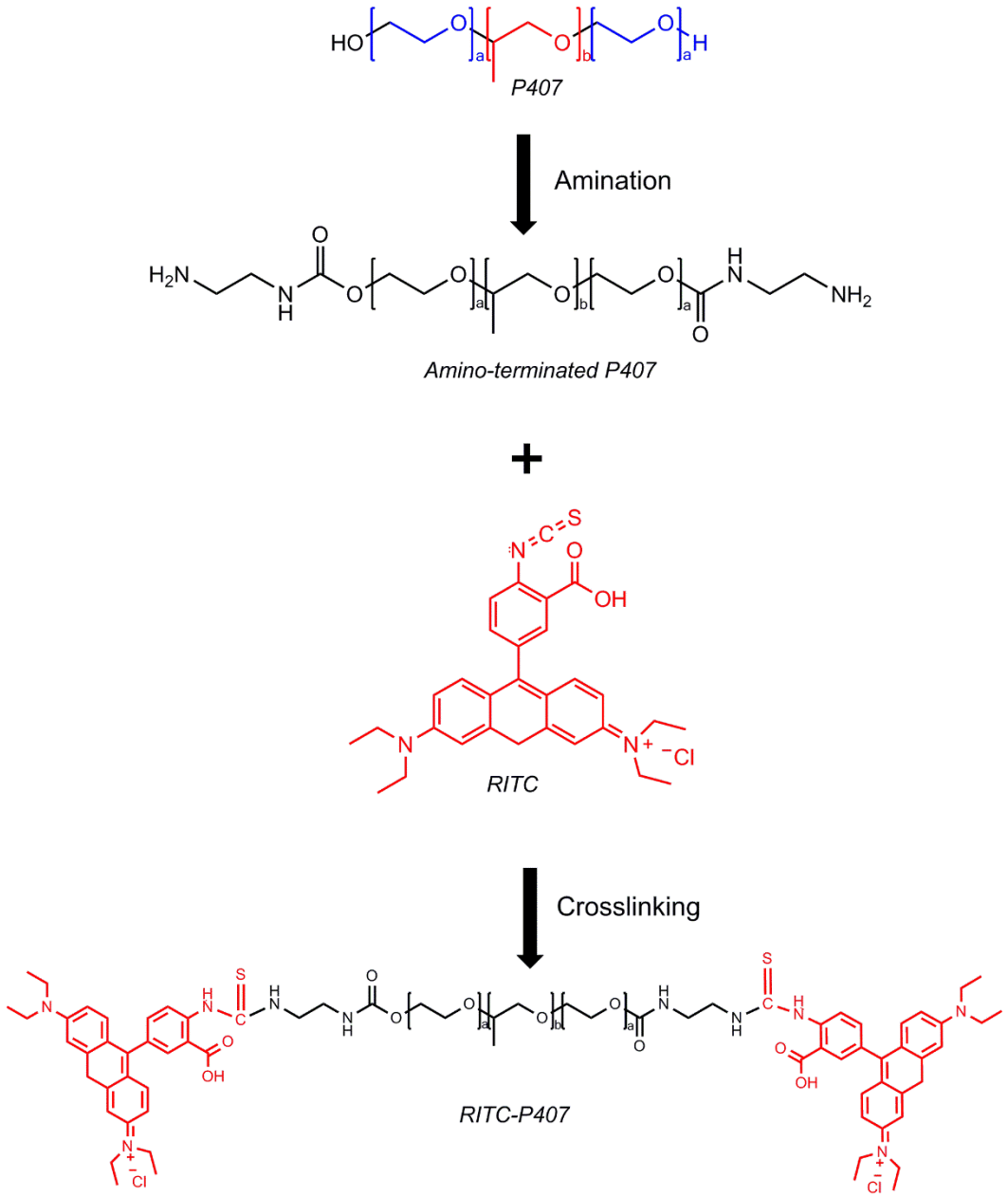

Figure 2.2 *Steps required for obtention of RITC-P407 polymer*

2.1.2.1 RITC-P407-DiO micelles

1 mL of 0.4 mM DiO solution in chloroform was added to 10 mL of a 5% (w/v) of P407, containing 0.5% RITC-P407, in water. The mixture was vortexed into an emulsion and the chloroform was evaporated as described in section 2.1.1 to obtain RITC-P407-DiO micelles.

2.2 Particle-characterisation techniques

2.2.1 Dynamic light scattering

2.2.1.1 Fundamental theory

The dynamic light scattering (DLS) technique, also known as photon correlation spectroscopy (PCS) or quasi-elastic light scattering (QLS), is a characterisation technique used to determine the size distribution of nanoscale particles in solution. This technique relies on measuring the Brownian motion of particles in solution to determine their hydrodynamic diameter. The Brownian motion is the resulting motion of particles after colliding with the fast-moving particles of the surrounding solvent. Following this idea, large particles have a slower Brownian motion than small particles as the particle collision has a bigger effect on the movement of small particles than larger ones. The DLS technique measures the velocity at which the particles diffuse in solution due to Brownian motion. This is done by directing a laser beam coming from the instrument source through the sample. When the beam hits the particles in suspension, the light is scattered. The intensity fluctuations of the scattered beam are registered by the detector situated at a specific angle to the beam. To ensure similarity within the detected signals, an auto-correlation function is calculated. Since large particles move slower than small particles, the detected signal changes less and therefore the correlation persists for a longer time than for smaller particles. The rate of decay of the correlation function is smaller for large particles than it is for small particles. The decay of the correlation function can then be associated to the velocity of the Brownian motion,

known as the particle diffusion coefficient[4]. With this information, the hydrodynamic diameter of the particles can be calculated using the Stokes-Einstein equation[5] (Equation 2.1).

$$d = \frac{k_B \cdot T}{3 \cdot \pi \cdot \eta \cdot D}$$

Equation 2.1 Stokes-Einstein equation, where d is the hydrodynamic diameter of the particles, k_B is the Boltzmann constant, T is the absolute temperature, η is the viscosity of the solution and D is the diffusion coefficient.

The size of the particles in solution can then be extracted from the correlation function by fitting a multiple exponential curve to the correlation function to obtain the mean size distribution of the particles. The width of the obtained distribution is the polydispersity index (PDI) of the sample. The distribution plot obtained represents the relative intensity of the light scattered by all the particles within different size bins. The intensity size distribution is always correct as it is the magnitude measured directly by the instrument. However, converting the size distributions by intensity to size distributions by volume or number can give more information about the sample[6]. Whilst the distribution by volume expresses the volume of the particles in different size bins, the number distribution shows the number of particles detected in each size bin. The transformation of the data can be explained by taking two sets of particles with sizes “a” and “b”. The number of “a” particles detected in the sample is N_a and the number of “b” particles detected is N_b. The relative contribution of each particle in terms of number is given by (Equation 2.2)

$$\%N_{a,b} = \frac{N_{(a,b)}}{N_a + N_b} \times 100$$

Equation 2.2 Relative contribution by number, where *a* and *b* size of particles and N_a and N_b represent number of particles[6].

Assuming the particles are spherical, the volume of the particles needs to include a term of [size]^3 therefore the relative contribution of each particle in terms of volume is expressed in (Equation 2.3)

$$\%V_{(a,b)} = \frac{N_{(a,b)} \cdot (a,b)^3}{N_a \cdot a^3 + N_b \cdot b^3} \times 100$$

Equation 2.3 Relative contribution by volume, where *a* and *b* size of particles and N_a and N_b represent number of particles[6].

Furthermore, according to Rayleigh's small size parameter approximation equation (Equation 2.4), the intensity of the light scattered is proportional to the diameter of the particle to the power of 6.

$$\mathrm{I} = I_0 \frac{1 + \cos^2\theta}{2R^2} \left(\frac{2\pi}{\lambda}\right)^4 \left(\frac{n^2 - 1}{n^2 + 2}\right)^2 \left(\frac{d}{2}\right)^6$$

Equation 2.4 Rayleigh's small size parameter approximation[7], where *I* is the intensity of the light scattered by the particles, I_0 is the intensity of the incident beam of wavelength λ, *R* is the distance to the particle, θ is the scattering angle and *n* is the refractive index of the particles of diameter *d*.

In terms of intensity, the relative contribution of each particle is then given by (Equation 2.5).

$$\%I_{(a,b)} = \frac{N_{(a,b)} \cdot (a,b)^6}{N_a \cdot a^6 + N_b \cdot b^6} \times 100$$

Equation 2.5 Relative contribution by Intensity, where *a* and *b* size of particles and N_a and N_b represent number of particles[6].

Since the size has a bigger contribution in the size distribution by intensity than in the volume or number distributions, the results are weighted towards large particles. For this reason, the intensity distribution is preferred to detect small amounts of aggregation. The size of the particles has no weighting effect on the number distribution which is why it is good to measure small particles. The volume distribution is a good balance between the intensity or number distribution besides it give more information on the quantity of particles aggregated. In some cases, some peaks can disappear when transforming the data from intensity to volume or number as their volume or number contributions are no longer considered relevant to the transformation.

2.2.1.2 DLS method

All DLS measurements were made using a Malvern Nano ZSP zetasizer (Malvern Instruments Ltd.). Prior to DLS measurements, all samples were filtered using a 0.2 μm cellulose acetate filter (VWR, 28145-477). 12 μL of micelle suspension were added to a quartz cuvette (Malvern Panalytical, ZEN2112). For simple particle size determination, the measurements were made at physiological temperature (37ºC). For

temperature dependent measurements, the measurements were taken from 4 to 37ºC with a temperature step size of 3ºC. The equilibration time at each temperature was 120 seconds. The initial cooling of the solution (from room temperature to 4ºC) was left to equilibrate for 10 minutes. The refractive index used in DLS measurements was 1.47 for P407 micelles.

2.2.2 Fluorimetry

2.2.2.1 Fundamental theory

Fluorimetry is a spectroscopic technique used to measure fluorescence of materials in solution usually called fluorophores. In fluorescence two phenomena are present, first excitation followed by relaxation. Excitation occurs when the electrons of a fluorophore molecule are excited to a higher energy state. This happens when the molecule absorbs incident photons from an electromagnetic radiation source. Relaxation occurs when the excited electrons relax back to their ground state losing energy through emission of a photon with lower energy, thus, longer wavelength. The relaxation step generates fluorescence of the material (Figure 2.3 A). In a spectrofluorometer a sample is irradiated with light of a chosen specific wavelength (usually $\lambda_{max\ excitation}$). The resulting emitted fluorescent light is measured by a detector set at 90º from the light source (Figure 2.3 B). The detection range of the detector is usually set around the value of $\lambda_{max\ emission}$. The values of $\lambda_{max\ excitation}$ and $\lambda_{max\ excitation}$ are specific to a material and hence are used to characterise fluorescent samples.

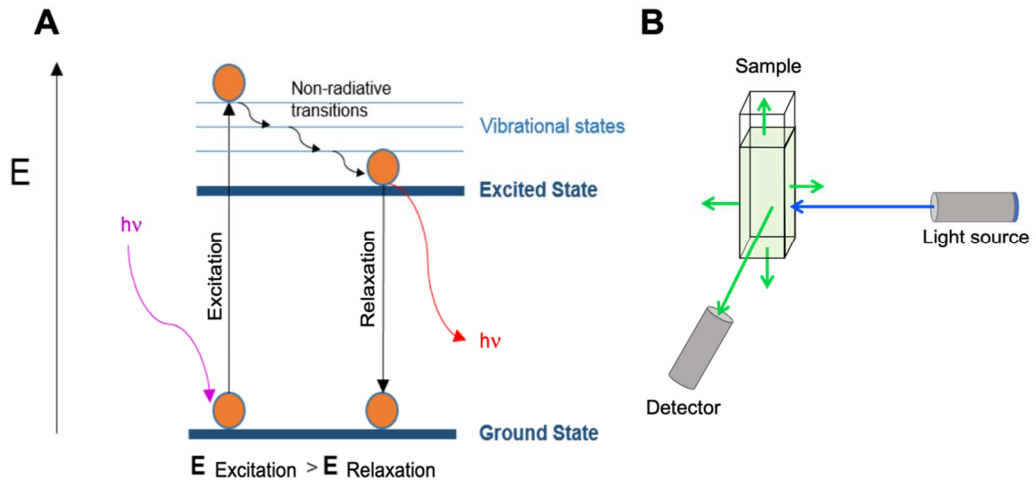

Figure 2.3 *Fluorimetry diagram. (A) Excitation and relaxation phenomena in fluorescence. (B) spectrofluorometer setup for fluorescence measurements.*

2.2.2.2 Fluorimetry method

Fluorimetry measurements were performed with a spectrofluorometer (Horiba scientific, FluoroMax-4). Prior to fluorescence measurements, all samples were filtered using a 0.2 μm cellulose acetate filter (VWR, 28145-477). After filtering, 700 μL of micelle suspension was inserted in a quartz cuvette with a PTFE lid (Thorlabs, CV10Q700FS). The measuring settings used can be found in Table 2.1.

Table 2.1 *Parameters used for fluorimetry measurements.*

Spectra	Sample	λ excitation (nm)	λ detection (nm)
Emission	P407-DiO	484	490-550
Excitation	RITC-P407	595	486-690
Emission	RITC-P407	540	550-650
Emission	RITC-P407-DiO	484	490-550

2.3 Cell-culture methods

Two different epithelial cell lines were used in this work as model systems to understand micelle uptake at a cellular level. Human placental BeWo b30 cells and Madin-Darby canine kidney cells (MDCK) were chosen for this work as they are found in two key barriers for nutrients and drugs transport in the human body[8–13].

2.3.1 Cell culture of BeWo b30 cells

The BeWo cell line derives from a human placenta choriocarcinoma therefore, this cell line was chosen as a model to evaluate P407 micelles transport in the placental barrier. The cells were obtained from Prof. Harry McArdle (Rowett Research Institute, Aberdeen) with permission from Dr. Alan Schwartz (Washington University, St Louis, MO, USA).

2.3.1.1 Cell culture conditions

BeWo b30 cells, used between passage 16 to 40, were seeded on day 0 at a concentration of 10^4 cells/cm^2 in a 75 cm^2 cell culture flask (Corning®, 430641) containing 24 mL of a medium solution of Dulbecco's modified Eagle's medium nutrient mixture F-12 (DMEM-F12, Sigma D6434 without phenol red) with the added supplements 10 % fetal bovine serum (FBS, Merck F9665), 1% amphotericin B (Amp B, Merck A2942) and 1% penicillin streptomycin L-glutamine solution (PSLG, Merck G6784). The cells were left to grow for 7 days at 37 ºC and a humidified atmosphere of 5% CO_2 with a change of medium on day 6 post-seeding.

2.3.1.2 Cell passage

Passage of BeWo b30 cells was carried out once the cells reached 70-80% confluence (usually on day 7 post-seeding). The cells were washed twice with 12 mL with a phosphate-buffered saline solution (PBS, Merck D8537) before trypinising with 5 mL of Trypsin-EDTA solution (Merck T4049) for 13 minutes at 37 ºC, 5% CO_2 (flask was tapped after 9 minutes to dislodge the cells from the flask). 5 mL of cell culture medium was added to the cell suspension to deactivate the trypsin solution and the clumps of cells were broken by passing the solution through a 10 mL pipette several times before centrifuging at 1500 g for 5 mins. The supernatant was removed, and the cells were resuspended in 5 to 8 mL of medium for counting using a heamocytometer. The appropriate volume of cell suspension was then added to a 75 cm^2 flask (Greiner CellStar, 658175) containing 24 mL of cell culture medium to give a final concentration of 10^4 cells/cm^2.

2.3.2 Cell culture of MDCK cells

MDCK cells are epithelial cells isolated from the kidney tubule of an adult Cocker Spaniel. This cell line is one of the best characterised epithelial cell lines[12], thus it provides a suitable model to study the uptake of micelles and compare the results with the BeWo b30 model. The cells were acquired from Professor N. L. Simmons (University of Newcastle, UK).

2.3.2.1 Cell culture conditions

MDCK strain I cells, used between passage 99 to 125, were seeded on day 0 at a concentration of 2 x 10^4 cells/cm^2 in a 75 cm^2 flask (Corning®, 430641) containing 10 mL of a medium solution of Eagle's minimal essential medium (EMEM, Merck D6171 with phenol red) supplemented with 10% fetal calf serum (Gibco, 10270), 1% nonessential amino acids (NEAA, Merck 7145) 1% kanamycin (Merck K0129) and 1% glutaMAX (Thermo Fisher 35050061). The cells were left to grow for 7 days at 37 ºC and a humidified atmosphere of 5% CO_2 with a change of medium on day 3 post-seeding.

2.3.2.2 Cell passage

Passage of MDCK cells was carried out once the cells reached confluency (usually on day 7 post-seeding). The cells were washed twice with PBS (Sigma D8537) before adding 5 mL of Trypsin-EDTA solution (Merck T4049) for 45 minutes to 1 hour at 37 °C, 5% CO_2 until the cells became detached from the surface. To deactivate the trypsin solution, 10 mL of cell culture medium was added to the cell suspension. The solution was then passed through a pipette with a 1 mL Gilson pipette tip attached 5-10 times to break the clumps of cells. The appropriate volume of cell suspension was then added to a 75 cm^2 containing 10 mL of cell culture medium to give a final concertation of 2 x 10^4 cells/cm^2.

2.3.3 Cell culture experimental set-up

2.3.3.1 Culture of cells on coverslips

For experiments involving confocal imaging, BeWo and MDCK cells were grown to from a monolayer on coverslips. Prior to cell seeding, 13 mm coverslips (VWR, thickness #1) were sterilised by laying the coverslips down on a piece of fibre-free tissue before covering them with a second piece of tissue and spraying them with 70 % ethanol until saturated. Once the ethanol was evaporated, each coverslip was placed into one well of a 12-well plate (Greiner CellStar, 685180) using sterile forceps.

The cell suspension obtained during the cell passage step described previously in sections 2.3.1.2 and 2.3.2.2 was diluted in cell culture medium to obtain a final concentration of 0.66 x 10^5 cells/mL. 1 mL of the diluted cells was added to each well containing coverslips and the plate was placed at 37 ºC and a humidified atmosphere of 5% CO_2 for 3 days.

2.3.3.2 Culture of cells on 96 well plates

For high content screening experiments BeWo b 30 and MDCK cells were grown to from a monolayer in each well of a 96-Well plate (Thermo Scientific 265301, Nunc™ MicroWell™ Optical-Bottom Plate with Polymer Base).

The cell suspension obtained during the cell passage (sections 2.3.1.2 and 2.3.2.2) was diluted in cell culture medium to obtain a concentration of 1.8 x 10^5 cells/mL and 100 µL of the cell suspension was added to each well.

The plate was placed at 37 ºC and a humidified atmosphere of 5% CO_2 for 2-3 days until a monolayer of cells was formed, this was assessed using phase contrast microscopy.

2.3.3.3 Culture of cells on transwells

For transport experiments, cells were grown to form a polarised monolayer on transwell 12-well plates with polyester membrane inserts (Corning 3460, membrane diameter 12 mm, membrane pore size 3.0 µm). On day 0 prior to seeding the cells, 0.5 and 1.5 mL of cell culture medium were added to the apical and basal chambers respectively and the plate was incubated at 37 ºC and a humidified atmosphere of 5% CO_2 for 1hour. The medium was removed from the apical chamber and replaced by 0.5 mL of cell suspension diluted to give a density of 1 x 10^5 cells/cm^2 for BeWo cells and 0.5 x 10^5 cells/cm^2 for MDCK cells. The plate was placed at 37 ºC and a humidified atmosphere of 5% CO_2 for 3 days, the medium from the basal and apical chambers was changed and the trans-epithelial electrical resistance (TEER) of the cell barrier was measured every day until the TEER values reached equilibrium (usually 5-6 days). Transport assays were run on day 6 after obtaining a polarised monolayer of cells on the transwell membrane.

2.3.4 Chemical inhibitor MiTMAB

A chemical endocytic inhibitor, namely myristyl trimethyl ammonium bromide (MiTMAB) was used to verify the uptake mechanism of RITC-P407 micelles. As seen in section1.3.2, previous works have found RME to be the uptake mechanism by which polymeric micelles enter epithelial cells. This molecule competitively prevents the dynamin protein from binding to phospholipids and thus, inhibits RME[14,15]. Inhibiting dynamin protein from binding is believed to directly block endocytic trafficking as this enzyme type protein is involved in the membrane constriction and fission during endocytosis[14]. This enzyme assembles as a helical polymer around the constricted neck formed by membrane invagination during early stages of endocytosis[16,17]. This separates the endocytic vesicles from the plasma membrane. Dynamin is involved in most endocytic pathways except CDC42 and ARF6 which can occur without dynamin[18,19]. However these two pathways are usually preferred by to particles with sizes greater than 50 and 100 nm respectively[17].

2.3.5 Antibody staining protocol

Cells on coverslips were fixed in using 4% PFA for 15 minutes at room temperature. After fixation, coverslips were washed twice for 5 minutes with PBS and permeabilised using 0.1 % saponin in PBS for 4 minutes. Unspecific binding sites were blocked using 3% of a solution of albumin from bovine serum (BSA; Merck, A9647) in PBS and 0.01% saponin in PBS for 30 minutes. After blocking, 50 μL of primary antibody (Table 2.2), diluted 1 in 200 in 3% BSA and 0.1% saponin in PBS solution, were added to each coverslip and incubated in the dark at room temperature. After incubation, the cells were washed three times for 5 minutes with a solution of 0.001% saponin in PBS. The wash was followed by the addition of the secondary antibody to each coverslip (Table 2.2) diluted 1 in 200 in 3% BSA and 0.1% saponin in PBS solution and incubated for 1 hour in the dark at room temperature. After incubation, the coverslips were washed three times for 5 minutes with a solution of 0.01% saponin in PBS. Finally, the coverslips were washed twice for 5 minutes in PBS and mounted onto a microscope slide using Vectashield containing DAPI (Vector laboratories, H-1200).

The choice of primary antibodies was made by their specific target proteins (Table 2.2). EEA1 gene encodes for the protein early endosome antigen 1. This protein is found exclusively in early endosomes and acts as a tethering molecule responsible for bringing the endosomes together for fusion and cargo delivery. Because of these properties, EEA1 antibody is widely used to specifically target early endosomes[20,21] . CD63 antigen is a protein encoded by the gene CD63. This protein is found in the endosomal

system and the cell surface. In most cells, CD63 protein is found in the late endosomes, multivesicular bodies and lysosomes. For this reason, this protein is used for targeting lysosomal membranes[22,23]. ApoB is a gene coding for the apolipoprotein B. This protein is the major component of very-low-density lipoproteins and is found in a region surrounding the lipid droplets. This makes it a good target protein to target lipid droplets[24,25].

Table 2.2 *Antibodies used for immunofluorescence*

Primary antibody	Maker and catalogue number	Used to target	Dilution	Secondary antibody	Maker and catalogue number	Dilution
EEA1 (mouse)	Transduction laboratories E41120	Early endosomes	1:200	**Alexa 594 (mouse)**	Thermofisher scientific A32754	1:200
CD63 (mouse)	Bio-Rad laboratories MCA2142	Late endosomes/ Lysosomes	1:200	**Alexa 594 (mouse)**	Thermofisher scientific A32754	1:200
ApoB (rabbit)	Abcam ab20737	Lipid droplets	1:200	**Alexa 594 (rabbit)**	Thermofisher scientific A32744	1:200

2.4 Confocal microscopy

2.4.1 Fundamental theory

Confocal microscopy or confocal laser scanning microscopy (CLSM) is a technique relying on the fluorescence (see section 2.2.2.1) properties of a sample. In CLSM, a laser beam at a specific wavelength, capable of exciting the electrons of the fluorophore molecules, scans the sample in a series of lines. The light emitted is detected by a detector set at a wavelength range. To obtain high resolution images, the two pinholes are placed to confine the laser beams, one in front of the laser source and the other on in front of the detector. The pinhole has a role of minimising the fluorescence out-of-focus (Figure 2.4). Since the field of view is reduced to a single point due to the pinhole, samples must be imaged in individual Z-sections or focal planes to finally produce a 3D representation of the sample after stacking. This technique was widely used in this work to detect the fate of the fluorescent cargo and polymer in the micelles.

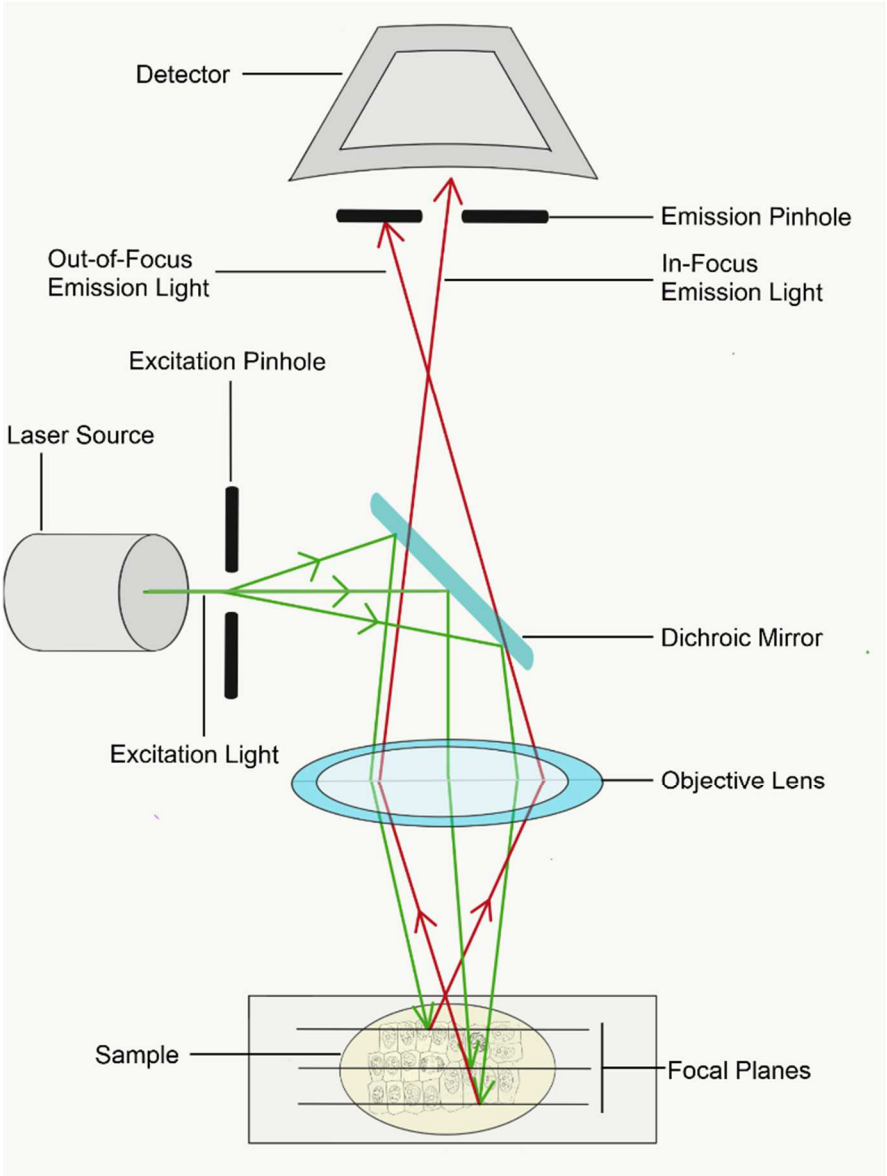

Figure 2.4 *Confocal microscope diagram*

2.4.1.1 Fluorescence resonance energy transfer (FRET)

Fluorescence or Förster resonance energy transfer is the process by which non-radiative energy is transferred from a fluorophore to another. In FRET as in fluorescence, the electrons of a fluorophore (donor) are initially excited to a higher energy state. However, instead of emitting fluorescence during relaxation the energy is transferred to another fluorophore (acceptor).

For this phenomenon to occur, the emission spectrum of the donor needs to overlap with the absorption spectrum of the acceptor[26]. The energy transfer occurs by intermolecular long-range dipole-dipole coupling, thus, the two fluorophores need to be at a proximity of between 1 and 10 nm[27]. Because of this size range, this technique is relevant to study the interactions of molecules and biomolecules in biological systems[28,29].

2.4.2 Method

Confocal images were obtained with a Leica SP5-II AOBS confocal laser scanning microscope attached to a Leica DM I6000 inverted microscope. Using a 63x oil-immersion lens (NA 1.4). The lasers used to acquire images were a 50 mW 405 nm diode laser, a 65 mW 488 nm argon laser and a 20 mW 561 nm solid state yellow laser. Filters used for visual inspection were I3 (blue), N2.1 (green) and A4 (UV). The pinhole was set to 1 AU and the line average to 1, The dimensions of the image were kept at 1024x1024 pixels, the zoom numbers used were 1, 2 and 3 depending on the detail needed in the image (image size: 1024 x 1024 pixels). Z-stacks of the cell monolayer were obtained at each experiment using a step size of 1 μm. All settings were kept constant over all samples and experiments to enable direct comparison. Through this thesis the CLSM methods relevant to each section will be described.

2.5 Transmission electron microscopy (TEM)

In transmission electron microscopy, electrons produced by an electron gun are confined into a beam that traverses the sample followed by a series of electromagnetic lenses to finally reach the observation plane (Figure 2.5). The image is generated by the scattering of the electrons, from the electron beam, by the electron-dense sample. The wavelength of an electron beam is in the order of magnitude of picometers therefore, the spatial resolution achieved by TEM is around 0.2 nm in contrast with conventional light microscopes which have spatial resolution around 200 nm[30].

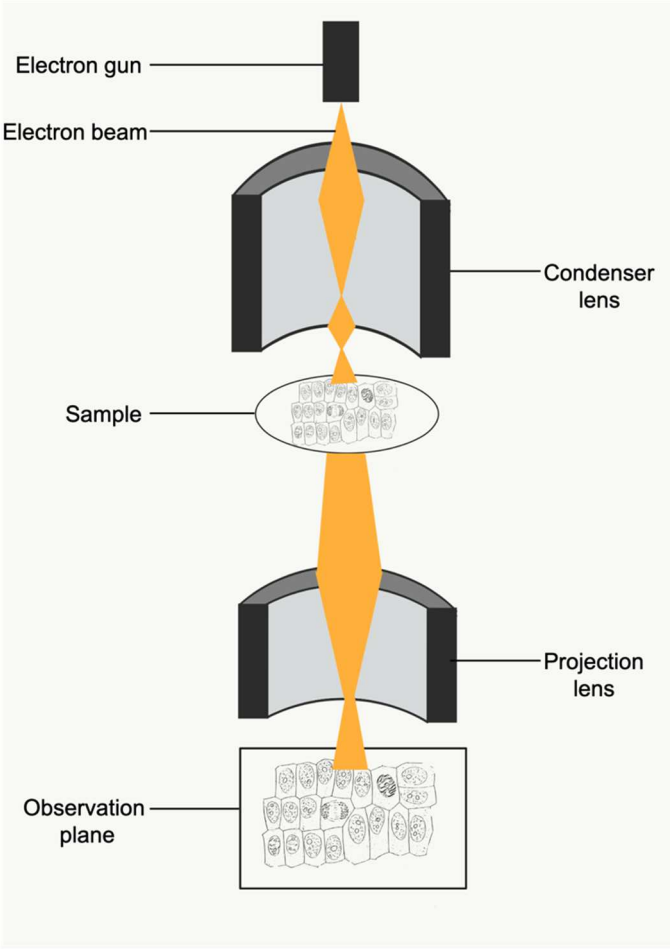

Figure 2.5 *Diagram of a TEM.*

2.6 Scanning electron microscopy (SEM)

Contrarily to TEM, where the electron beam crosses the sample, scanning electron microscopy gives surface information about the sample. To prevent the electron beam to traverse the sample, lower accelerating potentials are used in the electron gun than for TEM. When the electron beam hits the surface of the sample, electrons are detached from the surface and collected by the detector (Figure 2.6). The energy of the detached electrons is lower than 50 eV. The maximum spatial resolution achieved with SEM is approximatively 2 nm. SEM gives a good representation of surface topography of samples [31].

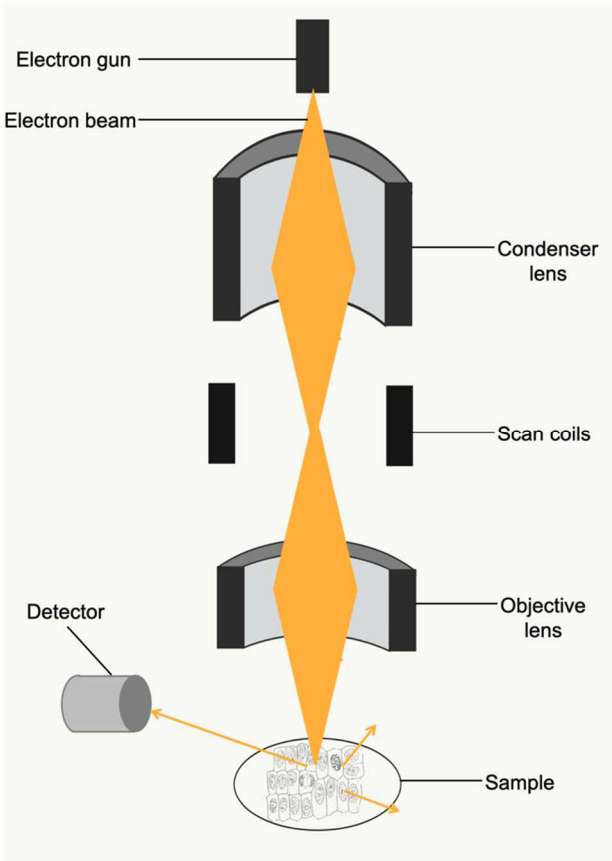

Figure 2.6 *Diagram of a SEM.*

2.7 References

1. Lu, H. F. *et al.* Galactosylated PVDF membrane promotes hepatocyte attachment and functional maintenance. *Biomaterials* **24**, 4893–4903 (2003).

2. Zhang, W. *et al.* Enhanced antitumor efficacy by paclitaxel-loaded pluronic P123/F127 mixed micelles against non-small cell lung cancer based on passive tumor targeting and modulation of drug resistance. *Eur. J. Pharm. Biopharm.* **75**, 341–53 (2010).

3. Singleton, W. *et al.* Convection enhanced delivery of tri-block copolymer nano-micelles: a method of direct intraparenchymal water-insoluble drug delivery for the treatment of high-grade glioma. *Neuro. Oncol.* **20**, i19–i19 (2018).

4. Goldburg, W. I. Dynamic Light Scattering (DLS). *Am. J. Phys.* **67**, 1152–1160 (1999).

5. Malvern Instruments Limited. Dynamic Light Scattering: An Introduction in 30 Minutes. *Dyn. Light Scatt. Tech. note* 1–8 (2014).

6. Malvern Instruments Limited. Intensity - Volume - Number Which size is correct? *Tech. note* (2017).

7. Seinfeld, John H.; Pandis, S. N. *Athmospheric Chemistry and Physics*. (John Wiley and Sons, 2006).

8. Cartwright, L. *et al.* In vitro placental model optimization for nanoparticle transport studies. *Int. J. Nanomedicine* **7**, 497–510 (2012).

9. Correia Carreira, S., Walker, L., Paul, K. & Saunders, M. The toxicity, transport and uptake of nanoparticles in the in vitro BeWo b30 placental cell barrier model used within NanoTEST. *Nanotoxicology* **9**, 66–78 (2015).

10. Elad, D., Levkovitz, R., Jaffa, A. J., Desoye, G. & Hod, M. Have We Neglected the Role of Fetal Endothelium in Transplacental Transport? *Traffic* **15**, 122–126 (2014).

11. Heaton, S. *et al.* BeWo cells as an in vitro model for iron transport across the placenta. *Am J Physiol Cell Physiol* **295**, 1445–1453 (2007).

12. Cho, M. J., Thompson, D. P., Cramer, C. T., Vidmar, T. J. & Scieszka, J. F. The Madin Darby Canine Kidney (MDCK) Epithelial Cell Monolayer as a Model Cellular Transport Barrier. *Pharmaceutical Research: An Official Journal of the American Association of Pharmaceutical Scientists* **6**, 71–77 (1989).

13. Irvine, J. D. *et al.* MDCK (Madin-Darby canine kidney) cells: A tool for membrane permeability screening. *J. Pharm. Sci.* **88**, 28–33 (1999).

14. Quan, A. *et al.* Myristyl Trimethyl Ammonium Bromide and Octadecyl Trimethyl Ammonium Bromide Are Surface-Active Small Molecule Dynamin Inhibitors that Block Endocytosis Mediated by Dynamin I or Dynamin II. *Mol. Pharmacol.* **72**, 1425–1439 (2007).

15. Joshi, S. *et al.* The Dynamin Inhibitors MiTMAB and OcTMAB Induce Cytokinesis Failure and Inhibit Cell Proliferation in Human Cancer Cells. *Mol. Cancer Ther.* **9**, 1995–2006 (2010).

16. Herzog, M., Gerard, D., Hirth, L. & Laustriat, G. Natural fluorescence properties of brome mosaic virus protein. *BBA - Protein Struct.* **493**, 167–177 (1977).

17. Canton, I. & Battaglia, G. Endocytosis at the nanoscale. *Chemical Society Reviews* **41**, 2718–2739 (2012).

18. Kirkham, M. *et al.* Ultrastructural identification of uncoated caveolin-independent early endocytic vehicles. *J. Cell Biol.* **168**, 465–476 (2005).

19. Donaldson, J. G., Porat-Shliom, N. & Cohen, L. A. Clathrin-independent endocytosis: A unique platform for cell signaling and PM remodeling. *Cellular Signalling* **21**, 1–6 (2009).

20. Duclos, C. M. *et al.* Caspase-mediated proteolysis of the sorting nexin 2 disrupts retromer assembly and potentiates Met/hepatocyte growth factor receptor signaling. *Cell Death Discov.* **3**, (2017).

21. Saxena, M. *et al.* Inducing cell death in vitro in cancer cells by targeted delivery of cytochrome c via a transferrin conjugate. *PLoS One* **13**, (2018).

22. Pols, M. S. & Klumperman, J. Trafficking and function of the tetraspanin CD63. *Experimental Cell Research* **315**, 1584–1592 (2009).

23. Rous, B. A. *et al.* Role of adaptor complex AP-3 in targeting wild-type and mutated CD63 to lysosomes. *Mol. Biol. Cell* **13**, 1071–1082 (2002).

24. Ohsaki, Y., Cheng, J., Fujita, A., Tokumoto, T. & Fujimoto, T. Cytoplasmic lipid droplets are sites of convergence of proteasomal and autophagic degradation of apolipoprotein B. *Mol. Biol. Cell* **17**, 2674–2683 (2006).

25. Ohsaki, Y., Cheng, J., Suzuki, M., Fujita, A. & Fujimoto, T. Lipid droplets are arrested in the ER membrane by tight binding of lipidated apolipoprotein B-100. *J. Cell Sci.* **121**, 2415–2422 (2008).

26. Dos Remedios, C. G. Fluorescence Resonance Energy Transfer Fret. in *Encyclopedia of life sciences* 1–9 (2001). doi:10.3109/9780203997352.101

27. Sekar, R. B. & Periasamy, A. Fluorescence resonance energy transfer (FRET) microscopy imaging of live cell protein localizations. *Journal of Cell Biology* **160**, 629–633 (2003).

28. Jares-Erijman, E. A. & Jovin, T. M. FRET imaging. *Nature Biotechnology* **21**, 1387–1395 (2003).

29. Morton, S. W., Zhao, X., Quadir, M. A. & Hammond, P. T. FRET-enabled biological characterization of polymeric micelles. *Biomaterials* **35**, 3489–3496 (2014).

30. Klang, V., Valenta, C. & Matsko, N. B. Electron microscopy of pharmaceutical systems. *Micron* **44**, 45–74 (2013).

31. Collins, A. M. *Nanotechnology Cookbook: Practical, Reliable, and Jargon-free Experimental Procedures*. *Nanotechnology Cookbook* (2012). doi:10.1016/B978-0-08-097172-8.00004-7

Chapter 3. Characterisation of P407-DiO and RITC-P407-DiO micelles

3.1 Introduction

Polymeric micelles are being studied to address problems associated with bioavailability and erratic absorption of drugs within the human body[1–8]. These micelles are formed by self-assembly of amphiphilic macromolecules and can act as drug carriers for poorly water-soluble drugs. However, the understanding of the internalisation of these drug carriers in the body is very limited.

In this work, the incorporation of fluorescent microscopy probes such as DiO on the inside (cargo), and RITC on the outside (corona) of P407 micelles was achieved. Such fluorophores were incorporated as markers to follow the uptake mechanism of the micelle within cells by using fluorescent microscopy techniques. Additionally, evidence of DiO and RITC as a FRET pair has been previously reported[9–12].

In this chapter, the characterisation of P407-DiO and RITC-P407-DiO micelles is discussed. The possibility of FRET occurring in RITC-P407-DiO micelles is also explored in this chapter.

3.2 Characterisation of P407-DiO micelles

P407-DiO micelles were prepared by the solvent evaporation method described in section 2.1.1. Prior to characterisation, the micelle solution was filtered to remove aggregates larger than 200 nm.

3.2.1 Fluorescence of P407-DiO micelles

The fluorescence spectrum of a P407 micelles solution encapsulating DiO was measured using a fluorimeter. The sample solution was excited at 484 nm to obtain an emission spectrum within the detection range of 490 to 560 nm (Figure 3.1). A maximum fluorescence intensity peak value was found around 505 nm. The value obtained was compared to the values in the literature; where the maximum fluorescence emission peak shows little variation (between 496 and 504 nm) depending on the solvent used to dissolve the dye [13–15]. Additionally, the shape of the emission spectrum matches the shape of the reported spectra for DiO dye. These last points suggest that the encapsulation of the dye into micelles has no significant effect on its fluorescence profile

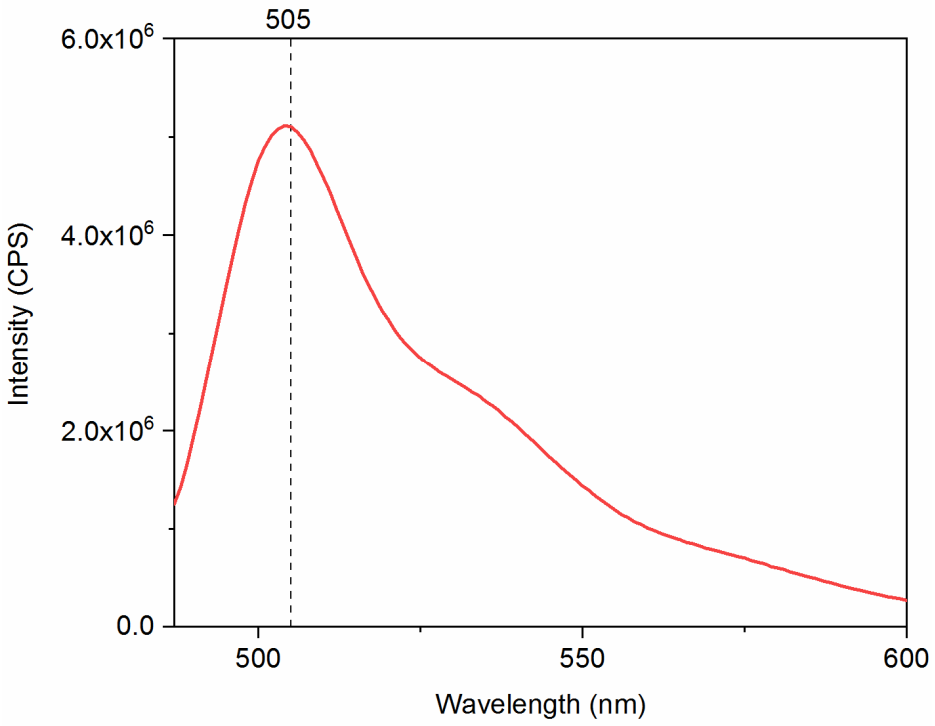

Figure 3.1 *Fluorescence emission spectrum of 200µL 5% w/v P407 micelles encapsulating 0.4 mM of DiO obtained at 37 ºC. The measured sample was excited at 484 nm and the detection range set between 490 to 600 nm*

3.2.2 Size of P407-DiO micelles

The size of the P407-DiO micelles was determined by dynamic light scattering (DLS). This technique measures the intensity fluctuations of the light scattered by the particles at 37 ºC (see section 2.2.1). Since the particles are in aqueous solution, the measured size value corresponds to the hydrodynamic diameter of the particles. Different transformations to the DLS data were done and compared to each other to fully characterise the behaviour of the particles in solution.

Initially, the relative intensity of the light scattered by the particles was measured within different size bins obtaining a size distribution graph by intensity (Figure 3.2 A). The size distribution by this method is considered the most accurate as it is the one directly measured by the instrument. The intensity size distribution expression contains a factor, dictated by Rayleigh's approximation, weighting the distribution by the sixth power of the particle diameter (Equation 2.5). Thus, larger particles are more likely to be detected even if present in small quantities. (Figure 3.2 A) shows two intensity distribution peaks. The first peak has a maximum value at 28 nm, while the second one has a maximum value at 5560 nm. Since the intensity distribution peaks detected are relative to each other, their difference in size indicate their relative amount detected in the measured sample. This suggest that most of the particles detected in the sample have hydrodynamic diameters around 28 nm and the other peak, at 5560 nm, correspond to aggregated particles present at a lower quantity. However, the diameter factor, by this method, has a disproportionate effect on the

amplitude of the peak, so the signal detected by traces of aggregates are overamplified misleading the interpretation of this data.

As described in section 2.2.1 (materials and methods), it is possible to transform the resulting intensity size distribution data to size distributions relative to the volume or number of particles detected (Figure 3.2 B and C respectively). Often, this reveals more information about the particles and their size distribution.

The volume size distribution equation includes a factor of volume in its expression weighting the relative volume size distribution by the third power of the particle diameter (Equation 2.3). Consequently, the diameter has a lower effect on the weighting of the relative distributions while traces of aggregates may still be visible after this transformation. The volume size distribution (Figure 3.2 B) displays just one peak with a maximum value of 14 nm. The loss of the peak associated with the traces of aggregates, detected in the distribution by intensity, is likely due to the lower contribution of the diameter by this method. In this case, the relative volume of the aggregates becomes so small that it becomes irrelevant in the transformation of the data from intensity to volume. Additionally, the volume distribution peak appears to be more narrowly distributed than the peak at 28 nm from (Figure 3.2 A) showing the reduced effect of larger particles on the distribution.

Although the transformation to volume reduces the effect of the diameter on the size distribution, the diameter of large aggregates still has a small contribution on the relative distribution of small particles. To further remove

the effect of the hydrodynamic diameter of large particles, the data was transformed to a size distribution by number. This transformation establishes the relative number of particles detected without taking the size of the particles in account to weight the result (Equation 2.2). This distribution is therefore adequate to determine the size of small particles since traces of aggregates are not expected to affect the size measurements. In Figure 3.2 C, the peak corresponding to small particles has a narrower distribution than the one seen for volume size distribution indicating a better data quality. Additionally, this transformation reveals that most of the particles detected in the sample have a hydrodynamic diameter around 11.6 nm.

To evaluate the quality of the DLS data acquired, the correlation function corresponding to the measurement is here presented (Figure 3.2D). The correlation function seems to correspond to a monomodal sample displaying only one decay pattern and the smooth line shows no evidence of fluorescence from the sample meaning that the micelles are not excited by the incident laser[16]. The fast decay of the correlation function is such of a sample containing particles with small diameters (see section 2.2.1.1., DLS fundamental theory) and the baseline of the function shows no fluctuations which are usually present when samples contain noise artefacts such as dust[17]. Furthermore the intercept value stands close to 1 meaning that the signal intensity detected from the analysed particles is large and the background noise is negligible[18]. These characteristics ensure the quality of the data acquired as well as supporting the idea of the presence of

aggregates in such small amounts that their concentration does not affect the decay of the correlation function.

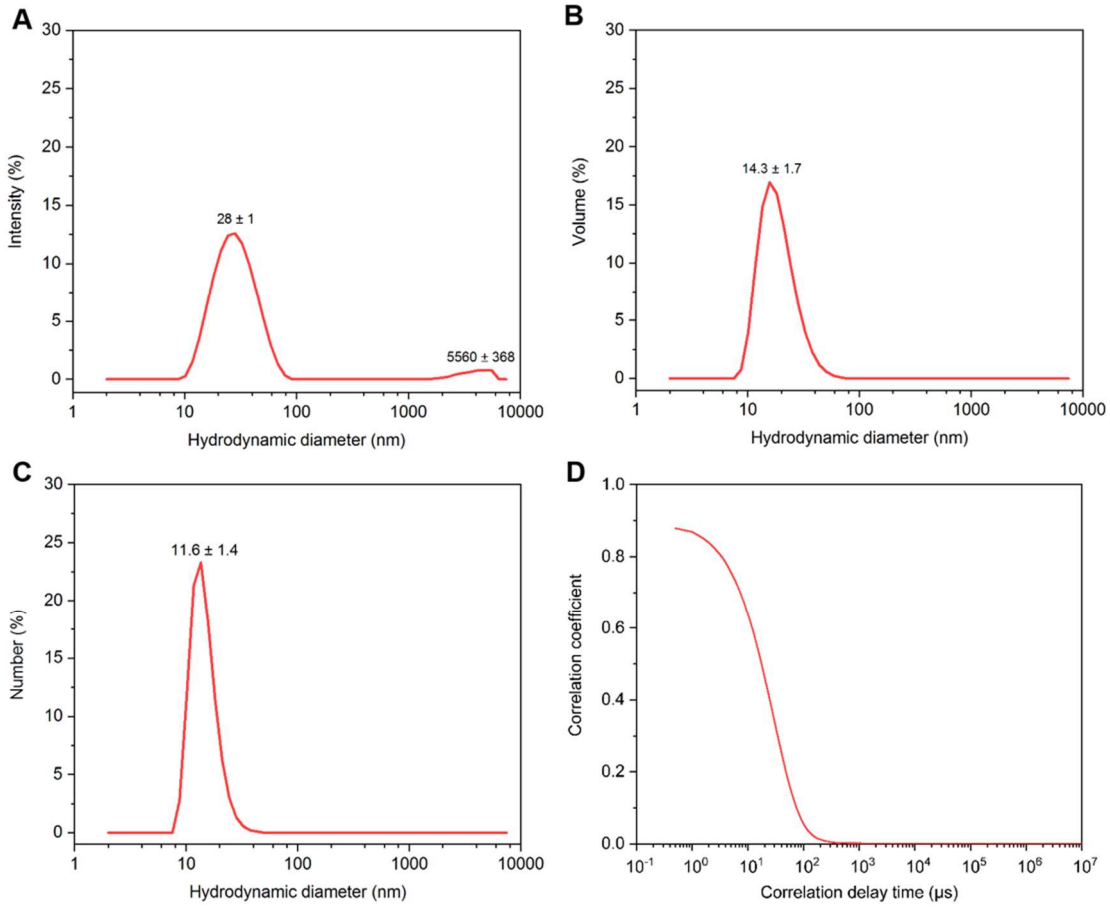

Figure 3.2 *DLS of 5% P407 micelles encapsulating 0.4 mM of DiO at 37 ºC.* ***(A)*** *Size distribution relative to the intensity of the light scattered.* ***(B)*** *Size distribution relative to the volume of particles detected.* ***(C)*** *Size distribution relative to the number of particles detected.* ***(D)*** *Correlation function corresponding to the measurement. Means and standard deviations of three DLS measurements are shown for each distribution.*

3.2.3 Temperature stability of P407-DiO micelles

3.2.3.1 Temperature dependent DLS

Self-assembled micelles form above a critical micellar concentration (CMC) and a critical micelle temperature (CMT)[19]. One of the main variables affecting the stability of self-assembled micelles is the temperature at which the micellar solution is used. To assess the stability of P407-DiO micelles, DLS was used to measure the size of the micelles in suspension at different temperatures.

The size of the micelles was determined every 3 ºC within a temperature range of 4 to 40 ºC, after thermal equilibrium was reached. The maximum value of the size distribution peaks found by intensity, volume and number were plotted against temperature (Figure 3.3). At low temperatures, such as 4 ºC, (Figure 3.3.A) the particle size distribution expressed by intensity shows two distribution peaks, at 4.8 ± 0.3 (peak 1) and 955.4 ± 296.0 nm (peak 3). As seen in Figure 3.2 A, the mean size distribution of the micelles at 37 ºC is approximatively 28 nm, suggesting that the smaller peak corresponds to submicellar structures (unimers) and the larger one corresponds to aggregated micelles.

At 25 ºC (Figure 3.3.B), three peaks are detected. Peak 1 is still present however; the standard deviation of this measurement is higher than the one found for this same peak at 4 ºC. This variation can be justified because the small particles were sometimes not detected in the repetitions of the measurements performed. A new peak at 42.3 ± 2.5 nm (peak 2) is now

detected and the maximum of peak 3 is reduced to 825.0 ± 240.0 nm. Peak 2 shows the presence of a new conformation of the micelles in solution.

When further increasing the temperature to 37 ºC, only two peaks are detected (Figure 3.3.C). The detected peaks correspond to peak 2 and 3 which maxima have decreased to 21.0 ± 3.3 and 531.2 ± 79.0 nm respectively.

As mentioned in section 3.2.2, to obtain full information about the particles present in solution the DLS measurements need to be analysed by intensity, volume and number. The trend of peaks 1,2 and 3 were compared expressing the data using the three previously mentioned methods (Figure 3.3. D, E & F). From 4 to 25 ºC, the value of the hydrodynamic diameters by intensity by volume and by number of Peak 1 (Figure 3.3.D) varies between 3 and 6 nm. However, from 25 ºC to 40 ºC, peak 1 is no longer detected meaning that unimers are no longer present in solution after 25 ºC. This signals the presence of a phase transition in the micellar solution around 25 ºC.

The trend of peak 2 (Figure 3.3. E) indicates that from 4 to 13 ºC no particles can be detected by intensity, by volume, or by number. However, from 15 ºC to 25 ºC particles with sizes between 60 to 80 nm size can only be detected by intensity. This is due to the overamplifying effect caused by the diameter factor associated to this transformation (see section 3.2.2). For the same reason, peak 2 is detected by volume, at 22 ºC, before being detected by number, at 25 ºC. After 25 ºC, peak 2 is detected by all methods and the

value of the hydrodynamic diameter of the particles remains constant until 40 ºC.

Furthermore, the sizes found by all methods, after 25 ºC match with the size values corresponding to single micelles in section 3.2.2. With this information, it is possible to say that the formation of P407-DiO micelles happens after 25 ºC and therefore the CMT can be found around this value. Additionally, Peak 3 (Figure 3.3. F) is only detected by intensity at all temperatures but cannot be detected by volume or number. Therefore, only small traces of aggregates are present in solution.

In order to verify the quality of the data, the correlation function associated to each measurement at all temperatures is presented (Figure 3.4). At all temperatures, the baseline of all correlation curves does not present fluctuations associated to dust or fluorescence caused by the incident laser beam[16,17]. This confirms that all changes detected in Figure 3.3 are due to a change in conformation and not to other noise artefacts. Furthermore, a slow decay of the correlation functions at temperatures from 4 to 25 ºC confirms the presence of large aggregates of micelles in solution as seen in Figure 3.3. Above 25 ºC (CMT) the correlation function decays at significantly lower times due to the detection of smaller sized particles associated to the dissociation of aggregates into micelles. The low intercept values from 4 to 25 ºC is explained by the low concentration of aggregates in solution since unimers are also present in solution[18]. The unimers detected in Figure 3.3A should cause a bimodal distribution, but the results are skewed by the large aggregates due to Rayleigh's approximation

(Section 2.2.1.1.). The correlation functions verify the quality of the data and highlight the changes in conformation seen previously in Figure 3.3.

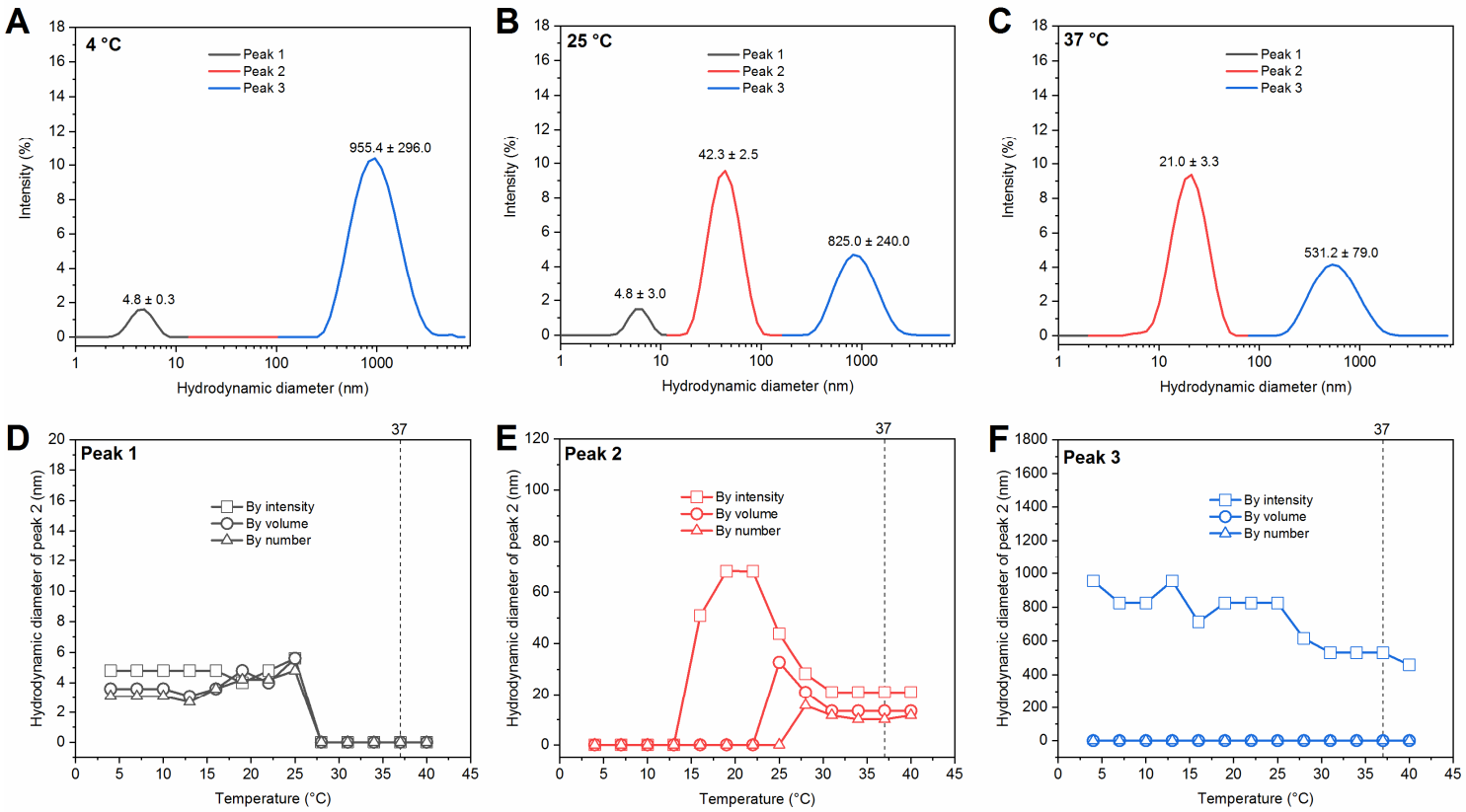

Figure 3.3 *Temperature dependent DLS of 5 % P407 micelles encapsulating 0.4 mM. of DiO.* ***(A)*** *Size distribution relative to the intensity of the light scattered at 4 ºC -peak 1 in grey and peak 2 in red and, peak 3 in blue.* ***(B)*** *Size distribution relative to the intensity of the light scattered at 25 ºC.* ***(C)*** *Size distribution relative to the intensity of the light scattered at 37 ºC. Means and standard deviations of three DLS measurements are shown for each size distribution graph.* ***(D)*** *Variations of the maximum value of the hydrodynamic diameter detected by peak 1 plotted as function of the temperature (-□- by intensity, by -○- volume and -Δ- by number).* ***(E)****Variations of the maximum value of the hydrodynamic diameter detected by peak 2 plotted as function of the temperature.* ***(F)*** *Variations of the maximum value of the hydrodynamic diameter detected by peak 3 plotted as function of the temperature*

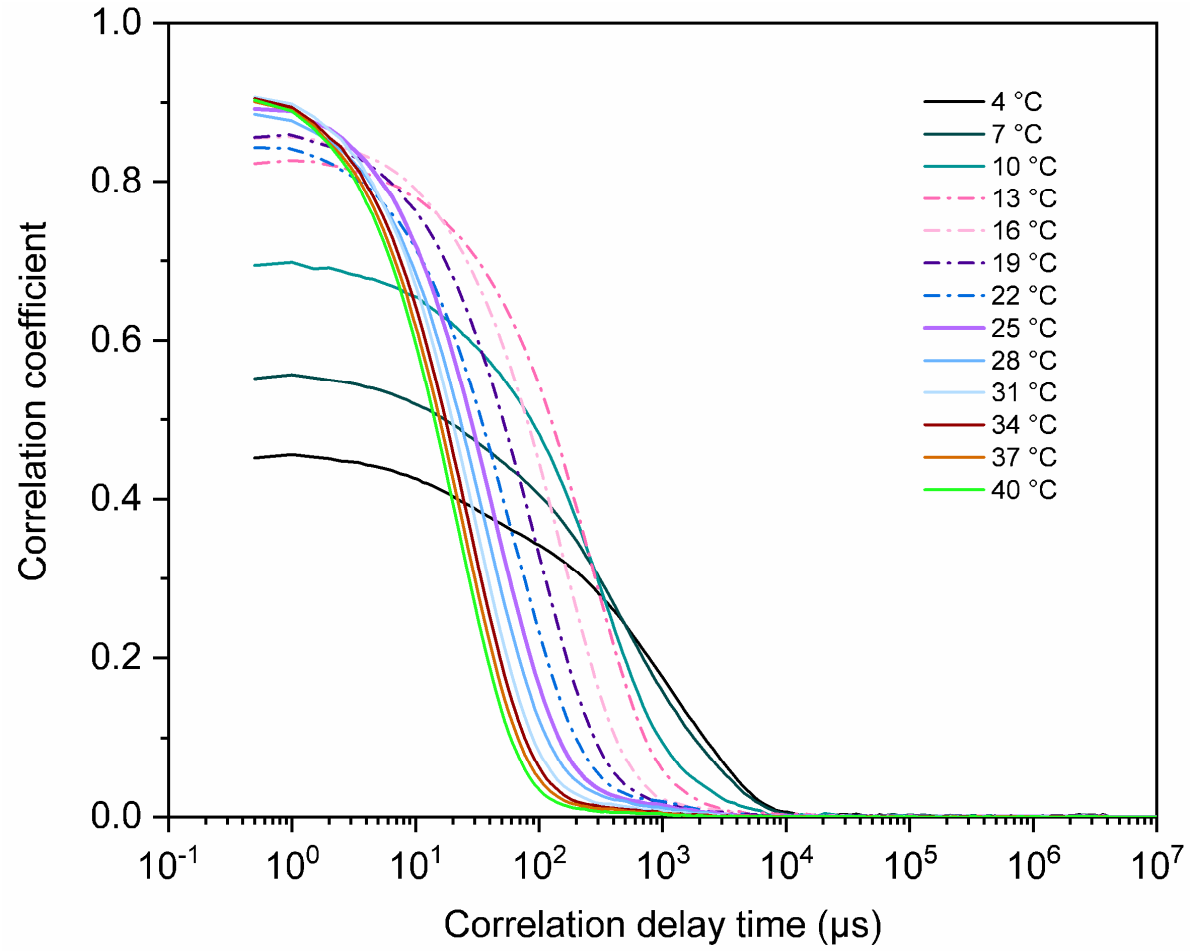

Figure 3.4 *Corresponding correlation functions for temperature dependent DLS measurements on 5% P407 micelles encapsulating 0.4 mM. of DiO (see also Figure 3.3). The dashed and dotted lines highlight a transition between large and small diameter particles detected.*

3.2.3.2 Temperature dependent fluorimetry

The stability of the fluorescence of P 407-DiO micelles was evaluated by measuring the fluorescence of the sample at different temperatures. This was made using a fluorimeter (Section 2.2.2).

The sample solution was excited at 484 nm to obtain a fluorescence emission spectrum measured every 3 ºC within a range of 4 to 40 ºC (Figure 3.5 A). The shape of the spectra remains unchanged at all temperatures meaning the chemical structure of the dye remains intact during the experiment. However, the fluorescence intensity increases with increasing the temperature as a result of the change in conformations of the micelles to unimers or aggregates in solution (see section 3.2.3.1). Changes in fluorescence reflect unimers-to-micelle transition and encapsulation of fluorophore in hydrophobic environment.

To follow the variations of fluorescence intensity, the maximum intensity values detected at 505 nm are plotted against temperature (Figure 3.5 B). The intensity signal remains practically unchanged from 4 to 13 ºC, followed by a burst increase from 13 to 19 ºC. Then, from 19 to 25 °C, the intensity remains constant. Above 25 °C (CMT) and up to 37 °C, the intensity increases linearly. Finally, it remains constant up to 40 ºC. The low intensity in the first temperature interval (4 to 16 °C) matches with the temperature range at which the polymer is present in solution either as aggregates or unimers leaving little hydrophobic environment for the dye to solubilise.The sudden increase of the intensity between 13 and 19 °C, can be attributed to the phase transition from unimers and aggregates to

micelles. This effect is due to the increase of available hydrophobic environments in solution capable to solubilise more DiO. In the temperature interval between 19 and 25 °C, the aggregates size is unchanged, and thus the fluorescence intensity remains constant, as can be seen in table 1.1. In Section 1.3.2.1, the aggregates showed to rapidly start dissociating into smaller fractions from 25 ºC when the solution had reached the CMT. This spontaneous change is also detected by fluorimetry at this same temperature. The intensity of the fluorescence increases gradually as more micelles are formed. The rate at which the intensity increases remains practically constant until reaching 37 ºC. After this temperature, no changes in intensity are detected, indicating that most of the polymer and dye are present in solution in the form of a single-micelle conformation.

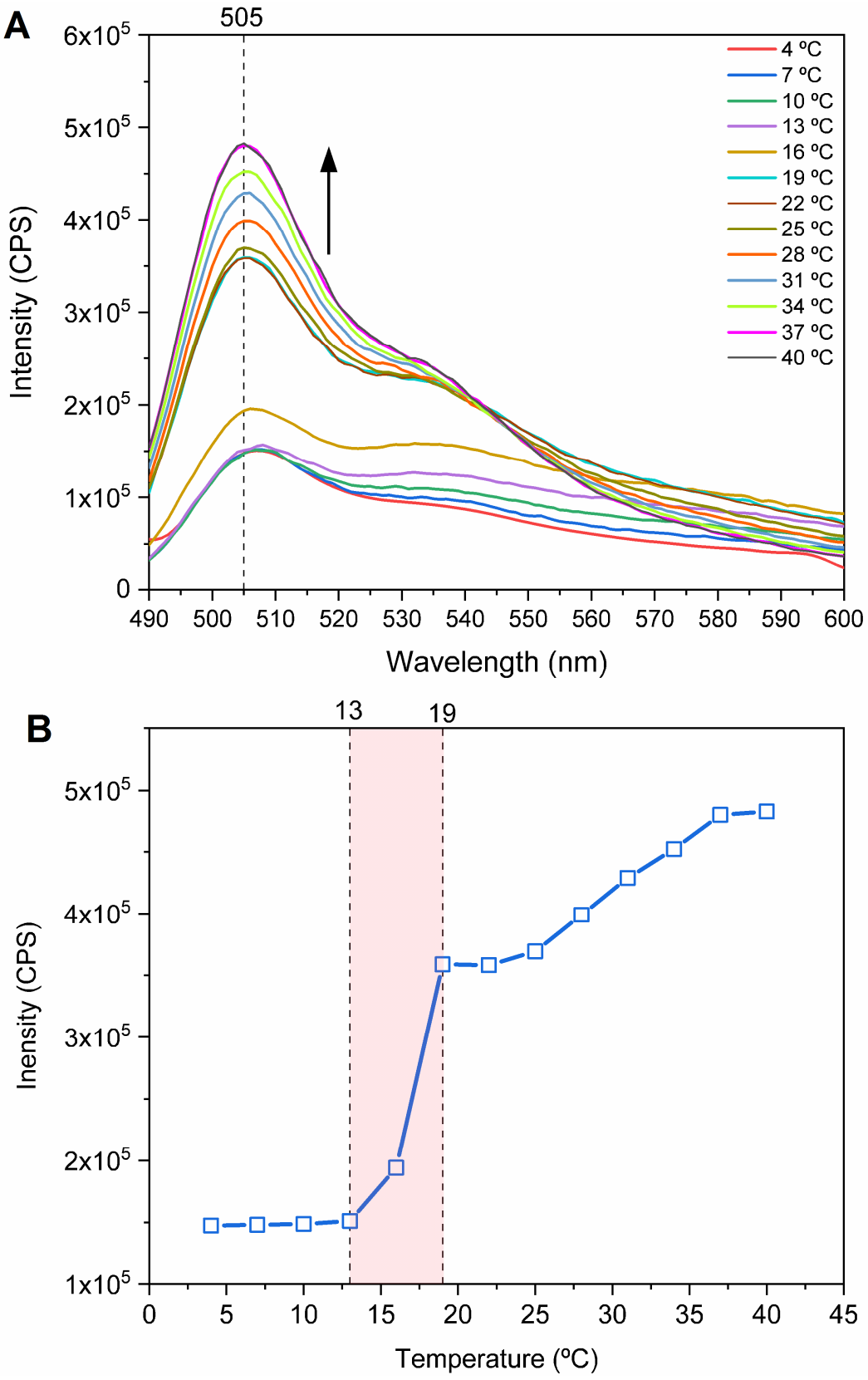

Figure 3.5 *Temperature stability of fluorescent P407-DiO micelles.* ***(A)*** *Fluorescence emission spectra of 5% P407 micelles encapsulating 0.4 mM of DiO measured at temperatures between 4 and 40 ºC (temperature step size = 3 ºC). The measured sample was excited at 484 nm and the detection range set between 490 to 600 nm.* ***(B)*** *Variation of the maximum florescence peak at temperatures between 4 and 40 ºC. The red coloured area designates the temperature range at which the polymer aggregates dissociate to from micelles.*

3.3 Characterisation of RITC-P407-DiO micelles

3.3.1 Fluorescence of RITC-P407-DiO micelles

Initially the excitation and emission spectrum of RITC-P407 polymer were obtained by fluorimetry (Figure 3.6). The maximum excitation is found around 553 nm which matches with the value of maximum absorption of the dye used to conjugate the polymer (Section 2.1.2). This confirms the conjugation of RITC to P407 polymer as well as showing that the chemical structure of the dye was maintained after the conjugation of the fluorophore. The maximum emission of the dye is found around 574 nm. Furthermore, the values obtained are comparable to a previous work using RITC conjugated to Pluronic L 61. Where the maximum excitation and emission values are 558 and 586 nm respectively[20].

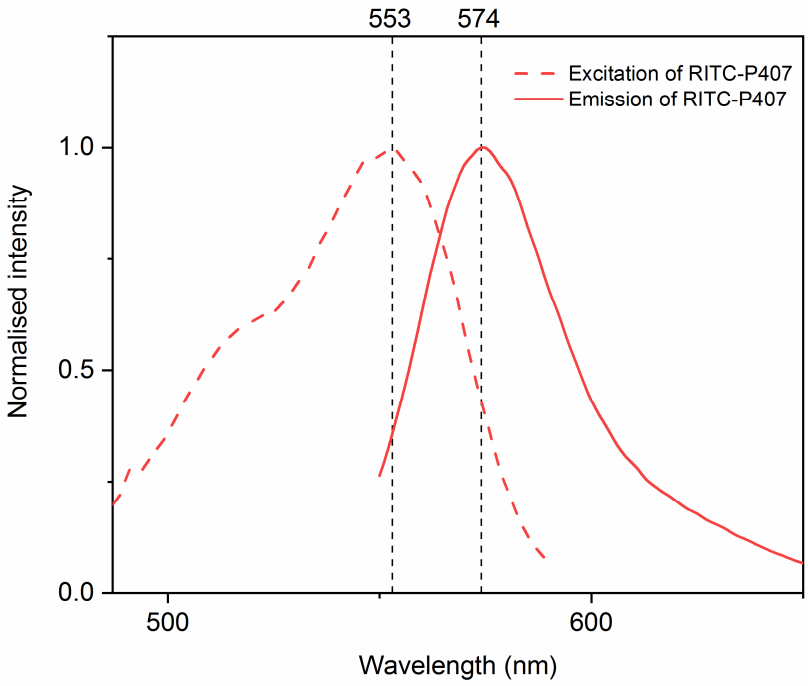

Figure 3.6 *Normalised excitation and emission spectra of RITC-P407 obtained at 37ºC. The excitation spectrum was obtained using the following parameters: λ_{em} = 486-690 nm; λ_{ex} = 595 nm. The emission spectrum was obtained using the following parameters: λ_{ex} = 540 nm; λ_{em} = 550-650 nm.*

Subsequently, fluorimetry measurements were made to RITC-P407-DiO micelles. The sample solution was excited at 484 nm and the detection range was set between 484 and 650 nm (Figure 3.7.C). The first detected emission peak at 505 nm corresponds to DiO (see Figure 3.7.A for comparison). The second emission peak detected at 574 nm corresponds to RITC (see Figure 3.7.B for comparison). This confirms the presence of the two fluorophores the micelles after encapsulation. Since the excitation value used corresponds to the maximum excitation value for DiO, the only peak expected was the one corresponding to DiO. However, the fluorescence emission of RITC is also detected at a higher intensity than DiO. Additionally, the intensity of the DiO peak seems to decrease as the intensity of the peak increases in RITC-P407-DiO micelles compared to the control peaks (Figure 3.7.A and B). These two phenomena suggest the presence of fluorescence quenching caused by an energy transfer between the two dyes, but further analysis may be required to confirm this.

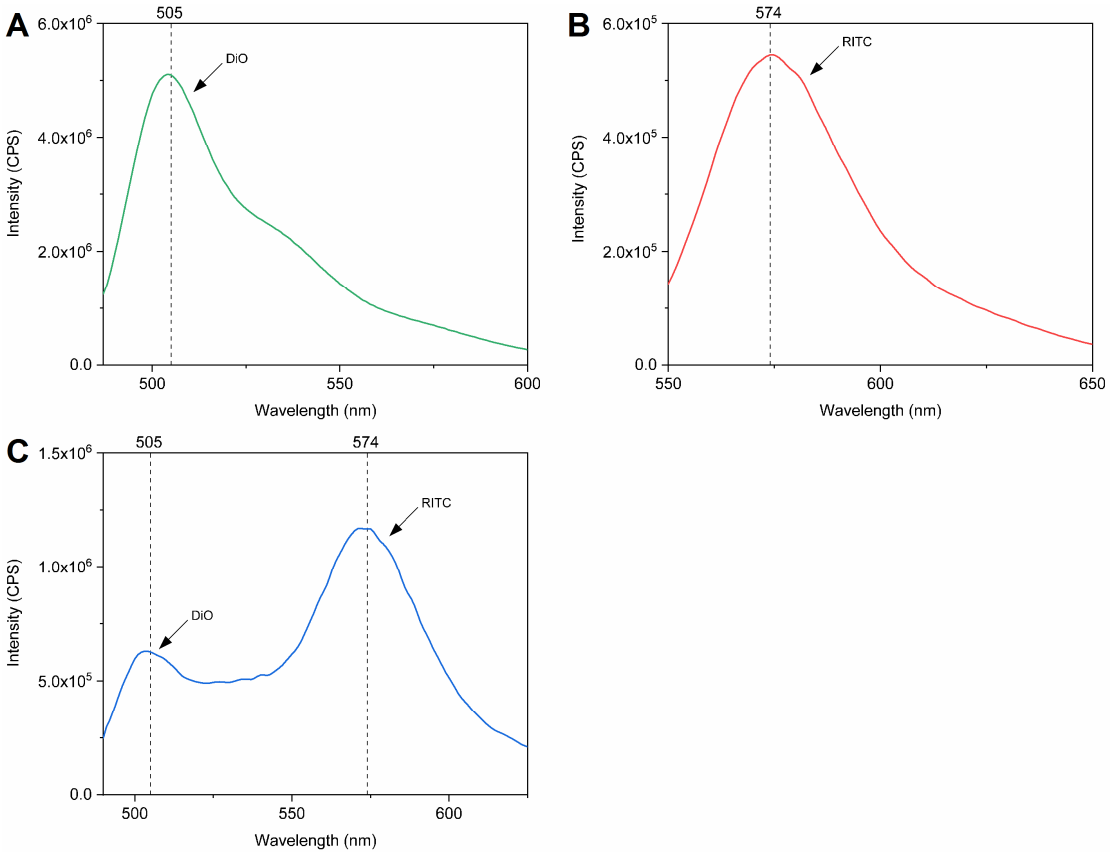

Figure 3.7 *Fluorescence emission spectrum of 200μL 5% w/v RITC-P407-DiO micelles encapsulating 0.4 mM of DiO obtained at 37 ºC.* ***(A)*** *Emission spectra of P407-DiO and* ***(B)*** *RITC-P407 micelles obtained individually are shown for comparison.* ***(C)*** *Emission spectrum showing two peaks corresponding to DiO and RITC-P407. The measured sample was excited at 484 nm and the detection range was set between 486 to 650 nm.*

To understand the phenomenon behind the excitation of both dyes at 484 nm, the emission spectrum of DiO plotted alongside the excitation spectrum of RITC (Figure 3.8). An important spectrum overlap is seen between DiO and RITC-P407. This leads to the assumption that an energy transfer (FRET) could be happening in the micelles between the two fluorophores explaining the double excitation detected previously. However, for FRET to occur, the fluorophores need to be at a distance less than 10 nm from each other[21] (Section 2.4.1.1). To confirm this an analysis of the micelles size is required.

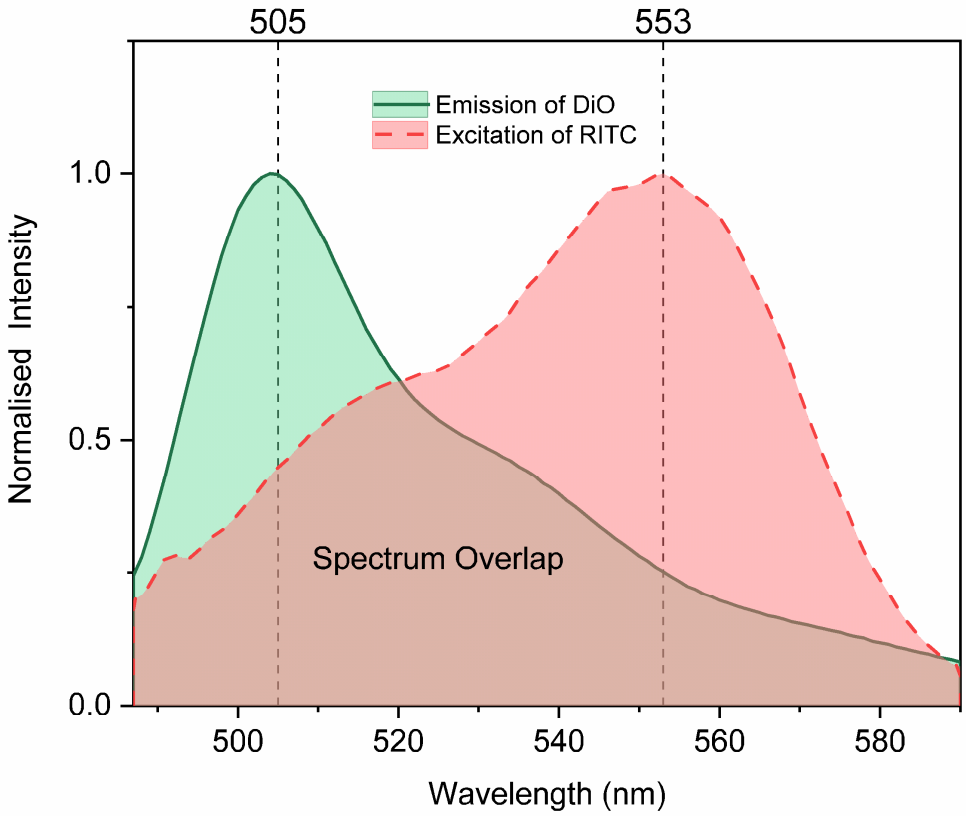

Figure 3.8 *Overlap between DiO emission spectrum (filled green line) and RITC-P407 excitation spectrum (dashed red line).Both spectra were obtained from (figures 1.1 and 1.6).*

3.3.2 Size of RITC-P407-DiO micelles

The size of RITC-P407-DiO micelles was determined by DLS at 37 ºC. Initially, an intensity size distribution was obtained. To gain more information about the sample solution, the intensity size distribution was transformed to volume and number distributions (see section 3.2.2).

The size distribution obtained by intensity (Figure 3.9 A) shows two peaks, the first one around the value of 26 nm and the second one with a maximum value of 5560 nm. The difference in intensities of these two peaks, reveals that the relative amount of large particle aggregates in the second intensity peak represent a small fraction of the total particles in the sample with a hydrodynamic diameter around 26 nm. Since the intensity of the light scattered is proportional to the sixth power of the particle diameter, the signal detected by traces of aggregates might be overamplified and therefore the relative amount of the aggregates in solution might be insignificant.

To confirm this, the data was transformed to a volume size distribution (Figure 3.9 B). This distribution displays only one peak with a maximum value around 15 nm. The peak detected at 5560 nm by intensity is no longer detectable by this method. In this transformation, the volume size distribution is proportional to the third power of the particle diameter. This transformation confers less significance to the size of the particles than in the intensity distribution explaining the loss of the peak corresponding to the traces of aggregates. For this same reason, the peak seen by volume has a narrower distribution than the one found by intensity.

To fully reduce the effect of the diameter on the size distribution, the data was transformed to a distribution by number (Figure 3.9 C). The peak seen at 12 nm has a narrower distribution than the one seen for volume distribution. In terms of number, the relative contribution of each particle compared to another is now just dictated by the number of particles detected without any contribution of the size. This transformation gives a clearer information about the size of the non-aggregated particles.

The quality of the measurement was assessed with the correlation function (Figure 3.9D). This curve presents a fast decay corresponding to small sized particles and the pattern of a monomodal distribution. The smooth line shows no evidence of fluorescence from the sample meaning that the micelles are not excited by the incident laser[16]. Furthermore, the baseline of the curve shows no fluctuations such as the ones seen in presence of noise artefacts[17]. The intercept value close to 1 means a good quality data, where the signal intensity detected from the particles is large and the background noise is negligible[18].

These characteristics ensure the quality of the data acquired as well as supporting the idea of the presence of aggregates in such small amounts that their concentration does not affect the decay of the correlation function.

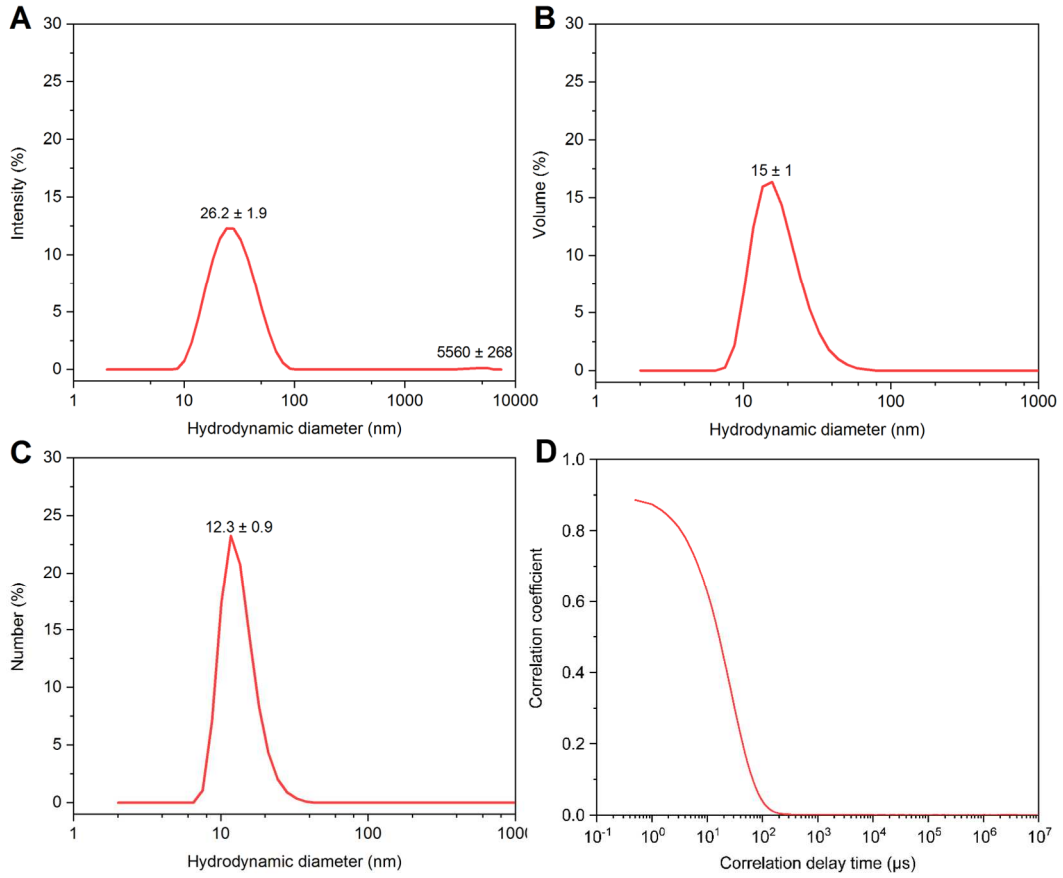

Figure 3.9 *DLS of 5% RITC-P407 micelles encapsulating 0.4 mM of DiO at 37 ºC.* ***(A)*** *Size distribution relative to the intensity of the light scattered.* ***(B)*** *Size distribution relative to the volume of particles detected.* ***(C)*** *Size distribution relative to the number of particles detected.* ***(D)*** *Correlation function corresponding to the measurement. Means and standard deviations of three DLS measurements are shown for each distribution.*

3.3.3 Temperature stability of RITC-P407-DiO micelles

3.3.3.1 Temperature dependent DLS

As established previously in section 3.2.3.1, one of the main variables affecting the formation and stability of self-assembled micelles is the temperature. To evaluate the stability of RITC-P407-DiO micelles, DLS measurements were done to measure the size of the micelles in suspension at different temperatures.

The size of the micelles was determined initially by cooling down the micelle solution from room temperature to 4 ºC and measuring the size every 3 ºC increment until reaching a temperature of 40 ºC. At every step, the solution was allowed to reach thermal equilibrium. At low temperatures such as 4 ºC (Figure 3.10 A) the particle size distribution by intensity shows two distribution peaks, at 91.3 nm (peak 1) and at 5560 nm (peak 2). However, the size of the micelles at 37ºC showed to be around 26 nm (Figure 3.9 A). This suggests that the particles detected at, 4ºC, by peak 1 and 2 are aggregates of micelles.

When increasing the temperature to 37 ºC (Figure 3.10 B), the first distribution peak, obtained by intensity, is reduced to 24 nm which corresponds to the size detected previously in in Figure 3.9.A and peak 2 disappears showing the thermoreversibility of the micelle formation.

Subsequently, the maximum value of each size distribution found, by intensity, volume, and size, was plotted against temperature to identify all the possible conformations of micelles in solution (Figure 3.10 C). The maximum values of peak 1 by intensity (Figure 3.10 C), show constant

values of 91 nm 4 to 10 ºC. After this, the hydrodynamic diameter, decreases until reaching 22 ºC. Above 22 °C, the HD remains practically constant. Although the same trend is seen for volume and number, the start and end values vary depending on the transformations used to express the data.

The hydrodynamic diameter of larger aggregates detected in peak 2 (Figure 3.10 D) remains also constant between 4 to 10 ºC when expressed by intensity and volume with values of 5560 and 4801 nm respectively. Above 10 ºC the presence of aggregates is no longer detected. As mentioned in the previous section, the intensity and volume distribution are more sensitive to small traces of aggregates than the number distribution. Therefore, the aggregates remain undetected by the distribution by number over all the temperature range.

Combining the information given by peaks 1 and 2 in Figure 3.10 C and D, it is clear that from 22 to 40 ºC the particles detected are for the most part single micelles.

In order to verify the quality of the data, the correlation function associated to each measurement at all temperatures is presented (Figure 3.11). At all temperatures, all correlation curves and their baselines do not present fluctuations associated to dust or fluorescence caused by the incident laser beam[16,17]. This confirms that all changes detected in Figure 3.10are due to a change in conformation and not to other noise artefacts. Furthermore, the decrease of decay times of the correlation functions at increasing temperatures is due to the detection of smaller particles

confirming the dissociation of large aggregates into micelles as seen in Figure 3.10. The intercept values close to 1 shows the large signal intensity and the negligible background noise[18]. The correlation functions verify the quality of the data and highlight the changes in conformation seen in Figure 3.10

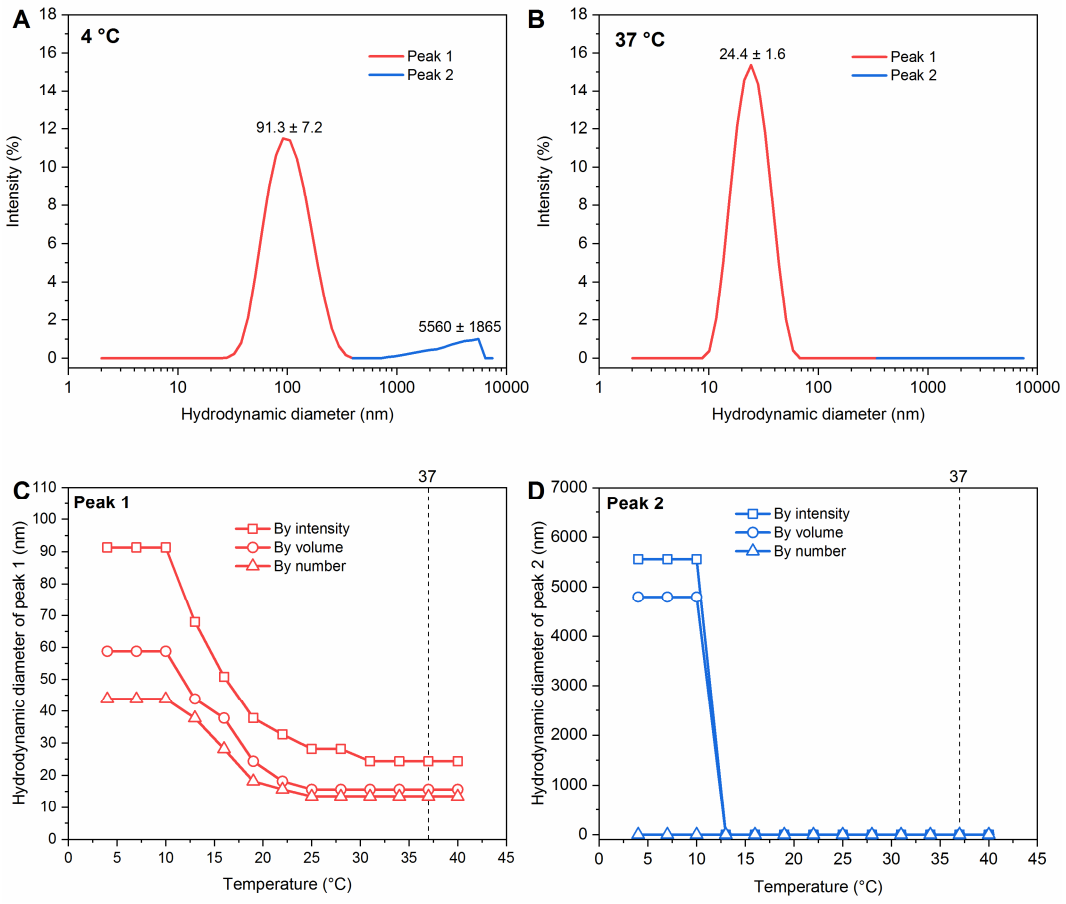

Figure 3.10 *Temperature dependent DLS of 5% RITC-P407 micelles encapsulating 0.4 mM of DiO* ***(A)*** *Size distribution relative to the intensity of the light scattered at 4 ºC -peak 1 in red and peak 2 in blue.* ***(B)*** *Size distribution relative to the intensity of the light scattered at 37 ºC.* ***(C)*** *Variations of the maximum value of the hydrodynamic diameter detected by peak 1 plotted as function of the temperature (-□- by intensity, by -○- volume and -Δ- by number.)* ***(D)****Variations of the maximum value of the hydrodynamic diameter, detected by peak 2 plotted as function of the temperature.*

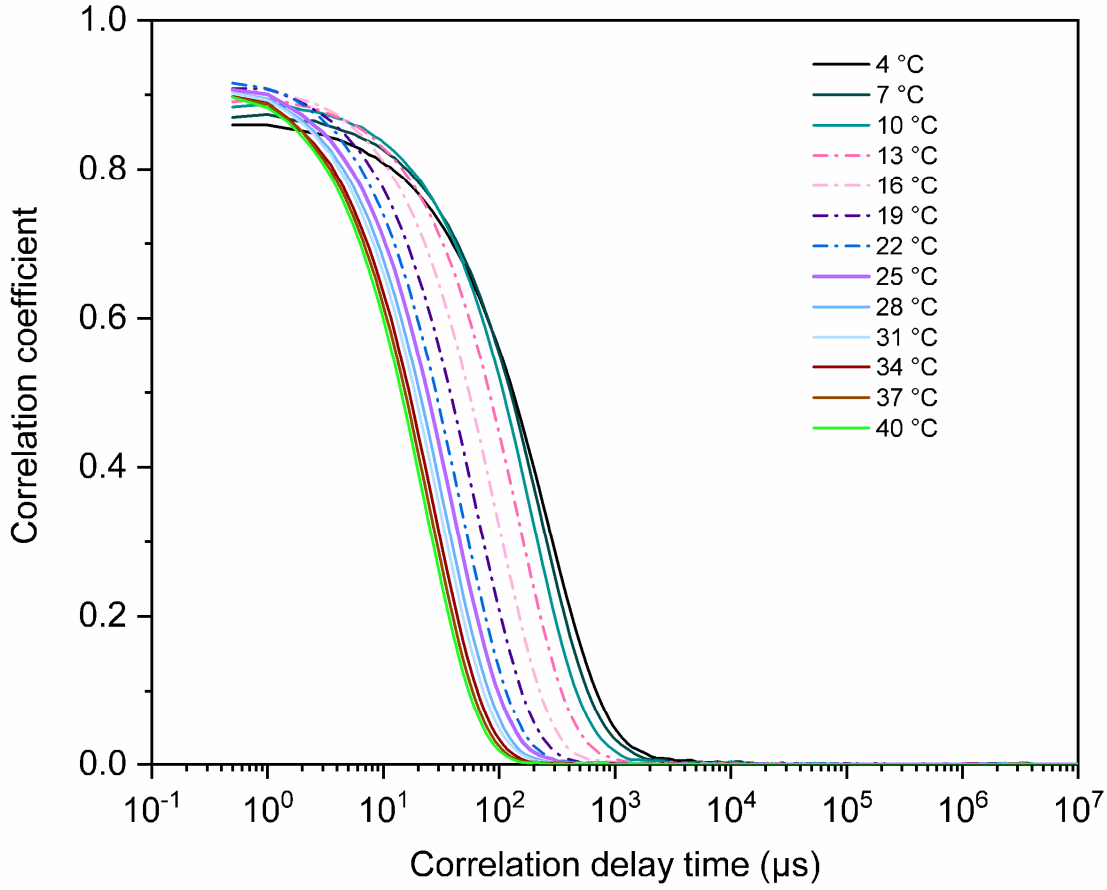

Figure 3.11 *Corresponding correlation functions for temperature dependent DLS measurements on 5% RITC-P407 micelles encapsulating 0.4 mM. of DiO (see also Figure 3.11). The dashed and dotted lines highlight a transition between large and small diameter particles detected.*

.

3.3.3.2 Temperature dependent fluorimetry

The stability of the fluorescence of RITC-P407-DiO micelles was analysed by measuring the fluorescence of the cargo (DiO) at different temperatures (section 2.2.1.2).

To obtain an emission spectrum at all temperatures, the sample solution was excited at 484 nm and the detection range was set between 486 to 600 nm. Each measurement was taken every 3 ºC within a temperature range of 4 to 40 ºC (Figure 3.12 A). The profile of the spectra is the same at all temperatures. Whereas the fluorescence intensity varies with the temperature.

The variations in the fluorescence intensity at 505 nm are plotted against temperature (Figure 3.12 B). Initially, the fluorescence intensity increases with the temperature between 4 to 13 ºC. At 13 °C the intensity reaches a maximum and decreases slowly up to 40 °C.

The initial increase in intensity is explained by the dissociation of aggregates and the gradual increase of available hydrophobic environments in solution capable to solubilise DiO.(see sections 3.2.3.1 and 3.3.3.1).

After 13 ºC, the fluorescence intensity of the sample diminishes as the temperature increases. This may be explained by the presence of FRET (Section 2.4.1.1) since the two dyes present in the sample have an overlap in their emission and excitation spectra (Section 3.3.1). According to figure 1.7 B, the hydrodynamic size of the micelles at 16 ºC, is approximatively 30 nm. The radius of the micelle is therefore <15nm. Thus, the distance

between the cargo (DiO) and the corona (RITC) of the micelle may be smaller than 10 nm which is small enough for a transfer of energy to occur[22]. In this case, DiO is the donor transferring energy to the acceptor, P407-RITC. Additionally, as shown in sections 3.2.3.1 and 3.3.3.1, Increasing the temperature decreases the size of the particles. The closer the fluorophores get to each other; the more energy transfer occurs between the donor and the acceptor leading to a decrease on the intensity of fluorescence of DiO. However, the peak corresponding to RITC at 574 nm does not increase with temperature as previously seen in RITC-P407-DiO micelles (Figure 3.7). One explanation to this could be due to a self-quenching effect previously reported for RITC[23]. This self-quenching effect is due to a high dye density which may have occurred at low temperatures when the polymer was present in solution as forms of aggregates. To resolve this without interference of self-quenching, the experiment should be repeated with longer equilibration times between measurements.

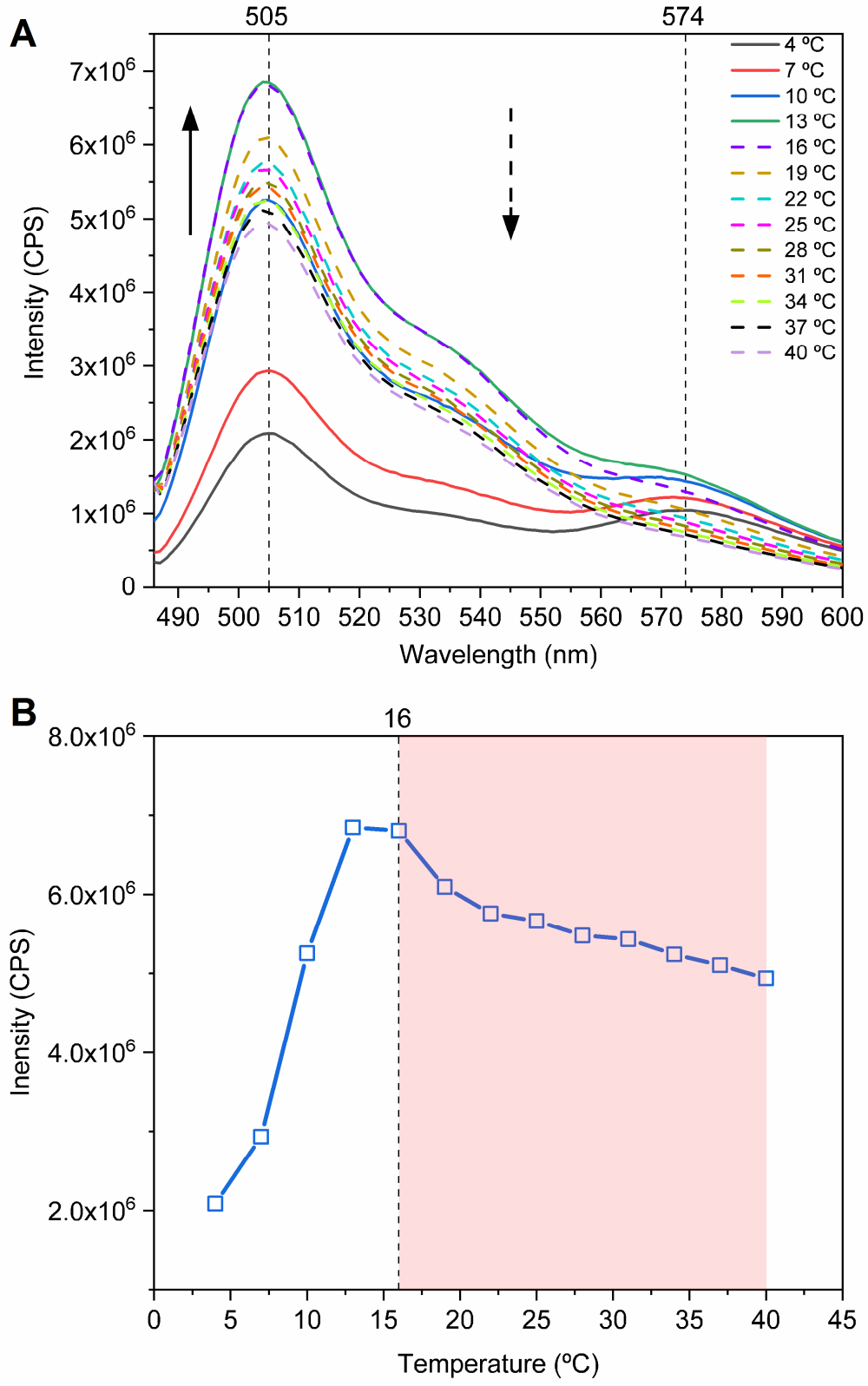

Figure 3.12 *Temperature stability of fluorescent RITC-P407-DiO micelles.* ***(A)*** *Fluorescence emission spectra of 5% RITC-P407 micelles encapsulating 0.4 mM of DiO measured at temperatures between 4 and 40 ºC (temperature step size = 3 ºC). The measured sample was excited at 484 nm and the detection range set between 490 to 600 nm. The filled lines indicate the increasing fluorescence intensities whereas the dashed lines indicate the decreasing fluorescence intensities due to variations in temperature.* ***(B)*** *Variation of the maximum florescence peak at 505 nm within temperatures between 4 and 40 ºC (temperature step size = 3 ºC). The red coloured area designates the temperature range at which FRET may be occurring.*

3.4 Discussion

This chapter has shown different approaches to characterise and understand the behaviour of P407-DiO and RITC-P407- DiO micelles in solution.

The fluorescence data at 37 ºC of the two type of micelles showed that in both cases, the encapsulation has no effect on the maximum value of the fluorescence peak of the cargo. This proves that the encapsulation occurs via a physical method rather than chemical. The RITC fluorophore showed to maintain its characteristic fluorescence after conjugation, meaning that the structure responsible of its fluorescence stayed intact. Furthermore, in the case of RITC-P407-DiO micelles, the fluorimetry showed to be a useful tool to assess the presence of both fluorophores in the micelles after encapsulation. However, evidence of fluorescence quenching between the two fluorophores was detected via this method leading to investigate further the possibility of FRET occurring in the micelles.

The data obtained by DLS at 37 ºC, allowed to determine the size of particles detected in solution and to identify different conformations when using different expressions of size distributions. For both types of micelles, aggregates were identified in the sample. Though, their relative amount proved to be insignificant compared to the amount of micelles in solution. Additionally, at this temperature, most of the particles in solution showed to have a HD around 12 nm for both type of particles. Furthermore, the size values found in this work agree with values found in the literature for unloaded P407 micelles[5,24,25] (values reported between10 and 20 nm

depending on the method used to determine particle size) suggesting that encapsulating DiO and functionalising the polymer does not affect the size of the micelles.

The temperature dependent DLS revealed information about the stability of the micelles in solution. Across all temperatures, three main conformations of micelles were found (sub-fractions of micelles or unimers, micelles and, aggregates) for P407-DiO micelles whereas just two were seen for RITC-P407-DiO micelles (micelles and aggregates). This difference may be explained by the steric hindrance caused by the RITC attached to the polymer impeding the micelles to adopt intermediate conformations in the transition from aggregates to micelles. Moreover, it was possible to identify an approximative value for the CMT for both micelles around 25 ºC. This shows the little effect of the conjugation of the polymer on the CMT value. At this value, most of the formed aggregates dissociated to form single micelles proving the self-assembly of the micelles as well as their thermal reversibility. However, the CMT values for P407-DiO and RITC-P407-DiO differ from the values found in literature for unloaded P407 micelles (19.5 ºC for 5% P407) in aqueous solution[19]. This suggests that the encapsulation of DiO affects the CMT of P407 micelles.

The temperature dependent fluorimetry showed that the fluorescence intensity of P407-DiO micelles increased with the temperature due to the dissociation of aggregates into micelles consolidating the data found by DLS. For RITC-P4047-DiO micelles, the temperature dependent fluorimetry helped follow all the micelles conformations until the radius of the micelles reached approximatively 10 nm. At this point, the intensity of fluorescence

of DiO decreased. This observed phenomenon supports the possibility of FRET occurring in the micelles. However, to fully prove the presence of FRET, the emission peak of RITC needs to be monitored alongside DiO allowing more equilibration time between measurements. Contrarily to DiO, an intensity increase on the emission peak would expect to be seen to confirm the energy transfer from the donor to the acceptor. Another way to support this data would be the measurement of the exponential decay of the fluorescence with time using fluorescence-lifetime imaging microscopy.

Finally, the study of the different characterisation techniques allowed to develop a quality control methodology for characterising and controlling the properties of the micelles before using in other experiments. This way, at 37 ºC, where biological experiments are performed, most of the particles found in solution are single micelles of approximatively 12 nm. But the sample must be kept at 37 ºC prior to the experiment.

3.5 References

1. Batrakova, E. V. & Kabanov, A. V. Pluronic block copolymers: Evolution of drug delivery concept from inert nanocarriers to biological response modifiers. *Journal of Controlled Release* **130**, 98–106 (2008).

2. Zhang, W. *et al.* Enhanced antitumor efficacy by paclitaxel-loaded pluronic P123/F127 mixed micelles against non-small cell lung cancer based on passive tumor targeting and modulation of drug resistance. *Eur. J. Pharm. Biopharm.* **75**, 341–53 (2010).

3. Akash, M. S. H. & Rehman, K. Recent progress in biomedical applications of pluronic (PF127): Pharmaceutical perspectives. *J. Control. Release* **209**, 120–138 (2015).

4. Wei, Z. *et al.* Paclitaxel-loaded Pluronic P123/F127 mixed polymeric micelles: formulation, optimization and in vitro characterization. *Int. J. Pharm.* **376**, 176–85 (2009).

5. Deller, R. C. *et al.* Functionalised triblock copolymer vectors for the treatment of acute lymphoblastic leukaemia. *Mol. Pharm.* **14**, 722–732 (2017).

6. Grimaudo, M. A. *et al.* Poloxamer 407/TPGS Mixed Micelles as Promising Carriers for Cyclosporine Ocular Delivery. *Mol. Pharm.* **15**, 571–584 (2018).

7. Hagan, S. A. *et al.* Polylactide−Poly(ethylene glycol) Copolymers as Drug Delivery Systems. 1. Characterization of Water Dispersible Micelle-Forming Systems. *Langmuir* **12**, 2153–2161 (1996).

8. Samaddar, P., Deep, A. & Kim, K. H. An engineering insight into block copolymer self-assembly: Contemporary application from biomedical research to nanotechnology. *Chem. Eng. J.* **342**, 71–89 (2018).

9. Xiao, W. *et al.* Extremely long tumor retention, multi-responsive boronate crosslinked micelles with superior therapeutic efficacy for ovarian cancer. *J. Control. Release* **264**, 169–179 (2017).

10. Li, Y., Xiao, K., Zhu, W., Deng, W. & Lam, K. S. Stimuli-responsive cross-linked micelles for on-demand drug delivery against cancers. *Advanced Drug Delivery Reviews* **66**, 58–73 (2014).

11. Li, Y. *et al.* Probing of the assembly structure and dynamics within nanoparticles during interaction with blood proteins. *ACS Nano* **6**, 9485–9495 (2012).

12. Huang, P. *et al.* Bridging the Gap between Macroscale Drug Delivery Systems and Nanomedicines: A Nanoparticle-Assembled Thermosensitive Hydrogel for Peritumoral Chemotherapy. *ACS Appl. Mater. Interfaces* **8**, 29323–29333 (2016).

13. Hume, R. I. & Honig, M. G. Fluorescent Carbocyanine Dyes Allow Living Neurons of Identified Origin to Be Studied in Long-Term Cultures. *J. Cell Biol.* **103**, 171–187 (1986).

14. Ragnarson, B., Bengtsson, L. & Hægerstrand, A. Labeling with fluorescent carbocyanine dyes of cultured endothelial and smooth muscle cells by growth in dye-containing medium. *Histochemistry* **97**, 329–333 (1992).

15. Höppner, M., Luhm, J., Schlenke, P., Koritke, P. & Frohn, C. A flow-cytometry based cytotoxicity assay using stained effector cells in combination with native target cells. *J. Immunol. Methods* **267**, 157–163 (2002).

16. Micromeritics Instrument Corporation. Simplifying the Interpretation of Dynamic Light Scattering Data. *AZO Materials* (2020). Available at: https://www.azom.com/article.aspx?ArticleID=16770.

17. Malm, A. V. & Corbett, J. C. W. Improved Dynamic Light Scattering using an adaptive and statistically driven time resolved treatment of correlation data. *Sci. Rep.* **9**, (2019).

18. Leszczyszyn, O. In pursuit of perfect data:DLS correlation function. *Malvern Panalytical* (2012). Available at: https://www.materials-talks.com/blog/2012/11/08/in-pursuit-of-perfect-data-dls-correlation-function/.

19. Alexandridis, P., Holzwarthf, J. F. & J, T. A. H. Micellization of Poly(ethylene oxide)-Poly(propylene oxide)-Poly(ethylene oxide) Triblock Copolymers in Aqueous Solutions Thermodynamics. *Macromolecules* **27**, 2414–2425 (1994).

20. Hong, W. *et al.* PH-sensitive micelles for the intracellular co-delivery of curcumin and Pluronic L61 unimers for synergistic reversal effect of multidrug resistance. *Sci. Rep.* **7**, 1–20 (2017).

21. Sekar, R. B. & Periasamy, A. Fluorescence resonance energy transfer (FRET) microscopy imaging of live cell protein localizations. *Journal of Cell Biology* **160**, 629–633 (2003).

22. Gordon, G. W., Berry, G., Liang, X. H., Levine, B. & Herman, B. Quantitative fluorescence resonance energy transfer measurements using fluorescence microscopy. *Biophys. J.* **74**, 2702–2713 (1998).

23. Widmer, S. *et al.* Incorporation of a FRET dye pair into mesoporous materials: a comparison of fluorescence spectra, FRET activity and dye accessibility. 1. Batrakova, E. V. & Kabanov, A. V. Pluronic block copolymers: Evolution of drug delivery concept from inert nanocarriers to biological response modifiers. *Journal of Controlled Release* **130**, 98–106 (2008).

24. Attwood, D., Collett, J. H. & Tait, C. J. The micellar properties of the poly(oxyethylene) - poly(oxypropylene) copolymer Pluronic F127 in water and electrolyte solution. *Int. J. Pharm.* **26**, 25–33 (1985).

25. Bodratti, A. M. & Alexandridis, P. Formulation of poloxamers for drug delivery. *Journal of Functional Biomaterials* **9**, 11 (2018).

Chapter 4. Evaluation of micelles uptake and cargo release in epithelial cells

4.1 Introduction

Over the past decades, the use of nanoparticles has become an important alternative for drug delivery systems. Because of their size, these particles have a large inherent surface area per unit volume which increases interactions with their surroundings[1,2]. Additionally, nanoparticles can be injected into the bloodstream without the risk of blocking the blood vessels[3].

Many drugs of potential interest for the treatment of several diseases such as cancer, schizophrenia or epilepsy have a complex chemical formulation which may compromise their solubility in common solvents like water. This insolubility compromises drug bioavailability in the organism and thus their therapeutic value[4,5].

Alternative formulations such as polymeric micelles are being studied to address poor solubility problems [6,7]. Polymeric micelles have proved to have a high solubilisation index, a high drug loading capacity as well as high stability in the blood stream[7–9]. These polymeric micelles can be composed of biocompatible and water-soluble polymeric side chains such as PEO[10–12] and hydrophobic core-forming segments (PPO) belonging to the family of Pluronics®[13]. A particular type of Pluronic® type polymer being used to encapsulate drugs is the triblock copolymer P407 also known as F127. So far, P407 has shown to be a good drug-delivery candidate used to efficiently encapsulate and deliver a wide range of water-insoluble drugs into target areas[14–18].

To use and design such drug delivery systems, it is essential to understand their mechanism of internalisation in cells and therefore in the human body. Endocytosis is a general process by which cells internalise molecules and macromolecules from the external cellular environment by enclosing them into the plasma membrane. This process can be subclassified into phagocytosis 'cell eating', which only happens in specialised cells, and pinocytosis 'cell drinking'. This last mechanism can be further divided into other sub-mechanisms such as receptor-mediated endocytosis (RME) or macropinocytosis amongst others[19]. Previous studies on polymeric micelles made with a similar triblock copolymer (P85) have shown them to undergo receptor mediated endocytic pathways to enter mammalian cells[20].

However, endocytic mechanisms involve structural changes in the cellular membrane[21]. Thus, the importance of understanding the interactions of triblock copolymers with the membrane. These copolymers have been shown to interact with the phospholipid membrane in two different ways depending on the duration of the exposure. Previous studies have found the ability of the polymer to be first adsorbed on the membrane, at early exposure times, creating a sealing effect. This adsorption is followed by the insertion of the hydrophobic chain of the polymer into the lipid bilayer increasing the permeability of the membrane[22,23]. This last step has been shown to facilitate the entry of particles from the external cell environment into the cell.

In this chapter, P407-DiO and RITC-P407-DiO micelles (characterised in chapter 3) are used as a study vector to try to understand their uptake mechanism and cargo release in two different cell monolayers (MDCK and BeWo). This was undertaken by combining different microscopy techniques, confocal microscopy, high content screening microscopy, immunofluorescence and FRET. Several hypotheses are tested in this chapter, these are: if polymeric micelles are uptaken by epithelial cells, they would be trackable and quantifiable with P407-DiO and RITC-P407-DiO micelles over time. If polymeric micelles are being uptaken by cells via RME as stated above, the use of inhibitors of such pathway would result in the complete inhibition of their uptake. Furthermore, the use of immunofluorescent markers of endocytic vesicles should help tracking their uptake path. Finally, if the cargo of the micelles is released after uptake this should be trackable using FRET technique in RITC-P407-DiO micelles.

4.2 Materials and methods

4.2.1 Cell culture methods

4.2.1.1 Imaging of micelle uptake over time

For time course exposures, MDCK and BeWo b30 cells were seeded on 13 mm sterile coverslips. Each coverslip was placed at the bottom of an individual well of a 12 well plate. 1 mL of cell suspension was added to each well at a concentration of 0.66 x 10^5 cells/mL and grown for 3 days at 37 °C in a humidified atmosphere of 5% CO_2. The prepared solution containing P407-DiO or RITC-P407-DiO micelles (Section 2.1) was filtered in a 0.2 µm filter and diluted 10-fold in the appropriate cell culture medium (Section 2.3) to be finally added to the cells for 1, 4, 8 and 24 hours at 37 °C in a humidified atmosphere of 5% CO_2. At the end of all exposure periods, the coverslips were washed with PBS to remove any extracellular material and fixed using 4% PFA. The coverslips were then mounted onto a microscope slide using Vectashield containing DAPI (Vector laboratories, H-1200).

Within a single experiment, each experimental condition was performed in duplicate. All experiments were performed at least three times on separate occasions.

4.2.1.2 Analysis of micelle uptake by high content screening

To quantify the fluorescence associated with P407-DiO micelles over time,100 µL of BeWo b 30 or MDCK cell suspension at a concentration of 1.8 x 10^5 cells/mL were seeded in each well of a 96-well plate and grown for 2-3 days until they formed a monolayer. The cells were exposed to P407-DiO micelles as explained in section 4.2.1.1 for a time course of 1, 2, 3, 4, 5, 6, 7, 8 and 24hours. At the end of all exposure periods, the wells were washed with PBS to remove any extracellular material and fixed using 4% PFA. The cells were then stained with a nucleus selective dye (Hoechst 33342, blue; Thermo scientific, 62249).

Additional experiments using inhibitors were undertaken on cells grown on 96 well plates as explained above. Treated cells were pre-exposed to a dynamin-II inhibitor MiTMAB (Merck, 1119-97-7) at a final concentration of 30 nM in cell culture medium (1 in 1000 from the stock solution at 30 µM) for 30 minutes. After this step, cells were exposed to a 1 in 10 dilution of filtered P407-DiO micelles with and without MiTMAB. The positive control used to test inhibitor efficacy was transferrin-488 (green;Invitrogen, T13342) at 25 µg/ml cell culture medium (1 in 200 dilution from a stock solution of 5 mg/mL). Additionally, cells were exposed to cell culture medium containing 30nM MiTMAB in the absence of micelles as a negative control for fluorescence. The total length of each exposure was 1 hour.

Each experiment included 6 replicate wells and was performed on two separate occasions.

4.2.1.3 Surfactant optimisation

To localise cell compartments containing DiO by immunofluorescence localisation, it was first necessary to establish conditions that allowed membrane permeabilisation for antibody entry while retaining DiO fluorescence within intracellular compartments. The selection of an appropriate surfactant for immunofluorescence experiments was carried out on MDCK cells grown in imaging dishes. 2 mL of cell suspension at a concentration of 0.88 x 10^5 cells/mL were seeded on cell culture imaging dishes and grown for 2 days at 37 ºC in a humidified atmosphere of 5% CO_2. After the incubation time, a 10-fold dilution of filtered P407-DiO micelles (section 4.2.1.1) in cell culture medium was added to the cells for 4 hours at 37 ºC in a humidified atmosphere of 5% CO_2. At the end of the exposure time, the coverslips were washed with PBS to remove any extracellular material and fixed using 2% PFA. To test the effect of the surfactant on fixed cells, the cells were imaged in 2 mL of PBS. After 30 seconds, 0.5 mL of PBS was removed from the dish and replaced with 0.5 mL of 0.4 % Saponin(Merck, S4521) or Triton™ x-100 (Merck, 9002-93-1) in PBS to give a final concentration of 0.1 % in the imaging dish. This experiment was repeated twice on separate occasions.

4.2.1.4 Localisation of sub-cellular compartments by immunofluorescence

MDCK and BeWo b30 experiments with antibodies was done on coverslips as previously described (section 4.2.1.1). The cells were exposed separately to P407-DiO micelles for 4 hours. An additional 24 hours experiment was set up for BeWo b30 cells only following the same procedure. Following fixation, the cells were permeabilised with 0.1% Saponin and incubated with a primary antibody followed by a secondary antibody selected for each specific target (Table 4.1). The full protocol can be found in Section 2.3.4.

Within a single experiment, each experimental condition was performed in duplicate. All experiments were performed at least three times.

Table 4.1 *Primary and secondary antibodies used*

Primary antibody	Used to target	Dilution	Secondary antibody	Dilution
EEA1 (mouse)	Early endosomes	1:200	Alexa 594 (mouse)	1:200
CD63 (mouse)	Late endosomes/ Lysosomes	1:200	Alexa 594 (mouse)	1:200
ApoB (rabbit)	Lipid droplets	1:200	Alexa 594 (rabbit)	1:200

4.2.1.5 Determination of cargo release using FRET

The same process described in section 4.2.1.1 was followed for FRET experiments on MDCK cells continuously exposed to RITC-P407-DiO micelles or using a pulse-chase protocol in which cells were exposed for one hour before replacing the experimental medium with cell culture medium. The cells were then kept at 37 ºC and a humidified atmosphere of 5% CO_2 for the required time.

4.2.2 Imaging methods

4.2.2.1 General confocal imaging conditions

Confocal images were obtained with a Leica SP5-II AOBS confocal laser scanning microscope attached to a Leica DM I6000 inverted microscope using a 63x oil-immersion lens (WD 0.1, NA 1.4). Filter cubes used for visual inspection were I3 (blue), N2.1 (green) and A4 (UV). The lasers used to acquire images were a 50 mW 405 nm diode laser, a 65 mW 488 nm Argon laser and a 20 mW 561 nm solid state yellow laser. The detectors used were a standard PMT with a detection range set at 415-470 nm, and two hybrid detectors with detection ranges of 498-545 nm and 575-650 nm respectively. The dimensions of the acquired images were 1024 x 1024 pixels with a resolution of 4.14580 pixels/µm.

For each condition, six random fields of view were selected in the cell monolayer and z-stacks were obtained using a step size of 1 µm. All settings were kept unchanged over all samples and experiments to ensure comparability. After image acquisition, the maximum intensity stack was selected using ImageJ/Fiji[24,25] software. The most representative images of the acquired data were chosen from at least 4 experiments and are presented in this work.

4.2.3 High content screening imaging

High content screening images were obtained by automated acquisition using a Perkin-Elmer Opera LX spinning disk confocal with autofocus and a 60x water-immersion lens (NA 1.2). Ten fields of view were randomly chosen for each well and 15 to 20 z-steps were acquired at 1 μm intervals. Approximatively 900 images were obtained for each individual condition within one experiment. The image analysis was performed using a batch-processing plugin within the ImageJ/Fiji software (written by Dr Stephen Cross see Appendix A for more details) giving information about the mean intensity of pixels inside and outside a selected size range of 3, 5 and 10 pixels around the nuclei of the cells (Figure 4.1). The minimum measured range was set at 3 pixels distance to evaluate the intensity in areas close to the nuclei whereas the maximum range at 10 pixels was chosen to measure the intensity within a full individual cell. The outcome of this analysis was statistically processed using a MATLAB code (see appendix B) where the outliers were removed using le Chauvenet's criterion[26] and the means and standard deviations of the data were obtained. Finally, the statistical values obtained, for each time point, were plotted against time and a second-degree polynomial regression was used to adjust the data.

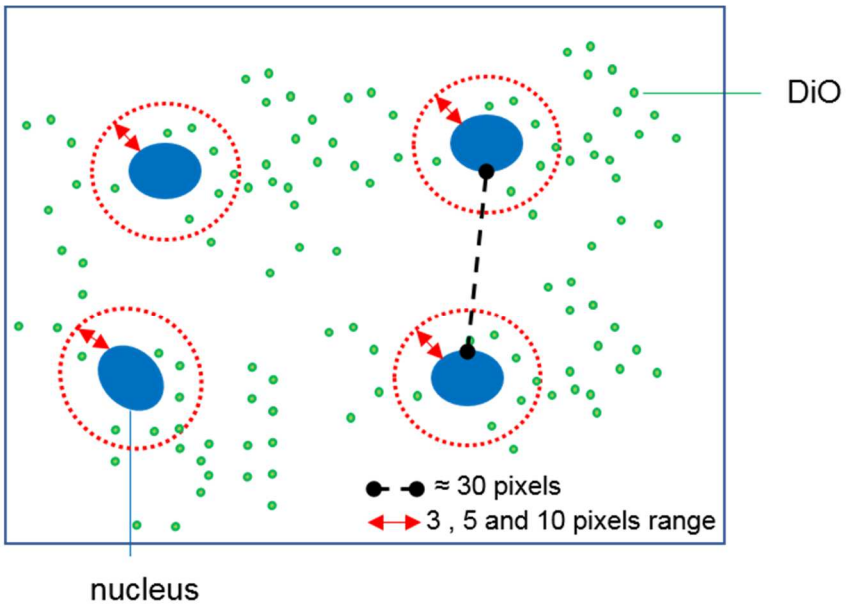

Figure 4.1 *Diagram of the area selected for image quantification of fluorescence in images obtained using high-content screening microscopy. The red dashed line illustrates the different measured areas around the nuclei3, 5, and 10 pixels (0.65μm, 1.08 μm, and 2.15 μm respectively). The black dashed line shows the average distance between nuclei (~30 pixels or 7 μm).*

4.2.4 Analysis of colocalisation of DiO with antibodies

The resulting images from the antibody staining experiments were analysed using CellProfiler[27] software. A pipeline was used to automate the analysis by applying the same processing steps (Figure 4.2) to all analysed images and finally obtain two numerical values associated with the amount of colocalisation between the antibodies and DiO. The obtained values correspond to the Mander's coefficients indicating the degree of overlap between two channels. All data are expressed as means of the measured coefficients. The significance of differences between means was assessed using a one-way ANOVA test and a Tukey post-test analysis with significance set at $P<0.001$.

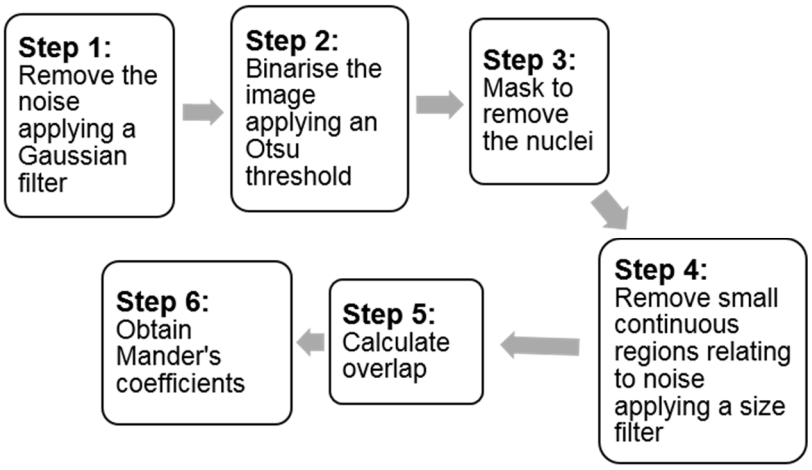

Figure 4.2 *Diagram of the cell profiler pipeline used to measure colocalisation.*

4.2.5 Imaging for FRET measurements

As a quenching effect was detected in RITC-P407-DiO micelles between the two fluorophores (results chapter 1 FRET section), FRET was used to evaluate the possible release of the DiO cargo from RITC-P407 micelles into fixed cells. This was done by measuring the energy transfer between the encapsulated fluorophore and the fluorophore conjugated to the polymer at different exposure times. FRET measurements were obtained using a Leica SP5-II AOBS confocal laser scanning microscope attached to a Leica DM I6000 inverted microscope. The capture of images was supported by the Leica Application Suite Advanced Fluorescence (LAS AF) software. Within the LAS AF, the FRET acceptor photo-bleaching wizard was used to measure the fluorescence intensity of the FRET donor (DiO) before and after bleaching the acceptor (RITC-P407). This difference of fluorescence intensity is directly related to the amount of FRET and therefore the FRET efficiency was quantified by the LAS AF using the following equation[28]:

$$FRET_{efficiency} = \frac{(D_{post} - D_{pre})}{D_{post}}$$

Equation 4.1 *FRET efficiency, where D_{post} corresponds to the fluorescence intensity of the donor after photo-bleaching and D_{pre} to the fluorescence intensity of the donor before photo-bleaching*

The settings used to acquire the images were as described in section 4.2.2.1. A region of interest (ROI) was defined by a squared region of 30 x 30 µm in the acceptor image including the cell cytoplasm and the nucleus. This ROI was bleached over 10 frames with the 561 nm laser with intensity increased using AOTF settings. After bleaching, a look-up table (LUT) was generated to display the fluorescence intensities.

For each timepoint, ten different fields of view were randomly selected on the cell monolayer. One ROI was defined within each field for bleaching. The amount of FRET efficiency (presented as an LUT) was recorded for each ROI defining three sub-ROI of 5x5 µm in the cytoplasm and one in the nucleus -where FRET was not expected to be detected. A mean value of all the FRET efficiencies detected within each sub-ROI was obtain using the LAS AF software. The mean values were then averaged and presented with their associated standard deviations.

Within a single experiment, each experimental condition was performed in duplicate and three independent experiments were performed.

4.3 Uptake of P407-DiO micelles over time

4.3.1 Uptake of P407-DiO micelles by MDCK cells

MDCK cells were exposed to P407-DiO micelles for 1, 4, 8, and 24 hours and compared to the control (cells grown in medium without micelles) (Figure 4.3). After exposing the cells to micelles for 1 hour, a green fluorescent signal is observed over all the cell monolayer excluding the nuclei (Figure 4.3). This green fluorescence appears to be distributed in the cytoplasm with some accumulation around the nucleus and is not present in the control indicating that the green fluorescence is due to the internalisation of the DiO dye and not to inherent fluorescence of the cells. After 4 hours of continuous exposure, some brighter punctate labelling is evident within cells in addition to the more uniform labelling seen at 1h (Fig 1.3) suggesting that some internalised DiO is accumulating in specific locations of the cell. Similar accumulation sites are also observed after 8 hours of exposure with a more uniform distribution in the cytoplasm (Figure 4.3). At a longer exposure time, such as 24h, the green fluorescence intensity in the entire monolayer seems to have increased as well as the number of accumulation sites compared to previous time points.

Over all measured timepoints, the green fluorescence associated with DiO can be detected throughout the cells indicating the effective continuous internalisation of DiO over time. Additionally, the confinement of the fluorophore into localised sites in the cytoplasm suggests that the fluorophore could be accumulating into the sub cellular compartment of the cells. Furthermore, cell morphology remains unaffected by the presence of

micelles after 24 hours of continuous exposure to micelles suggesting the polymer is relatively non-toxic.

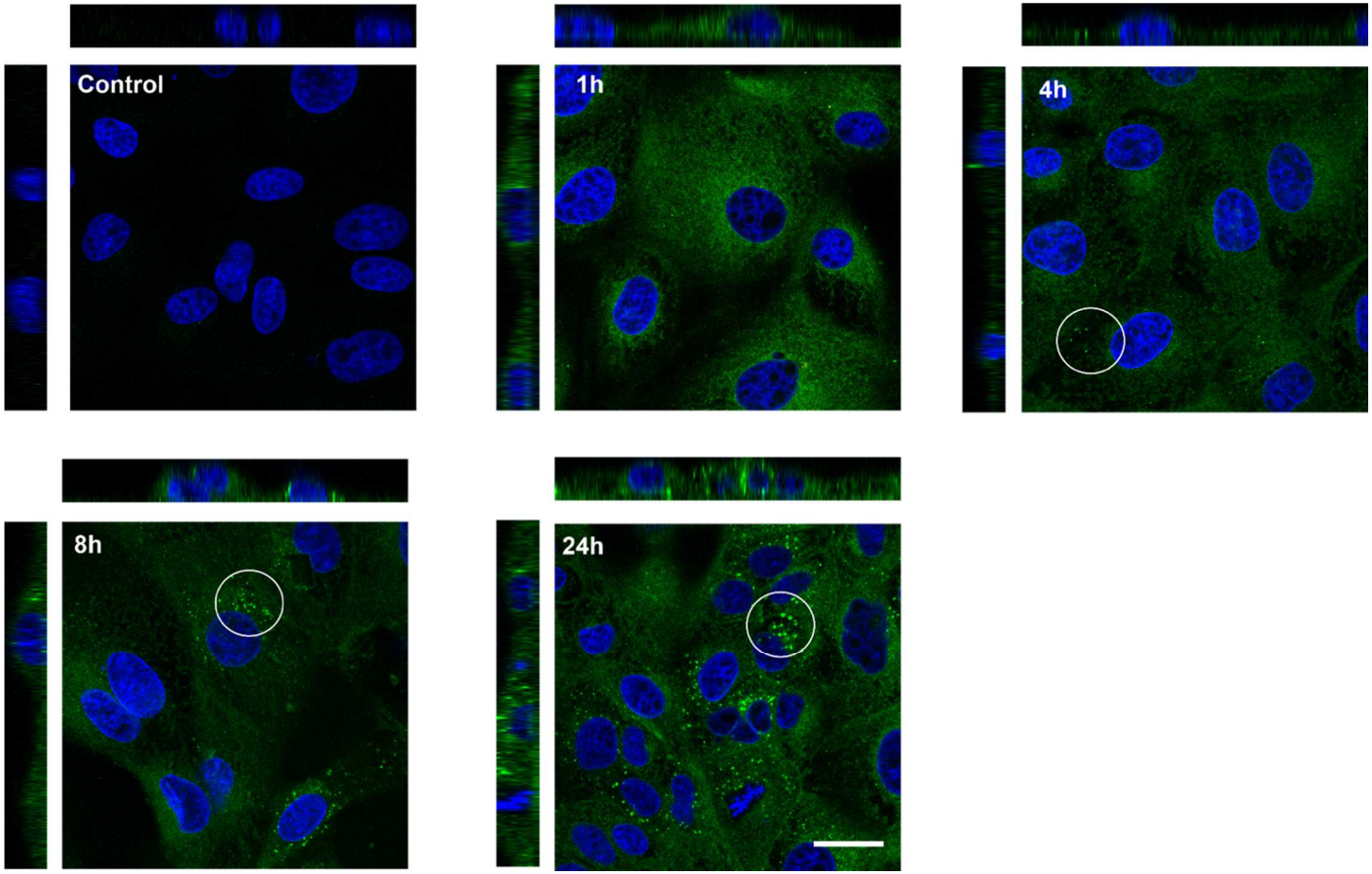

Figure 4.3 *Uptake of P407-DiO micelles (green) in MDCK cells over time. Confocal images were taken on fixed cells previously grown in medium (control) and exposed to P407-DiO micelles for 1, 4, 8 and 24 hours. The circled areas show the accumulation of DiO in specific cellular compartments. Nuclei labelled with DAPI (blue). The images shown are representative of those obtained in four separate experiments. Scale bar 25 μm.*

4.3.2 Uptake of P407-DiO micelles by BeWo b30 cells

BeWo b30 cells were exposed continuously to P407-DiO micelles over the same time range as previously used for MDCK cell exposure (Section 4.3.1). After 1-hour exposure, a green fluorescent signal is observed over all the cell monolayer excluding the cells' nuclei. The fluorescence intensity appears to be higher than in the control suggesting that the DiO dye is responsible for the observed green fluorescence. Similarly to the results found for MDCK cells, the dye seems to accumulate in certain areas of the cell forming bright punctuate structures. The number of dye-accumulation sites appear to increase with time as well as the overall fluorescence of the cells. In addition, the cell monolayer does not show any disruption after being exposed to micelles for 24 hours supporting the results found previously with MDCK cells.

MDCK and BeWo cells show comparable compartments when exposed to P407-DiO micelles. However, MDCK cells show more fluorescence than BeWo cells at early time points despite being exposed to identical experimental conditions. This suggests that the internalisation rates may be different for each cell line. Although the visual evaluation shows evidence of the dye being internalised in the cells over time, quantification of the green fluorescence is needed to validate the results.

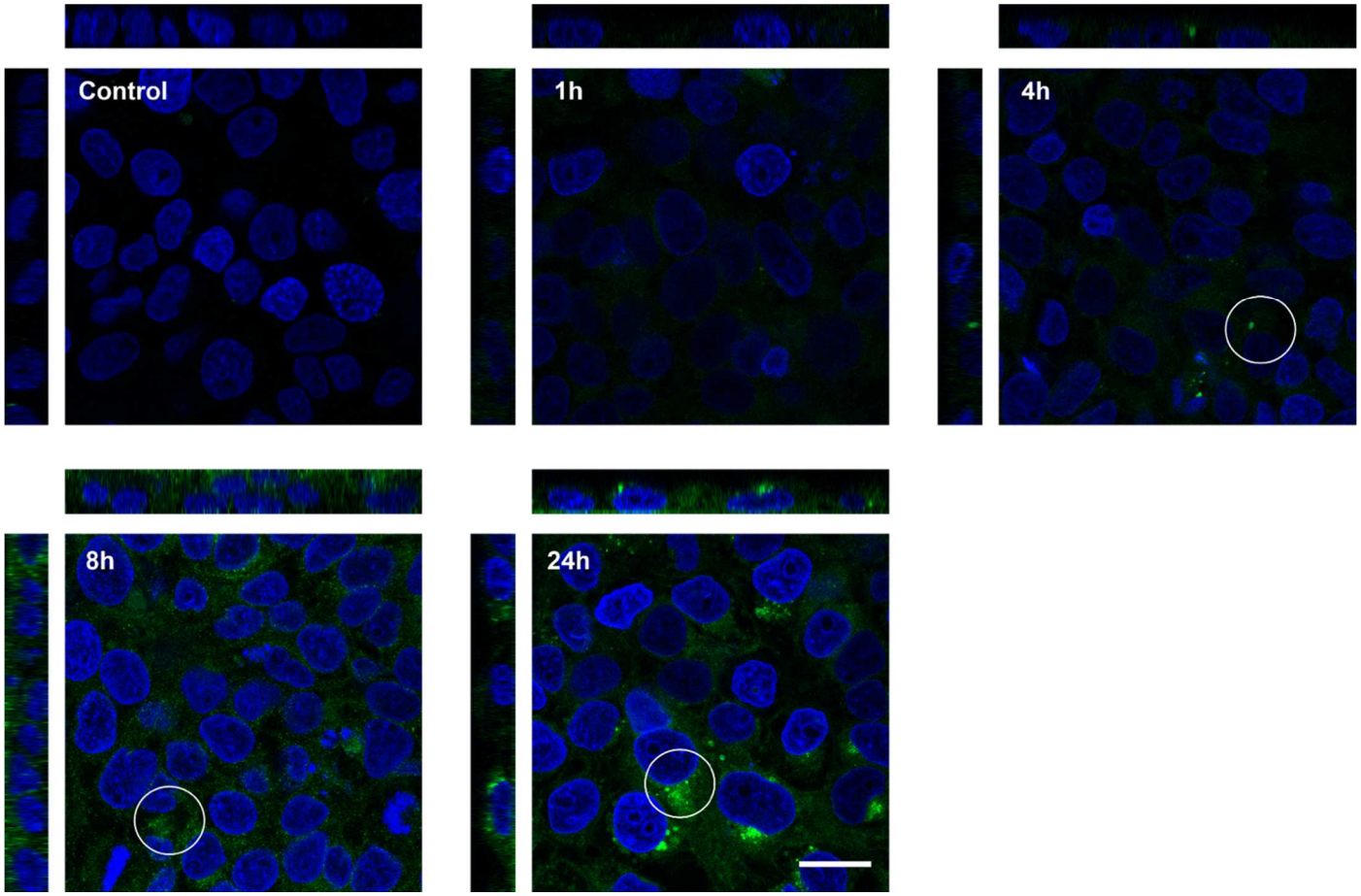

Figure 4.4 *Uptake of P407-DiO micelles (green) in BeWo b30 cells over time. Confocal images were taken on fixed cells previously grown in medium (control) and exposed to P407-DiO micelles for 1, 4, 8 and 24 hours. The areas signalled by a circle show the accumulation of DiO in specific cell compartments. Nuclei labelled with DAPI (blue). The images shown are representatives of those obtained in four separate experiments. Scale bar 25 μm.*

4.4 Quantification of fluorescence in cells over time

4.4.1 Quantification of DiO fluorescence in micelles-exposed MDCK cells

The quantification of the green fluorescence due to DiO internalisation was made using high-content screening imaging. This was used to corroborate the observations previously made (section 4.3.1) on the uptake of DiO dye into MDCK cells monolayers. The mean pixel intensity was measured in three different concentric rings around the nuclei (Figure 4.1) at different particle exposure times.

The mean fluorescence intensity detected in the first detection ring, set 3 pixels (0.65μm) apart from the edge of each nucleus, was measured and plotted against time of exposure. The mean intensity outside this range was also plotted against time to compare the amount of fluorescence measured in both areas of the cells (Figure 4.5.A). Although both curves present the same growth pattern, the curve corresponding to the mean intensity detected inside the range is lower than the one detected outside for all time points. The curves for 5 (1.08 μm) and 10 pixels (2.15 μm) range (Figure 4.5 B and C respectively), show the same growth type as seen for 3 pixels. This difference between the signal detected inside and outside the selected range is consistent with the nature of the experiment as the measured range represents only a fraction of the total fluorescence intensity measured in the monolayer. Furthermore, the increase of the fluorescence with time shows that the dye internalisation happens slowly at early time points but increases rapidly for later timepoints without reaching equilibrium or saturation over

25 hours after exposure. The growth pattern also shows that the dye accumulates into the cells over time without much recycling which would result in a constant gradient.

To compare the effects of changing the width of the measured range on the values of mean fluorescent intensities, the mean values found at 3, 5 and, 10 pixels were plotted together for measurements inside and outside the range (Figure 4.6 A and B). The curves seem to superimpose showing no difference for all measured areas. These results imply that the detected mean fluorescence intensity seems to be distributed across the cells even though the images show dye accumulation in specific cell compartments (Figure 4.3).

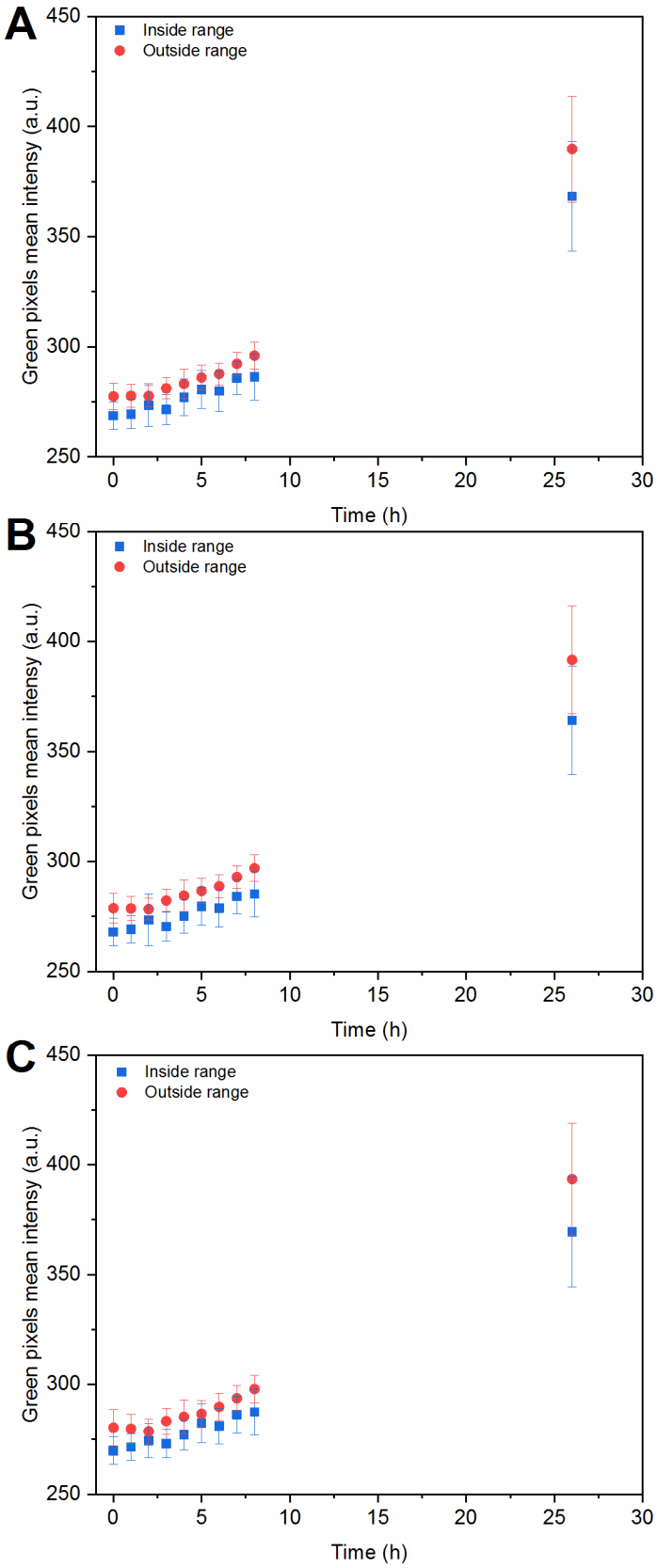

Figure 4.5 *Mean green fluorescence intensity measured in MDCK cells over time. Cells were exposed to P407-DiO micelles and the intensity was measured inside and outside selected ranges.* ***(A)*** *3 pixels,* ***(B)*** *5 pixels, and* ***(C)****10 pixels range. All the values are presented as means ± SD (n=60).*

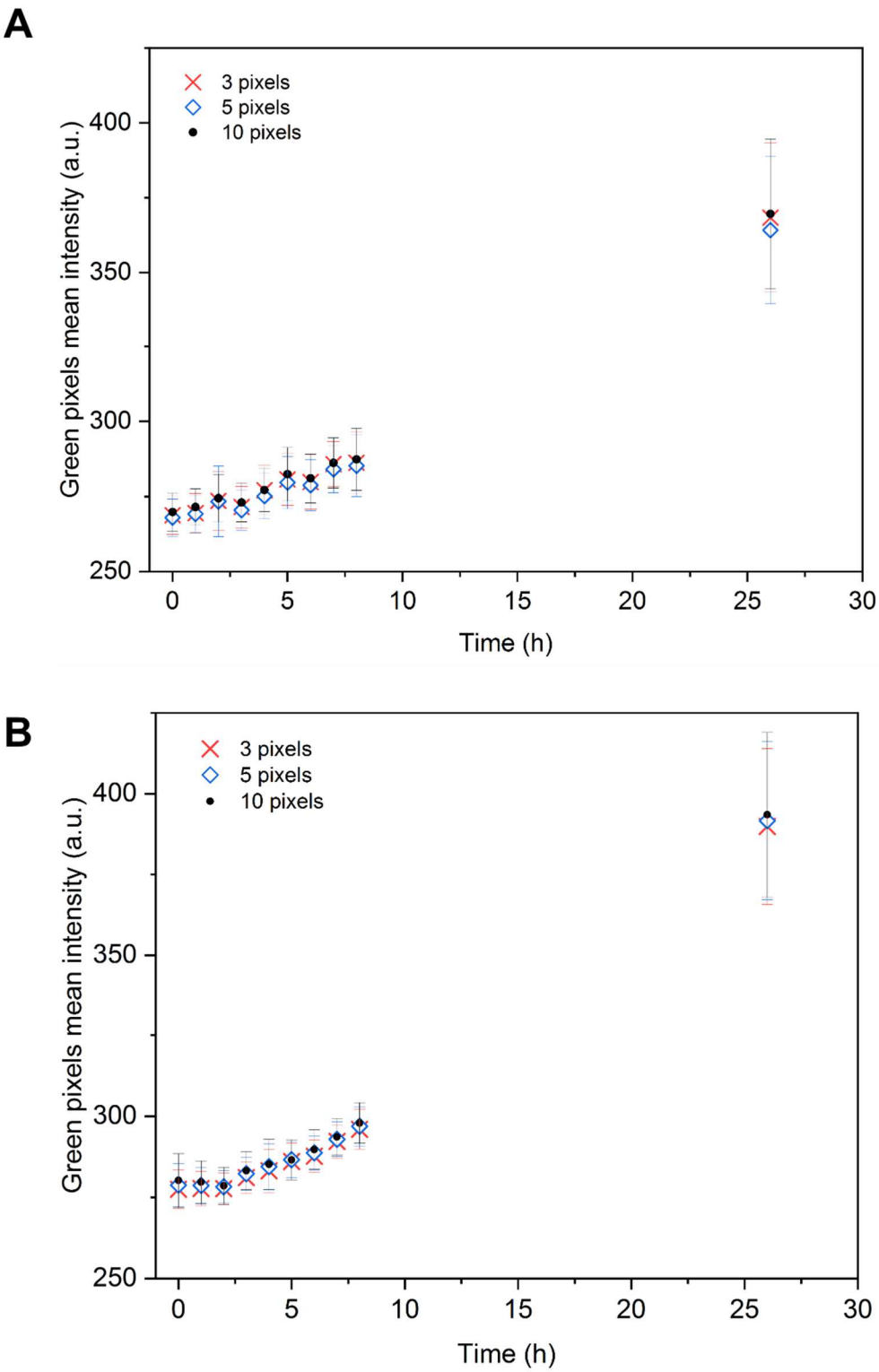

Figure 4.6 *Comparison of the mean green fluorescence intensities measured in MDCK cells at different measurement ranges* ***(A)*** *inside and* ***(B)*** *outside the selected range. All the values are presented as means ± SD (n=60) (see also Figure 4.5)*

4.4.2 Quantification of fluorescence in micelles-exposed BeWo b30 cells

High-content screening imaging was used to validate the observations made previously on the uptake of DiO dye into BeWo cells monolayers (section 4.3.2). To detect the accumulation in specific areas of the cytoplasm of BeWo b30 cells, the mean pixel intensity was measured in three different concentric rings around the nuclei (Figure 4.1) at different particle exposure times.

The first measured area was set at 3 pixels (0.65μm) distance from the nuclear membrane. The green fluorescence intensity of DiO within this range was quantified and plotted against time of exposure of micelles to the cells. Equally, the mean green intensity detected outside these areas was plotted against time (Figure 4.7.A). At all-time points, the green fluorescence intensity seems to be higher inside the measured range than outside. This suggests that the DiO could be accumulating more in areas close to the cell nucleus. Both curves present almost a linear growth at first with a slower growth at later timepoints such as 22 hours. This could be due to the dye reaching saturation in the cell being recycled or degraded after 22 hours.

When measuring the green fluorescence intensity within distances of 5 and 10 pixels (1.08 μm and 2.15 μm) from the nuclear edge (Figure 4.7 B and C respectively), the observed patterns are consistent with the ones observed at 3 pixels distance. The difference between inside and outside the range is still visible and both curves follow different types of growths similarly to the one seen previously at 3 pixels.

The mean values found at 3, 5 and, 10 pixels were plotted together to understand the effects of changing the radius of the measured rings outside and inside the range (Figure 4.8 A and B respectively). The curves superimpose showing no difference between the different measurements. This shows an even distribution of the dye in the cytoplasm despite the accumulation sites seen in the confocal images (Figure 4.4).

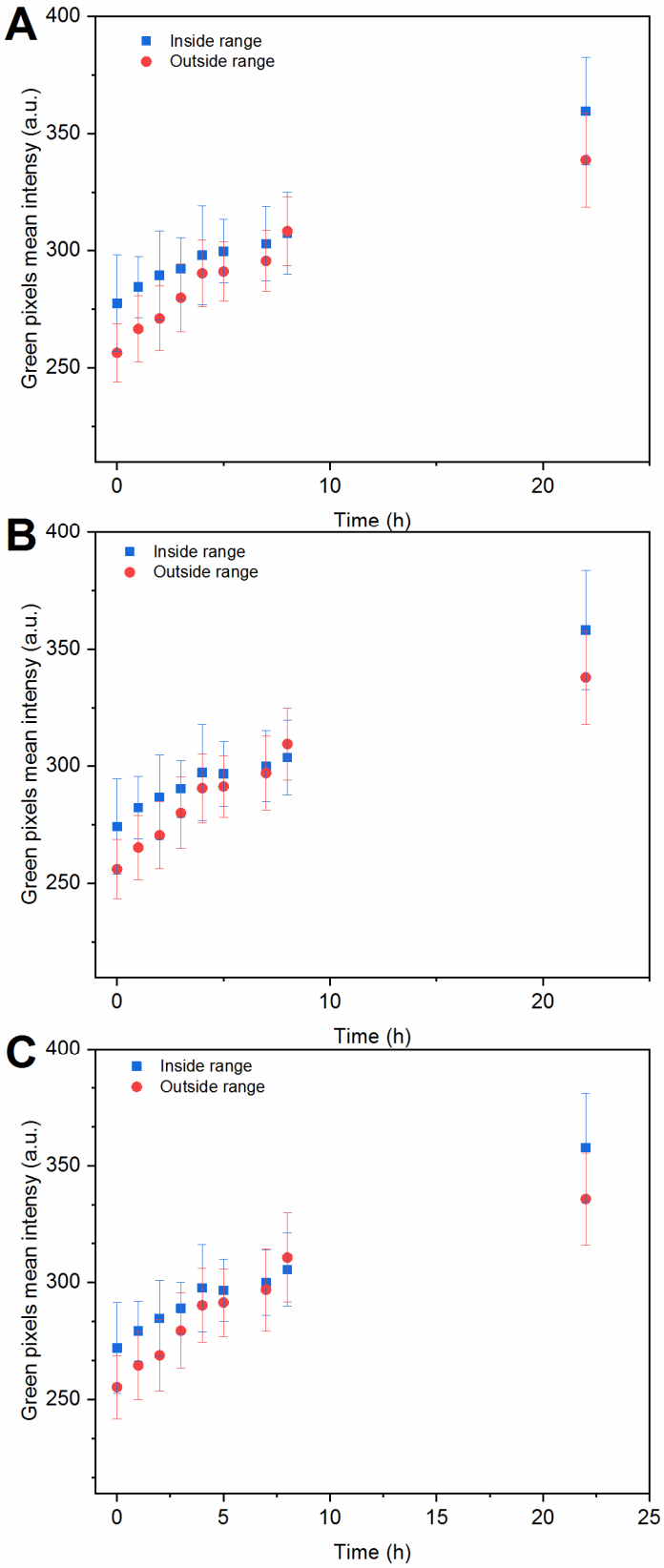

Figure 4.7 *Mean green fluorescence intensity measured in BeWo b30 cells over time. Cells were exposed to P407-DiO micelles and the intensity was measured inside and outside selected ranges.* ***(A)*** *3 pixels,* ***(B)*** *5 pixels, and* ***(C)****10 pixels range. All the values are presented as means ± SD (n=60).*

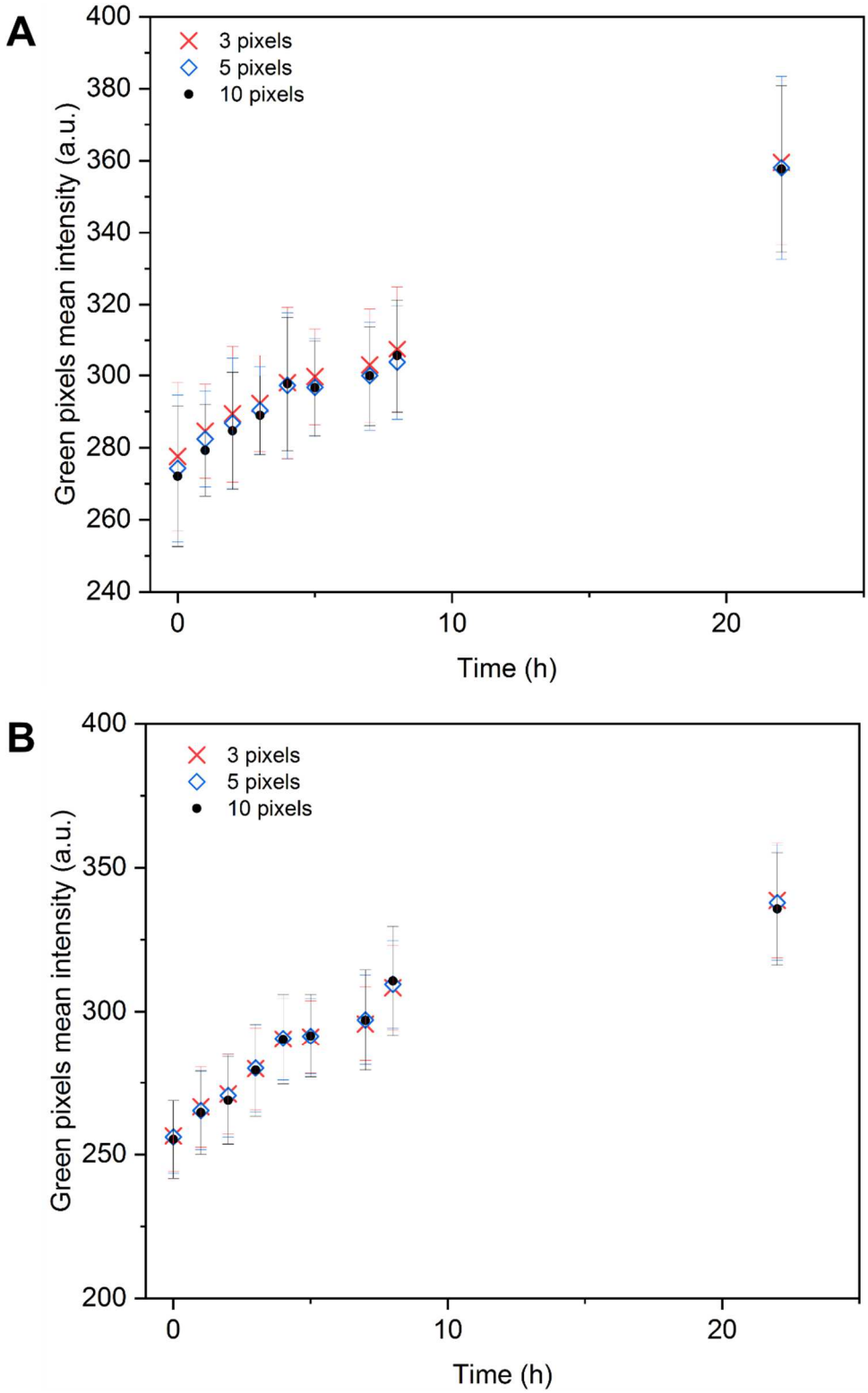

Figure 4.8 *Comparison of the mean green fluorescence intensities measured on BeWo b30 cells at different measurement ranges* ***(A)*** *inside and* ***(B)*** *outside the selected range. All the values are presented as means ± SD (n=60) (see also Figure 4.7)*

4.5 Effect of MiTMAB inhibitor on micelles uptake

Previous work has shown triblock copolymer micelles and unimers to enter mammalian cells through receptor-mediated endocytosis (RME)[20]. The internalisation pathway of P407-DiO micelles in BeWo b30 and MDCK cells was evaluated combining high-content screening microscopy technique alongside a chemical endocytic inhibitor, namely myristyl trimethyl ammonium bromide (MiTMAB). This molecule competitively prevents the dynamin protein from binding to phospholipids and thus, inhibits RME[29,30].

4.5.1 DiO fluorescence quantification in MDCK cells with MiTMAB

The green fluorescence observed in MDCK cells after exposure to P407-DiO micelles for 1 hour was quantified and compared to the fluorescence detected in presence of MiTMAB (Figure 4.9). The mean fluorescence intensity of DiO was significantly reduced by 30% ($P<0.001$) in the presence of MiTMAB (DiO/MM). Additionally, cells exposed to transferrin and MiTMAB were used as a control for the inhibitor efficacy. The mean fluorescence of cells exposed to transferrin (ALEXA FLUOR™ 488) also showed a significant decrease in the presence of MiTMAB but in this case inhibition was 98% ($P<0.001$) (Figure 4.9).

The decreased DiO fluorescence with MiTMAB suggests involvement of RME in P407-DiO internalisation in MDCK cells. However, the incomplete

inhibition of P407-DiO uptake contrasted with that of transferrin and suggests that additional pathway(s) contribute to micelle internalisation.

Since the use of MiTMAB has shown to inhibit cytokinesis in some cells[30], the cell viability count was performed in samples exposed to MiTMAB and DiO and DiO only (Figure 4.10). No significant difference in the number of nuclei with or without the use of MiTMAB inhibitor was detected. This shows that at the concentrations and exposure times used in this experiment, MiTMAB inhibitor did not present a toxic effect on MDCK cells.

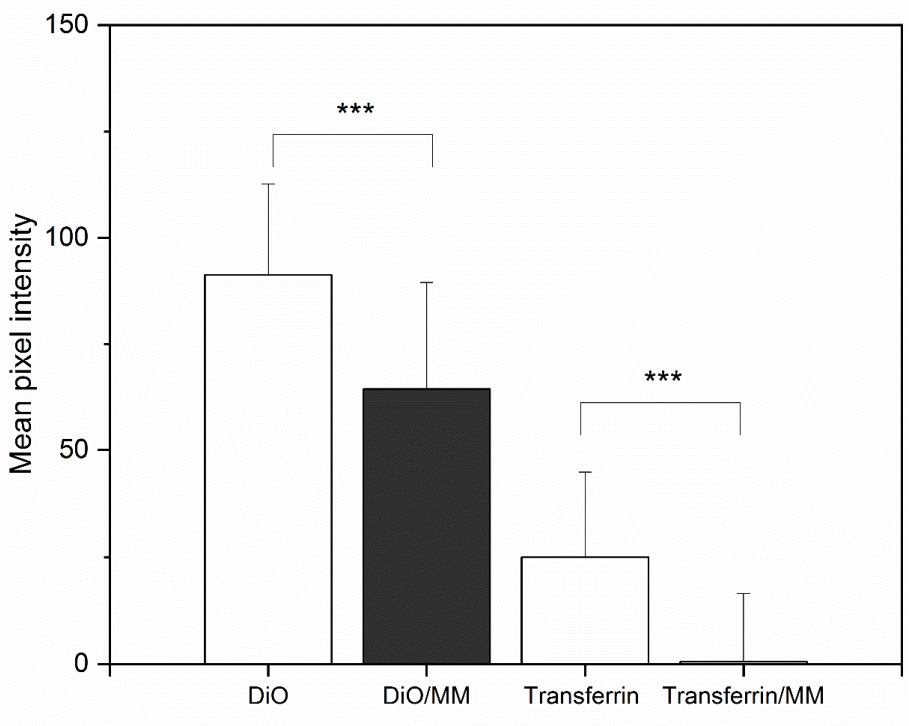

Figure 4.9 *Effect of MiTMAB inhibitor on the uptake of P407-DiO and transferrin (ALEXA FLUOR™ 488) in MDCK cells. Cells were exposed to P407-DiO micelles or transferrin (ALEXA FLUOR™ 488) with and without MiTMAB (MM) for 1 hour. All the values are presented as means ± SD (n=40) and the significance difference between means was evaluated using a one-way ANOVA followed by a post hoc comparison (Tukey test): *** P<0.001.*

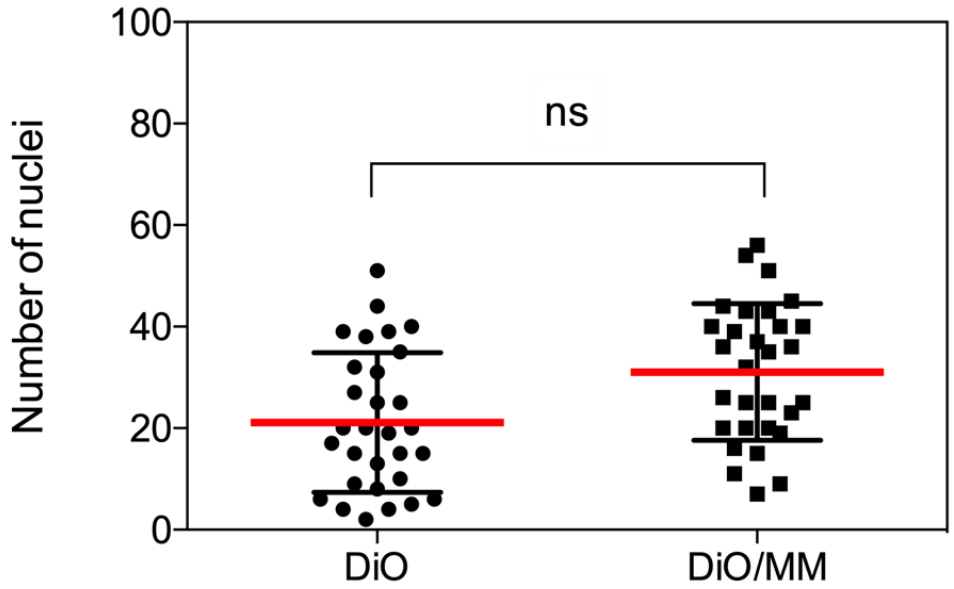

Figure 4.10 *Effect of MiTMAB inhibitor on the number of MDCK cells detected per field of view. The red and black bars represent mean ± SD (n=30) and the significance difference between means was evaluated using an unpaired t-test with significance set at P<0.05.*

4.5.2 DiO fluorescence quantification in BeWo b30 cells with MiTMAB

The effect of the dynamin inhibitor MiTMAB on P407-DiO uptake by BeWo b30 cells was measured to evaluate the potential role of RME in uptake (Figure 4.11). Addition of MiTMAB alongside P407-DiO micelles (DiO/MM) results in a decrease of the mean green fluorescence intensity detected in the monolayer by 22% (P<0.001) with respect to the control (cells exposed to P407-DiO micelles). The control used to test the inhibitor efficacy was transferrin. In the presence of MiTMAB, the mean fluorescence intensity decreases significantly by 77% (P<0.001) (Figure 4.11).

Comparably to MDCK cells, the fluorescence observed in cells exposed to micelles in presence of inhibitors indicates that one possible internalisation

pathway of P407-DiO micelles is through RME. Additionally, as seen in MDCK cells, the DiO uptake is not completely inhibited suggesting that RME is not the only internalisation pathway followed by P407-DiO micelles.

A cell viability count was performed in cells exposed to DiO in presence and absence of MiTMAB (Figure 4.12. No significant difference in the number of nuclei detected was seen in both cases. This indicates that the use of MiTMAB at the concentration and exposure time used in this experiment did not lead to cell toxicity in BeWo b30 cells.

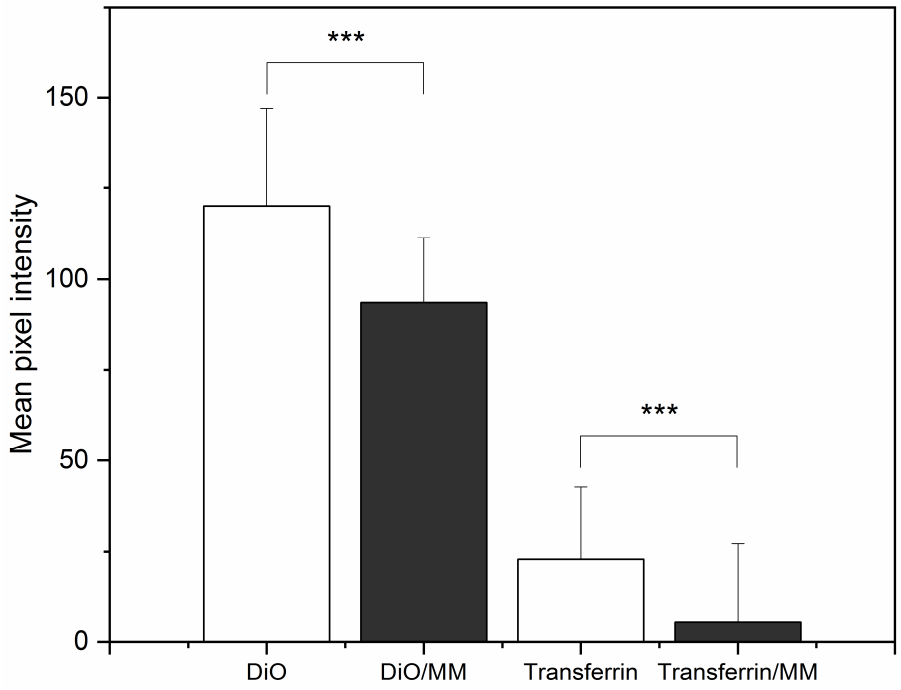

Figure 4.11 *Effect of MiTMAB inhibitor on the uptake of P407-DiO and transferrin (ALEXA FLUOR™ 488) in BeWo b30 cells. Cells were exposed to P407-DiO micelles or transferrin (ALEXA FLUOR™ 488) with and without MiTMAB for 1 hour. All the values are presented as means ± SD (n=60) and the significance difference between means was evaluated using a one-way ANOVA followed by a post hoc comparison (Tukey test): *** P<0.001.*

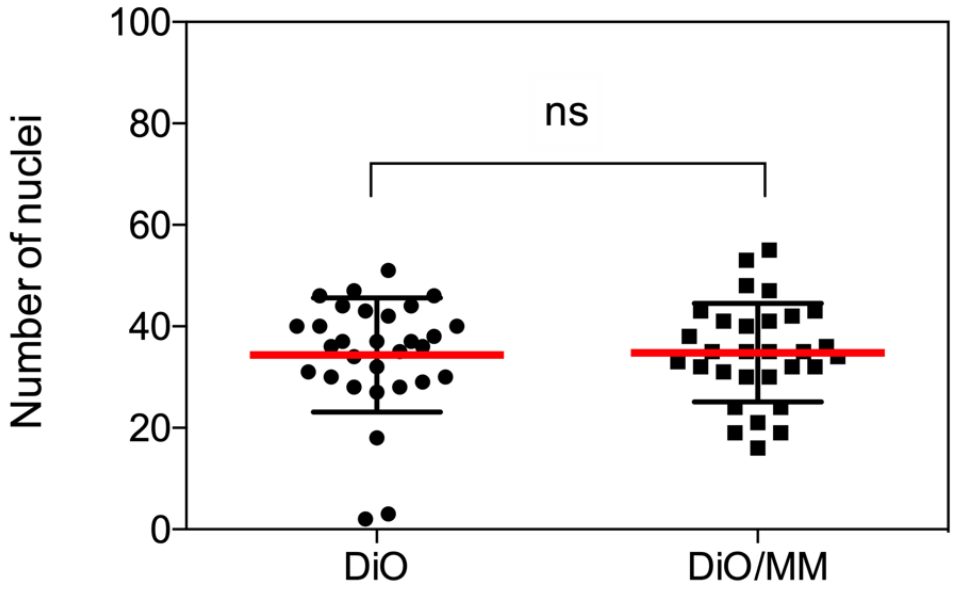

Figure 4.12 *Effect of MiTMAB inhibitor on the number of BeWo b30 cells detected per field of view. The red and black bars represent mean ± SD (n=30) and the significance difference between means was evaluated using an unpaired t-test with significance set at P<0.05.*

4.6 Localisation of endocytic sub-cellular compartments using immunofluorescence

To corroborate the results seen with inhibitors, immuno-fluorescence was used to examine the cellular colocalisation of the DiO dye with key compartments accessible through RME. For this, BeWo b30 and MDCK cells were exposed to P407-DiO micelles for 4 hours then fixed and stained with antibodies against early endosomes and lysosomes. Because of its hydrophobic properties, it was also hypothesised that DiO might accumulate in lipid-rich cellular compartments. Hence, an additional antibody marker for lipid-droplets (LD) was used.

4.6.1 Optimisation of the surfactant for antibody staining

One important step for immunolabelling is the permeabilisation of the plasma membrane prior to the addition of primary antibodies in order for the antibodies to access intracellular compartments. To proceed with immunofluorescent localisation of compartments containing DiO it was first necessary to establish conditions that allowed membrane permeabilisation to antibodies while retaining DiO fluorescence within intracellular compartments.

Triton X-100 is the most commonly used membrane-permeabilising agent in immunofluorescence. This non-ionic surfactant permeabilises the cellular membrane by inserting a hydrophobic monomer into the lipid membrane creating pores[31]. However, this surfactant is non-selective and

therefore it may extract proteins alongside lipids. The effect of Triton X-100 (0.1%) on MDCK cells previously exposed to P407-DiO micelles was followed with live-imaging during a 10 minutes period (Figure 4.13). Visually, the DiO fluorescence decreased with time so that by the end of the exposure almost all the fluorescence had disappeared, suggesting the surfactant had formed pores sufficiently large for DiO to escape the cells.

Saponin has been found to be specific for cholesterol rich sites in the cellular membrane forming 10 nm size pores[32]. 0.1% of saponin surfactant was added to MDCK cells under the same experimental conditions as the addition of Triton x-100 (Figure 4.14). The fluorescence of DiO was maintained after 10 minutes of permeabilising the cells with saponin. This shows that the loss of fluorescence is due to membrane permeabilisation and not to photobleaching as well as demonstrating the suitability of saponin as a membrane-permeabiliser agent for the purposes of this work.

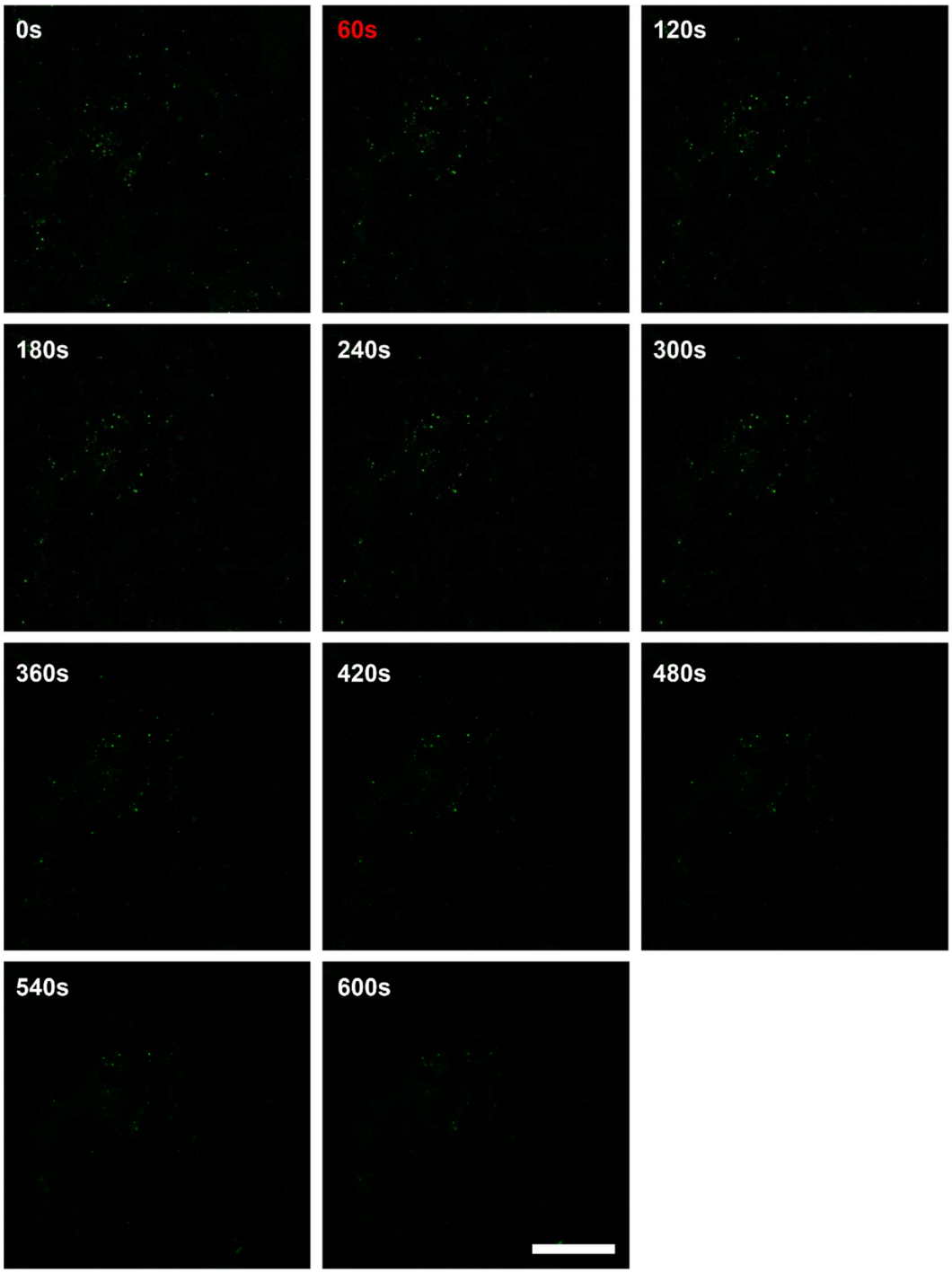

Figure 4.13 *Confocal imaging of the addition of 0.1% Triton X-100 to fixed MDCK cells previously exposed to P407-DiO micelles (green). The red highlighted time (60s) marks the time of addition of the surfactant. Scale bar 25 μm.*

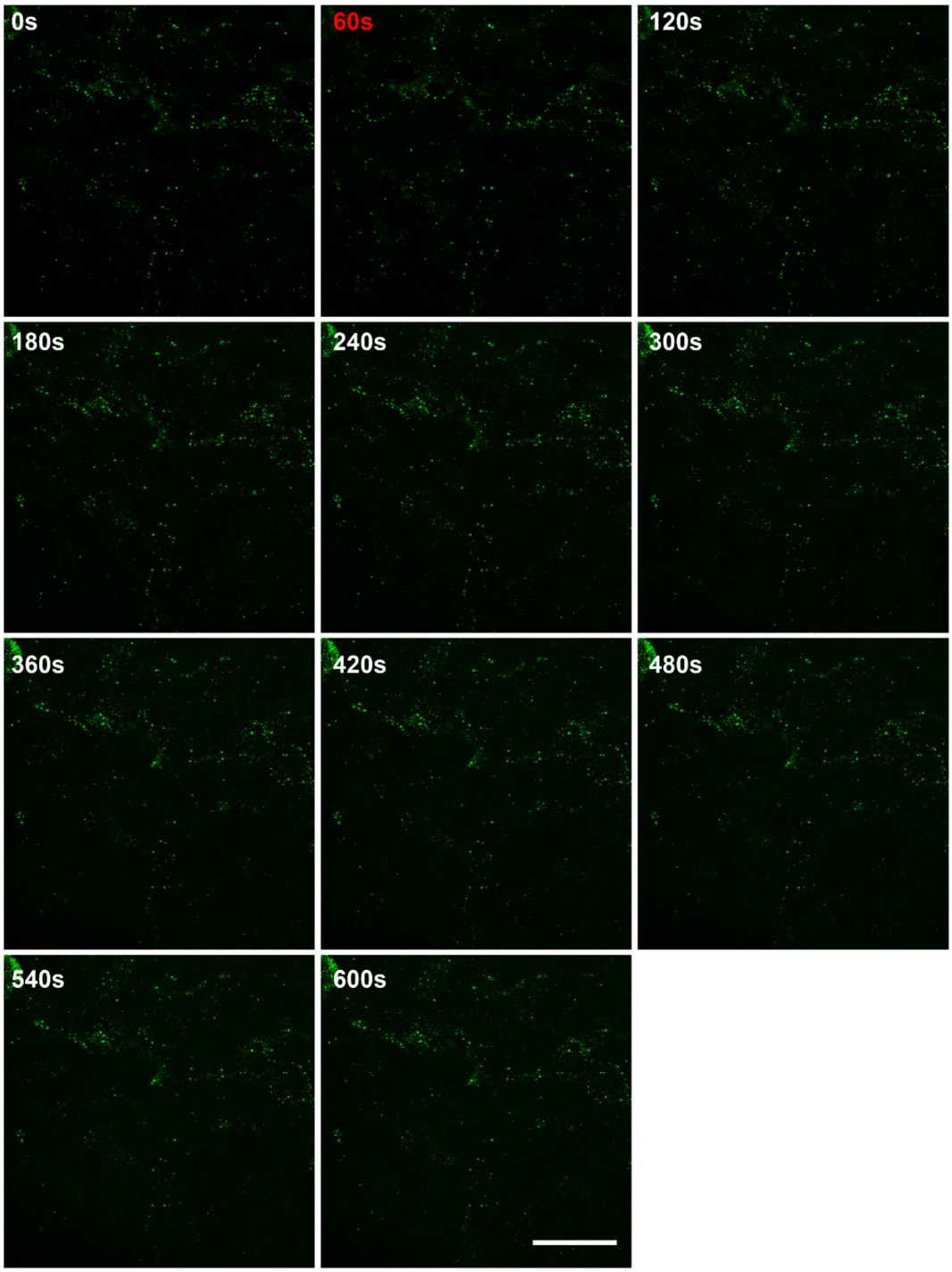

Figure 4.14 *Confocal -imaging of the addition of 0.1% Saponin to fixed MDCK cells previously exposed to P407-DiO micelles (green). The red highlighted time (60s) marks the time of addition of the surfactant. Scale bar 25 μm.*

4.6.2 Colocalisation of sub-cellular compartments with DiO in MDCK cells

As seen in previous sections, DiO fluorescence increased with time and accumulated in bright punctate structures following exposure of MDCK cells to P407-DiO (sections 4.3.1 and 4.4.1). Additionally, the use of a dynamin inhibitor reduced the uptake of DiO into cells suggesting that the DiO micelles might be internalised by the cells through RME. To validate the uptake of micelles through such endocytic pathway, immunolabelling was used to identify key cellular compartments such as early endosomes and lysosomes. Moreover, the accumulation of the dye in highly hydrophobic sites was suspected and thus, immunostaining of LD was carried out. The immunolabeling was undertaken on cells exposed to P407 DiO micelles for 4 hours (Figure 4.15). The immunolabelling of early endosomes with EEA1 primary antibody and ALEXA 594-labelled secondary antibodies shows a red punctate pattern superficially similar to that seen with DiO. However, the merged image shows little colocalisation between DiO and early endosomes (Figure 4.15). Late endosomes and lysosomes were stained with CD63 primary antibody. However, low amounts of red fluorescence were seen compared to that seen previously for early endosomes. This was only seen after doubling the intensity of the laser suggesting that the antibody labelling was unsuccessful. Yet, the merged image showed a small amount of colocalisation of DiO with the lysosomal marker which could be due to the background noise caused by the high laser power. The LD compartments labelled with ApoB primary

antibody, show red punctate structures but no colocalisation with DiO was seen in the merged channel.

The amounts of colocalisation between DiO and antibodies was determined calculating the Mander's coefficients (M1 and M2) (Figure 4.16). The value of M1 for EEA1 antibody indicates that only 20% of the red pixels corresponding to the antibodies colocalise with the green pixels detected for DiO. M2 shows that approximatively 5% of the pixels detected for DiO colocalise with the red pixels of EEA1. The low values of M1 and M2 indicate a very low amount of colocalisation of the DiO with the early endosomal marker. The value of M1 for CD63, shows that approximatively 60% of the red pixels corresponding to the lysosomal marker overlap with the DiO green pixels. However, the statistical difference analysis of this value shows no significance between this value and the one found for EEA1. This high value of overlap observed is therefore caused by the noise detected in the CD63 image (Figure 4.15 A) overlapping with DiO signal rather than the antibody colocalising with DiO. The values of M1 and M2 display no colocalisation between the LD marker and DiO with no significant difference between these results and the ones found for EEA1.

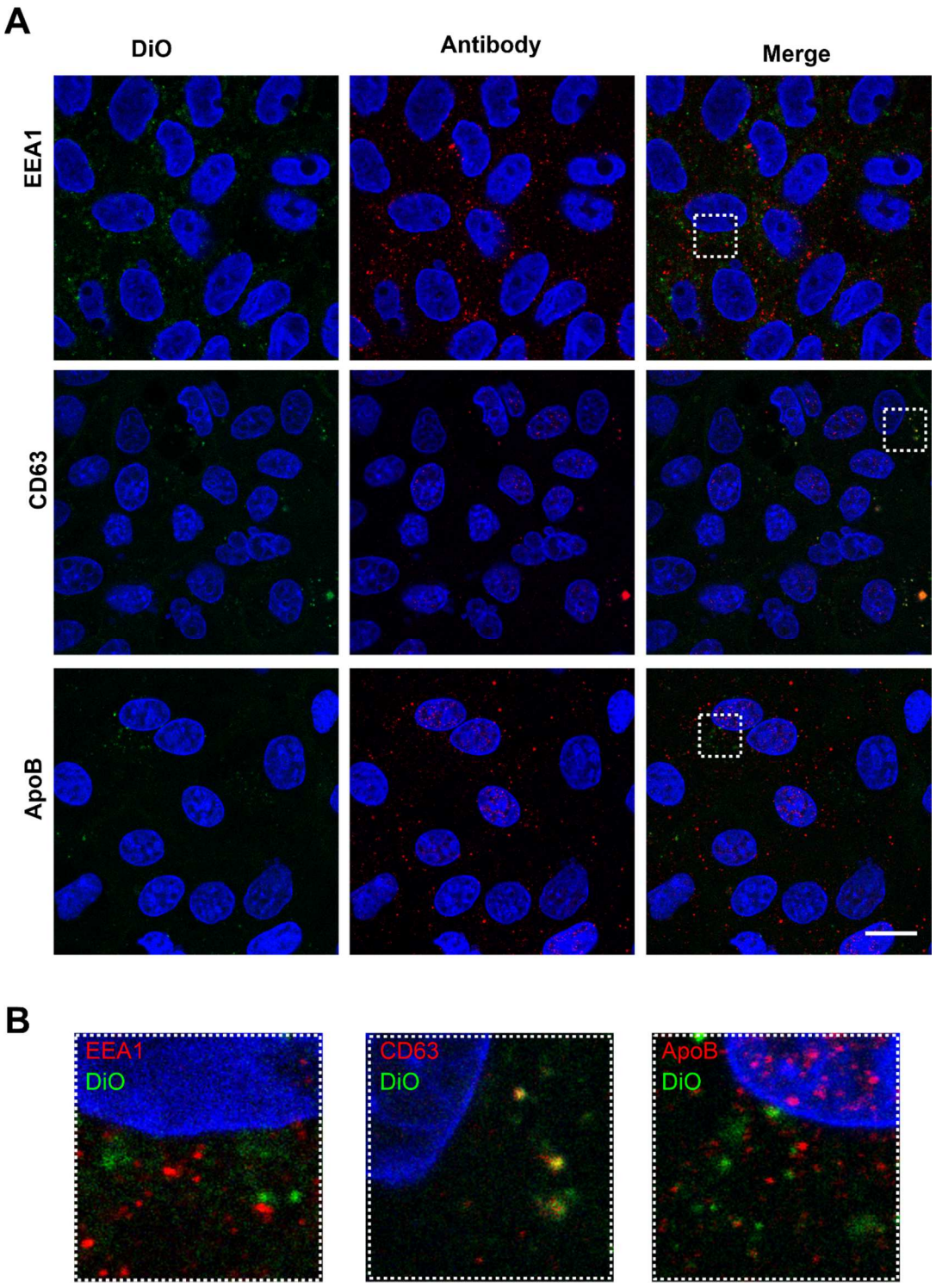

Figure 4.15 *Colocalisation of EEA1, CD63 and, ApoB with DiO in MDCK cells.(A) cells were exposed to P407-DiO micelles for 4h (green) and labelled with antibodies after fixation (red). Nuclei are labelled in blue with DAPI. Scale bar: 15μm (B) Magnifications of selected regions indicated by white dashed boxes. The colocalisation is shown in yellow. The images shown are representative of those obtained in three separate experiments.*

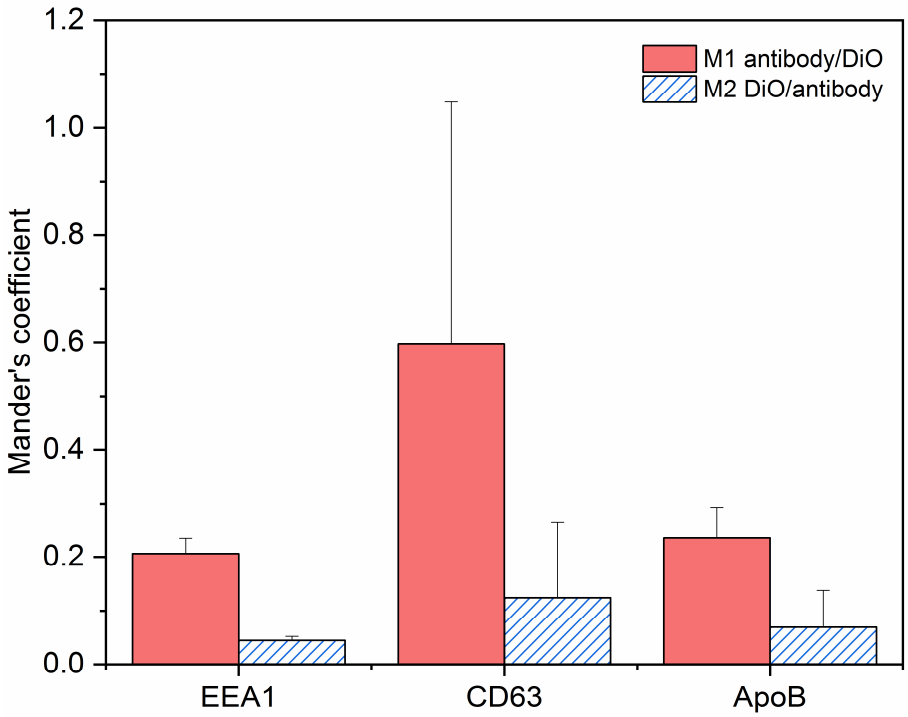

Figure 4.16 *Quantification of the colocalisation of EEA1, CD63 and ApoB with DiO in MDCK cells using Mander's coefficients (M1 and M2). M1 represents the fraction of antibody staining in colocalisation with DiO whereas M2 shows the fraction of DiO in colocalisation with the antibody staining. All the values are means ± SD (n=3) and the significance difference between means was evaluated using a one-way ANOVA followed by a post hoc comparison (Tukey test) with significance set at P<0.001.*

4.6.3 Colocalisation of sub-cellular compartments with DiO in BeWo b30 cells

To gain insight into the mechanism by which the DiO dye is being internalised into BeWo cells, the subcellular localisation of early endosomes, lysosomes and LD was investigated using immunolabelling. The immunostaining was undertaken on cells exposed for 4 hours to P407-DiO micelles (Figure 4.17). The DiO and EEA1 primary antibody show green and red punctate patterns respectively. The merged image shows negligible colocalisation between DiO and the early endosomal marker. The CD63 primary antibody used to label late endosomes and lysosomes also presents a red fluorescent punctate distribution. Although fewer DiO puncta are observed compared to CD63 labelling, the merged image shows substantial colocalisation of DiO and the lysosomal marker. The LD marked with the ApoB primary antibody showed fluorescent red punctate patterns which do not overlap with DiO green puncta in the merged image.

The amount of overlap between DiO in cells after 4h exposure to P407-DiO micelles and each antibody staining was expressed using Mander's coefficients (Figure 4.18.A). For EEA1, the value of M1 indicate that only 20% of the signal detected from the antibody was colocalised with the DiO signal. The value of M2 shows that a negligible amount of DiO signal colocalises with the early endosomal antibody. The low values of M1 and M2 indicate a very low amount of colocalisation of the DiO with the early endosomal marker. For CD63, the value of M1 shows that approximately 50% of the red pixels detected for the lysosomal marker overlaps with the

green pixels associated to DiO. The value of M2 for CD63 shows 80% of the DiO pixels colocalising with the antibody. Both coefficient values seem to confirm the observations made about the DiO colocalising with the lysosomal marker. Nevertheless, one coefficient is higher than the other since there are less green DiO pixels than red CD63 pixels. The low values of M1 and M2 for ApoB present no colocalisation between the lipid-droplets marker and DiO. Furthermore, the values of M1 and M2 for EEA1 and ApoB showed no significant difference with each other confirming that both antibodies do not show any colocalisation with DiO. The value of M2 for CD63 was shown to be significantly higher than the value for EEA1 (mean difference of 0.83 ± 0.11 and $P < 0.001$) and ApoB (mean difference of 0.78 ± 0.12 and $P < 0.001$) validating the colocalisation of DiO with the lysosomal marker. The value of M1 does not show any statistical difference with any other coefficient as the data is too disperse.

The same overlap was measured in cells exposed to P407-DiO micelles for a longer time period of 24h (Figure 4.18.B). For EEA1 and ApoB, the values of M1 and M2 show no colocalisation of the antibody staining and DiO. The value of M2 for CD63 shows only 60% of DiO in colocalisation with the lysosomal marker. This value decreased by 20% from 4h to 24h exposure. Furthermore, the mean difference of M2 for CD63 and for EEA1 decreased from 0.83 ± 0.11 with $P < 0.001$, at 4h exposure, to 0.46 ± 0.25 with $P < 0.05$ after 24h exposure. This suggests that the DiO might be released from the lysosomes and late endosomes over time.

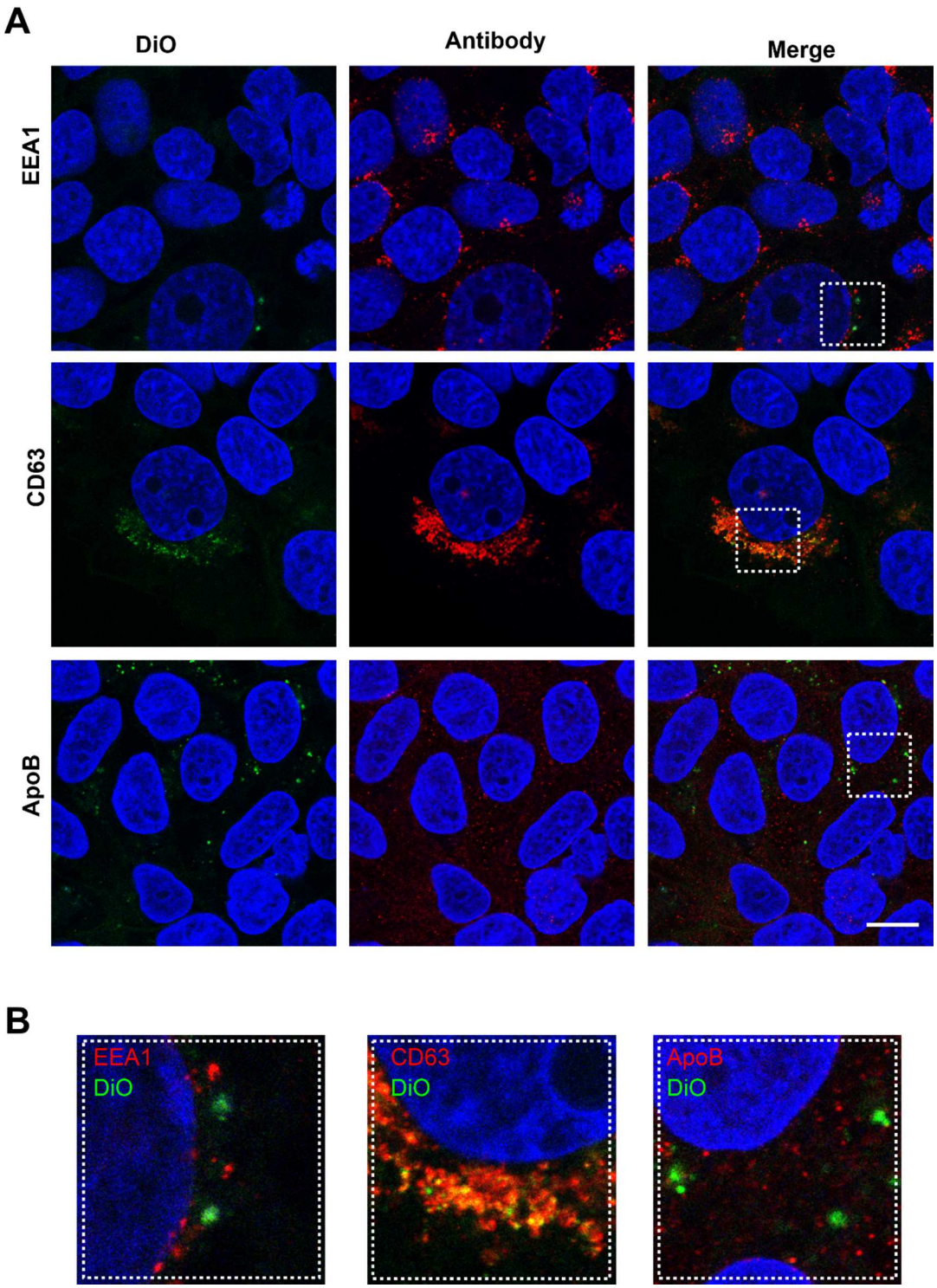

Figure 4.17 *Colocalisation of EEA1, CD63 and, ApoB with DiO in BeWo b30 cells.(A) cells were exposed to P407-DiO micelles for 4h (green) and labelled with antibodies after fixation (red). Nuclei are labelled in blue with DAPI. Scale bar: 15μm (B) Magnifications of selected regions indicated by white dashed boxes. The colocalisation is shown in yellow. The images shown are representative of those obtained in three separate experiments.*

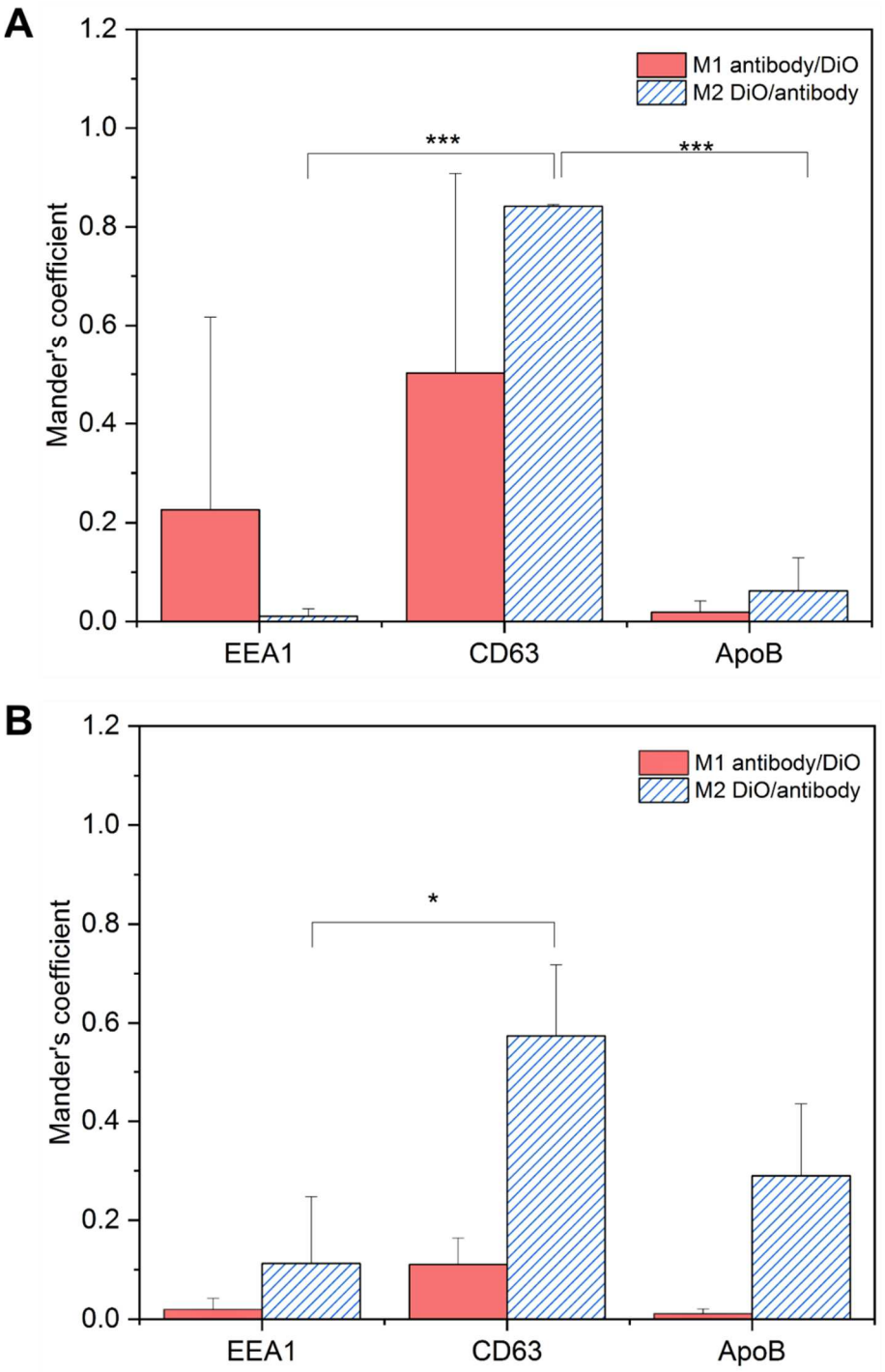

Figure 4.18 *Quantification of the colocalisation of EEA1, CD63 and, ApoB with DiO exposed for (A) 4h and (B) 24h in BeWo b30 cells using Mander's coefficients (M1 and M2). M1 represents the fraction of antibody staining in colocalisation with DiO whereas M2 shows the fraction of DiO in colocalisation with the antibody staining. All the values are means ± SD (n=3) and the significance difference between means was evaluated using a one-way ANOVA followed by a post hoc comparison (Tukey test) with significance set at P<0.001*

4.7 Uptake of RITC-P407-DiO micelles over time

4.7.1 Uptake of RITC-P407-DiO micelles on MDCK cells

In previous sections, the evaluation of the green fluorescence associated with DiO cargo showed evidence of the internalisation by MDCK cells as well as its accumulation in specific cell compartments. However, no information on whether the dye is still in micelles when internalised was found. To address this matter, MDCK Cells were exposed continuously to RITC-P407-DiO micelles for 1, 4, 8, and 24 hours (Figure 4.19). After 1-hour exposure, a red and green fluorescence can be seen in the cytoplasm of the cells. Neither fluorescence is seen in the control cells not exposed to micelles indicating the uptake by the cells of the RITC-P407 polymer as well as the cargo (DiO) after 1 hour of exposure. From 4 to 8 hours exposure, the green and red fluorescence seems to increase in the overall cell monolayer as the micelles continue to enter the cells. However, at 1, 4, and 8-hours, the green fluorescence appears to be lower than previously observed in MDCK cells exposed to P407-DiO micelles at the same time points (Figure 4.3). After 24 hours of continuous exposure, the green fluorescence is substantially higher than for the previous time points which is in marked contrast to the red fluoresce which seems to have slightly decreased. As seen previously (Chapter 3), the fluorescence of DiO seems to be quenched by RITC-P407 at 37 ºC. This could explain the low fluorescence observed in the cell monolayer when adding RITC labelled P407 to the micelle corona. This also suggests that from 1 up to 8 hours DiO may still be encapsulated into RITC-P407 micelles. At later time points,

the green fluorescence seems to increase as the red fluorescence decreases. This could be due to a reduced quenching effect if the polymer and the encapsulated dye might be following different pathways after 8 hours exposure.

From this experiment, evidence is seen of the dye being encapsulated into micelles when taken up by the cells. However, a deeper analysis of the fluorescence quenching is needed to confirm these results.

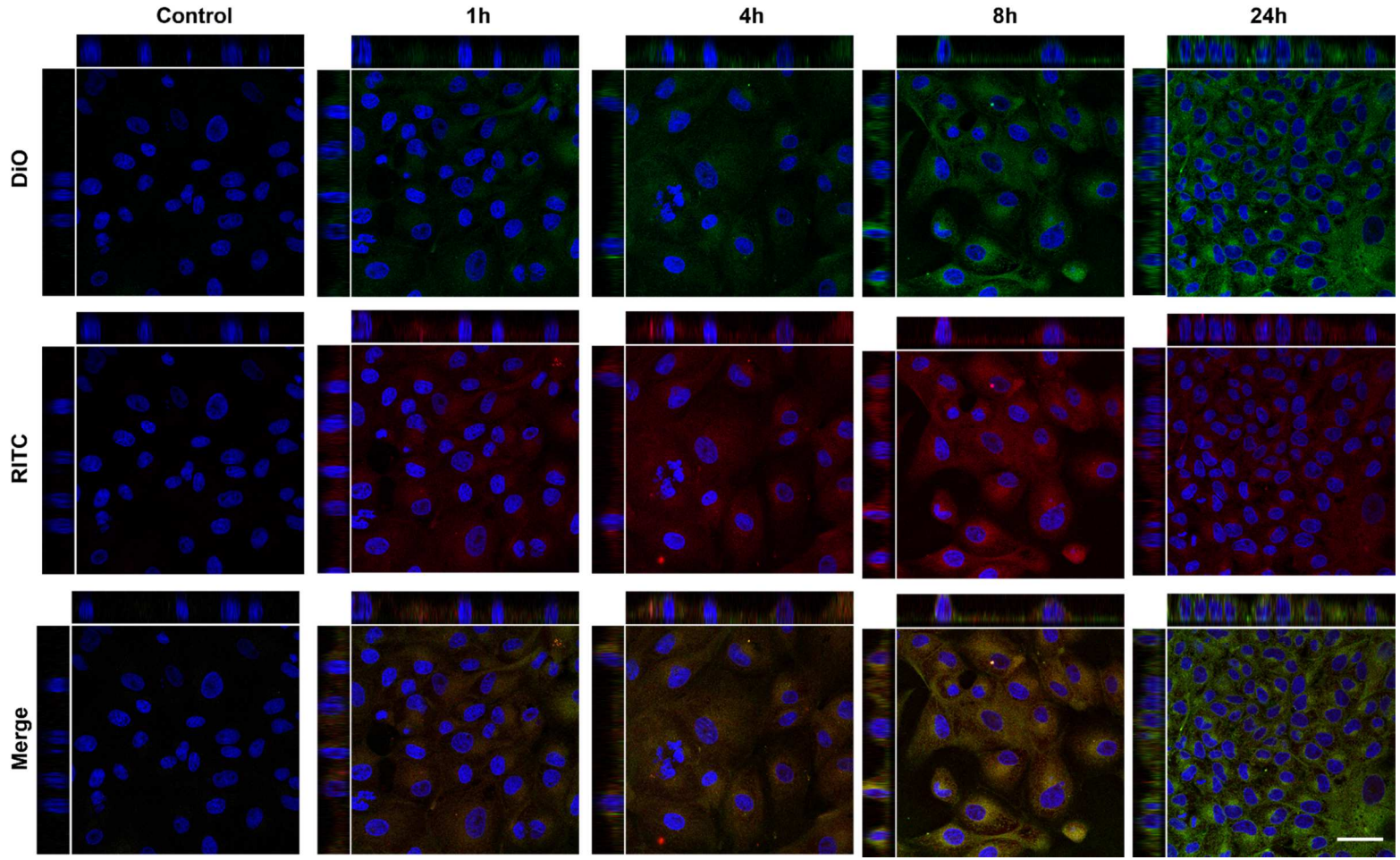

Figure 4.19 *Uptake of RITC-P407-DiO micelles in MDCK cells over time. Confocal images were taken on fixed cells previously exposed to RITC-P407-DiO micelles for 1, 4, 8 and 24 hours. The images shown are representative of those obtained in four separate experiments. Scale bar 50 μm.*

4.7.2 Uptake of RITC-P407-DiO micelles on BeWo b30 cells

BeWo cells were continuously exposed to RITC-P407-DiO micelles for 1, 4, 8, and 24 hours (Figure 4.20). After 1h exposure, a green and red fluorescence is seen in the cell monolayer in contrast to control cells confirming the uptake of the DiO dye and RITC-P407 polymer. At 4, 8, and 24 hours, the red fluorescence diminishes gradually whereas the green fluorescence slightly increases with time. After the first hour of exposure, the green and red fluorescence seem to overlap resulting in a yellow merged image. At later timepoints, the green fluorescence increases as the red fluorescence decreases suggesting that, as seen previously in MDCK cells, the RITC-P407 polymer could be quenching the fluorescence of DiO. Additionally, the overlap of the green and red channels seems to decrease with time and the cross-section images at 24h display green and red accumulation areas in different sites of the cells. This implies that the DiO may be following a different pathway than the RITC-P407 polymer and thus, indicates the potential release of the cargo from micelles to the cells after being internalised.

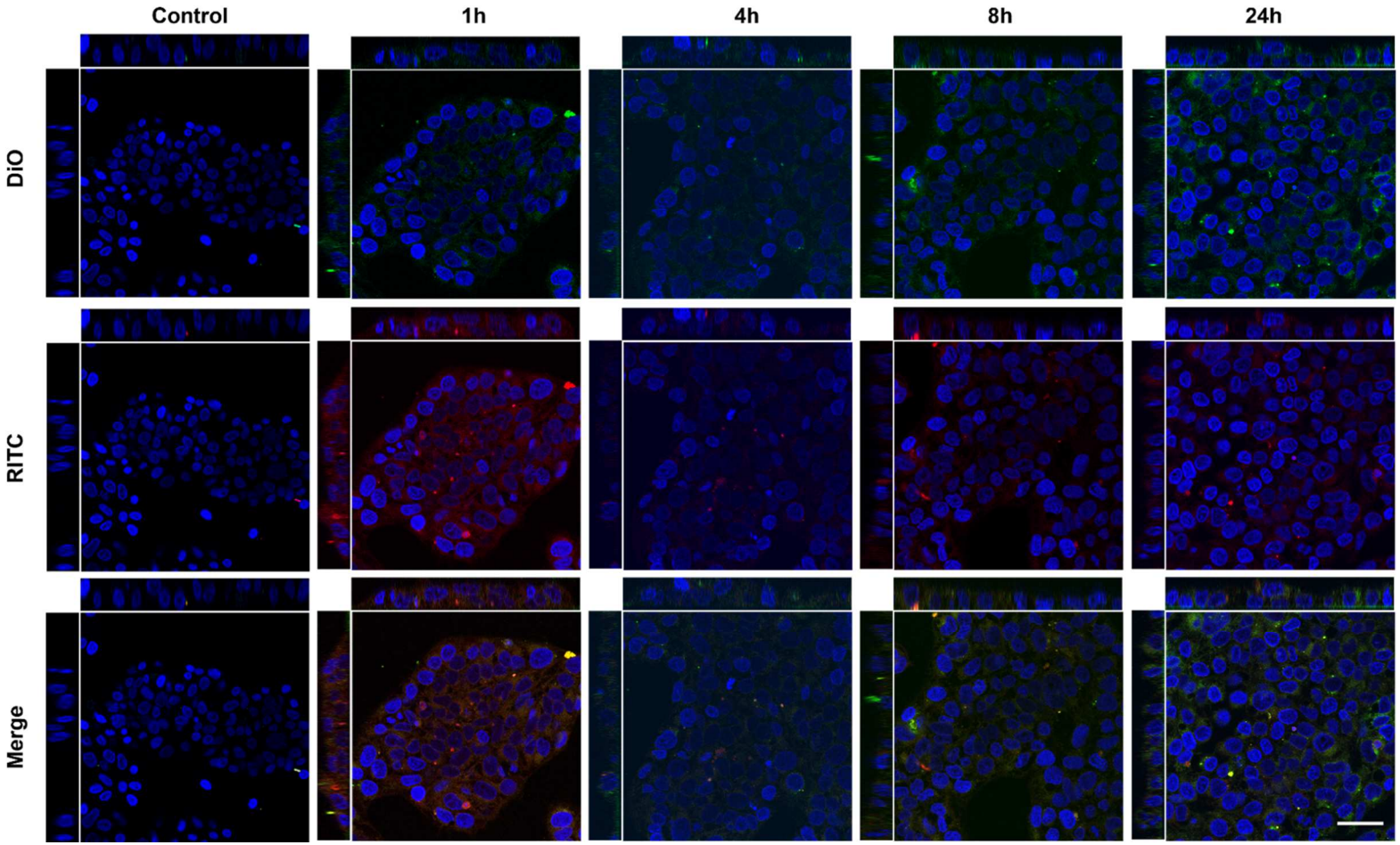

Figure 4.20 *Uptake of RITC-P407-DiO micelles in BeWo b30 cells over time. Confocal images were taken on fixed cells previously exposed to RITC-P407-DiO micelles for 1, 4, 8 and 24 hours. The images shown are representative of those obtained in four separate experiments. Scale bar 50 μm.*

4.8 Evaluation of the cargo release in cells over time using FRET

To further investigate the quenching effect observed when exposing RITC-P407-DiO micelles to cells (section 4.7), the quantification of FRET detected between RITC-P407 polymer and DiO dye was done on MDCK cells.

4.8.1 Determination of the FRET efficiency in MDCK cells during a continuous exposure to micelles

MDCK cells were continuously exposed to RITC-P407-DiO micelles using a protocol replicating the experiments presented in section 1.7. After exposure, the FRET efficiency, expressing the amount of energy transfer between the donor and acceptor (DiO and RITC respectively), was obtained by photo-bleaching the acceptor within a ROI. The result from this was displayed as a LUT image (Figure 4.21 A). The merged image, after 1h exposure, shows an overall orange fluorescence resulting from the overlap of the green fluorescence of DiO and the red fluorescence of RITC-P407. This indicates that both dyes are colocalised in the same sites of the cells hence, DiO might still be encapsulated in micelles for this time point. The pseudo colours in the LUT image show higher FRET signals detected in proximity to the nucleus. The merged image after 24h of continuous exposure presents green and red puncta in different loci of the cell suggesting that some cargo was released from micelles at this timepoint.

The LUT image indicates lower FRET efficiency than the one seen at 1h exposure and reveals the accumulation of the fluorescence into punctate structures in contrast to the uniform distribution seen at 1h.

The FRET efficiencies obtained from the LUTs at 1, 4, 8, and 24h were measured in the cytoplasm and compared to the values found in the nucleus where no fluorescence or FRET are visually observed (Figure 4.21 B). After 1h exposure, 30% of FRET efficiency is measured in the cytoplasm of the cells. This FRET efficiency confirms that after 1h, part of the cargo is still inside the micelles as fluorescence quenching is detected only when DiO is encapsulated inside 15 nm RITC-P407 micelles (Chapter 3).

From 1 to 4h exposure a considerable decrease in FRET is observed indicating the release of the dye from the micelles' core. From 4 to 24h, no substantial changes in FRET are seen with efficiency values of ~10%. These values differ significantly from the ones detected inside the nuclear area meaning that FRET is still occurring in the cytoplasm during this time period.

The significant decrease in FRET efficiency, suggests that most of the cargo is released from the micelles during the first 4h of exposure. Nevertheless, after 4h, a low amount of FRET is still detected. This could arise because new micelles continue to enter the cells during the experiment since the experimental setup inlcudes continuous exposure.

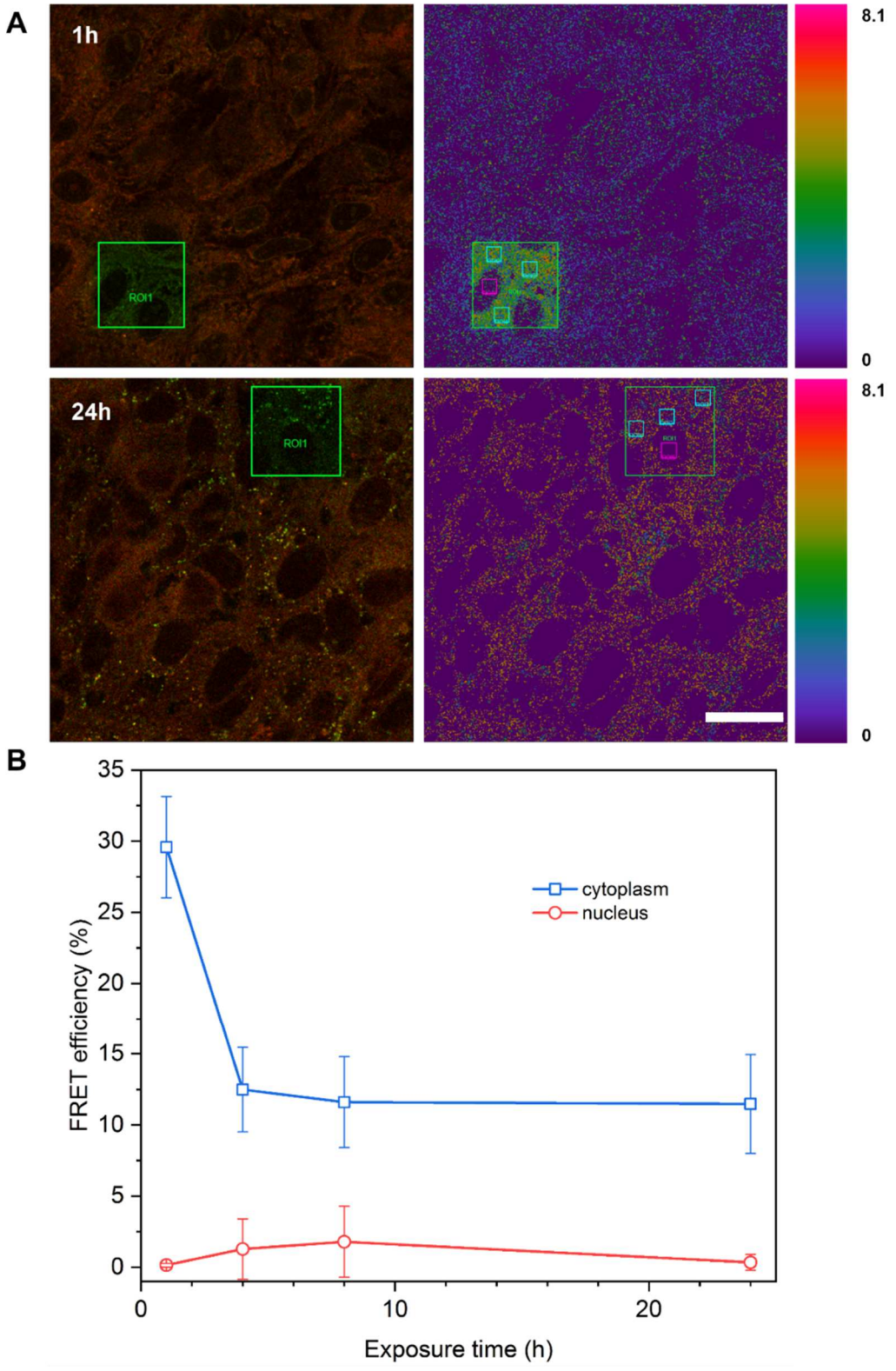

Figure 4.21 *FRET measurements on MDCK cells continuously exposed to RITC-P407-DiO micelles. (A) Conversion of the FRET signal detected from a confocal image (left) into LUT (right) after 1 and 24h of continuous exposure. The bleached ROI is designated by a green square. The FRET efficiency was measured in the cytoplasm of a cell (cyan squares) and compared to the one observed in the nucleus (pink squares). The images shown are representative of those obtained in 3 separate experiments. (B) FRET efficiencies measured over time. The measured values in the cytoplasm (blue) are compared to the ones found in the nuclei (red) All the values are presented as means ± SD..*

4.8.2 Determination of the FRET efficiency in MDCK cells during a pulse exposure to micelles

To further examine the time-course of RITC and DiO segregation in cells a pulse-chase RITC-P407-DiO exposure experiment was performed on MDCK cells followed by confocal and FRET analysis. The pulse-chase protocol was introduced with the intention of avoiding FRET signal from micelles entering the cells at all time points during a continuous exposure (section 4.8.1) and hence to provide a clearer analysis of time-dependent changes in DiO-RITC FRET. During this experiment, the cells were exposed to RITC-P407-DiO micelles only during the first hour of the experiment. The FRET efficiency occurring between DiO and RITC-P407 was imaged and displayed as a LUT image (Figure 4.22 A). The merged confocal image after 1h exposure shows a uniform orange fluorescence distribution due to the overlap between RITC-P407 and DiO fluorophores. Additionally, the pseudo colours seen on the LUT image show a higher FRET in the cytoplasm of the cells than in the nuclei. These observations are comparable to the ones seen for a continuous exposure (Figure 4.21) thus, the assumption can be made that some DiO is still encapsulated into micelles after 1h exposure. After 24h of experiment, evidence is seen of the cargo being released from the micelles as the merged image shows green and red dots accumulating into different sites of the cells. Furthermore, the LUT image shows lower FRET efficiency than the one seen at 1h.

The decrease of the FRET efficiencies was measured over time (Figure 4.22 B). During the first hour of the experiment, approximatively 20% of

FRET efficiency is detected in cells. This value decreases considerably to ~7% after four hours indicating some release of the cargo from the micelles. At the end of the experiment, the value of FRET efficiency obtained is approximatively 5% which is lower than the final value seen in the continuous exposure. This is to be expected as in the continuous experiment, had a constant exposure to RITC-P407-DiO micelles.

The observed decrease in FRET, within this experiment, support the results seen in the continuous experiment suggesting that most of the DiO encapsulated is released in the first 4 hours after being internalised. However, a small amount of FRET can still be detected after 24 hours meaning that some of the DiO is still in micelles.

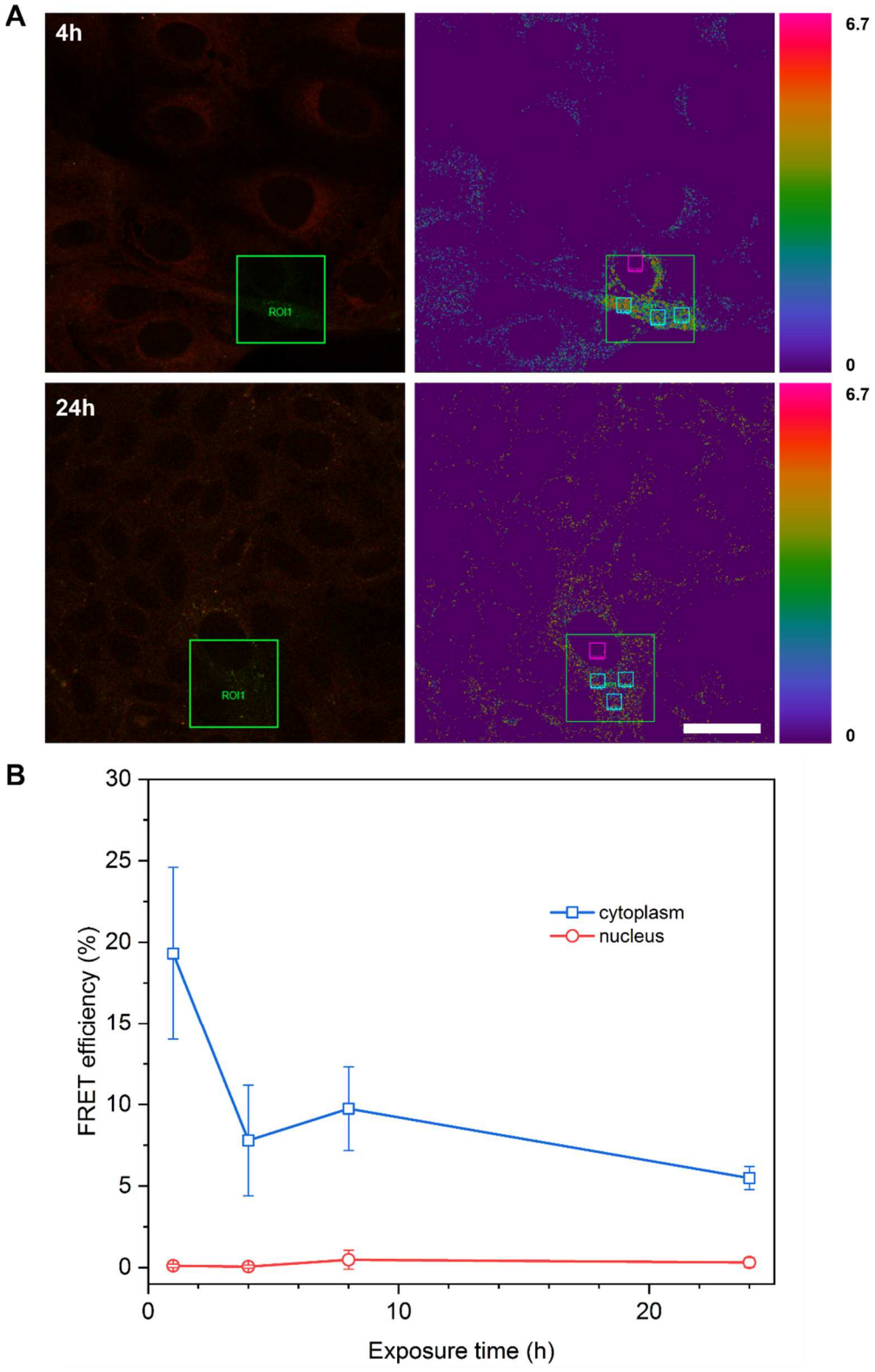

Figure 4.22 *FRET measuremets on MDCK cells exposed to RITC-P407-DiO micelles for 1 hour. (A) Conversion of the FRET signal detected from a confocal image (left) into LUT (right) after 1 and 24h of continuous exposure. The bleached ROI is designated by a green square. The FRET efficiency was measured in the cytoplasm of a cell (cyan squares) and compared to the one observed in the nucleus (pink squares). The images shown are representative of those obtained in 3 separate experiments. (B) FRET efficiencies measured over time. The measured values in the cytoplasm (blue) are compared to the ones found in the nuclei (red). All the values are presented as means ± SD.*

4.9 Discussion

In this chapter, the internalisation and cargo release of P407 micelles were assessed in BeWo b30 and MDCK cell monolayers. This was achieved by analysing P407-DiO and RITC-P407-DiO micelles with a range of imaging techniques.

Initially, P407-DiO was localised in cells at various time points using confocal microscopy. Over all time points examined, the green fluorescence signal corresponding to DiO was detected in MDCK and BeWo b30 cells indicating the effective internalisation of the cargo. In the first 4 hours of exposure DiO fluorescence appeared to be distributed throughput the cell with possible accumulation around the nucleus. Moreover, evidence of accumulation of the dye into sub-cellular compartments was seen in both cell lines for time points later than 4 hours. This fluorescence was not seen for controls confirming DiO uptake. Furthermore, no fluorescent staining was seen in cellular membranes indicating that the dye is entering the cells in a different way that the usual lipid membrane stain seen for DiO[33,34]. To support these observations, quantitative and mechanistic studies were made on cells.

Because of its randomised image acquisition and high throughput, high-content imaging using a spinning disk-based system was used to quantify DiO fluorescence in cells over time obtaining data with high statistical value. The results obtained confirmed the increase in fluorescence over time in MDCK and BeWo b30 cells. In both cases, the fluorescence increased in a non-linear way. In MDCK cells, the dye

internalisation happened slowly at early timepoints and increased more rapidly at later timepoints. The apparent non-linear internalisation is consistent with previous data showing triblock copolymers to have a double effect on membranes[35–39]. Depending on the incubation time and the hydrophobicity/hydrophilicity ratio of the polymeric chain, the polymer can seal and/or permeabilise the cellular membrane[22,23,40]. P407 polymer has more hydrophobic segments than P181 polymer and this hydrophobicity has previously been linked to an ability to permeabilise the lipidic membrane efficiently, enhancing the uptake of antitumor drugs in tumour cells[41]. However, the hydrophilic chains of P407 are longer than the ones of Poloxamer P188, a feature that has previously been associated with protection of lipid vesicles from peroxidation[23]. Overall, the hydrophobic/hydrophilic ratio of P407 confers a dual effect on the lipidic membrane. This effect might explain, at least in part, the biphasic nature of the increase in fluorescence in MDCK cells. Initially, when the fluorescence increases slowly the membrane may be partially sealed by free polymer in solution. The rapid increase in fluorescence at later time points may be due to the membrane being permeabilised as the hydrophobic section of the polymer is inserted into the membrane. This last step may allow more dye to enter the cell.

Although the high-content screening imaging proved to be suitable for quantifying the fluorescence of DiO in MDCK cells, the green fluorescence of DiO in BeWo b 30 cells was more challenging to quantify due to the irregularity in the size and morphology of the cells. For high-content screening acquisition, confocal settings such as the number of focal

planes acquired were set equal for all conditions. However, using fixed settings with such irregular cell monolayer led to variations in background signal causing considerable variability in the fluorescence detected at all timepoints. Nevertheless, the dye uptake rate in BeWo b30 cells showed to decrease at late timepoints indicating a level of saturation not seen previously in MDCK cells. For this cell line, using a manual acquisition of the images may be more appropriate for future quantification studies.

In contrast with the reported effects of polymer on membrane permeability, other evidence in the literature suggests Poloxamer micelles may be internalised by RME in A-549 and MDCK cells [20,42]. The dynamin inhibitor MiTMAB added to MDCK and BeWo b 30 cells partially inhibited DiO internalisation indicating that the micelles appear to be internalised via RME in addition to another internalisation pathway. The evidence seen previously of the membrane being sealed or permeabilised by P407 suggests an alternative internalisation mechanism which could be happening by diffusion of particles into the cells after membrane permeabilisation with P407 polymer. This proposed internalisation pathway can also explain the saturation level detected in BeWo b30 cells. However, other endocytic pathways also should be explored as it is a common observation that multiple cell entry mechanisms can operate simultaneously, making the identification of a single specific mechanism very difficult to identify without discarding others[19].

The use of antibodies helped to identify the compartments in the cells where accumulation was seen by confocal microscopy. The partial inhibition seen using an RME inhibitor prompted experiments to identify early

endosomes (using an anti-EEA antibody), and late endosomes and lysosomes (using and anti-CD63 antibody). Initial experiments were necessary to optimise cell permeabilisation to enable antibody labelling without affecting DiO localisation. These identified 0.1% saponin as a suitable surfactant for subsequent immunofluorescent staining. Antibody labelling revealed no colocalisation between accumulated DiO and early endosomes in either MDCK or BeWo b30 cells. In contrast, the punctate structures formed by dye accumulation were effectively colocalised with late endosomes and/or lysosomes in BeWo b30 cells. Unfortunately, the anti-CD63 antibody used was not successful on MDCK cells. One reason for this may be due to the available EEA1 antibody being raised against human protein which might not be compatible with the canine derived cell line. To investigate the colocalisation of DiO with MDCK late endosomes/lysosomes, an antibody raised against canine EEA1 may be useful. Alternatively, the use of a lysosome specific fluorescent dye such as Lysotracker™ might prove useful for further experiments[43].

Additionally, the lack of evidence of colocalisation with endosomes and the hydrophobic nature of the dye led to a suggestion of possible non-specific sequestration of the dye into lipid droplets. This idea was disproved by using a lipid-droplet antibody (anti-ApoB) which worked effectively in both cell lines but revealed no colocalisation with DiO.

The lack of localisation of DiO in early endosomes was somewhat surprising and led to several alternative hypotheses. One possibility is that the selected time points may have not been appropriate to capture the dye in the early endosomes since the trafficking from the endocytic vesicles to

late endosomes happens in the first 20 minutes of the exposure[19] leaving a small time-window for detection of the dye in early endosomes. To increase the probability of finding the dye in early endosomes, cells were exposed to DiO containing micelles continuously ensuring the constant internalisation of the particles over the time course but still no colocalisation of DiO with early endosomes was seen. An alternative explanation could be related to the sensitivity of the microscope being unable to detect individual micelles as they enter the cell. The detected signal in cells might be generated by the accumulation of multiple micelles or fluorophore molecules exceeding a detection threshold. To test this hypothesis, the use of alternative imaging techniques with greater sensitivity or ability to resolve single micelles may be warranted alongside CLSM[44]. An alternative possibility is that the apparent accumulation of DiO in late endosomes and/or lysosomes is not related to endocytosis but a by-product of DiO being internalised by diffusion through the membrane. Although the decreased accumulation of DiO observed in the presence of MiTMAB supports a role for RME in its uptake it is also possible that MiTMAB might exert an indirect effect. The dynamin inhibitor could exert a mechanical effect via its inhibition of membrane fission affecting the membrane tension and rigidity[45]. This mechanical stress might affect the way the polymer interacts with the membrane and delay the permeabilization process. Although on balance the data presented some evidence of RME playing a role in DiO-P407 uptake, the lack of evidence of early endosome localisation leaves this unproven at present. These findings appear to refute a current model for cell entry by Pluronics

micelles. And suggests that the entry mechanisms might happen via diffusion of micelles through the cellular membrane rather than by RME.

Having explored the internalisation pathways of DiO in cells, the question remained unclear on whether the dye was released from micelles or not. In Chapter 3, RITC-P407-DiO micelles showed fluorescence quenching between the fluorophore linked to the polymer (RITC) and the one encapsulated in micelles (DiO). To support this result and assess the release of the cargo, amount of FRET detected was tested on MDCK cells. The continuous exposure of cells to RITC-P407-DiO micelles showed a significant decrease of the FRET efficiency within the first 4 hours of exposure. This suggested that a significant part of the cargo was released from micelles during this time. However, after this time the FRET efficiency value was kept constant but not null. A pulse experiment showed the same significant decrease in FRET within the first 4 hours of exposure still the constant value was not null. This supported the conclusion of most DiO being released over the first 4 hours of exposure and proved that some of the DiO is still in micelles up to 24 hours after exposure.

Over all experiments, the micelles showed no apparent effect on the cell morphology even after exposed continuously for 24 hours. This highlights the suitability of this polymer as a non-toxic drug carrier [7,46]. To confirm this an attempt to assess the cytotoxicity of micelles on cells was made using a colorimetric toxicity assay (Lactate dehydrogenase assay) capable to indirectly measure the amount of lysed cells exposed to micelles. However, the fluorescent signal of the DiO interfered with the signal of fluorescent marker of the assay (Formazan). To prove the low toxicity of the

micelles, the cell lysis needs to be assessed using a different toxicity assay with a different colorimetric marker such as Bicinchoninic Acid (BCA) assay or assessed by Lactate dehydrogenase assay using dye-free micelles which would not interfere with the signal. However the latter would not give any information about the toxicity of the dye.

The results presented in this chapter helped explore and raise new questions on how polymeric micelles interact with cells using a simple *in vitro model.* However, in order to reach their target after being administrated into the blood stream, these drug-delivery systems need to overcome key barriers in the human body[47]. The cells found in these barriers have more structural complexities than the ones used in the *in vitro* model presented in this chapter. To address this problem, the development of more complex tissue culture methods capable to mimic physiological conditions of barriers need to be optimised and used to test transport of such drug delivery systems.

4.10 References

1. Leckband, D. & Israelachvili, J. Intermolecular forces in biology. *Q. Rev. Biophys.* **34,** 105 (2010).

2. Min, Y., Akbulut, M., Kristiansen, K., Golan, Y. & Israelachvili, J. The role of interparticle and external forces in nanoparticle assembly. *Nat. Mater.* **7,** 527–538 (2008).

3. Langer, R. *et al.* The controlled intravenous delivery of drugs using PEG-coated sterically stabilized nanospheres. *Adv. Drug Deliv. Rev.* **16,** 215–233 (1995).

4. R.T. Dorr. Pharmacology and Toxicology of Cremophor EL Diluent. *Ann. Pharmacother.* **28,** S11–S14 (1994).

5. Kirpotin, D. B. *et al.* Tissue affinity of the infusate affects the distribution volume during convection-enhanced delivery into rodent brains: Implications for local drug delivery. *J. Neurosci. Methods* **154,** 225–232 (2006).

6. Shuai, X., Merdan, T., Schaper, A. K., Xi, F. & Kissel, T. Core-cross-linked polymeric micelles as paclitaxel carriers. *Bioconjug. Chem.* **15,** 441–448 (2004).

7. Ahmad, Z., Shah, A., Siddiq, M. & Kraatz, H. B. Polymeric micelles as drug delivery vehicles. *RSC Advances* **4,** 17028–17038 (2014).

8. Rijcken, C. J. F., Soga, O., Hennink, W. E. & van Nostrum, C. F. Triggered destabilisation of polymeric micelles and vesicles by changing polymers polarity: an attractive tool for drug delivery. *J. Control. release* **120,** 131–48 (2007).

9. Lu, J., Owen, S. C. & Shoichet, M. S. Stability of self-assembled polymeric micelles in serum. *Macromolecules* **44,** 6002–6008 (2011).

10. Molineux, G. Pegylation: Engineering improved pharmaceuticals for enhanced therapy. *Cancer Treat. Rev.* **28,** 13–16 (2002).

11. Lee, J. H., Bang Lee, H. & Andrades, J. D. *Blood compatibility of polyethylene oxide surfaces*. *Pergamon hog. Polym. Sci* **20,** (1995).

12. Woodle, M. C. & Lasic, D. D. Sterically Stabilized Liposomes Therapeutics. *Biochim. Biophys. Acta - Gen. Subj.* **1113,** 171–199 (1992).

13. Kabanov, A. V, Batrakova, E. V & Yu, V. Pluronic® block copolymers as novel polymer therapeutics for drug and gene delivery. *J. Control. Release* **82,** 189–212 (2002).

14. Batrakova, E. V. & Kabanov, A. V. Pluronic block copolymers: Evolution of drug delivery concept from inert nanocarriers to biological response modifiers. *Journal of Controlled Release* **130,** 98–106 (2008).

15. Zhang, W. *et al.* Enhanced antitumor efficacy by paclitaxel-loaded pluronic P123/F127 mixed micelles against non-small cell lung cancer based on passive tumor targeting and modulation of drug resistance. *Eur. J. Pharm. Biopharm.* **75,** 341–53 (2010).

16. Deller, R. C. *et al.* Functionalised triblock copolymer vectors for the treatment of acute lymphoblastic leukaemia. *Mol. Pharm.* **14,** 722–732 (2017).

17. Singleton, W. *et al.* Convection enhanced delivery of tri-block copolymer nano-micelles: a method of direct intraparenchymal water-insoluble drug delivery for the treatment of high-grade glioma. *Neuro. Oncol.* **20,** i19–i19 (2018).

18. Schillén, K. *et al.* A fluorescence study of the loading and time stability of doxorubicin in sodium cholate/PEO-PPO-PEO triblock copolymer mixed micelles. *J. Colloid Interface Sci.* **540,** 593–601 (2019).

19. Canton, I. & Battaglia, G. Endocytosis at the nanoscale. *Chemical Society Reviews* **41,** 2718–2739 (2012).

20. Sahay, G., Batrakova, E. V & Kabanov, A. V. Different internalization pathways of polymeric micelles and unimers and their effects on vesicular transport. *Bioconjug. Chem.* **19,** 2023–2029 (2008).

21. Fonseca, S. B., Pereira, M. P. & Kelley, S. O. Recent advances in the use of cell-penetrating peptides for medical and biological applications. *Advanced Drug Delivery Reviews* **61,** 953–964 (2009).

22. Wang, J. Y., Chin, J., Marks, J. D. & Lee, K. Y. C. Effects of PEO-PPO-PEO triblock copolymers on phospholipid membrane integrity under osmotic stress. *Langmuir* **26,** 12953–12961 (2010).

23. Wang, J. Y., Marks, J. & Lee, K. Y. C. Nature of interactions between PEO-PPO-PEO triblock copolymers and lipid membranes: (I) Effect of polymer hydrophobicity on its ability to protect liposomes from peroxidation. *Biomacromolecules* **13,** 2616–2623 (2012).

24. Schindelin, J. *et al.* Fiji: An open-source platform for biological-image analysis. *Nat. Methods* **9,** 676–682 (2012).

25. Rueden, C. T. *et al.* ImageJ2: ImageJ for the next generation of scientific image data. *BMC Bioinformatics* **18,** 1–26 (2017).

26. Lin, L. & Sherman, P. D. Cleaning Data the Chauvenet Way. *SESUG Proc.* 1–11 (2007).

27. Carpenter, A. E. *et al.* CellProfiler: image analysis software for identifying and quantifying cell phenotypes. *Genome Biol.* **7,** R100 (2006).

28. Letter, C. A. FRET - Acceptor Photobleaching on Leica SP5. *Confocal application letter* **28,** (2007).

29. Quan, A. *et al.* Myristyl Trimethyl Ammonium Bromide and Octadecyl Trimethyl Ammonium Bromide Are Surface-Active Small Molecule Dynamin Inhibitors that Block Endocytosis Mediated by Dynamin I or Dynamin II. *Mol. Pharmacol.* **72,** 1425–1439 (2007).

30. Joshi, S. *et al.* The Dynamin Inhibitors MiTMAB and OcTMAB Induce Cytokinesis Failure and Inhibit Cell Proliferation in Human Cancer Cells. *Mol. Cancer Ther.* **9,** 1995–2006 (2010).

31. Jamur M.C., O. C. Permeabilization of Cell Membranes. , vol 588. *Immunocytochemical Methods Protoc. Methods Mol. Biol. (Methods Protoc. Humana Press* **588,** 63–66 (2009).

32. Lacaille-Dubois, M. A. & Wagner, H. *A review of the biological and pharmacological activities of saponins*. *Phytomedicine* **2,** (1996).

33. Höppner, M., Luhm, J., Schlenke, P., Koritke, P. & Frohn, C. A flow-cytometry based cytotoxicity assay using stained effector cells in combination with native target cells. *J. Immunol. Methods* **267,** 157–163 (2002).

34. Honig, M. G. & Hume, R. I. Fluorescent carbocyanine dyes allow living neurons of identified origin to be studied in long-term cultures. *J. Cell Biol.* **103,** 171–187 (1986).

35. Wu, G. *et al.* Lipid Corralling and Poloxamer Squeeze-Out in Membranes. *Phys. Rev. Lett.* **93,** 28101-1–4 (2004).

36. Wu, G. *et al.* Interaction between lipid monolayers and poloxamer 188: An X-ray reflectivity and diffraction study. *Biophys. J.* **89,** 3159–3173 (2005).

37. Johnsson, M., Bergstrand, N., Edwards, K. & Stålgren, J. J. R. Adsorption of a PEO−PPO−PEO Triblock Copolymer on Small Unilamellar Vesicles: Equilibrium and Kinetic Properties and Correlation with Membrane Permeability. *Langmuir* **17,** 3902–3911 (2007).

38. Demina, T. *et al.* Relationship between the structure of amphiphilic copolymers and their ability to disturb lipid bilayers. *Biochemistry* **44,** 4042–4054 (2005).

39. Krylova, O. O. *et al.* Pluronic L61 accelerates flip-flop and transbilayer doxorubicin permeation. *Chem. - A Eur. J.* **9,** 3930–3936 (2003).

40. Cheng, C. Y. hydration dynamics reveale, Wang, J. Y., Kausik, R., Lee, K. Y. C. & Han, S. Nature of interactions between PEO-PPO-PEO triblock copolymers and lipid membranes: (II) Role ofd by dynamic nuclear polarization. *Biomacromolecules* **13,** 2624–2633 (2012).

41. Venne, A., Li, S., Mandeville, R., Kabanov, A. & Alakhov, V. Hypersensitizing effect of pluronic L61 on cytotoxic activity, transport, and subcellular distribution of doxorubicin in multiple drug- resistant cells. *Cancer Res.* **56,** 3626–3629 (1996).

42. Zhang, W. *et al.* Multifunctional Pluronic P123/F127 mixed polymeric micelles loaded with paclitaxel for the treatment of multidrug resistant tumors. *Biomaterials* **32,** 2894–2906 (2011).

43. Duvvuri, M., Feng, W., Mathis, A. & Krise, J. P. A Cell Fractionation Approach for the Quantitative Analysis of Subcellular Drug Disposition. *Pharm. Res.* **21,** 26–32 (2004).

44. Polishchuk, R. S. *et al.* Correlative light-electron microscopy reveals the tubular-saccular ultrastructure of carriers operating between Golgi apparatus and plasma membrane. *J. Cell Biol.* **148,** 45–58 (2000).

45. Morlot, S. *et al.* Membrane shape at the edge of the dynamin helix sets location and duration of the fission reaction. *Cell* **151,** 619–629 (2012).

46. Singleton, W. G. *et al.* Convection enhanced delivery of panobinostat (LBH589)-loaded pluronic nano-micelles prolongs survival in the F98 rat glioma model. *Int. J. Nanomedicine* **12,** 1385–1399 (2017).

47. Francia, V., Aliyandi, A. & Salvati, A. Effect of the development of a cell barrier on nanoparticle uptake in endothelial cells. *Nanoscale* **10,** 16645–16656 (2018).

Chapter 5. Optimisation of *in vitro* models to test transport of micelles across epithelial barriers

5.1 Introduction

In recent years, the development of *in vitro* models capable of mimicking *in vivo*-like conditions have gathered increased attention. This is due to the interest in using ethical models to solve scientific problems such as drug design and testing[1]. One of the main problems to address in drug delivery is the transport of therapeutics across biological barriers before reaching the target tissue. As mentioned in chapter 1, epithelial cells can be found in internal and external barriers of the human body. These cells are interconnected by strong intercellular junctions regulating the diffusion of particles in developed epithelial barriers. The regulation of diffusion allows the differentiation of the cellular membrane into apical and basolateral sides[2]. Culture of epithelial cells on porous filters can model *in vivo* conditions by allowing nutrient transport from the apical to the basolateral side of cells (Figure 5.1) promoting cellular differentiation and increasing the similarities with native tissue[3,4].

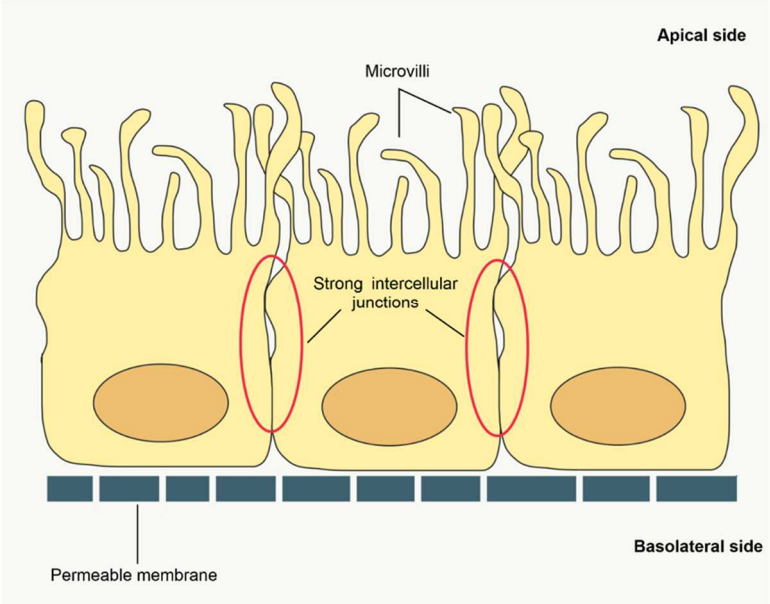

Figure 5.1 *Schematic of a polarised cell barrier grown on a PE membrane filter.*

Formation of junctions and cell barrier integrity can be assessed by measuring trans epithelial electrical resistance (TEER). In this method, a current passes through the cellular barrier and resistance to the flow of current is measured. The measured TEER is the combination of the transcellular resistance (basal and apical membrane) and the paracellular resistance (cell-cell junctions)[5] and is notably increased by the presence of junctional complex proteins[6]. The junctional complex comprises three types of junctions, tight junctions, adherens junctions, and desmosomes. Each junction is characterised by the expression of different proteins as seen in Figure 5.2. Tight junctions (TJ), also known as zonulae occludentes (ZO) are composed of at least 40 different proteins[7]. Among these proteins, claudins and occludins are the main transmembrane proteins. TJ are usually situated near the apical side of polarised cells. Adherens junctions, also known as zonulae adherentes, are constituted of cadherin and catenin proteins. Desmosomes, also known as maculae adherentes, are binding bodies specialised in cell-cell adhesion and are mainly composed of desmoglein and desmocollin proteins. While TJ and adherens junctions are actin rich complexes, desmosomes are supported by intermediate filaments (Figure 5.2). Previous works have shown that the overexpression of claudin-1 protein (found in tight junctions) in MDCK cell monolayers increases the TEER values[8] relating directly the presence of tight junctions with high TEER values. However, the expression of such protein depends on the nature of the cells forming the cellular barrier and therefore different TEER values are seen depending on the barrier. Previous works on MDCK strain

1 cells reported[1] high TEER values between 1500 and 2000 Ω.cm^2 whereas TEER values reported[9–11] for BeWo b30 cells vary from 14 up to 300 Ω.cm^2.

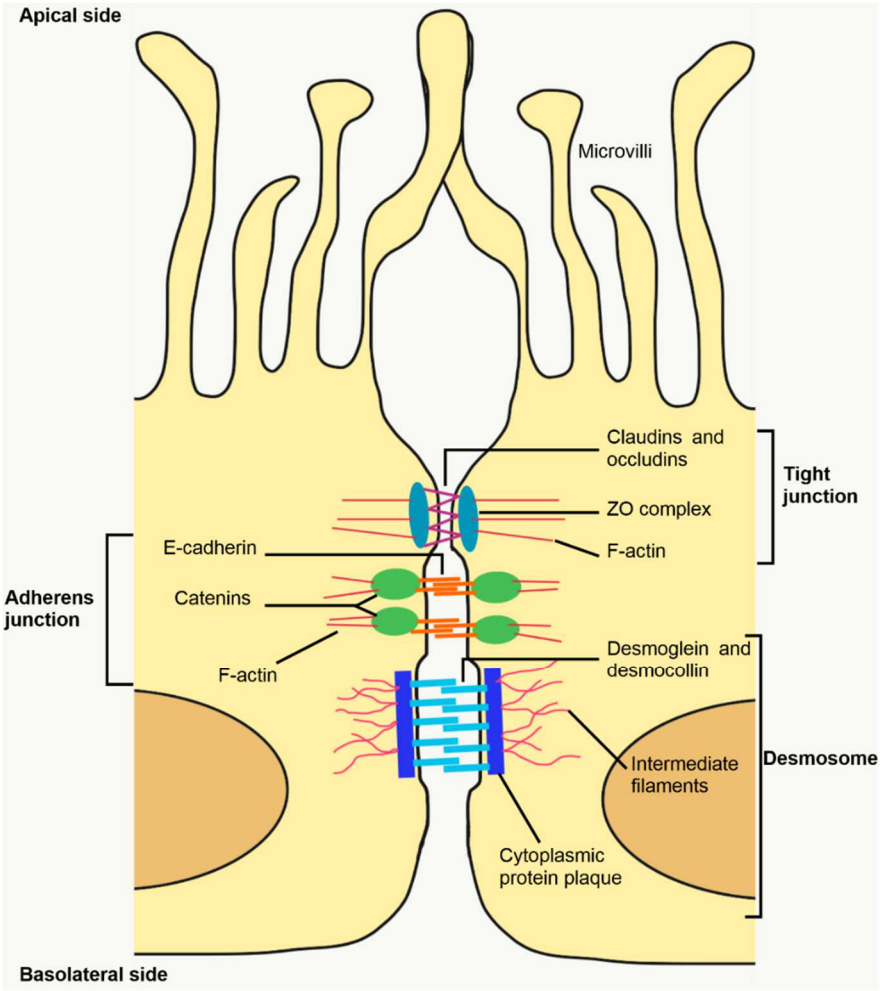

Figure 5.2 *Schematic of the intercellular junctional complex in polarised cells.*

Furthermore, when external cues such as nutrient transport or blood flow are applied to cells, actin concentrates into the apical side of the cells creating membrane protrusions (Figure 5.1 and Figure 5.2) called microvilli (MV). The formation of such affects the membrane tension and causes the inhibition of MV in the basolateral side. These actin rearrangements result

in morphological differences seen in polarised cells such as organelle reorganisation and cellular cytoskeleton asymmetry [12–14].

Finally, culturing epithelial cells under a fluid shear stress (FSS) can also mimic *in vivo* conditions by simulating the blood flow present in tissues. This model has previously been shown to trigger the formation of microvilli on the apical surface of BeWo b30 cells [15] as well as altering membrane transport proteins such as glucose transporters which are essential for placental barrier function and development[16]. More information on the effects of cell polarisation and FSS can be found in sections 1.4.2 and 0.

In this chapter, cell cultures on filter membranes and under FSS are explored to obtain suitable models to assess particle transport and test the hypothesis that if epithelial cells are differentiated, the uptake mechanism of P407-DiO will be different from non-differentiated cells.

5.2 Methods

5.2.1 Cell culture methods

5.2.1.1 *In vitro* model of polarised cells

MDCK and BeWo b30 cell monolayers were grown as confluent layers on Transwell® (Costar, 3462) inserts with polyester (PE) membrane inserts to promote polarisation and facilitate particle transport studies. The diameter of the membrane used was 12 mm and the pore size 3.0 μm. Cells were seeded on day 0 by adding 0.5 mL of cell suspension at a concentration of 1.13 x 10^5 and 2.26 x 10^5 cells/mL for MDCK and BeWo b30 cells respectively to the apical chamber (Figure 5.3). Additionally, 1.5 mL of growing medium were added to the basolateral chamber. The cells were incubated for 3 days at 37 °C and a humidified atmosphere of 5% CO_2. From day 3 to 6 post-seeding, the medium was changed daily.

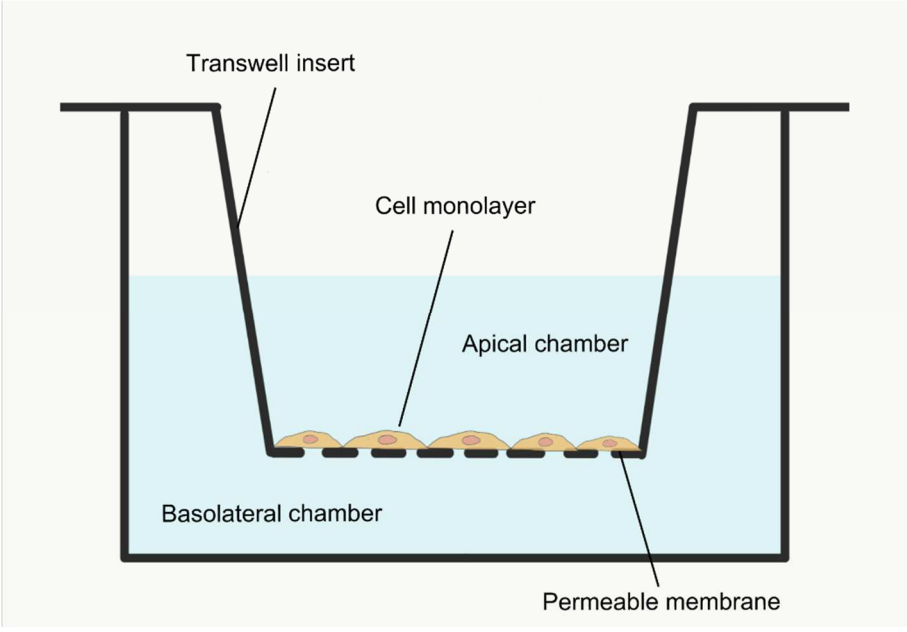

Figure 5.3 *Diagram of a Transwell® system used* as *in vitro* cell-barrier model.

5.2.1.2 Trans-epithelial electrical resistance measurements

The development and integrity of the MDCK and BeWo b30 cell monolayers was monitored by measuring trans-epithelial electrical resistance (TEER) after day 3 post-seeding. TEER measurements were done using two different techniques to find the most suitable for each cell line. The first technique consisted of using a removable electrode pair(World precision instruments, STX-2/chopstick) (Figure 5.4 A). These measurements were compared to the ones obtained using a fixed electrode (World precision instruments, EndOhm) (Figure 5.4 B) containing 3 mL of cell culture medium. Both EndOhm chamber and chopsticks electrodes, were attached to an EVOM system (World precision instruments) measuring resistance. All measurements were performed at room temperature to prevent variations associated with temperature fluctuations. The TEER value of a blank sample consisting of a permeable membrane without cells was measured as a control. This value was then subtracted from the measured resistance of the cell monolayers on the semipermeable membranes (Equation 5.1)[1].

Within a single experiment, six replicates of Transwells® containing cells were measured. The TEER value for each Tanswell® was measured in triplicate to discard outliers associated with the measurement using le Chauvenet's criterion[17]. The entire experiment was performed at least three times for each cell line.

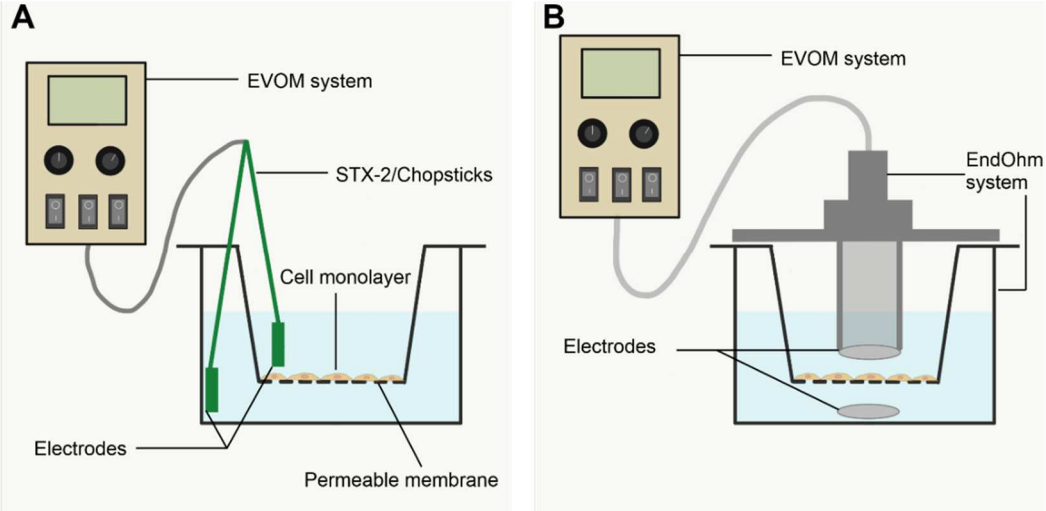

Figure 5.4 *Diagram of instruments set-up for trans epithelial electrical resistance (TEER) measurements using* ***(A)*** *removable electrodes STX-2/chopstick electrode pair and* ***(B)*** *an EndOhm fixed electrode.*

$$R_{Tissue}(\Omega) = R_{Total}(\Omega) - R_{Blank}(\Omega)$$

Equation 5.1 *Determination of the cell-specific resistance (**R_{Tissue}**). **R_{Total}** corresponds to the value of resistance measured on a cell monolayer grown on a membrane and **R_{Blank}** is the value of resistance measured on a membrane without cells,*

The value of resistance is proportional to the inverse of the measured area (Equation 5.2)[18]. The reported values were reported as shown in Equation 5.3[19].

$$R_{Tissue}(\Omega) \propto \frac{1}{M_{Area}(cm^2)}$$

Equation 5.2 *Relation between the measured cell-specific resistance (**R_{Tissue}**) and the effective area of the membrane insert (**M_{Area}**).*

$$TEER_{Reported}\,(\Omega.cm^2) = R_{Tissue}(\Omega) \times M_{Area}(cm^2)$$

Equation 5.3 *Reported TEER measurements. **R_{Tissue}** corresponds to the calculated cell-specific resistance (Equation 5.1) and **M_{Area}** = 1.13 cm^2 for 12 mm inserts.*

5.2.1.3 *In vitro* model to test barrier development under dynamic conditions

To test the effect of fluid shear stress (FSS) on epithelial barrier development, the optimisation of a microfluidics-based *in vitro* cell culture was carried out. Cells were grown into a Vena8 Endothelial+™ (Cellix Ltd) biochip. Prior to cell addition, each channel was coated with 20 µL of an extra cellular matrix (ECM) component (fibronectin or collagen) or poly-L-lysine at 100 µg/mL. For other experiments, different concentrations (25, 50, 75, or 100 µg/mL) of fibronectin were tested. The biochips were left overnight (O.N.) at 4 ºC in a humidified chamber. After incubation, 20 µL of cell suspension at a density of 4 x 10^6 cells/mL were added to each channel and incubated for 1 hour at 37 ºC in a humidified atmosphere containing 5% CO_2. The attached cells were then perfused with cell culture medium using a KIMA (Cellix Ltd) recirculation pump at a pulse flow rate of 300 µL/min for 2 minutes and 0 µL/min for 20 min for 12 or 16 hours.

Experiments to test DiO uptake under flow conditions were carried out on cells grown under dynamic conditions for 16 hours. The previously prepared and characterised solution containing P407-DiO micelles (Section 2.1) was filtered in a 0.2 µm polyester filter and diluted 10-fold in the appropriate growing medium (Section 2.3) before being perfused using an EXiGO (Cellix Ltd) pump under a constant flow rate of 1.67 µL/min for 40 minutes .A post-perfusion wash with cell culture medium was done under the same perfusion conditions. The cells were continuously imaged using widefield fluorescence microscopy.

5.2.2 Imaging methods

5.2.2.1 Staining of polarised cell monolayers grown on inserts for confocal microscopy

For visual assessment of the integrity and formation of the cell monolayer on Transwell® inserts, confocal microscopy was performed.

On day 6 post-seeding, MDCK and BeWo b30 cells were washed with PBS to remove extracellular material and fixed using 2% PFA. The cellular membrane was then permeabilised with 0.3% Triton X-100 for 10 minutes to increase internalisation of the staining dye, this step being omitted for cells exposed to DiO-containing micelles. After permeabilisation, 50 μL of TRITC-phalloidin at 500 ng/mL was added to the polyester membrane resting on a flat surface covered with parafilm and incubated in the dark for 45 minutes at room temperature. After incubation, the membranes were washed with PBS, removed using a scalpel and mounted onto a microscope slide using Vectashield containing DAPI.

Within a single experiment, three inserts were imaged. The experiment was performed at least three times on separate occasions.

5.2.2.2 Sample processing for scanning electron microscopy

The microvilli formation of cells grown on inserts was used as an indicator of cell polarisation[20]. The comparison of polarised and non-polarised cell monolayers was done using scanning electron microscopy (SEM).

Confluent monolayers of MDCK and BeWo cells grown on coverslips and on inserts were removed from the cell culture medium and washed with PBS to remove any extra cellular material. The cells were posteriorly fixed with 2% glutaraldehyde in PBS overnight. Next, the cells were washed with PBS and dehydrated using a concentration gradient of ethanol for 20 minutes each as follows: 25%, 50%, 75%, and 100%. 50 μL of hexamethyldisilazane (HDMS) was added to the dehydrated samples and left to dry completely at room temperature. The samples were mounted onto a stub and coated with a thin film of Au/Pd using a sputter coater (Emitech, K575X).

Within a single experiment, three inserts were imaged. The experiment was performed twice on separate occasions.

5.2.2.3 Sample processing for transmission electron microscopy

The examination of tight junctions (TJ) formed between cells grown on inserts was used as a quality control indicator to validate the suitability of this *in vitro* model as a well-differentiated barrier system[21]. This validation was made using TEM images of cells grown on inserts. This was accomplished by following and adapting the protocol described by Ye *et al*[21].

On day 6 post-seeding, cells were washed with PBS to remove any extracellular material and fixed with 2.5% glutaraldehyde in PBS overnight. After fixation, cells were washed for 10 minutes using Sørensen's buffer. 1% Osmium tetroxide OsO_4 was added to the cells for 30 minutes and washed with Sørensen's buffer for 10 minutes. Next, the cells were

dehydrated using a concentration gradient of ethanol for 10 minutes in the following order: 25%, 50%, 70%, 90%, 95, and 100%(x2). Cells were then pre-embedded with a 1:1 epoxy-resin/ethanol for 1 hour before embedding with 100% epoxy resin for 2 hours to allow the ethanol evaporation. After ethanol evaporation, a section of the PE membrane was cut using a scalpel and embedded into a flat embedding mould with 100% epoxy-resin. The resin was then left to polymerise in a 65 ºC oven for 48 hours. Thin cross sections (70 nm) were finally obtained (with help from Mr Tom Stewart) and stained with uranyl acetate and lead citrate before TEM imaging (with help from Dr Chris Neal).

Within a single experiment, three inserts were imaged. The experiment was performed twice on separate occasions.

5.2.2.4 Enhanced resolution confocal microscopy

Confocal images at enhanced resolution were obtained using Leica's HyVolution 2 technique reducing the pinhole to 0.5 Airy units and pixel size ~50 nm followed by applying a custom deconvolution algorithm. Image acquisition was carried out with a Leica SP8 AOBS confocal laser scanning microscope attached to a Leica DMi8 inverted epifluorescence microscope using a 63x oil-immersion lens (NA 1.4). The lasers used to acquire images were a 120 mW 405 nm diode laser and a white light laser 470-670 nm (2.5 mW/nm). Filters used for visual inspection were DAPI (excitation: 350/50, dichroic mirror: 400, emission: 460/50) and Rhodamine (excitation: 546/40, dichroic: 560, emission: 585/40). For each condition, three random fields of

view were selected in the cell monolayer and z-stacks were obtained using a step size of 0.18μm. All settings were kept unchanged over all samples and experiments to ensure comparison was valid. The resulting image stacks were deconvolved using Huygens software (Scientific Volume Imaging). After image acquisition 3D rendering and cross sectional views were obtained using ImageJ/Fiji[22,23] software. The most representative images of the acquired data were chosen from at least 3 experiments and are presented in this work.

5.2.3 Transport of P407-DiO micelles across developed cell barriers

5.2.3.1 Determination of DiO transport over time

Once the cell barrier was formed and characterised (Section 5.2.1.1 and 5.2.1.2), transport experiments were performed. At t_0, 0.5 mL of the previously prepared and characterised solution containing P407-DiO micelles (Section 2.1) was filtered using a 0.2 µm polyester filter, diluted 10-fold in the appropriate culture medium (Section 2.3) and added to the apical chamber at 37 ºC and a humidified atmosphere of 5% CO_2. For each time point, a 50 µL sample was removed from the basal chamber and replaced with 50 µL of cell culture medium. Each sample was placed into a 96-well plate. After the last timepoint, the membrane with cells was removed and prepared for imaging as described in section 5.3.3.1. Confocal imaging was performed as described in (Section 4.2.2). At the end of the experiment the fluorescence of each sample in the 96-well plate was determined using an OPTIMA FLUOstar plate reader. The concentration of DiO in each sample was determined using the Beer-Lambert law (Equation 5.4) using ε obtained from a standard curve.

$$A = \varepsilon \times C \times l$$

Equation 5.4 *Beer-Lambert law. Where **A** corresponds to the absorbance detected, **ε** is the extinction coefficient obtained from a standard curve, **C** is the concentration of the sample and **l** the path length (l = 1.)*

The number of moles transported Q_m across the cell barrier was determined as explained in Figure 5.5 and was reported as transport efficiency relative to the initial moles added to the system ($n°_{total}$) (Equation 5.5).

$$Transport\ effciency = \frac{Q_m}{n^{\circ}_{Total}} \times 100$$

Equation 5.5 *Transport efficiency across a cellular barrier. Q_m represents the moles transported across the cell barrier and $n°_{total}$ the moles of particles added to the apical chamber at t_0.*

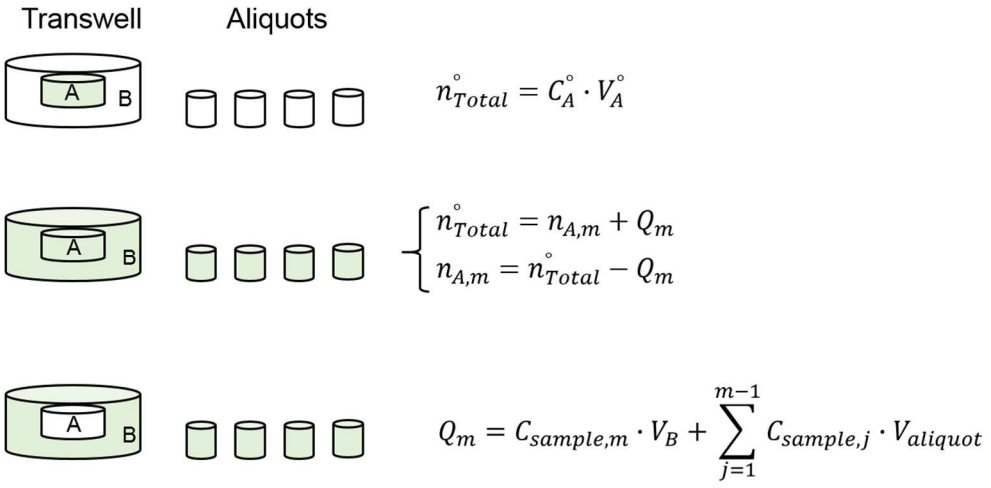

Figure 5.5 *Calculation of the moles transported across cell barriers. **Q_m** represents the moles transported from the apical (**A**) to the basolateral chamber (**B**) at all times (**m**). **$n°_{total}$** is the moles of particles added to the apical chamber at t_0 (m = 0).*

All experiments were performed three times in separate occasions. For a single experiment, three Transwell® systems were sampled at each time point.

5.2.3.2 Determination of the permeability coefficient of DiO across cell barriers.

The apparent permeability coefficient of DiO across cell barriers and blank PE membrane inserts (P_{app}) was calculated as described by Cartwright *et al*[9] (Equation 5.6).

$$P_{app} = \frac{\Delta Q/\Delta t}{A \cdot C_0}$$

Equation 5.6 *Apparent permeability coefficient of the Transwell®-cell barrier system* $\boldsymbol{P_{app}}$ *(See also Figure 5.5).*

In the cell barrier model, the particles need to cross two permeable membranes (the cellular barrier and the PE membrane) set in parallel, the permeability coefficient of the system is calculated as described in Equation 5.7.

$$\frac{1}{P_e} = \frac{1}{P_{app}} - \frac{1}{P_{app,blank}}$$

Equation 5.7 *Permeability coefficient of the cell barrier.* $\boldsymbol{P_{app}}$ *is the apparent permeability coefficient of the Transwell®-cell barrier system and* $\boldsymbol{P_{app,\ blank}}$ *is the permeability of the PE membrane (See also Equation 5.6).*

All experiments were performed three times on separate occasions. For a single experiment, three Transwell® systems were sampled at each time point.

5.3 Cell polarisation model to study transport of P407-DiO micelles in epithelial barriers

5.3.1 Trans-epithelial electrical resistance of MDCK cell barrier

TEER measurements were performed on MDCK cells grown on Transwell® inserts to assess barrier formation and integrity. Electrical resistance of the cell monolayer was measured using a set of EndOhm fixed electrodes. The measured values were compared to the ones obtained using removable STX-2/chopstick electrodes. (Figure 5.6). The resistance values, using an EndOhm system, start to equilibrate around a value of 1000 $\Omega.cm^2$ after day 4 post-seeding (Figure 5.6 A) indicating the development of a fully developed high resistance epithelial barrier at this stage. The chopstick electrodes measurements also revealed a plateau of resistance after day 4 at around 2000 $\Omega.cm^2$ (Figure 5.6 B). The variability of the data obtained using removable electrodes was less than that observed with the fixed electrodes despite the expected variation associated with the position of the removable electrodes for each measurement. This indicates the suitability of the removable electrodes as a method to measure electrical resistance of MDCK cell layers. The TEER values obtained are comparable to previously reported data for MDCK strain I cells[1,24].

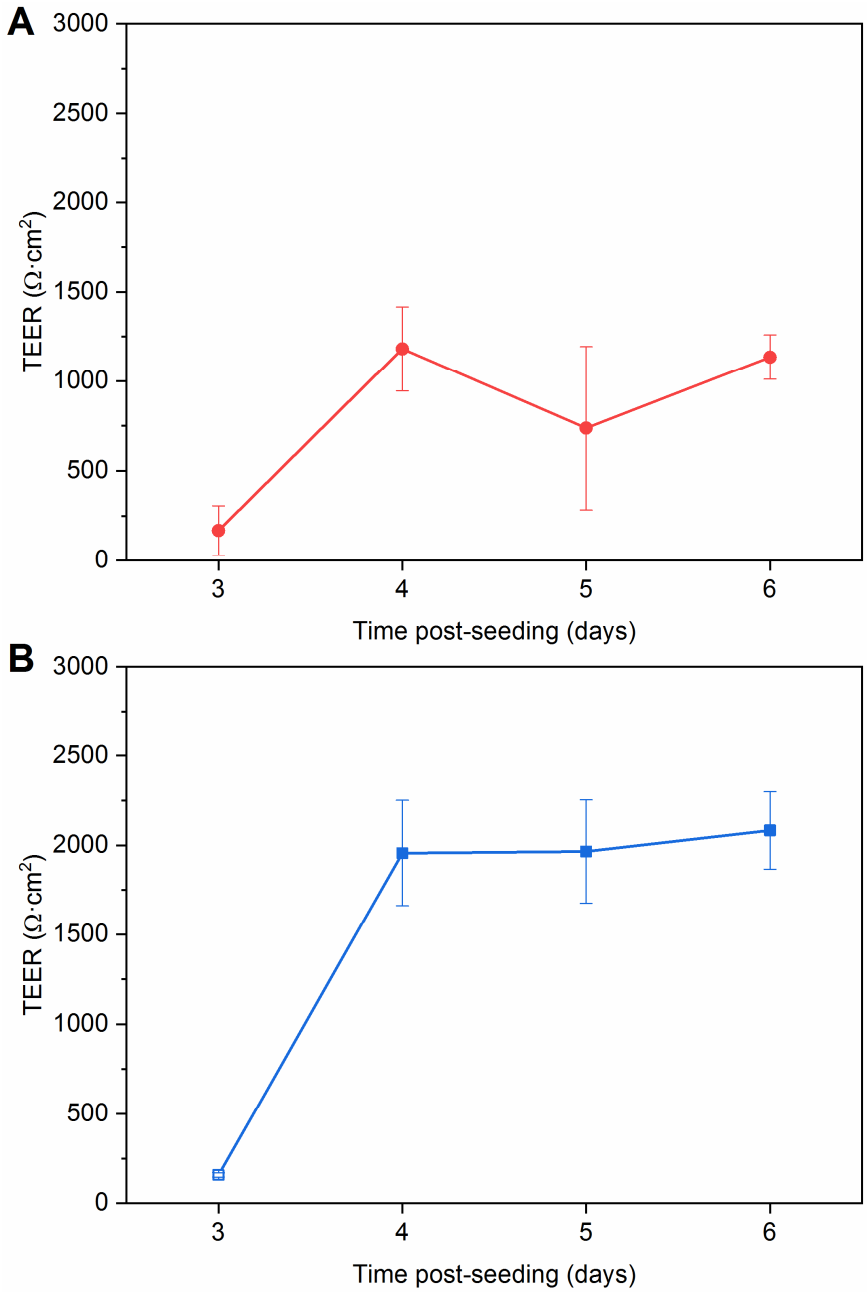

Figure 5.6 *Trans-epithelial electrical resistance (TEER) of MDCK cells measured after day 3 post-seeding. Cells were seeded on 12 mm polyester Transwell® inserts. TEER values were measured using* ***(A)*** *EndOhm fixed electrodes and* ***(B)*** *Chopsticks removable electrodes. All values are presented as means ± SD (N=18).*

5.3.2 Trans-epithelial electrical resistance of BeWo b30 cell barrier

Barrier formation and integrity of BeWo b30 cells grown on Transwell® inserts were assessed using TEER measurements. Fixed and removable electrodes (section 5.2.1.2) were used to measure electrical resistance of the cell monolayer (Figure 5.4). The values of electrical resistance obtained using fixed electrodes begins to plateau after day 4 post seeding (Figure 5.7 A) indicating the integrity and development of the barrier after this stage. The TEER values obtained after this time are in the range of 70 $\Omega.cm^2$ with a low variation in the measured data. Using the removable electrodes, the TEER values plateau after day 5 post-seeding with values between 65 and 80 $\Omega.cm^2$ (Figure 5.7 B). Although TEER values measured by both methods are within the range of those reported in literature[9,25,26], the data measured using removable electrodes presented a much higher variation than those obtained using fixed electrodes suggesting the suitability of the fixed electrodes for TEER measurements of BeWo b30 cell layers.

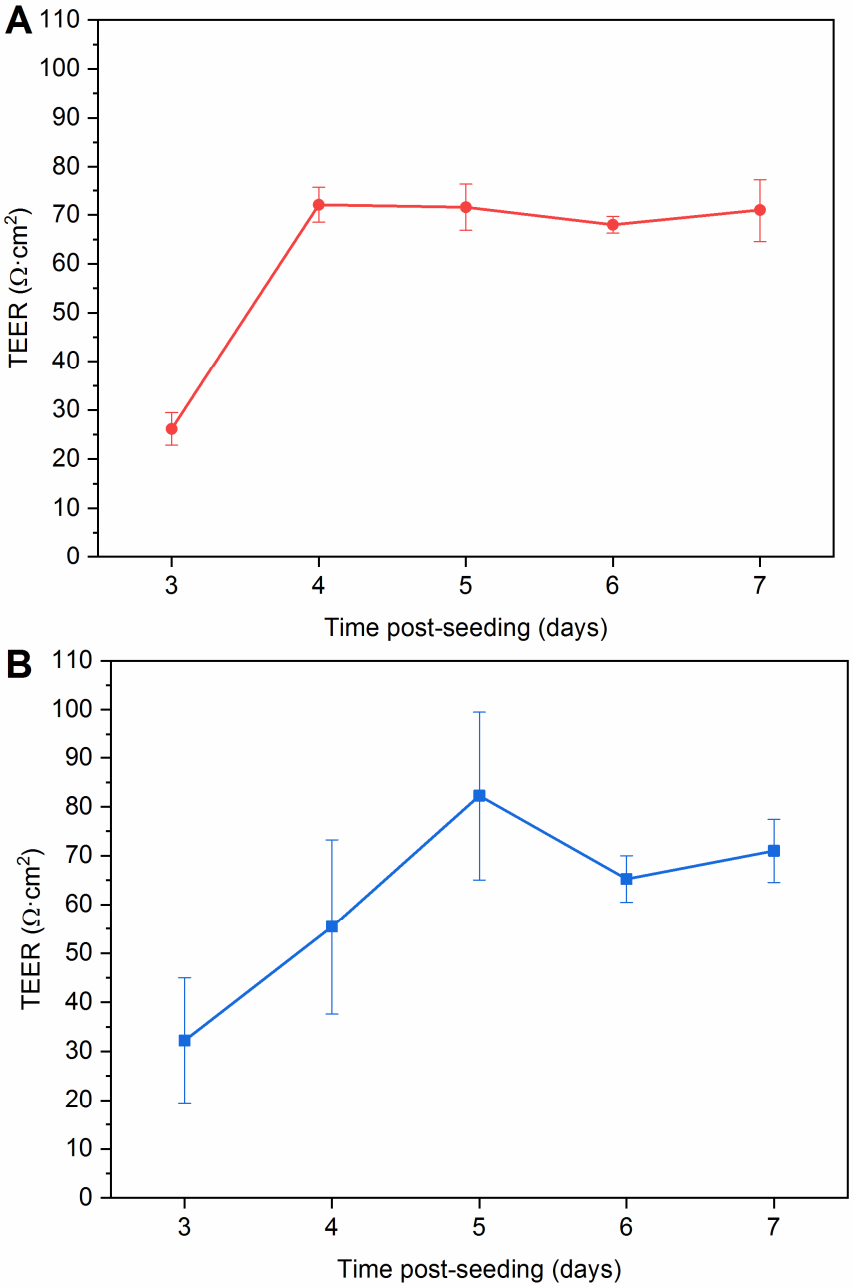

Figure 5.7 *Trans-epithelial electrical resistance (TEER) of BeWo b30 cells measured after day 3 post-seeding. Cells were seeded on 12 mm polyester Transwell® inserts. TEER values were measured using* ***(A)*** *EndOhm fixed electrodes and* ***(B)*** *Chopsticks removable electrodes. All values are presented as means ± SD (N=18).*

5.3.3 Visual characterisation of the kidney epithelial barrier model

The visual assessment of the integrity and formation of MDCK cell monolayers on Transwell® inserts was achieved using light and electron microscopy techniques.

5.3.3.1 Visualisation of MDCK epithelial cell barriers using confocal laser scanning microscopy (CLSM)

Since microvilli (MV) formation is a key feature of fully developed epithelia, a visual analysis was performed using confocal microscopy with enhanced resolution (HyVolution 2) following F-actin labelling of MDCK cells grown on Transwell® inserts for 6 days (Figure 5.8). A continuous single layer of cells grown on the PE membrane was observed. Additionally, a significant visual difference between the apical and the basal side of the cell monolayer is seen with dense hair-like membrane projections covering the surface of the apical side. These microvillus (MV) protrusions are approximatively 2 μm long and are not visible on the basal side of the cell monolayer. The presence of MV was apparent over all the cell monolayer implying the morphological differentiation of the MDCK cell monolayer to a well differentiated, polarised epithelial layer on day 6 post-seeding. Furthermore, intense F-actin labelling between cells (Fig. 1.8) is consistent with the formation of intercellular junctions (IJ) after 6 days growth, as previously demonstrated by TEER measurements (section 5.3.1). Together, these observations of actin distribution and TEER are consistent with

formation of tight junctions between epithelial cells, although further characterisation is needed to specifically localise TJ sites.

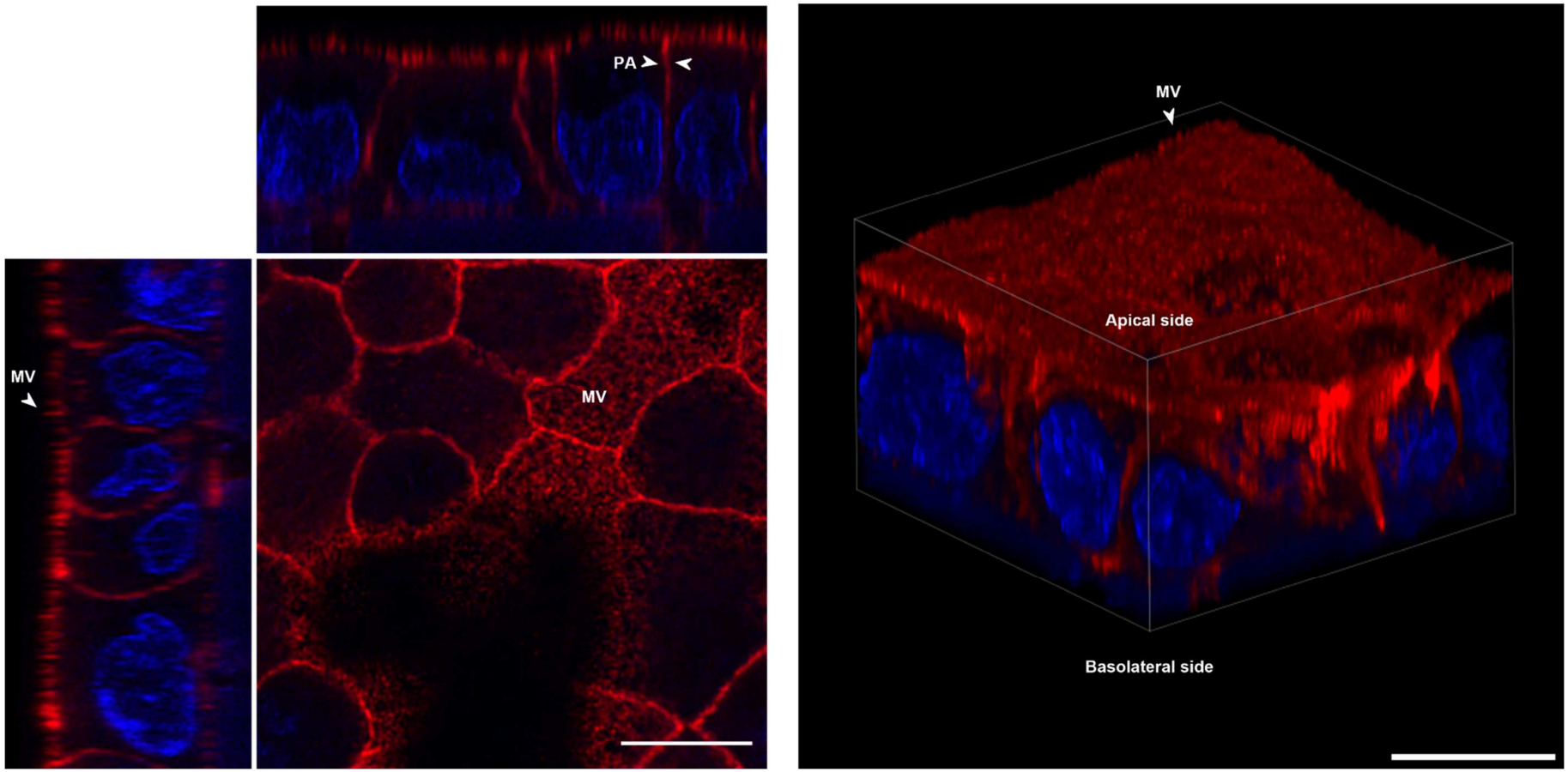

Figure 5.8 *Microvilli (MV) expression on polarised MDCK cells. Enhanced-resolution images were taken on fixed MDCK polarised cells at day 6 post-seeding. F-actin filaments were stained with TRITC-phalloidin (red) and cells' nuclei were counterstained with DAPI (blue). Cross-sectional views (left) and three-dimensional rendering (right) show MV formed on the surface of the apical side of cells and peri-junctional actin (PA) formed between adjacent cells. Scale bar: 10μm. The images shown are representative of those obtained in three separate experiments*

5.3.3.2 Visualisation of MDCK cell barrier using scanning electron microscopy (SEM)

To confirm the presence of MV on the MDCK developed cellular barrier model, SEM imaging was performed on the surface of the apical side of cells grown on Transwell® inserts and was compared to confluent cells grown on coverslips (Figure 5.9). The micrographs of cells grown on coverslips (Figure 5.9 A, B, and B1) show the presence of short and relatively sparse microvillus-like protrusions on the surface of all cells. In contrast, the micrographs of Transwell-grown cells (Figure 5.9 C, D, and D1) show a denser distribution of longer and frequently branched MV on the cell. This morphological difference confirms the cell barrier differentiation and supports the results found with CLSM. Furthermore, the reduced expression of MV seen on cells grown on coverslips highlights the importance of growth on a permeable support for full epithelial differentiation.

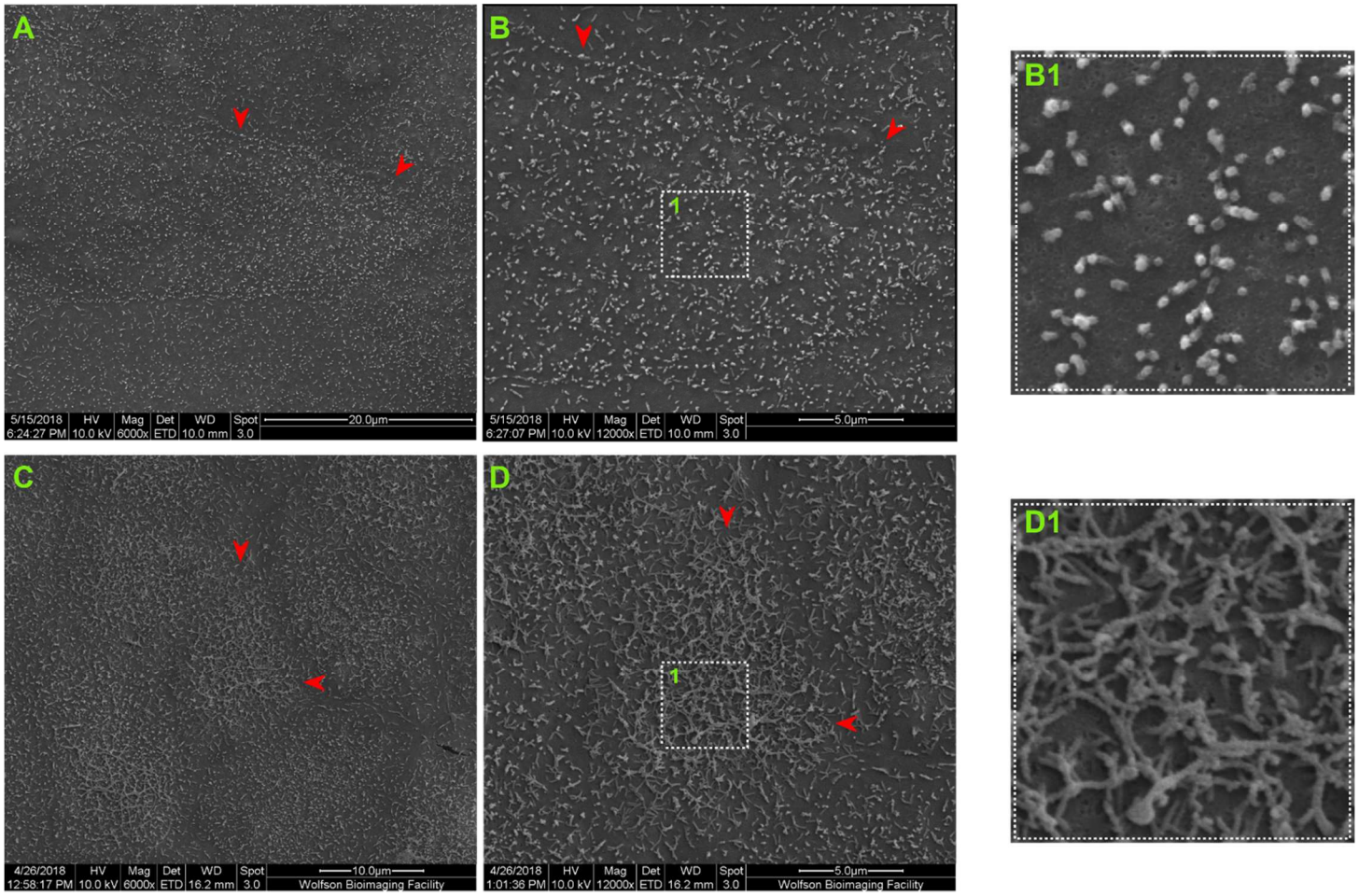

Figure 5.9 *SEM micrographs of the brush border on the apical side of* ***(A&B)*** *polarised MDCK cells and* ***(C&D)*** *non-polarised cells.* ***(B1 & D1)*** *Magnifications of selected regions, of* ***(B)*** *and* ***(D)*** *respectively, indicated by white dashed boxes. The images shown are representative of those obtained in two separate experiments*

5.3.3.3 Visualisation of MDCK epithelial cell barriers using transmission electron microscopy (TEM)

Further characterisation of the key features of a fully developed cellular barrier, such as MV and TJ formation, was achieved by imaging polarised MDCK cells by TEM. For this, cross-sections of cells grown on PE membrane filters were imaged on day 6 post-seeding (Figure 5.10 A). The micrographs confirm the presence of brush borders seen by CLSM and SEM only on the apical sides of the cell barrier (Figure 5.10 B and C). Additionally, the length of the MV observed is between 1 and 2 μm in accordance to the length seen in CLSM and SEM (sections 5.3.3.1 and 5.3.3.2). Moreover, the structure of the MV appears to be branched (Figure 5.10 C) as seen previously in SEM micrographs (section 5.3.3.2). The paracellular space between cells appears to be sealed by the presence of tight junctions observed as electron dense regions in the between the plasma membrane of two adjacent cells (Figure 5.10 D, E, and F). The indication of TJ detected by TEM in MDCK cells complemented the observations previously seen with CLSM (section 5.3.3.1). Two key features, MV and TJ formation, were observed in MDCK cells confirming the development of a fully differentiated cell barrier model suitable to test particle transport.

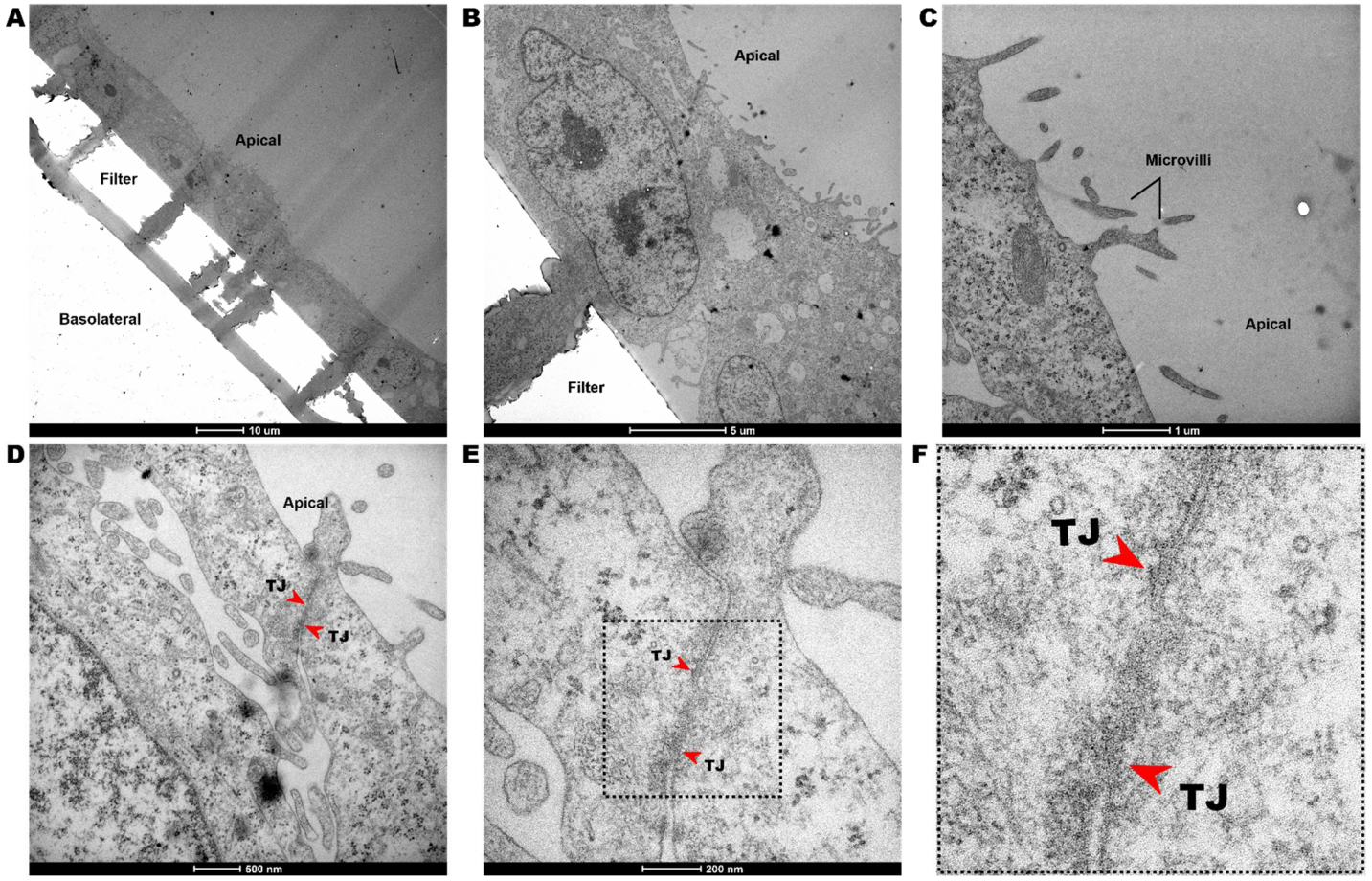

Figure 5.10 *TEM micrographs showing key features of the developed MDCK cell barrier.* ***(A&B)*** *Cross-sections of MDCK cell monolayer grown on Transwell® polyester membrane filters with 3 μm pores.* ***(C)*** *Microvilli expression in the apical side of polarised cells.* ***(D, E &F)*** *Indication of tight junctions (TJ) sealing the space between adjacent cells of the barrier (region indicated between red arrows). The images shown are representatives of those obtained in two separate experiments*

5.3.4 Visual characterisation of the placental barrier model

The integrity and formation of BeWo b30 cell barrier was assessed using light and electron microscopy techniques.

5.3.4.1 Visualisation of BeWo b30 cell barrier using confocal laser scanning microscopy (CLSM)

Enhanced resolution confocal microscopy (HyVolution 2) was used to image BeWo b30 cells grown on Transwell® inserts for 6 days. This imaging technique, alongside a fluorescent stain of F-actin filaments, was used to assess the MV expression which corresponds to a key feature of fully developed epithelia (Figure 5.11). After day 6 post-seeding, a continuous monolayer of cells is seen on the PE membrane. The apical side of the cells appear to be different than the basal side presenting membrane projections covering the surface of the cells. This brush border covering only the apical side of the cells is composed of MV with sizes between 2 and 5 μm long. The presence of MV was consistently observed on BeWo b30 cell monolayer implying that the cellular model developed after 6 days of cell culture on Transwell® membranes is morphologically differentiated to a cell barrier model. The actin filament stain is also consistent with the presence of IJs between adjacent cells as previously demonstrated by increasing TEER after 4 days growth on Transwell supports (section 5.3.2).

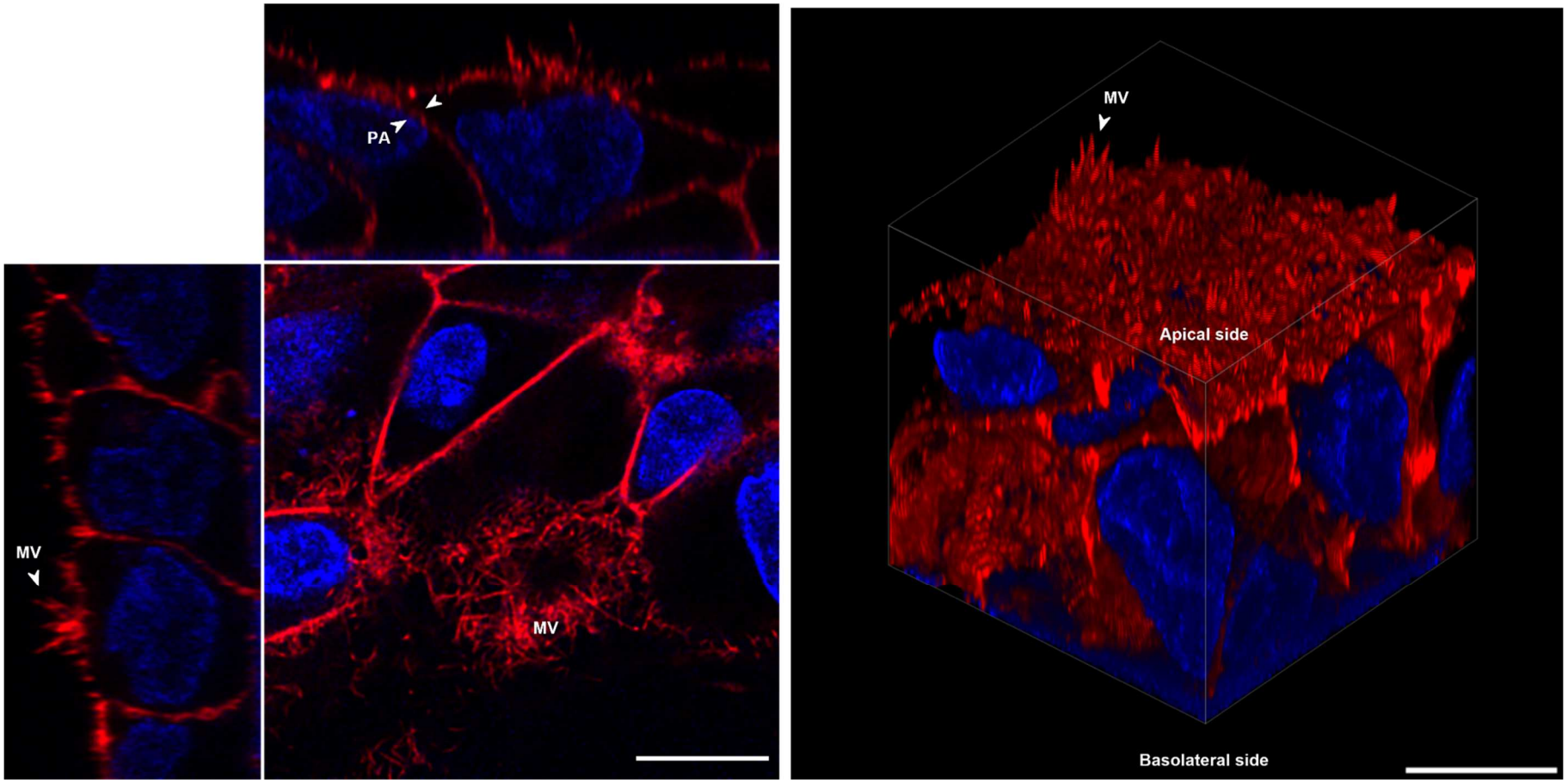

Figure 5.11 *Microvilli (MV) expression on polarised BeWo b30 cells. Enhanced resolution images were taken on fixed BeWo b30 polarised cells at day 6 post-seeding. F-actin filaments were stained with TRITC-phalloidin (red) and cells' nuclei were counterstained with DAPI (blue). Cross-sectional views (left) and three-dimensional rendering (right) show MV formed on the surface of the apical side of cells and peri-junctional actin (PA) formed between adjacent cells. The images shown are representative of those obtained in three separate experiments. Scale bar: 10μm.*

5.3.4.2 Visualisation of BeWo b30 cell barrier using scanning electron microscopy (SEM)

To verify the expression of the MV on the developed placental barrier model, SEM imaging was carried out on the surface of cells grown on Transwell® inserts. The brush border obtained was compared to the one seen on the surface of cells grown on coverslips (Figure 5.12). Cells grown on coverslips (Figure 5.12 A, B, B1, and B2) present sparse MV of approximatively 1μm long. In contrast, cells grown on PE membranes present MV with sizes between 3 and 5 μm. Additionally, the MV seen in polarised cells show several branch points within an individual MV leading to a denser distribution on the cells surface. The morphological difference between polarised and non-polarised cells confirms barrier differentiation and confirms the features seen using CLSM. As seen with MDCK cells (section 5.3.3.2), the poor development of MV on coverslip-grown cells highlights the importance of growth on permeable supports for development of a polarised placental barrier model.

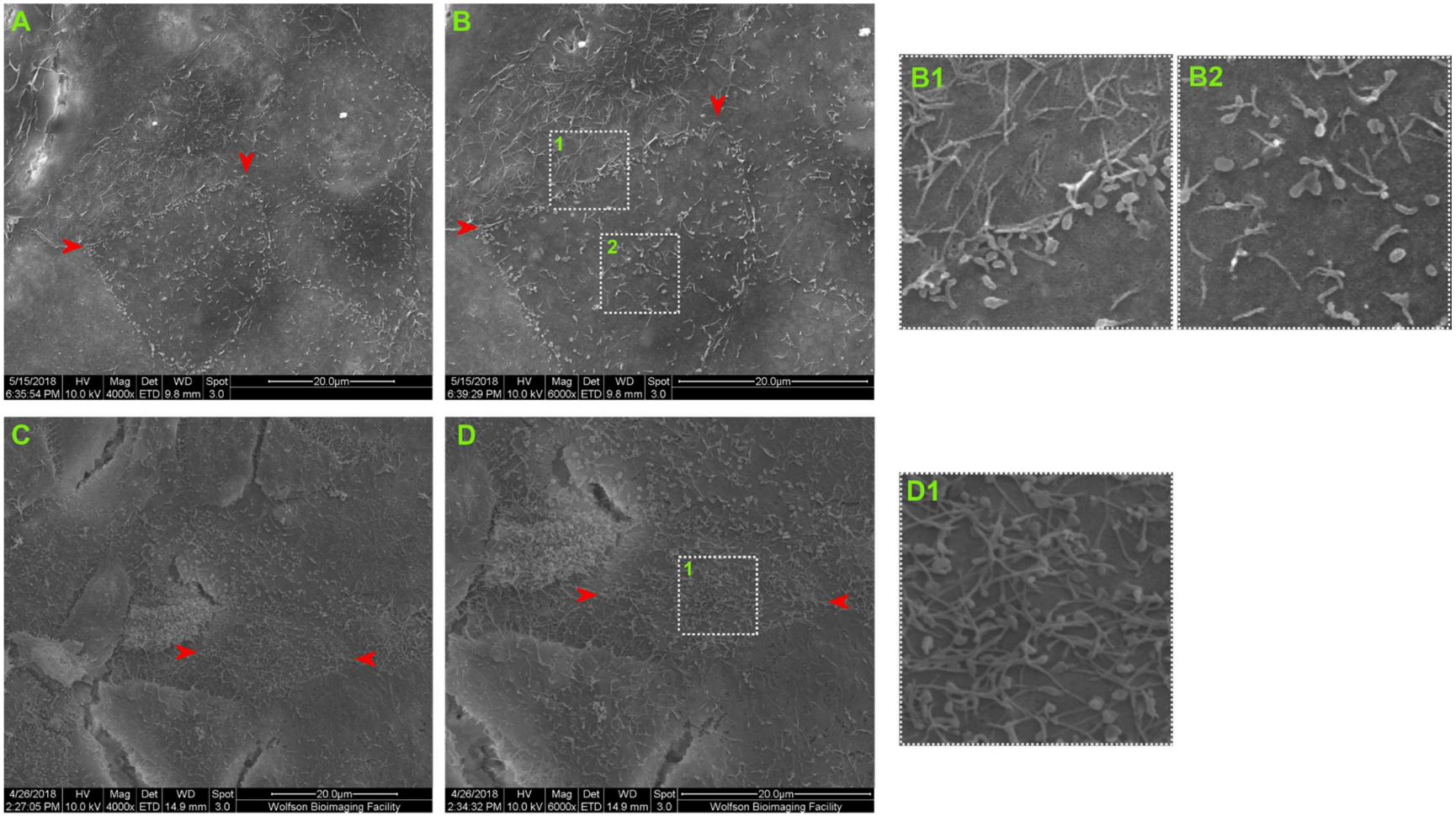

Figure 5.12 *SEM micrographs of the brush border on the apical side of* ***(A&B)*** *polarised BeWo b30 cells and* ***(C&D)*** *non-polarised cells.* ***(B1, B2 & D1)*** *Magnifications of selected regions of* ***(B)*** *and* ***(D)*** *indicated by white dashed boxes. The images shown are representatives of those obtained in two separate experiments*

5.3.4.3 Visualisation of BeWo b30 cell barrier using transmission electron microscopy (TEM)

Alongside MV development, the expression of TJ is a key feature of epithelial differentiation and development of a cellular barrier. To characterise both features, TEM was made on cross-sections of polarised BeWo b30 cells on day 6 post-seeding (Figure 5.13 A). The presence of MV on the apical side of cells seen previously by CLSM and SEM (Sections 5.3.4.1 and 5.3.4.2) is confirmed (Figure 5.13 B). Additionally, the length of MV observed by this method varies between 1.5 and 3 μm supporting the data seen previously. Additionally, TJ are observed in TEM micrographs by electron dense regions seen between the plasma membrane of two adjacent cells (Figure 5.13 C and D). Furthermore, the presence of desmosomes in the cell-cell junction (Figure 5.13 E) confirms the presence of a developed epithelial cell junctional complex.

The features observed by TEM support the observations seen previously by other microscopy methods and TEER measurements and confirms the development and integrity of the cellular barrier model suitable for studying and understanding particle transport in the placenta.

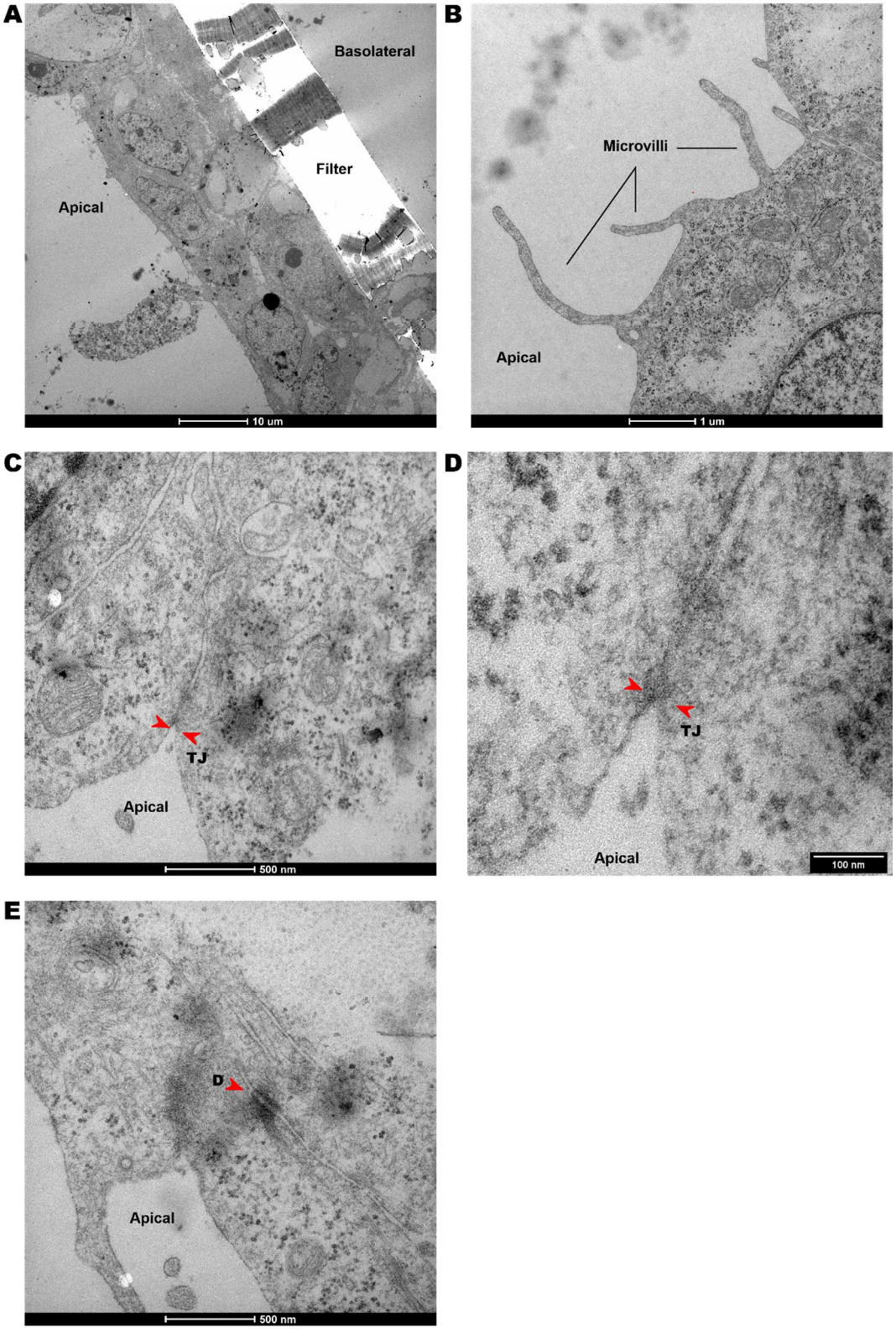

Figure 5.13 *TEM micrographs showing key features of the developed placental cell barrier.* ***(A)*** *Cross-section of BeWo b30 monolayers grown on Transwell® polyester membrane filters with 3 μm pores.* ***(B)*** *Microvilli expression on the apical side of polarised cells.* ***(D & C)*** *Expression of tight junctions (TJ) sealing the space between adjacent cells of the barrier.* ***(E)*** *Evidence of the presence of desmosomes (D) as part of the intercellular junctional complex. The images shown are representative of those obtained in two separate experiments*

5.3.5 Transport of P407-DiO micelles across the kidney barrier model

Transport efficiency of P407-DiO micelles across the developed MDCK barrier was assessed quantifying the amount of DiO transported from the apical to the basolateral chamber of the cell barrier model. For this, the fluorescence of the cell culture medium of the basal chamber was monitored over 25 hours (Figure 5.14). The transport efficiency across the PE membrane in the absence of cells over time shows a non-linear increase with up to 60 % of the initial concentration of DiO effectively transported to the basolateral chamber after 25 hours. The transport across the cell barrier model on PE membranes shows a similar increase pattern with a lower transport efficiency of 5 % after 25 hours. This substantial difference in transport seen after 25 hours highlights the effect of the presence of the cell barrier reducing the transfer of DiO across MDCK cell barrier to the basal chamber. The transport efficiency of DiO shown in Figure 5.14 enabled the permeability of MDCK cells to be derived (Table 5.1). The permeability coefficient was calculated at 5 hours and 25 hours since the transport of DiO across the barrier seems to increase more rapidly during the first 5 hours than for later timepoints. Although the calculated permeability coefficient (P_e) was higher at 5 hours compared with 25 hours, the difference was not statistically significant so the suggested change in transport kinetics over time remains unconfirmed. It is important to note the expected saturation value is above 50% and is expected at 75%. This is due to the volume ratio between apical and basal chambers which are in a ration of 1:3.

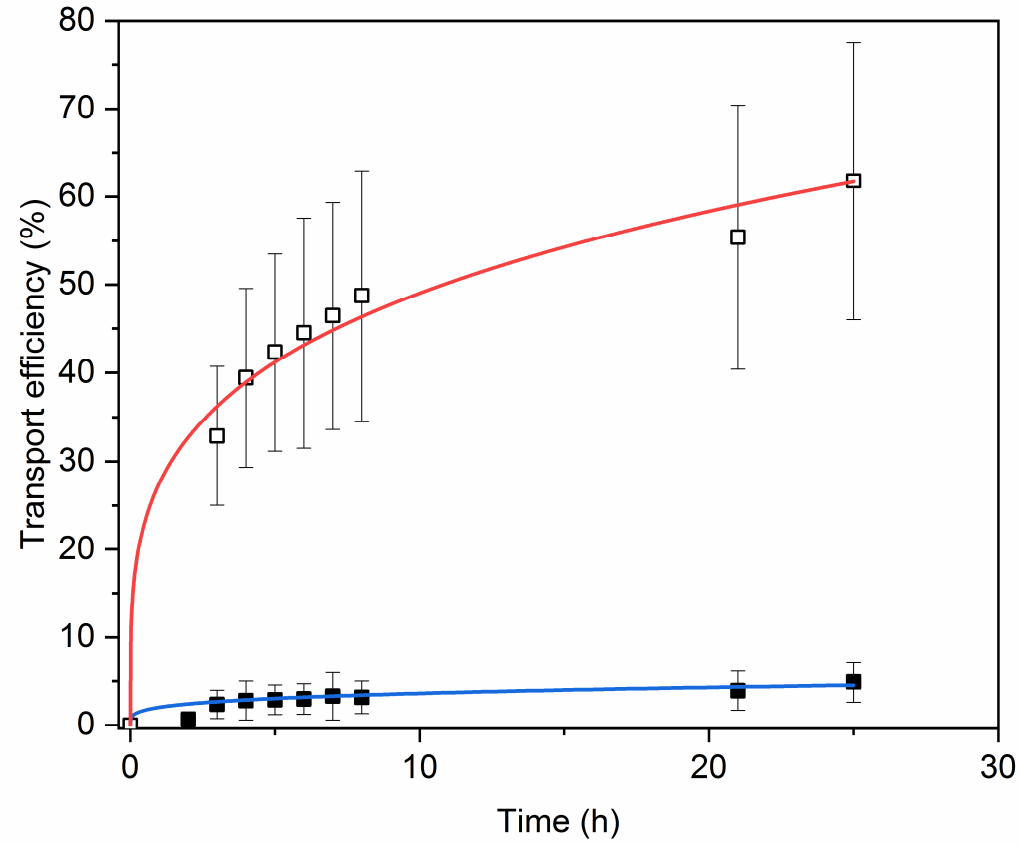

Figure 5.14 *Transport of DiO across developed MDCK cell barriers grown on Transwell® inserts. The transport of particles from the apical to the basolateral chamber was monitored over 25 hours. Three Transwell® systems were sampled at each time point for a single experiment. The initial concentration of DiO added to the apical chamber (n_0) was 1.05 µM. The transport efficiency was calculated relative to n_0. The transported data is shown in presence (blue line and filled squares) and absence of cells (red line and empty squares. All the values are presented as means ± SD (n=3).*

Table 5.1 *Permeability coefficients (P_e) across developed MDCK cell barriers grown on Transwell® inserts. Measurements were made at t = 0h and t = 25h. The significance difference between means was evaluated using an unpaired t-test showing no statistical significance. All the values are presented as means ± SD (n=3).*

Time (h)	P_e (cm/s)
5	$3.2 \times 10^{-6} \pm 2.3 \times 10^{-6}$
25	$1.4 \times 10^{-6} \pm 9.1 \times 10^{-7}$

5.3.6 Confocal imaging of MDCK cellular barrier model exposed to P407-DiO micelles

The MDCK barrier used to determine P407-DiO micelles transport was imaged at the end of the experiment (Figure 5.15). The cell barrier morphology remains unaffected after 25 hours of exposure to micelles indicating the non-toxicity of the micelles as well as supporting the results seen in Chapter 4 The punctate green fluorescence seen previously on coverslip-grown MDCK cell monolayers was also present in polarised cells, however, the number of punctate structures appear to be lower than previously seen in non-polarised cells (Chapter 4). This difference indicates the effect of monolayer polarisation on the uptake of P407-DiO micelles after 25 hours. Furthermore, the presence of green fluorescence confirms the dye transport results seen in section 5.3.5 where only 5% of the initially added DiO is transported across the membrane meaning that the remaining DiO is either on the cellular membrane or in the apical chamber of the Transwell® system.

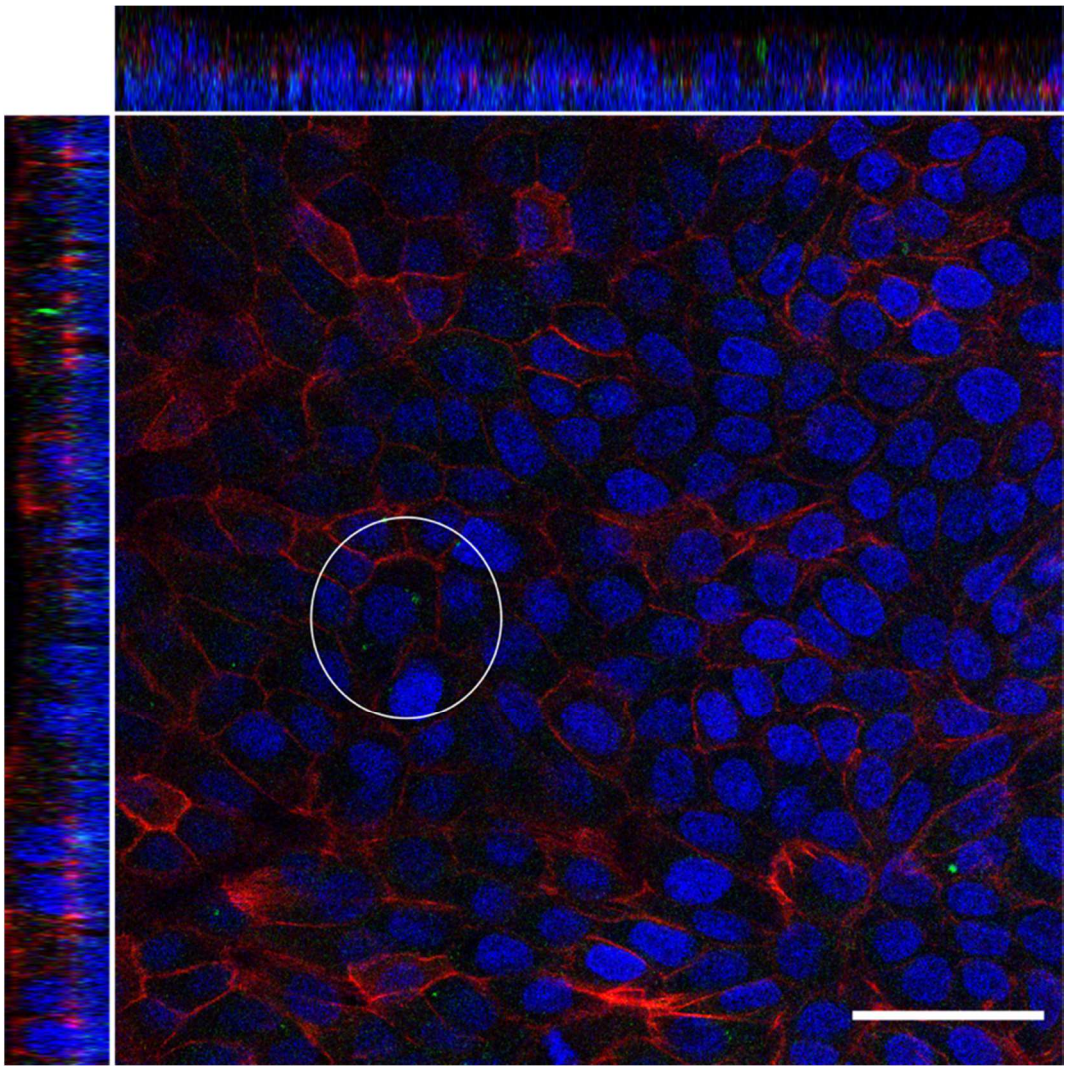

Figure 5.15 *Retention of DiO by a developed MDCK cell barrier after a 25-hours transport study (see also Figure 5.14 and Table 5.1). The areas signalled by a circle shows the accumulation of DiO in specific sites of the cytoplasm. The images shown are representatives of those obtained in three separate experiments. Scale bar: 50μm.*

5.3.7 Transport of P407-DiO micelles across the placental barrier model

The transport efficiency of the developed BeWo b30 cell barrier was determined by monitoring the fluorescence collected from the basolateral chamber of the cell barrier model over 25 hours (Figure 5.16). The transport efficiency measured on a PE membrane without cells shows a logarithmic increase with 60% of the moles of DiO, initially added to the apical chamber, transported after 25 hours. The moles transported across the cellular barrier grown on PE filters shows a significantly lower (~ 3%) transport after 25 hours. This difference in transport efficiency shows the effect of the presence of the cellular barrier on the transport of particles. To determine the specific permeability of the cellular barrier, the P_e was calculated at 5 and 25 hours. Both measurements present similar values showing a constant transport rate of DiO particles over 25 hours. It is important to note the expected saturation value is above 50% and is expected at 75%. This is due to the volume ratio between apical and basal chambers which are in a ration of 1:3.

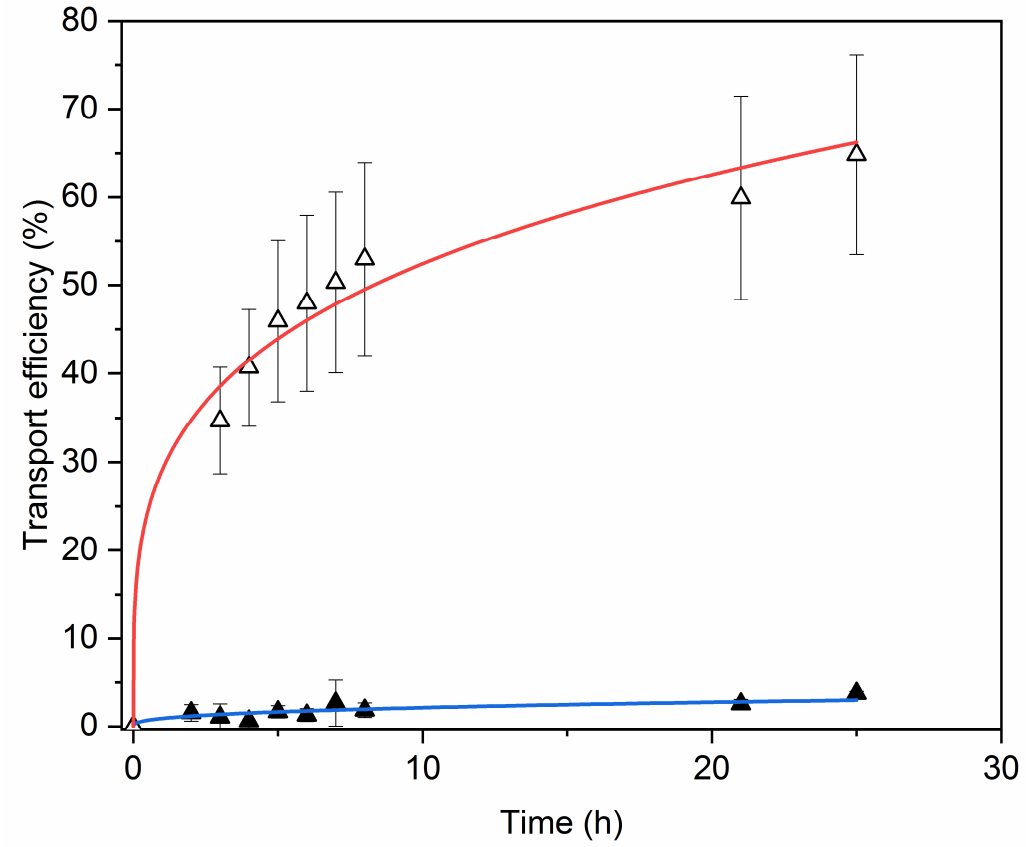

Figure 5.16 *Transport of DiO across developed BeWo b30 cell barriers grown on Transwell® inserts. The transport of particles from the apical to the basolateral chamber was monitored over 25 hours. Three Transwell® systems were sampled at each time point for a single experiment. The initial concentration of DiO added to the apical chamber (n_0) was 1.05 µM. The transport efficiency was calculated relative to n_0. The transported data is shown in presence (blue line and filled triangles) and absence of cells (red line and empty triangles. All the values are presented as means ± SD (n=3).*

Table 5.2 *Permeability coefficients (P_e) across developed BeWo b30 cell barriers grown on Transwell® inserts. Measurements were made at t = 0h and t = 25h. The significance difference between means was evaluated using an unpaired t-test showing no statistical significance. All the values are presented as means ± SD (n=3).*

Time (h)	Pe (cm/s)
5	$7.0 \times 10^{-7} \pm 6.5 \times 10^{-7}$
25	$7.9 \times 10^{-7} \pm 4.1 \times 10^{-7}$

5.3.8 Confocal imaging of BeWo b30 cellular barrier model exposed to P407-DiO micelles

After measuring the transport of P407-DiO micelles for 25 hours, the cellular barrier was imaged (Figure 5.17). Over the 25-hours exposure period, the cell barrier remains intact displaying a non-toxic effect of the micelles on polarised cells. This result is comparable to the one seen with non-polarised BeWo b30 cells (Chapter 4). The dye accumulation, for the Transwell® system, displays a punctate pattern similar to that seen in cells grown on coverslips (Chapter 4). The presence of the green puncta in the imaged placental barrier (Figure 5.17) indicate some retention of the dye by the cellular barrier supporting the incomplete transport, from the apical to the basolateral chamber, seen previously (Figure 5.16).

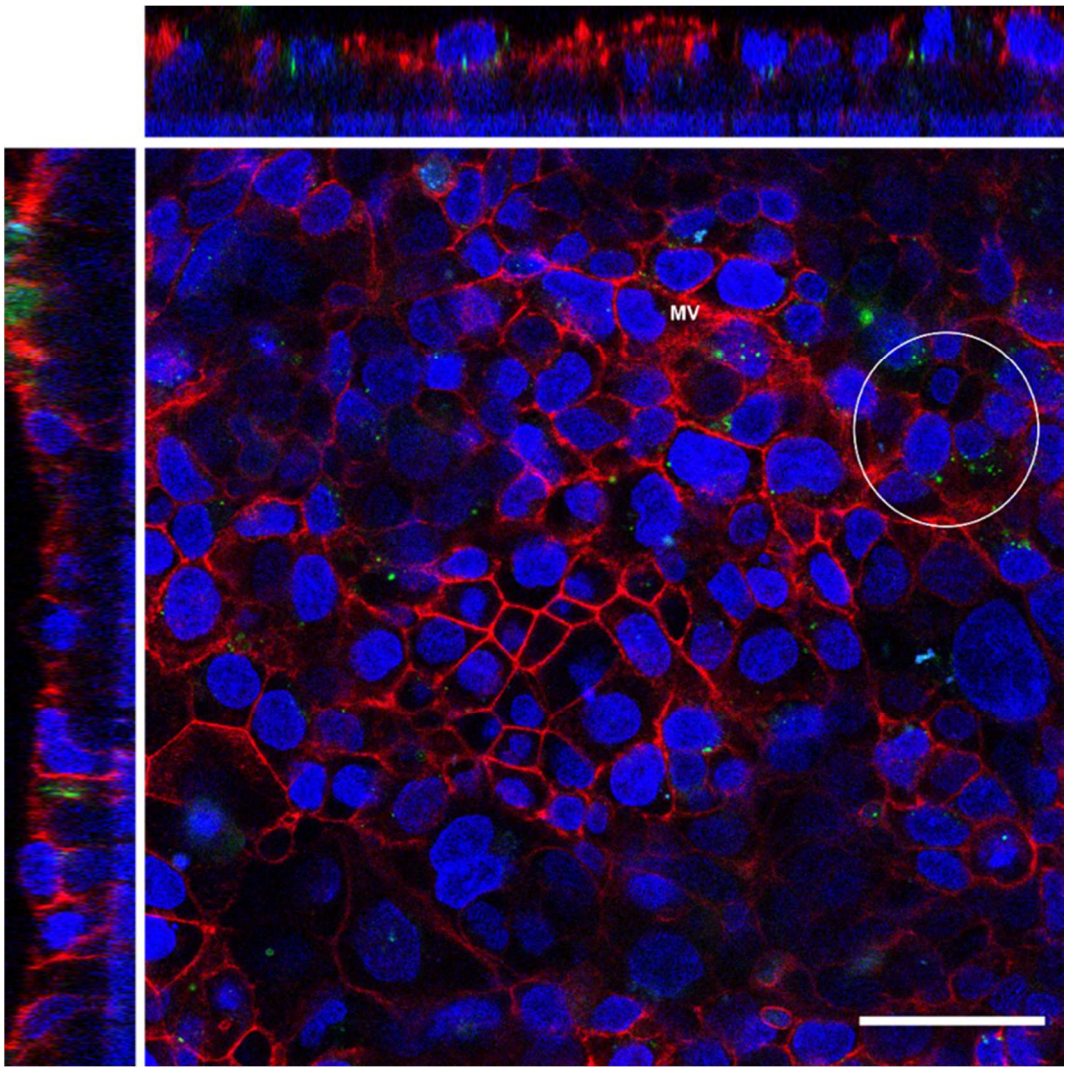

Figure 5.17 *Retention of DiO by a developed BeWo b30 cell barrier after a 25-hours transport study. (see also Figure 5.16 and Table 5.2) The areas signalled by a circle shows the accumulation of DiO in specific sites of the cytoplasm. The images shown are representatives of those obtained in three separate experiments. Scale bar: 50µm.*

5.4 Microfluidics-based cell barrier model

An important variable to consider to obtain an *in vitro* model capable of reproducing physiological functions is the effect of the blood flow on the barrier formation and cell differentiation. This variable can be mimicked by adding a tangential force (or fluid shear stress, FSS) on cell monolayers and is usually made using microfluidics techniques. Different variables were tested on BeWo b30 cells grown into a microfluidics device to optimise a relevant cell culture model for understanding the effects of FSS on cell development.

5.4.1 Extra cellular matrix (ECM) optimisation

Optimisation of the appropriate ECM for BeWo b30 cells is essential to ensure adhesion of the cells to the microfluidics channel before medium perfusion. This optimisation was carried out in two stages consisting in finding the most appropriate ECM coating followed by concentration optimisation. The first stage of optimisation consisted of testing different components usually found in ECM to coat the channels of the biochip. The immediate adhesion of the cells to the biochip as well as after 1 hour of incubation was monitored (Table 5.3). BeWo b30 cells show no attachment to the channel when seeded in medium without ECM coating even after 1-hour incubation. Coating the channel with collagen and poly-L-lysine does not improve the adherence of the cells after 1-hour incubation even if the cells seem to attach to the channel coated with poly-L-lysine just after seeding. The channel coated with fibronectin allow the cells to attach when

initially added to the biochip and improves the cell attachment after 1-hour incubation. Similarly, the cells present an effective attachment to the channel coated with a mixture of collagen and fibronectin. Since the collagen coating results in a poor cell adhesion, the attachment of the cells to the mixed-coated channel can be attributed to the presence of fibronectin. This indicates that, of those tested, the optimal coating to ensure cell attachment for microfluidics experiments is fibronectin.

Different concentrations of fibronectin were tested to find a suitable one to prevent the cells from washing off when perfusing the microfluidics channel with medium (Table 5.4). All concentrations tested show a similar attachment of the cells to the channel after the incubation period and prior to perfusion. However, the only effective concentration ensuring the attachment of the cells after an over-night (O.N.) perfusion is 100 µg/ml. At this concentration the BeWo b30 cells remain adhered to the biochip and an intact monolayer seems to have developed O.N. whereas at lower concentrations the monolayer developed significant gaps due to the stress caused by perfusion.

Table 5.3 *Adhesion of BeWo b30 cells to microfluidic channels coated with different extracellular matrix (ECM) components. The images shown are representative of those obtained in three separate experiments. Scale bar: 50 μm.*

ECM coating	Cell addition	1h incubation
Medium	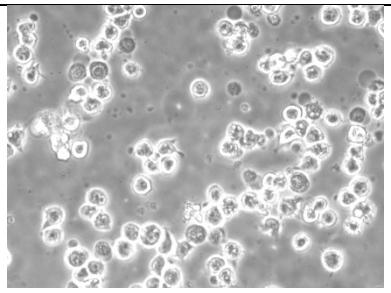	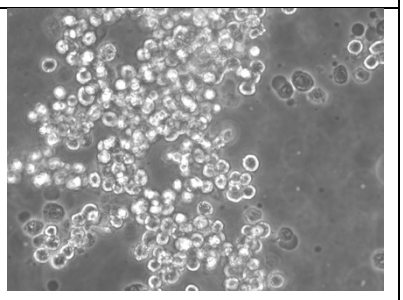
Fibronectin (100 μg/ml)	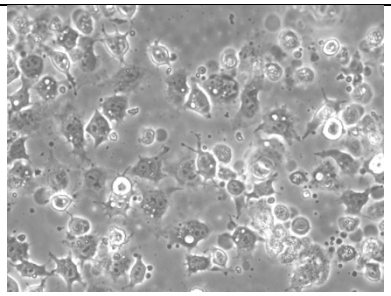	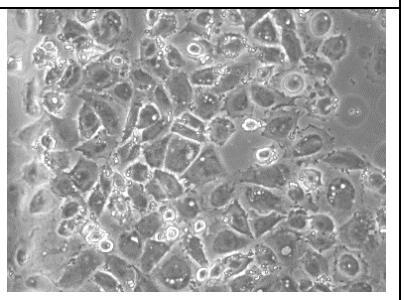
Collagen (100 μg/ml)	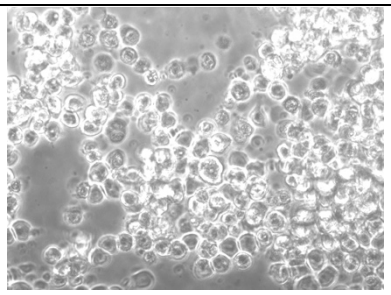	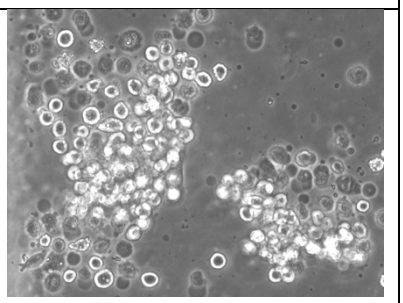
Poly-L-lysine (100 μg/ml)	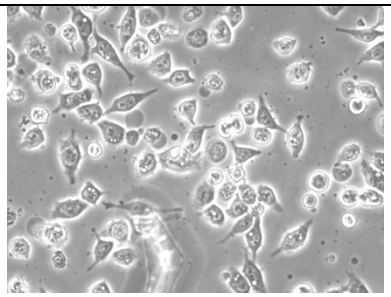	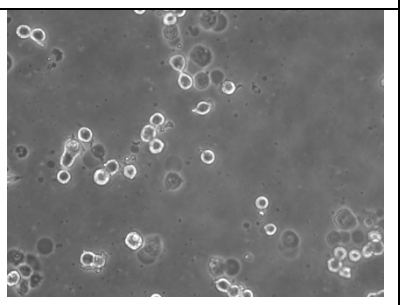
Collagen/Fibronectin 1:1 (100 μg/ml)	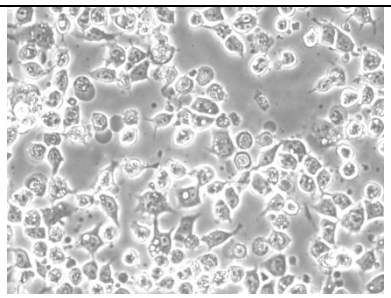	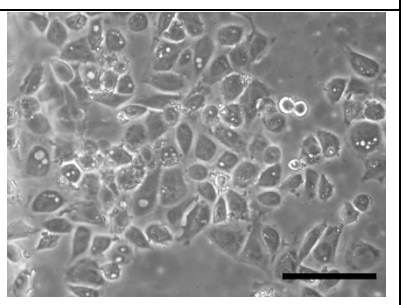

Table 5.4 *Adhesion of BeWo b30 cells to microfluidic channel coated with different concentrations of Fibronectin after an overnight perfusion with a pulse flow (flow rates: 300 µl/min for 2 minutes and 0 µl/min for 20 minutes). The images shown are representative of those obtained in three separate experiments Scale bar: 200 µm.*

ECM coating	Pre-perfusion	After O.N. perfusion
Fibronectin 25 µg/ml	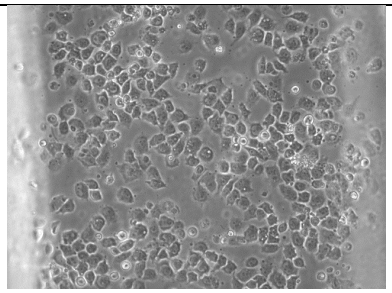	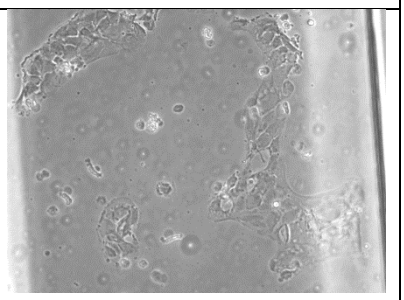
Fibronectin 50 µg/ ml	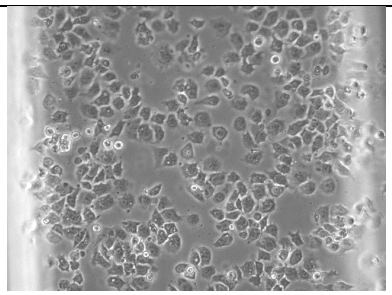	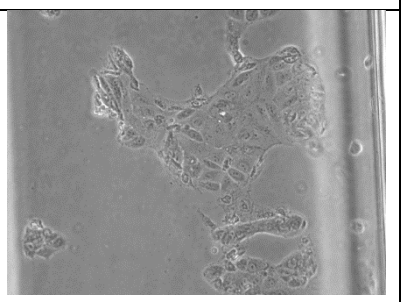
Fibronectin 75 µg/ml	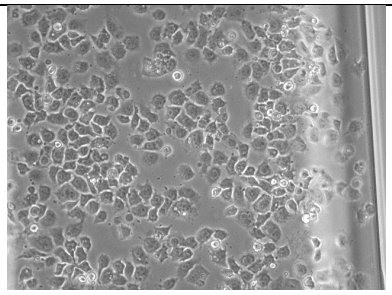	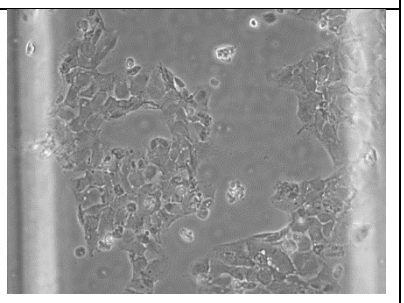
Fibronectin 100 µg/ml	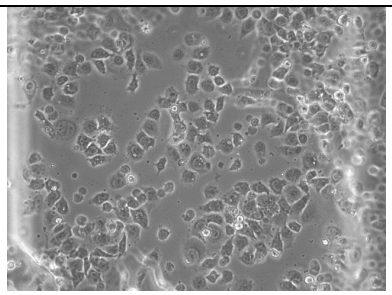	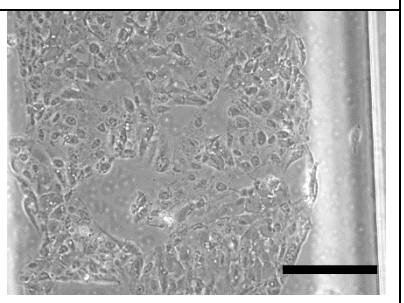

5.4.2 Effect of fluid shear stress (FSS) on cell morphology

To study the effect of the FSS on cells morphology, BeWo b30 cells attached to the biochip were perfused over a 12 hour period and compared to cells grown in the biochip under static conditions (Figure 5.18). Cells incubated for 1 hour in the microfluidics channel previously coated with 100 µg/ ml of fibronectin (Figure 5.18 A) show a good adherence to the channel as seen in section 5.4.1. After 12 hours of incubation, the cells grown under static conditions (Figure 5.18 B) are still attached to the channel. However, the density of the attached cells seems to be reduced compared to after 1-hour incubation. In contrast, the channel perfused with medium for 12 hours shows a higher density of cells adhered to the channel (Figure 5.18 C). The decrease of cell density after the 12-hour incubation under static conditions may be due to the lack of CO_2 exchange between the medium in the biochip and the exterior conditions causing a pH increase non optimal for cell growth. This disruption is not seen for flow conditions because the perfusion of the cell culture medium is made with a recirculation pump ensuring the correct CO_2 exchange with the cell culture environment. Furthermore, cells grown under flow conditions appear to present stronger cell-cell junctions and a more elongated morphology than the ones grown under static conditions. This could be due to the presence of FSS causing the cells to form stronger interactions with their surrounding neighbours encouraging the cell-cell adhesion and spatial reorganisation of the cytoskeleton[27,28].

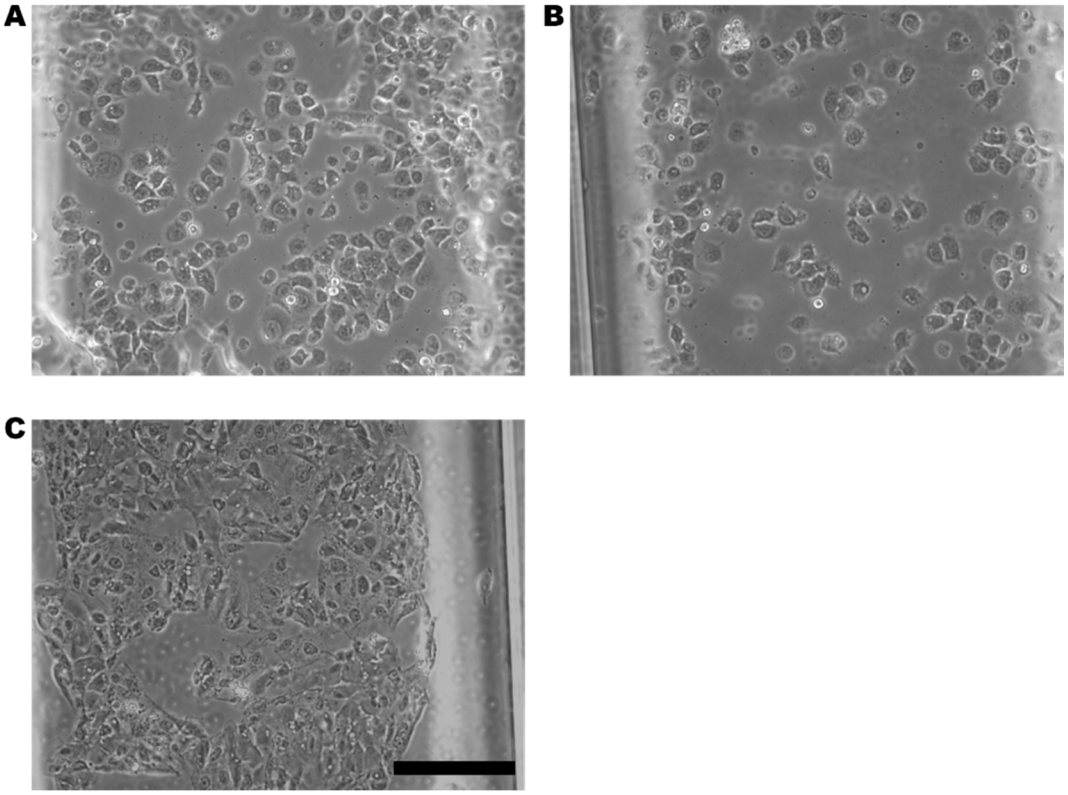

Figure 5.18 *BeWo b30 cells grown into a microfluidics channel coated with fibronectin (100 µg/ml).* ***(A)****Cells pre-perfusion and after 1 hour of static incubation,* ***(B)*** *cells grown without perfusion for 12 hours, and* ***(C)*** *cells grown under a pulse perfusion (flow rates: 300 µl/min for 2 minutes and 0 µl/min for 20 minutes) for 12 hours. The images shown are representative of those obtained in two separate experiments Scale bar 200 µm.*

5.4.3 Uptake of P407-DiO micelles by BeWo b30 under fluid shear stress (FSS)

BeWo b30 cells grown under flow conditions for 16 hours were exposed to P407-DiO micelles over a 40-minute continuous flow of 1.67 µL/min which was monitored using live-cell imaging. At the start of the perfusion, the cells look tightly packed into the channel with no gaps between cells. After 40 minutes of perfusion, some gaps between cells can be seen. The green fluorescence of the DiO particles perfused in the channel make their detection on cells challenging. A 2-minutes post-perfusion wash with medium shows an important retention of the particles by the cell monolayer indicating the uptake of a fraction of the perfused particles by the cells. The uptake seen in 40 minutes of perfusion appears to be greater than the one seen in static experiments (Chapter 4) suggesting that the presence of a FSS may increase the uptake rate of micelles into cells. Furthermore, the presence of gaps between cells seen at the end of the perfusion suggest that exposing BeWo b30 cells to P407-DiO micelles may affect the integrity of cell-cell junctions.

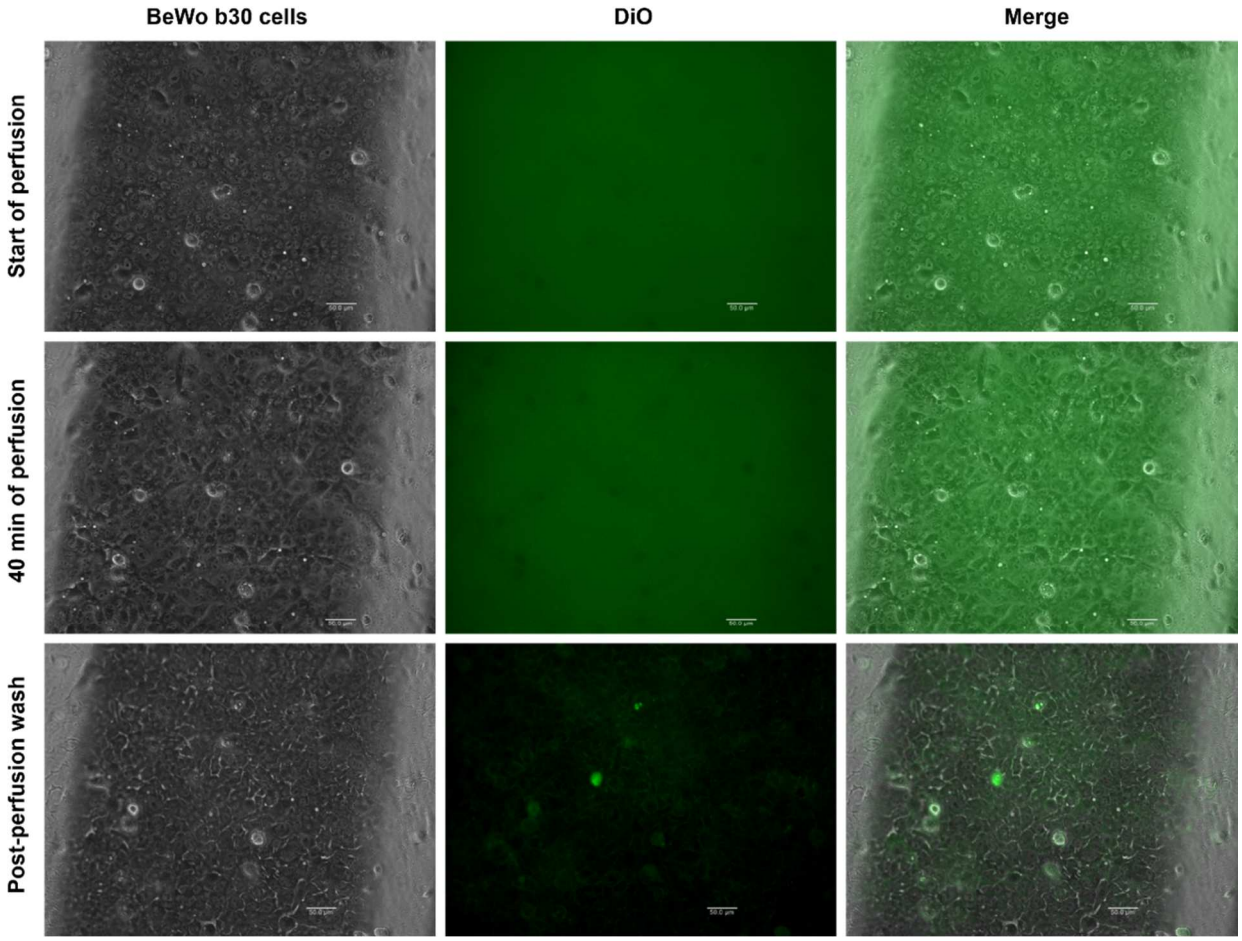

Figure 5.19 *Uptake of DiO by BeWo b30 under flow conditions. A solution of P407-DiO micelles was perfused over 40 minutes (flow rate: 1.67 µl/min) followed by a 2 minutes wash with cell culture medium perfused at the same flow rate. Prior to particle perfusion, cells were grown under a pulse perfusion (flow rates: 300 µl/min for 2 min and 0 µl/min for 20 min) over 16 hours. Scale bar: 50µm. The images shown are representative of those obtained in two separate experiments.*

5.5 Discussion

The aim of this chapter was to develop and characterise cell barrier models for understanding particle transport and interaction in epithelial barriers. This was done by introducing factors mimicking physiological conditions found *in vivo*.

The first model used was based on growing cells in a permeable tissue culture Transwell® system which enables transport of nutrients from one side of the cell monolayer to the other and promotes differentiation of a fully polarised epithelial barrier. Barrier formation was monitored by measuring the electrical resistance (TEER) of BeWo and MDCK cells as an indication of the formation of TJs[4,6,8]. TEER measurements on MDCK and BeWo b30 cells showed the formation of the barrier after day 4 post-seeding. Two techniques for measuring TEER values were used and compared. The STX-2/chopstick electrodes proved to be adequate for measuring TEER values on MDCK whereas the EndOhm fixed electrode was more suitable for BeWo b30 cells. The TEER value measured for developed MDCK cells was 2000 $\Omega.cm^2$ and is consistent with the ones found in literature[1,24]. Similarly, the TEER value found for BeWo b30 cells is consistent with previously reported data[9,25,29] at 70 $\Omega.cm^2$. These results are also consistent with the design of the EndOhm being specific for low TEER endothelia[1].

To further characterise the formed cellular barriers visual assessment; using CLSM, SEM, and TEM was performed for both cell lines at day 6 post-seeding. CLSM showed fully confluent cells grown on PE membranes with a clearly differentiated apical and basal side. This proved the effective

polarisation of MDCK and BeWo b30 cells. In both cases, formation of MV was evident by this method with approximative lengths of 2 and 5 µm (MDCK and BeWo b30 respectively). Indication of strong peri-junctional actin labelling was also seen consistent with the presence of TJs and adherens junctions (Figure 5.2) and confirming barrier integrity indicated by TEER data. This visual examination provides evidence of epithelial barrier development in both cell lines and future studies could expand on this by further characterisation of the TJs using immuno-labelling of TJ proteins such as claudins, occludins, or ZO-1. SEM images supported one of the morphological differences seen with CLSM. Shorter and sparser MV were seen for non-polarised cells than for polarised cells in MDCK and BeWo b30 cells. Furthermore, the MV seen in polarised cells appear to be branched. This from the mechanistical point of view, results in an increase in the surface area of the cellular membrane and may have implications for the interaction of the cells with particles. The microvilli formation in cells proves that the polarisation of cells promotes full epithelial differentiation of cells[30]. Therefore, the obtention of a polarised cell monolayer is essential prior to particle interaction experiments. The last imaging technique used to characterise the formed cellular barriers was TEM. The length of MV seen in CSLM images was confirmed by this method for each cell line. Furthermore, indication of the presence of TJs seen in TEM images support the peri-junctional actin staining seen with CLSM as well as the high TEER values detected. The presence of desmosomes was seen in BeWo b30 cells supporting the formation of a developed epithelial junctional complex (Figure 5.2). All visual analyses made in polarised MDCK and BeWo b30

cells indicated barrier development and integrity suggesting the achievement of a fully developed *in vitro* model mimicking an *in vivo* feature such as nutrient transport[16,31].

The previously developed and characterised *in vitro* model was used to test P407-DiO transport across the placental and kidney epithelial barriers over 25 hours. The transport efficiency of DiO was calculated over time. At the end of the transport experiment MDCK and BeWo cells only 5 and 3% respectively of the initial DiO added on the apical chamber was transported to the basolateral chamber in contrast to the 60% transport efficiency seen on PE membranes without cells during the same time range. This showed that the transport of DiO is restricted by the presence of cells in the Transwell® system as well as showing a relatively low amount of transcytosis across cells. The permeability coefficients after 5 and 25 hours were compared in both cell lines since two uptake kinetics were identified. However no statistically significant difference was seen between these time points for both cell lines. Although the calculated permeability coefficients of BeWo b30 and MDCK barriers appeared different, a t-test revealed no statistical difference between means but there was substantial variability between individual measurements. It would also be interesting to calculate the amount of DiO retained in the cell monolayer. However, the error bars are too large to quantify this significantly. Therefore, a more appropriate way to measure low amounts of fluorescence is needed to accurately determine whether or not the permeabilities of the two cell barrier models are significantly different.

The cellular barriers were examined after transport by CLSM. Morphology of the MDCK and BeWo b30 cells remained unaffected after being exposed to P407-DiO micelles revealing no apparent toxicity of the P407-DiO micelles on polarised cells as seen for non-polarised cells (Chapter 4). Furthermore, after 25 hours, DiO seemed to accumulate into punctate subcellular structures in MDCK as seen in Chapter 4 but at lower quantities. This decrease can be explained by previous works showing that, in MDCK cells, endocytosis specialises into apical and basolateral endocytosis as well as showing that endocytosis is down regulated in polarised MDCK cells[32–37]. This could be supported by the lack of caveolae expression in the apical side of polarised MDCK cells observed in other works[38,39]. In BeWo b30 cells the punctate structures were also present. Though, these structures seemed to be present in similar amounts to non-polarised cells (Chapter 4). Previous works have shown nanoparticle uptake through caveolae-mediated endocytosis in polarised BeWo b30[10] confirming the presence of caveolae coated pits in the apical side of cells. This way, the presence of DiO fluorescence in polarised BeWo cells and the reduced fluorescence in polarised MDCK can be directly related to the presence or absence of caveolae coated pits. This shows that one endocytic pathway for P407-DiO micelles uptake in epithelial cells could be by caveolae-mediated endocytosis. However, some DiO uptake of is still seen in MDCK polarised cells showing that other endocytic pathways are occurring simultaneously and need to be further explored. These observations are only based on a visual examination and in order to be conclusive appropriate quantification of DiO in polarised cells is needed. In order to

determine the effect of the cell polarisation on the DiO uptake by polarised MDCK and BeWo b30 cells, a series of biochemistry assays need to be performed such as the use of chemical inhibitors and antibody staining (see Chapter 4).

The second *in vitro* model used based on applying a fluid tangential force (fluid shear stress, FSS), mimicking the blood flow found in the placental barrier, to promote cell differentiation[16,31]. The optimisation of this model was carried out and an optimal ECM coating for cell adhesion in the biochip was found. Further optimisation experiments revealed the importance of CO_2 exchange for optimal cell growth into biochips. Furthermore, it was found that the presence of FSS caused cells to form stronger interactions with surroundings as well as causing spatial reorganisation of the cells. This was demonstrated by the reduced gaps between cells and their elongating morphology after being perfused with a pulse flow O.N. Initial exposure of the *in vitro* model to P407-DiO micelles showed a faster uptake of DiO in cells than the one seen in cells gown on coverslips (Chapter 4). This could be due to the increased surface area of the cellular membrane by appearance of MV which has previously been shown to be enhanced by FSS[31]. Moreover, operating in flow contributes maintaining a high concentration of particles in the interphase proximity, thus maintaining a high driving force for mass transfer to occur. The appearance of intercellular space after exposure suggests that the presence of flow conditions may have an effect on the integrity of the cell-cell junctional complex. This could be supported by previous works on epithelial

and endothelial cells showing a reorganisation of junction-associated and membrane transport proteins caused by the presence of FSS on cells[16,40].

The results found using the two different *in vitro* models highlight the importance of using more complex models to assess particle transport and uptake across epithelial barrier. Finally, the information obtained with the experiments described in this chapter represent critical first steps to consider towards the development of more complex *in vitro* models, such as placenta and kidney-on-a-chip[41,42], used in translational science.

5.6 References

1. Srinivasan, B. *et al.* TEER Measurement Techniques for In Vitro Barrier Model Systems. *J. Lab. Autom.* **20,** 107–126 (2015).

2. Matter, K. & Balda, M. S. Functional analysis of tight junctions. *Methods* **30,** 228–234 (2003).

3. Zegers, M. M. P., O'Brien, L. E., Yu, W., Datta, A. & Mostov, K. E. Epithelial polarity and tubulogenesis in vitro. *Trends in Cell Biology* **13,** 169–176 (2003).

4. Chen, S., Einspanier, R. & Schoen, J. Transepithelial electrical resistance (TEER): a functional parameter to monitor the quality of oviduct epithelial cells cultured on filter supports. *Histochem. Cell Biol.* **144,** 509–515 (2015).

5. Powell, D. W. Barrier function of epithelia. *Am. J. Physiol.* **241,** G275-88 (1981).

6. Lo, C. M., Keese, C. R. & Giaever, I. Cell-substrate contact: Another factor may influence transepithelial electrical resistance of cell layers cultured on permeable filters. *Exp. Cell Res.* **250,** 576–580 (1999).

7. Anderson, J. M. & Van Itallie, C. M. Cite this article asPhysiology and Function of the Tight Junction. *Cold Spring Harb Perspect Biol* **1,** 2584–2585 (2009).

8. Anderson, J. M. Molecular structure of tight junctions and their role in epithelial transport. *News Physiol. Sci.* **16,** 126–30 (2001).

9. Cartwright, L. *et al.* In vitro placental model optimization for nanoparticle transport studies. *Int. J. Nanomedicine* **7,** 497–510 (2012).

10. Tang, H. *et al.* Uptake and transport of pullulan acetate nanoparticles in the BeWo b30 placental barrier cell model. *Int. J. Nanomedicine* **13,** 4073–4082 (2018).

11. Heaton, S. J. *et al.* The use of BeWo cells as an in vitro model for placental iron transport. *Am. J. Physiol. Physiol.* **295,** C1445–C1453 (2008).

12. Kozlov, M. M. & Mogilner, A. Model of Polarization and Bistability of Cell Fragments. *Biophys. J.* **93,** 3811–3819

13. Roth, S. Mathematics and biology: A Kantian view on the history of pattern formation theory. *Development Genes and Evolution* **221,** 255–279 (2011).

14. Turing, A. M. The chemical basis of morphogenesis. *Bull. Math. Biol.* **52,** 153–197 (1990).

15. Miura, S., Sato, K., Kato-Negishi, M., Teshima, T. & Takeuchi, S. Fluid shear triggers microvilli formation via mechanosensitive activation of TRPV6. *Nat. Commun.* **6,** 1–11 (2015).

16. Blundell, C. *et al.* A microphysiological model of the human placental barrier. *Lab Chip* **16,** 3065–3073 (2016).

17. Lin, L. & Sherman, P. D. Cleaning Data the Chauvenet Way. *SESUG Proc.* 1–11 (2007).

18. Haorah, J., Schall, K., Ramirez, S. H. & Persidsky, Y. Activation of protein tyrosine kinases and matrix metalloproteinases causes blood-brain barrier injury: Novel mechanism for neurodegeneration associated with alcohol abuse. *Glia* **56,** 78–88 (2008).

19. Watson, P. M. D. *et al.* Modelling the endothelial blood-CNS barriers: A method for the production of robust in vitro models of the rat blood-brain barrier and blood-spinal cord barrier. *BMC Neurosci.* **14,** 1–21 (2013).

20. Fischer, R. S. Move your microvilli. *J. Cell Biol.* **207,** 9–11 (2014).

21. Ye, D., Dawson, K. A. & Lynch, I. A TEM protocol for quality assurance of in vitro cellular barrier models and its application to the assessment of nanoparticle transport mechanisms across barriers. *Analyst* **140,** 83–97 (2015).

22. Schindelin, J. *et al.* Fiji: An open-source platform for biological-image analysis. *Nat. Methods* **9,** 676–682 (2012).

23. Rueden, C. T. *et al.* ImageJ2: ImageJ for the next generation of scientific image data. *BMC Bioinformatics* **18,** 1–26 (2017).

24. Cho, M. J., Thompson, D. P., Cramer, C. T., Vidmar, T. J. & Scieszka, J. F. The Madin Darby Canine Kidney (MDCK) Epithelial Cell Monolayer as a Model Cellular Transport Barrier. *Pharmaceutical Research: An Official Journal of the American Association of Pharmaceutical Scientists* **6,** 71–77 (1989).

25. Heaton, S. *et al.* BeWo cells as an in vitro model for iron transport across the placenta. *Am J Physiol Cell Physiol* **295,** 1445–1453 (2007).

26. Aengenheister, L. *et al.* An advanced human in vitro co-culture model for translocation studies across the placental barrier. *Sci. Rep.* **8,** 5388 (2018).

27. Schnittler, H. J. *et al.* Role of actin filaments in endothelial cell-cell adhesion and membrane stability under fluid shear stress. *Pflugers Arch. Eur. J. Physiol.* **442,** 675–687 (2001).

28. Galbraith, G. G., Skalak, R. & Chien, S. Shear stress induces spatial reorganization of the endothelial cell cytoskeleton. *Cell Motil. Cytoskeleton* **40,** 317–330 (1998).

29. Aengenheister, L. *et al.* An advanced human in vitro co-culture model for translocation studies across the placental barrier. **8,** 5388 (2018).

30. Miura, S., Sato, K., Kato-Negishi, M., Teshima, T. & Takeuchi, S. Fluid shear triggers microvilli formation via mechanosensitive activation of TRPV6. *Nat. Commun.* **6,** 8871 (2015).

31. Miura, S., Sato, K., Kato-negishi, M., Teshima, T. & Takeuchi, S. Fluid shear triggers microvilli formation via mechanosensitive activation of TRPV6. *Nat. Commun.* **6,** 1–11 (2015).

32. Naim, H. Y., Dodds, D. T., Brewer, C. B. & Roth, M. G. Apical and basolateral coated pits of MDCK cells differ in their rates of maturation into coated vesicles, but not in the ability to distinguish between mutant hemagglutinin proteins with different internalization signals. *J. Cell Biol.* **129,** 1241–1250 (1995).

33. von Bonsdorff, C. H., Fuller, S. D. & Simons, K. Apical and basolateral endocytosis in Madin-Darby canine kidney (MDCK) cells grown on nitrocellulose filters. *EMBO J.* **4,** 2781–92 (1985).

34. Foerg, C., Ziegler, U., Fernandez-Carneado, J., Giralt, E. & Merkle, H. P. Differentiation restricted endocytosis of cell penetrating peptides in MDCK cells corresponds with activities of Rho-GTPases. *Pharm. Res.* **24,** 628–642 (2007).

35. Gottlieb, T. A., Ivanov, I. E., Adesnik, M. & Sabatini, D. D. Actin microfilaments play a critical role in endocytosis at the apical but not the basolateral surface of polarized epithelial cells. *J. Cell Biol.* **120,** 695–710 (1993).

36. Bomsel, M., Prydz, K., Parton, R. G., Gruenberg, J. & Simons, K. Endocytosis in filter-grown Madin-Darby canine kidney cells. *J. Cell Biol.* **109,** 3243–3258 (1989).

37. Fölsch, H. Regulation of membrane trafficking in polarized epithelial cells. *Current Opinion in Cell Biology* **20,** 208–213 (2008).

38. Zhao, S. *et al.* Monitoring the transport of polymeric micelles across MDCK cell monolayer and exploring related mechanisms. (2012). doi:10.1016/j.jconrel.2011.12.018

39. Vogel, U., Sandvig, K. & van Deurs, B. Expression of caveolin-1 and polarized formation of invaginated caveolae in Caco-2 and MDCK II cells. *J. Cell Sci.* **111 (Pt 6,** 825–32 (1998).

40. Seebach, J. *et al.* Endothelial barrier function under laminar fluid shear stress. *Lab. Investig.* **80,** 1819–1831 (2000).

41. Blundell, C. *et al.* Placental Drug Transport-on-a-Chip: A Microengineered In Vitro Model of Transporter-Mediated Drug Efflux in the Human Placental Barrier. *Adv. Healthc. Mater.* **7,** 1700786 (2018).

42. Chang, S. Y., Weber, E. J., Van Ness, K. P., Eaton, D. L. & Kelly, E. J. Liver and Kidney on Chips: Microphysiological Models to Understand Transporter Function. *Clin. Pharmacol. Ther.* **100,** 464–478 (2016).

Chapter 6. Conclusions and future opportunities

The global aim of this work was to provide insight into the nature of micellar drug delivery into kidney and placenta epithelia. Previous work has provided evidence that triblock copolymers can effectively incorporate hydrophobic drugs and carry these into cells but relatively little is known about the mechanisms underlying their uptake and trafficking or the extent to which they are transported across epithelia.

To further understand such interactions required development and characterisation of a model drug delivery system using poloxamer P407 and its fluorescent derivative (RITC-P407) to form micelles encapsulating DiO as a cargo model. The micelles obtained showed hydrodynamic diameters of 12 nm similar to the ones seen for P407 micelles[1] meaning that the encapsulation did not change significantly the size of the micelles. Furthermore, the micelles showed a temperature dependent self-assembly with a CMT around 25 ºC which differed from that in the literature[2]. This difference was shown to be due to a direct effect of the cargo on the self-assembly and stability of micelles and highlighted the importance of fully characterising polymeric micelles before using for drug delivery studies. Interesting results showing fluorescence resonance energy transfer between RITC-P407 and DiO were found when characterising the micelles which were exploited to monitor cargo release in cells. However, to take these results further the use of imaging techniques such as fluorescence-lifetime imaging microscopy is required. Overall, the study of different characterisation methods facilitated quality control methodology for characterising and understanding the properties of polymeric micelles before using for drug delivery experiments.

The uptake mechanisms of P407-DiO micelles in non-polarised MDCK and BeWo b30 cells were investigated using advanced microscopy techniques. Initially, DiO was found to accumulate into sub-cellular compartments with a distribution pattern distinct from the usual lipid membrane stain resulting from DiO exposure seen when not in micelles[3–5]. This confirmed the carrier function of P407 micelles to facilitate the entry of hydrophobic cargoes. The dye accumulations sites were further investigated by different methods using high content screening, immunofluorescence, and chemical inhibitors. Indication of a new possible internalisation pathway was identified for P407-DiO micelles, namely, by particle diffusion through the membranes. This finding refutes previous results found in literature[6–9]. Furthermore, the lack of evidence of early endosomal accumulation supports the particle diffusion uptake mechanism. To support this finding other imaging techniques capable of resolving single micelles should be explored alongside CLSM[10]. Furthermore, other endocytic pathways that remained unexplored should be studied as multiple cell mechanisms can operate simultaneously, making the identification of single specific mechanism very difficult without discarding others[11].

More complex tissue culture techniques capable of mimicking features found in fully developed placental and kidney barriers were explored. Fully developed *in vitro* barriers were achieved by growing cells in Transwell® systems. The characterisation of these barriers was successfully accomplished using different imaging techniques. However further characterisation using molecular biology can be done to support these findings. The cell polarisation showed that caveolae-mediated endocytosis

is one of the main endocytic pathways by which P407-DiO micelles are taken up by epithelial cells although exploration of other endocytic pathways occurring simultaneously still need to be done. The permeability of barriers to P407-DiO micelles was determined. This gives more insight on one of the main challenges in drug delivery which is overcoming these biological barriers to effectively transport therapeutics into specific organs or tissues[12,13]. Furthermore, preliminary data were obtained using a microfluidics-based *in vitro* model to promote cell differentiation following initial optimisation. Initial indications of spatial reorganisation of cells were detected as well as an accelerated uptake of P407-DiO micelles in cells grown under dynamic conditions. Further characterisation of these features as well as a full comparison with the experiments and results of non-polarised cells are still needed. However, the morphological and mechanistic differences seen so far already suggest the importance of developing models mimicking physiological conditions found *in vivo*, such as placenta or kidney-on-a-chip models[14,15], to assess particle transport and uptake across epithelia.

The findings obtained in this work represent important first steps towards the understanding and development of polymeric micelle-based drugs as well as the appropriate *in vitro models* to assess their interactions with the human body.

References

1. Deller, R. C. *et al.* Functionalised triblock copolymer vectors for the treatment of acute lymphoblastic leukaemia. *Mol. Pharm.* **14**, 722–732 (2017).

2. Alexandridis, P., Holzwarthf, J. F. & J, T. A. H. Micellization of Poly(ethylene oxide)-Poly(propylene oxide)-Poly(ethylene oxide) Triblock Copolymers in Aqueous Solutions Thermodynamics. *Macromolecules* **27**, 2414–2425 (1994).

3. Hume, R. I. & Honig, M. G. Fluorescent Carbocyanine Dyes Allow Living Neurons of Identified Origin to Be Studied in Long-Term Cultures. *J. Cell Biol.* **103**, 171–187 (1986).

4. Höppner, M., Luhm, J., Schlenke, P., Koritke, P. & Frohn, C. A flow-cytometry based cytotoxicity assay using stained effector cells in combination with native target cells. *J. Immunol. Methods* **267**, 157–163 (2002).

5. Ragnarson, B., Bengtsson, L. & Hægerstrand, A. Labeling with fluorescent carbocyanine dyes of cultured endothelial and smooth muscle cells by growth in dye-containing medium. *Histochemistry* **97**, 329–333 (1992).

6. Sahay, G., Alakhova, D. Y. & Kabanov, A. V. Endocytosis of nanomedicines. *Journal of Controlled Release* **145**, 182–195 (2010).

7. Sahay, G., Batrakova, E. V & Kabanov, A. V. Different internalization pathways of polymeric micelles and unimers and their effects on vesicular transport. *Bioconjug. Chem.* **19**, 2023–2029 (2008).

8. Verkade, P., Harder, T., Lafont, F. & Simons, K. Induction of caveolae in the apical plasma membrane of Madin-Darby canine kidney cells. *J. Cell Biol.* **148**, 727–739 (2000).

9. Vogel, U., Sandvig, K. & van Deurs, B. Expression of caveolin-1 and polarized formation of invaginated caveolae in Caco-2 and MDCK II cells. *J. Cell Sci.* **111 (Pt 6**, 825–32 (1998).

10. Polishchuk, R. S. *et al.* Correlative light-electron microscopy reveals the tubular-saccular ultrastructure of carriers operating between Golgi apparatus and plasma membrane. *J. Cell Biol.* **148**, 45–58 (2000).

11. Canton, I. & Battaglia, G. Endocytosis at the nanoscale. *Chemical Society Reviews* **41**, 2718–2739 (2012).

12. Blanco, E., Shen, H. & Ferrari, M. Principles of nanoparticle design for overcoming biological barriers to drug delivery. *Nat. Biotechnol.* **33**, 941–51 (2015).

13. Muro, S. Challenges in design and characterization of ligand-targeted drug delivery systems. *J. Control. Release* **164**, 125–137 (2012).

14. Chang, S. Y., Weber, E. J., Van Ness, K. P., Eaton, D. L. & Kelly, E. J. Liver and Kidney on Chips: Microphysiological Models to Understand Transporter Function. *Clin. Pharmacol. Ther.* **100**, 464–478 (2016).

15. Blundell, C. *et al.* Placental Drug Transport-on-a-Chip: A Microengineered In Vitro Model of Transporter-Mediated Drug Efflux in the Human Placental Barrier. *Adv. Healthc. Mater.* **7**, 1–9 (2018).

Appendix A

Fiji Batch processing

Intensity distribution proximal to nuclei was measured using MIA, a workflow automation and object analysis plugin for the image processing platform, Fiji [1,2,3]. First, noise in the blue fluorescence channel was removed using a 2D Gaussian filter (σ=1px). This was then binarised using a 3D-modified version of the stock Fiji local mean threshold function, with applied threshold set to 0.75x the automatically calculated version and a minimum threshold value of 250 greyscale units. Noise in the binarised image was reduced using a 2D median filter (σ=4px), sequential binary dilation and erosion steps (σ=2px for both) and a 2D hole filling process. Adjacent nuclei which had become merged into contiguous regions of foreground pixels were split using a 3D distance-based watershed transform[4]. Remaining regions of contiguous pixels in 3D space were converted to MIA "objects". Small nuclei objects were assumed to correspond to false detection events, so were excluded from further analysis. Mean fluorescence intensity was measured separately for green and red channels in two regions of the image: (1) In pixels within 3px of the nuclear object surface and (2) in all remaining pixels except those coincident with the nucleus itself. In addition to this, the intensity-weighted distance of the fluorescent signal from the nuclear surface was also measured for green and red channels. This metric

reported both how close the signal was to the nucleus (the mean distance value) and how disperse it was (the standard deviation of the distance).

1 Rueden, C. T.; Schindelin, J. & Hiner, M. C. *et al.* (2017), "ImageJ2: ImageJ for the next generation of scientific image data", *BMC Bioinformatics* **18** 529

2 Schindelin, J.; Arganda-Carreras, I. & Frise, E. *et al.* (2012), "Fiji: an open-source platform for biological-image analysis", *Nature methods* **9(7)** 676-682

3 Cross, S. (13 December 2018), “Modular Image Analysis v0.2.1”, *Zenodo*, doi: 10.5281/zenodo. 2616081

4 Legland, D.; Arganda-Carreras, I. & Andrey, P. (2016), "MorphoLibJ: integrated library and plugins for mathematical morphology with ImageJ", *Bioinformatics* **32(22)** 3532-3534

Appendix B

MATLAB code

```
clc;
format compact;
close ALL;
%-------------------------------------------------------------
%step 1, import data from excel file
%% matrix for each timepoint
J=reshape(GREEN_IMINT_DISTRNUCLEI_MEAN_INT_INRANGE,10,10,6);%cada
columna es letra-numero,cada matriz es una letra
Jt0=reshape(J(:,10,:),10,6);
Jt1=reshape(J(:,9,:),10,6);

Jt2=reshape(J(:,8,:),10,6);
Jt3=reshape(J(:,7,:),10,6);
Jt4=reshape(J(:,6,:),10,6);
Jt5=reshape(J(:,5,:),10,6);
Jt6=reshape(J(:,4,:),10,6);
Jt7=reshape(J(:,3,:),10,6);
Jt8=reshape(J(:,2,:),10,6);
Jt26=reshape(J(:,1,:),10,6);
%% calculations
%mean
Jm=mean(J);
Jt0m=reshape(Jm(:,10,:),1,6);
Jt1m=reshape(Jm(:,9,:),1,6);
Jt2m=reshape(Jm(:,8,:),1,6);
Jt3m=reshape(Jm(:,7,:),1,6);
Jt4m=reshape(Jm(:,6,:),1,6);
Jt5m=reshape(Jm(:,5,:),1,6);
Jt6m=reshape(Jm(:,4,:),1,6);
Jt7m=reshape(Jm(:,3,:),1,6);
Jt8m=reshape(Jm(:,2,:),1,6);
Jt26m=reshape(Jm(:,1,:),1,6);
%std dev
Js=std(J);
Jt0s=reshape(Js(:,10,:),1,6);
Jt1s=reshape(Js(:,9,:),1,6);
Jt2s=reshape(Js(:,8,:),1,6);
Jt3s=reshape(Js(:,7,:),1,6);
Jt4s=reshape(Js(:,6,:),1,6);
Jt5s=reshape(Js(:,5,:),1,6);
Jt6s=reshape(Js(:,4,:),1,6);
Jt7s=reshape(Js(:,3,:),1,6);
Jt8s=reshape(Js(:,2,:),1,6);
Jt26s=reshape(Js(:,1,:),1,6);
%% find outliers
[n,p,k] = size(J);
% Create a matrix of mean values by
% replicating the mu vector for n rows
```

```
MeanMat = repmat(Jm,n,1);
% Create a matrix of standard deviation values by
% replicating the sigma vector for n rows
SigmaMat = repmat(Js,n,1);
% Create a matrix of zeros and ones, where ones indicate
% the location of outliers
Jout = abs(J - MeanMat) > (1.96*1)*SigmaMat;
% Calculate the number of outliers in each column
nout = sum(Jout);

Jt0out=reshape(Jout(:,10,:),10,6);
Jt1out=reshape(Jout(:,9,:),10,6);
Jt2out=reshape(Jout(:,8,:),10,6);
Jt3out=reshape(Jout(:,7,:),10,6);
Jt4out=reshape(Jout(:,6,:),10,6);
Jt5out=reshape(Jout(:,5,:),10,6);
Jt6out=reshape(Jout(:,4,:),10,6);
Jt7out=reshape(Jout(:,3,:),10,6);
Jt8out=reshape(Jout(:,2,:),10,6);
Jt26out=reshape(Jout(:,1,:),10,6);
%%
Jt0mpost=mean(Jt0(logical(1-Jt0out)));
Jt1mpost=mean(Jt1(logical(1-Jt1out)));
Jt2mpost=mean(Jt2(logical(1-Jt2out)));
Jt3mpost=mean(Jt3(logical(1-Jt3out)));
Jt4mpost=nanmean(Jt4(logical(1-Jt4out)));
Jt5mpost=mean(Jt5(logical(1-Jt5out)));
Jt6mpost=mean(Jt6(logical(1-Jt6out)));
Jt7mpost=mean(Jt7(logical(1-Jt7out)));
Jt8mpost=mean(Jt8(logical(1-Jt8out)));
Jt26mpost=mean(Jt26(logical(1-Jt26out)));

Jt0spost=std(Jt0(logical(1-Jt0out)));
Jt1spost=std(Jt1(logical(1-Jt1out)));
Jt2spost=std(Jt2(logical(1-Jt2out)));
Jt3spost=std(Jt3(logical(1-Jt3out)));
Jt4spost=nanstd(Jt4(logical(1-Jt4out)));
Jt5spost=std(Jt5(logical(1-Jt5out)));
Jt6spost=std(Jt6(logical(1-Jt6out)));
Jt7spost=std(Jt7(logical(1-Jt7out)));
Jt8spost=std(Jt8(logical(1-Jt8out)));
Jt26spost=std(Jt26(logical(1-Jt26out)));

%corroborate with boxplots
%boxplot(Jt0)




%% plot results
%time vector
t=[[0:8],26];
Jtm=[Jt0mpost,Jt1mpost,Jt2mpost,Jt3mpost,Jt4mpost,Jt5mpost,Jt6mpos
t,Jt7mpost,Jt8mpost,Jt26mpost];
Jts=[Jt0spost,Jt1spost,Jt2spost,Jt3spost,Jt4spost,Jt5spost,Jt6spos
t,Jt7spost,Jt8spost,Jt26spost];

%errorbar(t,Jtm,Jts,'o')
```

```
%% same but with K
K=reshape(GREEN_IMINT_DISTRNUCLEI_MEAN_INT_OUTRANGE,10,10,6);%each
colum is letter-number, each mtx is a number
Kt0=reshape(K(:,10,:),10,6);
Kt1=reshape(K(:,9,:),10,6);
Kt2=reshape(K(:,8,:),10,6);
Kt3=reshape(K(:,7,:),10,6);
Kt4=reshape(K(:,6,:),10,6);
Kt5=reshape(K(:,5,:),10,6);
Kt6=reshape(K(:,4,:),10,6);
Kt7=reshape(K(:,3,:),10,6);
Kt8=reshape(K(:,2,:),10,6);
Kt26=reshape(K(:,1,:),10,6);
%% calculations
%mean
Km=mean(K);
Kt0m=reshape(Km(:,10,:),1,6);
Kt1m=reshape(Km(:,9,:),1,6);
Kt2m=reshape(Km(:,8,:),1,6);
Kt3m=reshape(Km(:,7,:),1,6);
Kt4m=reshape(Km(:,6,:),1,6);
Kt5m=reshape(Km(:,5,:),1,6);
Kt6m=reshape(Km(:,4,:),1,6);
Kt7m=reshape(Km(:,3,:),1,6);
Kt8m=reshape(Km(:,2,:),1,6);
Kt26m=reshape(Km(:,1,:),1,6);
%std dev
Ks=std(K);
Kt0s=reshape(Ks(:,10,:),1,6);
Kt1s=reshape(Ks(:,9,:),1,6);
Kt2s=reshape(Ks(:,8,:),1,6);
Kt3s=reshape(Ks(:,7,:),1,6);
Kt4s=reshape(Ks(:,6,:),1,6);
Kt5s=reshape(Ks(:,5,:),1,6);
Kt6s=reshape(Ks(:,4,:),1,6);
Kt7s=reshape(Ks(:,3,:),1,6);
Kt8s=reshape(Ks(:,2,:),1,6);
Kt26s=reshape(Ks(:,1,:),1,6);
%% find outliers
[n,p,k] = size(K);
% Create a matrix of mean values by
% replicating the mu vector for n rows
MeanMat = repmat(Km,n,1);
% Create a matrix of standard deviation values by
% replicating the sigma vector for n rows
SigmaMat = repmat(Ks,n,1);
% Create a matrix of zeros and ones, where ones indicate
% the location of outliers
Kout = abs(K - MeanMat) > (1.96*1)*SigmaMat;
% Calculate the number of outliers in each column
nout = sum(Kout);

Kt0out=reshape(Kout(:,10,:),10,6);
Kt1out=reshape(Kout(:,9,:),10,6);
Kt2out=reshape(Kout(:,8,:),10,6);
Kt3out=reshape(Kout(:,7,:),10,6);
Kt4out=reshape(Kout(:,6,:),10,6);
Kt5out=reshape(Kout(:,5,:),10,6);
Kt6out=reshape(Kout(:,4,:),10,6);
Kt7out=reshape(Kout(:,3,:),10,6);
```

```
Kt8out=reshape(Kout(:,2,:),10,6);
Kt26out=reshape(Kout(:,1,:),10,6);
%%
Kt0mpost=mean(Kt0(logical(1-Kt0out)));
Kt1mpost=mean(Kt1(logical(1-Kt1out)));
Kt2mpost=mean(Kt2(logical(1-Kt2out)));
Kt3mpost=mean(Kt3(logical(1-Kt3out)));
Kt4mpost=nanmean(Kt4(logical(1-Kt4out)));
Kt5mpost=mean(Kt5(logical(1-Kt5out)));
Kt6mpost=mean(Kt6(logical(1-Kt6out)));
Kt7mpost=mean(Kt7(logical(1-Kt7out)));
Kt8mpost=mean(Kt8(logical(1-Kt8out)));
Kt26mpost=mean(Kt26(logical(1-Kt26out)));

Kt0spost=std(Kt0(logical(1-Kt0out)));
Kt1spost=std(Kt1(logical(1-Kt1out)));
Kt2spost=std(Kt2(logical(1-Kt2out)));
Kt3spost=std(Kt3(logical(1-Kt3out)));
Kt4spost=nanstd(Kt4(logical(1-Kt4out)));
Kt5spost=std(Kt5(logical(1-Kt5out)));
Kt6spost=std(Kt6(logical(1-Kt6out)));
Kt7spost=std(Kt7(logical(1-Kt7out)));
Kt8spost=std(Kt8(logical(1-Kt8out)));
Kt26spost=std(Kt26(logical(1-Kt26out)));

%corroborate with boxplots
%boxplot(Kt0)


%% plot results
%time vector
t=[[0:8],26];
Ktm=[Kt0mpost,Kt1mpost,Kt2mpost,Kt3mpost,Kt4mpost,Kt5mpost,Kt6mpos
t,Kt7mpost,Kt8mpost,Kt26mpost];
Kts=[Kt0spost,Kt1spost,Kt2spost,Kt3spost,Kt4spost,Kt5spost,Kt6spos
t,Kt7spost,Kt8spost,Kt26spost];

%errorbar(t,Ktm,Kts,'x')
figure
subplot(1,2,1)
errorbar(t,Jtm,Jts,'o')
title('GREEN_IMINTENSITYMEAN')
subplot(1,2,2)
errorbar(t,Ktm,Kts,'x')
title('GREEN_IMINT_DISTRNUCLEI_N_PX_OUTRANGE')
```